Magnetic and Structural Properties of Pseudo-1D Substituted Compounds of $Ca_3Co_2O_6$

A
Thesis Submitted
in Partial Fulfillment of the Requirements
for the Degree of
DOCTOR OF PHILOSOPHY
By

GAJENDRA SINGH BISHT
176121101
Under the Supervision of
Prof. DILIP PAL

Department of Physics
Indian Institute of Technology Guwahati
June, 2023

DECLARATION

This is to certify that the thesis entitled "**Magnetic and Structural Properties of Pseudo-1D Substituted Compounds of** $Ca_3Co_2O_6$", submitted by me to the *Indian Institute of Technology Guwahati*, for the award of the degree of DOCTOR OF PHILOSOPHY, is a bonafide work carried out by me under the supervision of Prof. Dilip Pal. The content of this thesis have not been submitted to any other University or Institute for the award of any degree.

Signed: ______________________________

Gajendra Singh Bisht
Department of Physics,
Indian Institute of Technology Guwahati,
Guwahati-781039, Assam, India.

Date: 22/06/2023


भारतीय प्रौद्योगिकी संस्थान गुवाहाटी
Indian Institute of Technology Guwahati

CERTIFICATE

This is to certify that the thesis entitled "**Magnetic and Structural Properties of Pseudo-1D Substituted Compounds of** $Ca_3Co_2O_6$", submitted by Gajendra Singh Bisht (176121101), a research scholar in the *Department of Physics*, *Indian Institute of Technology Guwahati*, for the award of the degree of DOCTOR OF PHILOSOPHY, is a record of an original research work carried out by him under my supervision and guidance. The thesis has fulfilled all requirements as per the regulations of the institute and in my opinion has reached the standard needed for submission. The results embodied in this thesis have not been submitted to any other University or Institute for the award of any degree.

Signed: Dilip Pal

Supervisor: Prof. Dilip Pal
Department of Physics,
Indian Institute of Technology Guwahati,
Guwahati-781039, Assam, India.

Date: 22/06/2023

ACKNOWLEDGMENTS

In science, we stand on the shoulders of giants, but we also rely on the support and encouragement of our peers. I am humbled and grateful for the many people who have helped me along the way, without whom this work would not have been possible. I am grateful for the opportunity to indulge my curiosity in the fascinating field of condensed matter physics. I am honored to have been a small part of this great endeavor, and I am thankful for the many individuals who have supported and encouraged me in my work.

I would like to express my deepest gratitude to my advisor, Prof. D. Pal, for his unwavering support and guidance throughout my doctoral studies. His expertise, patience, and willingness to share knowledge have been invaluable in shaping my research and academic career. His mentorship extended beyond the technical aspects of my research, providing me with valuable advice and support during challenging times. I am truly grateful for his mentorship and friendship.

I would also like to thank my thesis committee members, Prof. D. Pamu, Prof. P. K. Padmanabhan, and Prof. L. M. Kundu, for their insightful feedback and constructive criticism, which helped me to improve my work and broaden my perspective. Their extensive knowledge in the field of condensed matter physics, critical evaluation of my research, and guidance on my career path has been invaluable. I would like to thank the current (Prof. A. Perumal) and former (Prof. P. Poulose and Prof. S. Ghosh) head of the Department of Physics for their generous support for attending conferences. I also acknowledge other faculty members from the Department of Physics, especially Prof. A. Srinivasan and Prof. S. Thota, for stimulating my interest in magnetism. I am also grateful to Dr. Sidananda Sarma and Mr. Aditya Kalita for assisting me in running various instruments and Mr. Basab B. Purkayastha for technical support.

I am deeply grateful to the anonymous reviewer who took the time to review my research paper for my thesis. Your thoughtful and detailed comments have helped me to refine my research and strengthen my arguments. Your expertise and knowledge in the field have been instrumental in guiding me toward a more thorough understanding of the topic. Thank you for your time, effort, and commitment to the advancement of knowledge in our field.

I extended my gratitude towards seniors from Physics department Dr. V. M. Gaikwad, Dr. B. B. Dash, Dr. P. Bahera, Dr. Aakansha, Dr. R. Borah, Mr. Sunil Mohan, Dr. N. Kumar, Dr. Karuna, Dr. S. Goswami, Dr. S. Ghosh, and Dr. S. Lahiri for brotherly gesture and helping me in various ways. I am thankful to my lab mates Beenita di, Pragya, Koushik, Joya, and Amit for the pleasant and peaceful environment in the lab to carry out work. My appreciation extends to my fellow graduate students, postdocs, and lab colleagues Subrata, Manisha, Nitu, Suresh, Shilpi, Jyotirmoi, Rony, Shuvendu, Vikki, Pushpesh, Pushpanjali, Akanshu, Suchit, Ravi, Shaona, Shiva, Alok, Didwamsha, Dev, Harekrushna, Somnath, and Arijit, who provided a stimulating and supportive research environment. I am grateful for the discussions, collaborations, and friendships that we have formed over the years. Your feedback and insights have been invaluable in shaping my research, and I will always cherish the memories of the long hours spent in the lab, brainstorming ideas, and discussing results.

I also acknowledge the DST India for granting PPMS under FIST-II Program (SR/FST/PSII-037/2016), CIF IIT Guwahati for XRD, FESEM, XPS facility, and MHRD for teaching assistantship.

Last but not the least my deepest gratitude to my family, parent, sister, and wife for making things easier for me so that I could make a balance between research and personal life, and this work is dedicated to them. Their support and understanding have been the foundation of my success. I am forever grateful for their love and support and for always believing in me.

Thank you all for your contributions to this work and for being a part of my journey.

Sincerely
Gajendra Singh Bisht

SYNOPSIS

Low-dimensional magnetic systems are in the limelight due to their non-trivial features originating from strong electron correlation and quantum effects. Apart from the simplest long-range order observed in conventional magnetic materials, complex magnetic phases arising due to the degeneracy in the ground state have been seen in low-dimensional systems. In addition to the complex magnetic phases, fascinating features such as quantum-phase transition, superconductivity, large anisotropy, quantum Hall effect, and multiferroicity are also observed in these systems. Owing to these features, the search for pseudo-1D systems started picking up momentum. In this kind of system, the crystal structure is three-dimensional, but it contains infinite parallel chains of magnetic ions. An enormously strong intra-chain interaction compared to inter-chain interaction allows us to probe the low-dimensionality effects.

The physics of low-dimensional systems becomes much more interesting if the magnetic ions are arranged on a frustrated lattice (triangular, kagome, and pyrochlore lattice). In this category, the pseudo-1D spin chain compounds of structure $A_3BB'O_6$ are classic examples. Here **A** is a non-magnetic ion, and **B**, **B′** are transition metals. Such systems acquired geometrical frustration due to the arrangement of magnetic ions on a triangular lattice. Furthermore, the flexibility of $A_3BB'O_6$ in accompanying a wide range of elements provides an opportunity to deal with the different aspects of low-dimensional magnetism. Some of the unique features of this class of materials are strong Ising-like anisotropy, spin density wave order, large coercivity (55 T), colossal magnon gaps, quantum tunneling of magnetization, superparamagnetic behavior, and multiferroicity. Among the family of $A_3BB'O_6$ structure, the $Ca_3Co_2O_6$ (A = Ca, B and B′ = Co) compound was intensively studied due to the strong Ising-like behavior, dynamic magnetic structure, and quantum magnetic phenomena. The discovery of quantum tunneling of magnetization in this system was new because earlier such features were limited to molecular magnets only. Thus, this system allows us to probe the quantum effects experimentally in the family of magnetic oxides. In addition, the coexistence of short-range and long-range order in this system leads to a complex phase diagram.

The $Ca_3Co_2O_6$ system crystallizes in the rhombohedral structure, having space group $R\bar{3}c$. In the $R\bar{3}c$ setting, the Ca(**A**), Co1(**B**), Co2(**B′**), and O atoms were fixed at 18e

(x, 0, 0.25), $6b$ (0, 0, 0), $6a$ (0, 0, 0.25), and $36f$ (x, y, z) sites, respectively. The crystal structure contains spin chains of alternating Co1O$_6$ octahedra and Co2O$_6$ trigonal prisms running parallel to the c-axis. Characteristic features of low-dimensional materials can be expected in this system because the intra-chain distance of Co ions is approximately half of the inter-chain separation. The crystal field effect leads to dissimilar spin states of Co^{3+} ions at two different environments. In the octahedral site, the Co^{3+} ions are in the low spin (S = 0) state, while in the trigonal prism environment, they are in the high spin (S = 2) state. The intra-chain Co ions are coupled through a strong ferromagnetic interaction ($J_1 \approx 25$ K) along the chain, while the inter-chain antiferromagnetic coupling is relatively weak ($J_2 \approx 1$ K). Furthermore, the weak inter-chain antiferromagnetic coupling between magnetic ions arranged on a triangular lattice in the ab-plane leads to geometrical frustration in this system. The system undergoes an incommensurate amplitude-modulated spin density wave structure below 25 K (T_{c1}), which, over a time scale of few hours, partially transforms into commensurate antiferromagnetic phase. Furthermore, suppression of spin density wave phase and stabilization of commensurate antiferromagnetic structure was also observed in the pressure-dependent neutron diffraction study at high-pressure P = 2.1 GPa. In addition to the dynamic magnetic transition, coexistence of short-range and long-range magnetic order was also observed below 10 K (T_{c2}). The novelty of this material is the observed successive steps in the isothermal M-H curves, which correspond to non-equilibrium state. Origin of such features in the M-H curves is controversial because their appearance is strongly dependent on the magnetic field sweep rate. However, these steps are reminiscent of the quantum tunneling of magnetization occurring in molecular magnets. Thus, this system provides an ideal opportunity to study the quantum magnetic phenomena in the family of oxides.

In recent years, low-dimensional materials that exhibit geometrical frustration have attracted tremendous attention due to their potential application in topological magnetism, spintronic, and thermal memory devices. Therefore, the unique combination of low-dimensional features and geometrical frustration observed in Ca$_3$Co$_2$O$_6$ can contribute to the future development of this material. It is also clear that the Ca$_3$Co$_2$O$_6$ system exhibits a complex magnetic structure due to the reduced dimension of spin interactions and competing lattice, spin, electric, and orbital degrees of freedom. Additionally, the magnetic structure of the system is extremely sensitive to external perturbations such as temperature, pressure, and magnetic field. The unconventional features and the dynamic magnetic structure of the system are indicative of degeneracy in the magnetic ground state; therefore, the $Ca_3Co_2O_6$ system is ideal for a thorough understanding of low-dimensional magnets, which is a topic of enormous interest from condensed matter physics point of view.

In addition to the external perturbation effects, the flexibility of the $A_3BB'O_6$ structure in accompanying a wide range of elements provides additional degree of freedom in modifying the magnetic structure of the system by an appropriate amount of lower/higher valence ions substitution. It is concluded that depending on the alignment of dopant ion moment with Co ion moment, the dominant interaction is antiferromagnetic for Fe, Cr, and Mn substitution and ferromagnetic for Ir and Rh substitution. Due to the dominance of ferromagnetic/antiferromagnetic interaction with substitution, the ground state degeneracy is lifted, and the exotic magnetic features of the system are gradually suppressed.

As it is clear that the transition metals substitution in this system leads to a strong magnetoelectric coupling which has potential applications but dramatically influences the characteristic feature of the system. Thus modifying the magnetic structure of this system with magnetic dopants no longer be a good choice from condensed matter physics point of view, and strongly suggested to look for non-magnetic dopants, which may have little effect on the intra-chain and inter-chain interactions so that the key features remain unaltered. As suggested by Ruan *et al.*, the non-magnetic Sc substitution for Co2 ions (up to 60 %) does not influence the intra-chain ferromagnetic interaction. However, the doping effects of other non-magnetic ions in this system are still unexplored.

Considering all these ideas, this system is ideal for exploring the novel aspects of magnetism and provides an ideal platform to play around with the metastable phases of the system. In addition, the Co ion in this system has the possibility of spin state transition when a higher/lower valence ion is substituted. Thus, the magnetic and electronic structure of the system is extremely sensitive to external perturbation and doping content. This thesis is focused on understanding the complex magnetic and electronic structure of $Ca_3Co_2O_6$ and the substituted (magnetic/non-magnetic) compound through experimental results and theoretical predictions. The experimental part involves the characterization of structural, magnetic, and electronic states of these samples by X-ray diffraction, Raman, magnetization, and X-ray photoelectron spectroscopy measurements. On the other hand, these features were theoretically predicted by first-principles-based density functional theory calculations results.

This work is organized into 6 chapters:

1. Introduction
2. Experimental and Computational methods
3. $Ca_{3-x}Dy_xCo_2O_6$: Evidence of Cluster-Glass-like Freezing
4. $Ca_3Co_{2-x}Mg_xO_6$: Spin-state Transition of Co ion $\left(S = 2 \rightarrow S = \frac{5}{2}\right)$
5. $Ca_3Co_{2-x}Bi_xO_6$: Chemical Disorder effect and Multilevel thermal memory cell
6. Summary and Conclusions

A brief description of each chapter is as follows:

Chapter 1 introduces low-dimensional magnetism and its technological importance, followed by a detailed discussion on pseudo-1D spin chain compounds of structure $A_3BB'O_6$. The fundamental aspects of magnetism, such as long-range order and spin models also discussed here. It is well known that frustrated magnets often undergo the short-range spin-glass state at low temperatures; therefore, this chapter also discusses the key features of the spin-glass system along with the associated models such as the Edwards-Anderson, Sherrington-Kirkpatrick, and Cluster-glass model. Furthermore, based on previous studies, a detailed description of structural, magnetic, electrical, and magneto-dielectric features of the studied compound $Ca_3Co_2O_6$ is also given here. Finally, the motivation to undertake this work has also been discussed.

Chapter 2 describes the various experimental tools used to carry out this work. The basic principle of the solid-state reaction method, with the necessary precaution that should be taken care during the sintering process is discussed here. A brief description of various instruments such as X-ray diffractometer, Raman spectrometer, Field Emission Scanning Electron Microscope, XPS spectrometer, and Physical Property Measurement System, and their working principle is also given here. Furthermore, the operating condition of these instruments is also provided here. It also briefly discusses the computational methods used for magnetic and electronic structure determination of the studied compounds.

This chapter also covers the various implementation of density functional theory, such as the plane wave basis, norm-conserving pseudopotentials, ultrasoft pseudopotentials, and the projector augmented wave. Here we used the projector augmented wave method implemented in the Vienna ab initio simulation package, commonly known as VASP. The essential input files required to run the VASP calculations are also discussed here.

Chapter 3 is the first working chapter, starting with the synthesis technique of parent $Ca_3Co_2O_6$ and its Dy-doped substituents, followed by the analysis of the X-ray diffraction data of these samples to determine the crystal structure. Here we found evidence of cluster-glass-like freezing phenomena in these samples and proposed the procedure for detecting the softness/hardness of ferromagnetic material whose transition lies at non-zero field. The observed X-ray diffraction, XPS, and magnetization results indicate partial transform of the Co^{3+} ion into Co^{2+} ion with Dy substitution to maintain charge neutrality. Magnetic properties were found to be sensitive to Dy substitution, due to which the transition temperatures T_{c1} and T_{c2} decreases, and the glassy behavior gradually suppressed with Dy concentration. The higher experimental value of μ_{eff} for Dy-doped samples indicates the strong anisotropic magnetic character identified from the non-equilibrium nature of magnetic properties. Isothermal magnetization curve depicts step-like change indicative of the first-order transition, which decreases with the increase of substitution. The Brillouin function was used to determine the 'spins', participating at this first-order transition $\left(\mathrm{J}\left(\frac{1}{2}\right) \rightarrow \mathrm{J}\left(\frac{3}{2}\right)\right)$. Relaxation measurements revealed the existence of short-range Cluster-glass-like behavior. Analyzing the results using Vogel-Fulcher law shows that the Vogel-Fulcher temperature (T_0) and the relaxation time are around 10 K and 10^4 sec, respectively.

Chapter 4 deals with the spin-state transition of Co ion $\left(\mathrm{S} = 2 \rightarrow \mathrm{S} = \frac{5}{2}\right)$ in hole substituted (Mg) 1D chain of $Ca_3Co_2O_6$ apparent in the magnetic susceptibility, XPS, and first-principles study. We have prepared the polycrystalline samples by standard solid-state reaction method. Rietveld refinement of XRD data confirms that the doped Mg ion occupies the high spin trigonal prism site without altering its 1D character, which lefts its mark on the M-H curves. M-T ZFC-FC data reveals that the transition temperatures T_{c1} and T_{c2} remain unaffected with the doping content of Mg, whereas the μ_{eff} increases and θ decreases. The increase in μ_{eff} and decrease in θ is associated with the induced Co^{4+} (S = 5/2) ions arising due to the substitution of Mg^{2+} ions. Our study shows a reasonable agreement between effective magnetic moment (μ_{eff}) determined from the

Curie–Weiss fit with that from the XPS analysis and first-principles calculations study. We have attributed the decrease in positive intra-chain exchange interaction constant ($J_1/\ k_B$) to the antiferromagnetically coupled induced Co^{4+} ions (S = 5/2) arising from the Mg^{2+} ions substitution. The in-field metamagnetic transitions in the isothermal M-H curves below the critical field (H_c) have been accurately mapped and successfully explained by the change in magnetic entropy ($\mathit{\Delta S}$) calculations and Arrott plots. We also examine the effect of Mg substitution on the magnetic and electronic structure of $Ca_3Co_2O_6$ by first-principles calculations. It involves generalized gradient approximation with Coulomb interaction (U) in exchange-correlation energy functional. Electronic structure study reveals hole-type doping of Mg atom, and the Fermi level (E_F) shifts below. Density of state and band structure calculation indicates strong hybridization between partial states of Co-3d and O-2p orbitals for the Mg-doped compound due to which the band crossing at Fermi level is observed, and a hole-type Fermi surface is formed.

Chapter 5 mainly discusses the technological importance of parent $Ca_3Co_2O_6$ and its Bi-doped substituents in thermal memory cell. We prepared polycrystalline samples of $Ca_3Co_{2-x}Bi_xO_6$ (x = 0, 0.05, 0.1, 0.15, and 0.2) by standard solid-state reaction method and proposed a new route of multilevel storage based on thermal manipulation that can be utilized in thermal memory cell to make it feasible. Rietveld refinement of XRD data confirms the single-phase formation, and the compound crystallizes in the Rhombohedral structure with space group $R\bar{3}c$. The bond-length analysis indicates the interplay of reduced dimensionality and bond randomness effect. Magnetic properties were found to be sensitive to Bi-substitution, due to which the T_{c1} decreases while the T_{c2} increases. The μ_{eff} decreases monotonously with Bi-content while the θ shows unusual dependence on Bi-concentration. The phenomena of virgin M-H curves lying outside the M-H loop suggested the kinetic arrest of spin dynamics of the system. The cyclic temperature experiments have been performed to demonstrate the recurrence in the multilevels of the relaxed magnetization paths, which was not noticed earlier. The exquisite reproducibility of relaxed magnetization as a function of temperature under a non-equilibrium phase makes such a phenomenon unique. We showed that the information could be stored in terms of a constant magnetization value corresponding to each temperature below T_{c2}, which is easily recoverable with temperature cycling. Our results suggested that this new approach will be much more efficient than the reported ones and has the potential to make thermal memory devices faster and stable. This work will lead to the exploration in a variety of such materials having non-ergodicity as a possible route of thermal memory storage which should eventually lead a new outlook toward data storage.

Chapter 6 presents the summary and conclusion of the work carried out in this thesis. It also provides the future scope of the current work.

Contents

List of Figures

List of Tables

Chapter 1

Introduction

Investigation of quantum magnetic phenomena in the reduced spatial dimension of spin interactions is an advanced field of research from a fundamental science angle and application point of view. Also, it provides an ideal platform for a physicist to study the quantum effects experimentally and describe such novel phenomena using theoretical low-dimensional spin models. Ernst Ising was the first who introduced the importance of dimensionality in the one-dimensional (1D) chain of spins and concluded that no long-range ordered state is possible above absolute zero temperature [1]. The absence of long-range ordering in the 1D system at finite temperatures leads to peculiar phenomena which are not possible in three dimensions. Although it was impossible to construct an ideal 1D magnetic system experimentally, therefore, the search for pseudo-1D materials started picking up momentum to demonstrate these unconventional features. In the pseudo-1D systems, although the crystal structure is three-dimensional, it contains an infinite number of parallel chains of magnetic ions with strong intra-chain coupling (J) and a relatively much weaker inter-chain coupling (J'). An enormously large value of J/J' ratio allows an experimentalist to probe the low-dimensionality effects along with the long-range magnetic order over an accessible range of temperature. Therefore, the pseudo-1D systems are ideal for studying the combined effects of low-dimensional quantum phenomena and long-range order, a topic of enormous interest in condensed matter physics. In this category, the pseudo-1D spin-chain compounds are the classical examples acquiring exotic quantum magnetic phenomena such as superconductivity [2–5], quantum-phase transition [6, 7], multiferroicity [8–10], quantum Hall effect [11, 12], spin-density wave order (SDW) [13–16], and large anisotropy [17–19]. Considering these results, this class of materials alone can cover most of the field of quantum magnetism and is also important for application purposes. Therefore, discovering new low-dimensional materials is essential for an insightful understanding of strongly correlated electron systems and quantum magnetism, which can bring tremendous progress in the field of condensed matter physics.

In addition to the success of pseudo-1D spin-chain compounds in revolutionizing the field of experimental condensed matter physics, most of the materials belonging to this family have been found to follow the low-dimensional spin models. It is well known that the numerical and analytical treatment of magnetic systems to obtain various structural and magnetic parameters is greatly simplified when the magnetic interactions are confined. Section 1.1 describes some simplified spin models for low-dimensional systems. In addition, as the peculiar features in correlated electron systems strongly depends on its microscopic characteristics, such as the geometry of the system, nature of magnetic interactions, electronic structure, and spin arrangements, therefore, it opens up the scope to study these effects using first-principles based density functional theory calculations. Such studies at the microscopic level can be helpful in the description of puzzling features of quantum magnetism. Thus, this class of materials potentially gives scope for a thorough understanding of the unsolved issue of quantum magnetism from both theoretical and experimental perspectives.

Among the family of pseudo-1D spin-chain compounds, a particular class of materials of structure $A_3BB'O_6$ (**A** is a non-magnetic ion, and **B** and **B′** can be transition metals and non-magnetic ions) has drawn tremendous attention due to the flexibility of accompanying a wide range of elements. Thus, it provides an enormous number of materials with unique properties of crystal field effects, strong anisotropy, and quantum effects, which can be helpful in solving the issue of modern-day condensed matter physics. Compounds belonging to the $A_3BB'O_6$ structure crystallize in the rhombohedral structure of space group $R\bar{3}c$ [9, 14]. However, if the **B** and **B′** are Jahn-Teller active ions, the compound

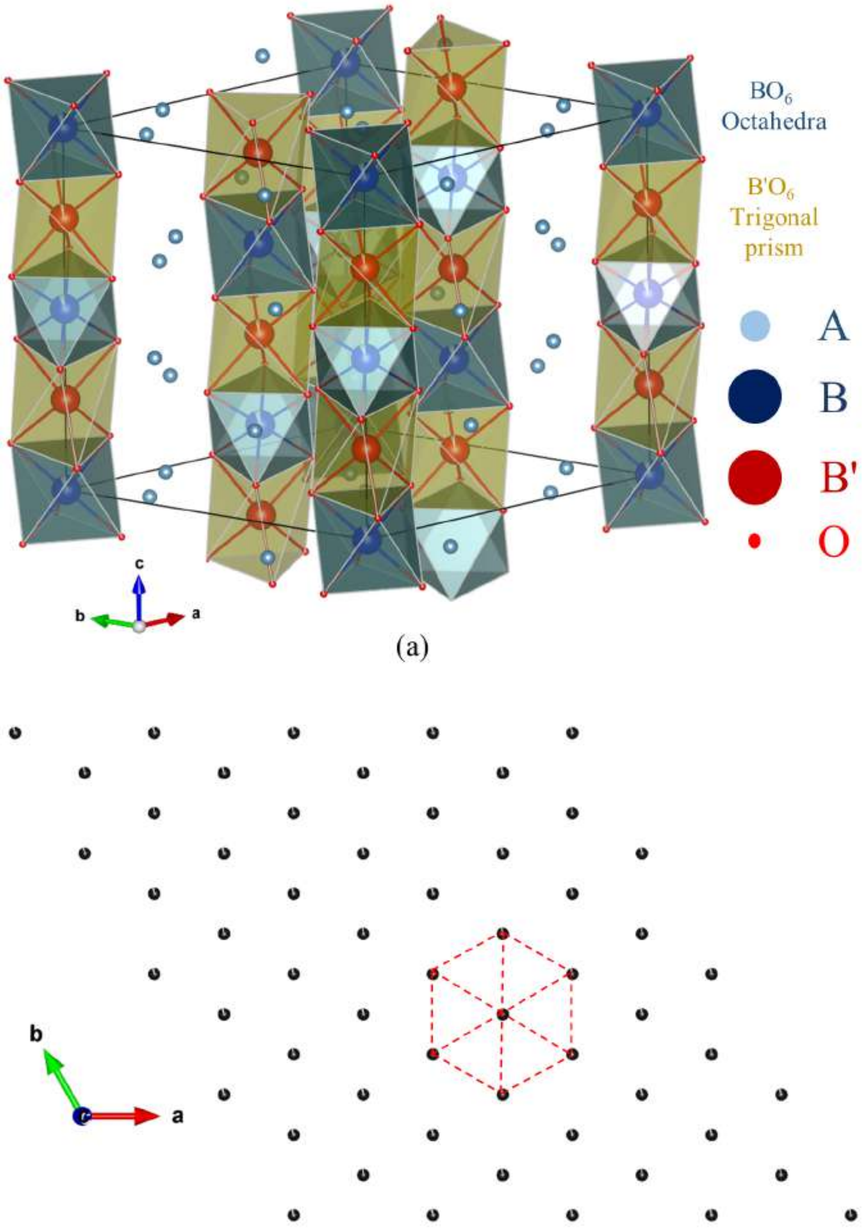

(a)

(b)

FIGURE 1.1: (a) Crystal structure of pseudo-1D spin-chain compound of type $A_3BB'O_6$ formed by the chains of alternating BO_6 octahedra and $B'O_6$ trigonal prisms along the c-axis (b) projection view of these chains on the ab plane.

undergoes monoclinic distortion (space group $C2/c$). In the rhombohedral setting, the **A**, **B**, **B′**, and O atoms were fixed at $18e$ (x, 0, 0.25), $6b$ (0, 0, 0), $6a$ (0, 0, 0.25), and $36f$ (x, y, z) sites, respectively. The crystal structure consists of an infinite number of magnetic chains of alternating BO_6 octahedra and $B'O_6$ trigonal prisms running along the c-axis, separated by non-magnetic **A** ion (Fig. 1.1(a)). As shown in the projection view on the ab plane (Fig. 1.1(b)), these chains are arranged on a triangular lattice, which leads to geometrical frustration in the system. In the $A_3BB'O_6$ structure, the **A** ion is divalent (2+), whereas the **B** and **B′** can be either both trivalent (3+) or tetravalent (4+) and divalent (2+), respectively. The crystal field variation creates a low-spin (LS) state at the octahedral site, and a high-spin (HS) state at the trigonal prism environment. The pseudo-1D character in this type of structure is primarily due to stronger intra-chain interaction of magnetic ions and a comparatively much weaker inter-chain interaction. Thus, the emergence of exotic magnetic features in this system is a result of frustrated geometry with low-dimensional nature. Some of the important features of materials belonging to this family are strong ferromagnetic anisotropy [20], superparamagnetic behavior [21], enormously large coercive field [22], strong Ising behavior [23], multiferroicity [24], magnetic field-dependent dynamic ordering [25], colossal spin-wave gap [26], and quantum tunneling of magnetization (QTM) [27].

This thesis investigates the structural, magnetic, and electronic properties of the $Ca_3Co_2O_6$ and its substituents, a material belonging to the $A_3BB'O_6$ family (A = Ca, B and B′ = Co). In this system, the crystal field splitting leads to different spin states LS (S = 0) and HS (S = 2) of Co^{3+} ions at the octahedral (Co1) and trigonal prism (Co2) environments, respectively [28, 29]. Furthermore, the Co2 ions along the chain are coupled through a strong ferromagnetic interaction, while the inter-chain antiferromagnetic coupling is comparatively much weaker [30, 31]. The interplay of competing interactions with spin-orbit coupling leads to strong Ising-like anisotropy along the c-axis [18]. In addition, earlier studies suggested that the spin chains can be treated as a giant moment, and the overall system can be considered as two-dimensional Ising spins (↑ or ↓) [32–34]. Therefore, these results allow the description of the intriguing magnetism of this system by simplified spin models. The following section discusses a few of the simplified low-dimensional spin models.

1.1 Spin Models

In condensed matter physics, the electrons are well localized at each site of the lattice; therefore, the magnetism of the system can be well described by considering spin degrees of freedom only. The model Hamiltonian that describes the nearest neighbor exchange interaction between spins is given by

$$\mathcal{H} = -\sum_{ij} \left[J_x S_i^x S_j^x + J_y S_i^y S_j^y + J_z S_i^z S_j^z \right] \tag{1.1}$$

where J is the strength of the exchange interaction between nearest neighbor (i^{th} and j^{th}) pair of spins. It is a three-dimensional spin model commonly known as the Heisenberg XYZ model. The $J > 0$ corresponds to a ferromagnetic ground state with parallel spins, while for $J < 0$, the ground state is antiferromagnetic with antiparallel spins. Some of the spin models depending on J values are summarized in Table 1.1. There is no constraint on the spatial dimension of the lattice, and these models can apply to 1, 2, or 3-dimensional systems. However, the classification is based on the dimensionality of the magnetic order parameter. In the XXX model, the exchange interactions are isotropic ($J_x = J_y = J_z$). However, for the XY and Ising models, the exchange interaction has planar and uniaxial anisotropy, respectively.

TABLE 1.1: Some of the spin models for magnetic systems.

Model	Type	Magnetic Order Parameter	Spin Dimension
XYZ	Anisotropic	$J_x \neq J_y \neq J_z$	3
XXX	Isotropic	$J_x = J_y = J_z$	3
XY	Planar anisotropy	$J_x = J_y \neq 0, J_z = 0$	2
Ising	Uniaxial anisotropy	$J_x = J_y = 0, J_z \neq 0$	1

It is well known that the long-range magnetic order in a system is a three-dimensional effect. For the low dimensional systems (1D or 2D lattice), the ordered state is not possible above absolute zero temperature for both XY and Heisenberg models. On the other hand, for the Ising model in a 2D square lattice, the phase transition is observed at finite temperatures [35, 36]. The following subsections discuss the Ising model in one and two dimensions.

1.1.1 1D Ising model

It is the simplest model in magnetism, consisting of a linear chain of spins that can be either up (↑) or down (↓) [1]. In the 1D Ising model, the spin and spatial dimensions are one, and each spin can only interact with its nearest neighbors. The greatest advantage of this model is that it can be solved analytically. Let us consider a linear chain of N spins where each spin can have a value of either +1 for the up configuration or -1 for the spin down configuration. Thus, a total of 2^N spin configurations are possible for the system. The Hamiltonian for this system is defined as

$$\mathcal{H} = -J\sum_{i=1}^{N} S_i S_{i+1} - B\sum_{i=1}^{N} S_i \tag{1.2}$$

where the first term represents the exchange interaction energy of the spins (S_i and $S_{i+1} = \pm 1$), and the second term stands for the coupling of spins with external magnetic field B. For simplicity, consider the case of the ferromagnetic Ising chain ($J > 0$) in which spins are aligned parallel (Fig. 1.2) under the periodic boundary condition

$$S_{N+1} = S_1. \tag{1.3}$$

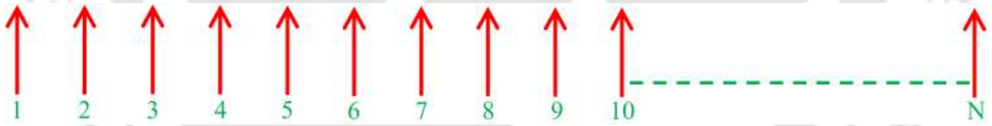

FIGURE 1.2: One-dimensional ferromagnetic Ising chain.

The partition function Z is given by

$$Z = \sum e^{-\beta\mathcal{H}} = \sum exp\left[\beta\left(J\sum_{i=1}^{N} S_i S_{i+1} + B\sum_{i=1}^{N} S_i\right)\right] \tag{1.4}$$

where $\beta = \frac{1}{kT}$ and $S_i = \pm 1$. Using the transfer matrix method [37], the partition function can be written as

$$Z = (\lambda_+)^N + (\lambda_-)^N \tag{1.5}$$

where

$$\lambda_\pm = e^{\beta J}\left[\cosh(\beta B) \pm \sqrt{\cosh^2(\beta B) - 2e^{-2\beta J}\sinh(2\beta J)}\right]. \tag{1.6}$$

The Helmholtz free energy F can be obtained by using the relation

$$F = -k_{\mathrm{B}} T \ln Z. \tag{1.7}$$

In the thermodynamic limit ($N \to \infty$), the second term in Eq. 1.5 is negligible so that the free energy per spin can be expressed as

$$\frac{F}{N} = -k_{\mathrm{B}} T \ln \lambda_{+} = -J - k_{\mathrm{B}} T \ln \left[\cosh(\beta B) + \sqrt{\cosh^2(\beta B) - 2e^{-2\beta J} \sinh(2\beta J)} \right]. \tag{1.8}$$

The average magnetization can be obtained from the free energy expression

$$\frac{M}{N} = -\frac{1}{N} \frac{\partial F}{\partial B} = \frac{\sinh(\beta B)}{\sqrt{\cosh^2(\beta B) - 2e^{-2\beta J} \sinh(2\beta J)}}. \tag{1.9}$$

It is clear from Eq. 1.9 that at zero magnetic field ($B = 0$), the average magnetization vanishes for all the temperatures. Thus, the 1D Ising model does not exhibit ferromagnetism.

1.1.2 2D Ising model

In 1944, Onsager solved the Ising model on a 2D square lattice for the zero magnetic field case [35]. It is predicted that long-range magnetic ordering can occur at finite temperatures. To understand this, let us consider a 2D square lattice of $L \times L$ sites, where each site represents spin $S_{i,j}$ (i and j run from 1 to L) that can be either +1 or -1. The boundary condition for this system is that the end points of each row and column are connected. Considering the nearest-neighbor interaction only, the Hamiltonian for this system can be written as

$$\mathcal{H} = -J \sum_{i,j=1}^{L} S_{i,j} \left(S_{i,j+1} + S_{i,j-1} + S_{i+1,j} + S_{i-1,j} \right) - B \sum_{i,j=1}^{L} S_{i}. \tag{1.10}$$

In solving the 2D Ising model, L. Onsager used the transfer matrix method. Onsager's solution for the 2D Ising model ($B = 0$) predicts a phase transition at a finite temperature

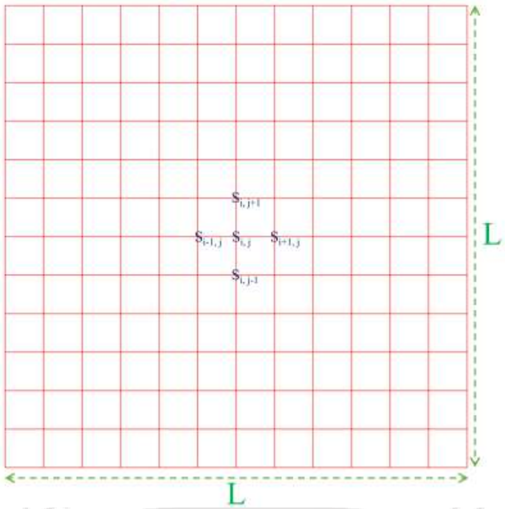

FIGURE 1.3: 2D square lattice configuration where endpoints are connected. Each site in this lattice represents spin, and each spin is coupled to its four nearest neighbors.

T_{C},

$$T_{\mathrm{C}} = \frac{2J}{k_{\mathrm{B}} \ln\left(1+\sqrt{2}\right)} \tag{1.11}$$

and the magnetization M corresponding to this transition is given by

$$M = \left[1 - \left(\sinh^2\left(2\beta J\right)\right)^{-2}\right]^{\frac{1}{8}}. \tag{1.12}$$

Thus, it is clear from the theoretical models that at finite temperatures, the long-range magnetic order is possible for higher dimensions (2D and 3D) only. However, long-range magnetic ordering is still important in the context of pseudo-1D systems, as these compounds show phase transition at finite temperatures. The phase transition in such system is due to the three-dimensional crystal structure of the system. The following section deals with the magnetically long-range ordered states.

1.2 Magnetic Order and Structures

In the previous section, various spin models of magnetism are presented in detail. Now, the different magnetic ground states arising due to the alignment of spins will be discussed. In an atom with partially filled localized d or f electrons shell, magnetization occurs due to the net orbital angular moment and intrinsic spin of the unpaired electrons. The exchange interaction between these electrons is an important consequence of repulsive Coulomb force and the antisymmetric wavefunction characteristics for fermions. Thus, the long-range magnetic ordering arising due to exchange interactions is a quantum magnetic phenomenon, and it is an equilibrium state. The equilibrium state is a result of symmetry breaking, an abrupt change [38]. Thus, the phase transition at critical temperature is a sharp change between disordered (symmetric) and ordered (broken symmetry) states, and the corresponding order parameter is magnetization. The following subsections discussed the various magnetically ordered states.

1.2.1 Ferromagnetism

It refers to the parallel alignment of spins such that the electrostatic energy of electron interaction is minimum for the case when all spins are parallel to each other compared to any other spin configuration (Fig. 1.4(a)). Thus, the parallel-spin configuration is the most stable structure for the case $J_{ij} > 0$ in Eq. 1.13. The defining feature of ferromagnetism is spontaneous magnetization below a characteristic temperature T_C, even in the absence of a magnetic field. However, above T_C, the thermal fluctuations dominate over the magnetic exchange interaction energy leading to paramagnetic phase. In order to know the underline cause of the alignment of spins (Fig. 1.4(a)), one has to solve the Hamiltonian

$$\mathcal{H} = -\sum_{ij} J_{ij} S_i . S_j + g\mu_B \sum_j S_j . B \qquad (J_{ij} > 0). \tag{1.13}$$

In solving Eq. 1.13, Weiss used the Langevin model and define an effective molecular field B_{eff} of neighboring spins at the i^{th} site

$$B_{eff} = -\frac{2}{g\mu_B} \sum_j J_{ij} S_j. \tag{1.14}$$

Using this approximation, the Hamiltonian in Eq. 1.13 can be simplified to

$$\mathcal{H} = g\mu_B \sum_i S_i . (B + B_{eff}) \tag{1.15}$$

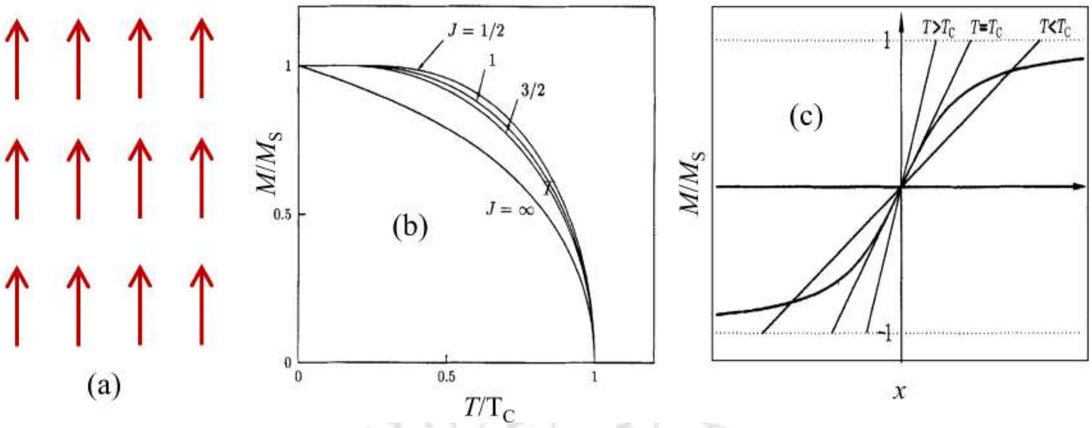

Figure 1.4: Characteristic features of ferromagnets (a) parallel alignment of spins (b) mean-field magnetization with the temperature at different J values (c) Graphical representation of Eq. 1.17 for different temperature regions at $B = 0$ [38].

which is similar to the Hamiltonian for a paramagnet under a field of $B + B_{eff}$. In the case of a ferromagnet, the molecular field tends to align the neighboring spins; therefore, it is proportional to the magnetization [38, 39]

$$B_{eff} = \alpha M \qquad \text{(where } \alpha > 0 \text{ for a ferromagnet).} \tag{1.16}$$

Now the problem can be treated as a paramagnet under an applied field of $B + B_{eff}$

$$\frac{M}{M_s} = \mathrm{B}_J(x) \tag{1.17}$$

where $\mathrm{B}_J(x)$ is the Brillouin function with $x = \frac{gJ\mu_B\,(B+B_{eff})}{k_B T}$ and $M_s = NgJ\mu_B$. Let us consider the case of zero field $B = 0$. At higher temperatures, there is no solution for Eq. 1.17 except for x = 0 and $M_s = 0$ case; hence no spontaneous magnetization occurs. On the other hand, below a critical temperature T_C, Eq. 1.17 is solvable, and spontaneous magnetization occurs even in the absence of a magnetic field, which increases with the decreasing temperature, characteristics of ferromagnets (Figs. 1.4(b) and (c)). The transition temperature is given by

$$T_C = \frac{N g^2 \mu_B^2\, J(J+1)\,\alpha}{3\,k_B}. \tag{1.18}$$

Above this temperature T_C, the susceptibility $\chi \propto \frac{1}{T-T_C}$. From Fig. 1.4(b), it is clear that the derivative of magnetization must be discontinuous at $T = T_C$; therefore, the

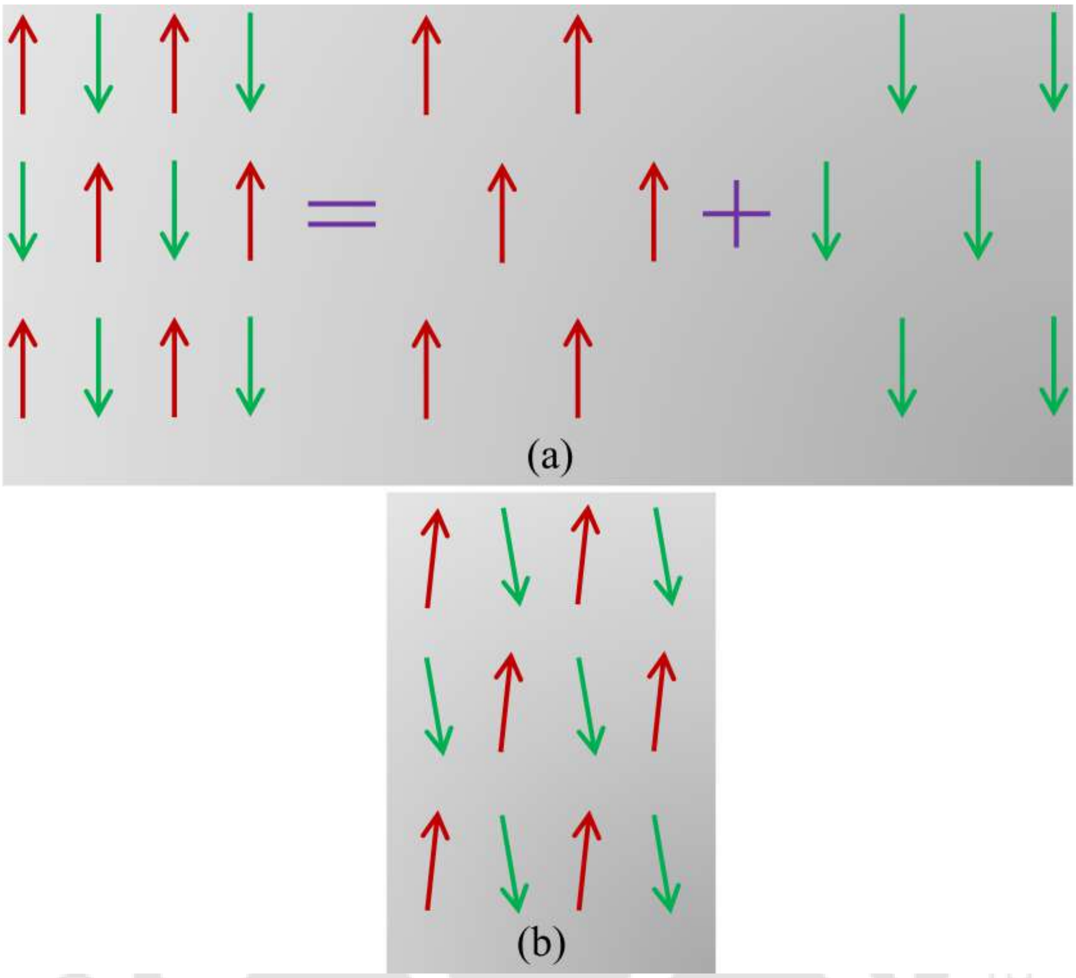

FIGURE 1.5: (a) Spin arrangement in the antiferromagnetic structure consisting of two interpenetrating sublattices of spin-up (red arrow) and spin-down (green arrow) configurations. (b) Canted antiferromagnetic structure.

ferromagnetic transition is a second-order phase transition.

1.2.2 Antiferromagnetism

According to Weiss's theory, if the J_{ij} in Eq. 1.13 is negative, the molecular field is adjusted such that the electrostatic energy of electron interaction is minimum for the case when all the neighboring spins are antiparallel to each other compared to any other spin configuration (Fig. 1.5(a)) [38]. Such a configuration of spins in a lattice is called an antiferromagnetic structure. Usually, it occurs in systems having two interpenetrating sublattices. Out of these two sublattices, one point for the spin-up configuration and the other for down spins (Fig. 1.5(a)). The molecular field for up ($B_{eff}^{\uparrow}$) and down ($B_{eff}^{\downarrow}$)

sublattices is given by

$$\begin{aligned} B_{eff}^{\uparrow} &= -\left|\alpha\right| M_{\downarrow} \\ B_{eff}^{\downarrow} &= -\left|\alpha\right| M_{\uparrow} \end{aligned} \tag{1.19}$$

where $\alpha < 0$, and $M_{\downarrow}$, $M_{\uparrow}$ are given by

$$\begin{aligned} M_{\uparrow} &= M_{\mathrm{s}}\,\mathrm{B}_J\left(\frac{gJ\mu_{\mathrm{B}}\left(B + B_{eff}^{\uparrow}\right)}{k_B T}\right) \\ M_{\downarrow} &= M_{\mathrm{s}}\,\mathrm{B}_J\left(\frac{gJ\mu_{\mathrm{B}}\left(B + B_{eff}^{\downarrow}\right)}{k_B T}\right). \end{aligned} \tag{1.20}$$

As the sublattices are identical in everything except opposite spins, therefore the $|M_{\downarrow}| = |M_{\uparrow}| = |M|$. Considering the case for $B = 0$, the magnetization for both the sublattices has the same form as in Eq. 1.17 but has opposite directions so that the net magnetization $(M_{\uparrow} + M_{\downarrow})$ will be zero. However, for a single sublattice, the system follows the same trend as for the ferromagnet (Figs. 1.4(b) and (c)) below a critical temperature called Neel temperature T_{N}. Above this temperature, the susceptibility $\chi \propto \frac{1}{T+T_{\mathrm{N}}}$. Thus depending on the nature of the exchange interaction, the magnetic susceptibility above a critical temperature has the Curie Weiss dependence

$$\chi = \frac{C}{T-\theta} \tag{1.21}$$

where C is the Curie constant and θ is the Weiss temperature. For ferromagnets $\theta > 0$ while for the antiferromagnets $\theta < 0$.

However, in some cases (Hematite) [40], the cancellation of two interpenetrating sublattices magnetization is incomplete due to the tilting of exchange bonds and defects in the lattice or impurities (Fig. 1.5(b)). It leads to spin canting, and the system exhibits a canted antiferromagnetic structure that has the characteristics of ferrimagnet and ferromagnet.

1.2.3 Ferrimagnetism

In the case of antiferromagnets, the two opposite sublattices were identical, so the net magnetization was zero (Fig. 1.5(a)). However, in the case of different crystal environments at these sublattices, they may not be opposite and identical. Thus, the net magnetization will not be zero, and the temperature dependence on magnetization might be quite different from Fig. 1.4(b). Such a spin configuration of two non-equivalent sublattices is called a ferrimagnetic structure. It usually occurs in ferrites and garnets, which have non-equivalent sites of opposite sublattices [38]. Ferrites have a spinal crystal structure (AB_2O_4), where **A** and **B** ions sit at tetrahedral and octahedral sites, respectively [38]. Thus, due to the non-identical environment and different ions at these sites, these sublattices are non-equivalent. On the other hand, the garnets ($R_3Fe_5O_{12}$) have a cubic crystal structure, where **R** is the rare earth ion. Similar to the ferrites, the garnets also have non-equivalent sublattices [38]. Out of the five Fe^{3+} ions, three are at the tetrahedral site, the remaining two are in the octahedral environment, while the rare earth ion $\mathbf{R}^{3+}$ is at the dodecahedral site. In general, ferrimagnets are insulator; therefore, they are more suitable for practical applications than ferromagnets.

1.3 Magnetic Frustration and Short-range Order

The long-range magnetic order (ferromagnetic, antiferromagnetic, and ferrimagnetic) are briefly discussed in section 1.2. It is concluded that depending on the sign of J_{ij} in Eq. 1.13, the neighboring spins can align parallel or antiparallel. However, in some systems, all the exchange interactions can't be satisfied simultaneously, which leads to frustration in the system. Therefore, the frustrated system exhibits degeneracy in the ground state, leading to a complex magnetic phase diagram such as the short-range ordering of incompatible spin interactions. These unconventional phenomena usually occur due to geometrical features or competing magnetic interactions.

1. Geometrical frustration is a well-defined characteristic of Ising antiferromagnet on an edge-sharing triangular lattice arrangement [41, 42]. In this arrangement, when two spins are antiparallel, the third spin is either up or down (Fig. 1.6).

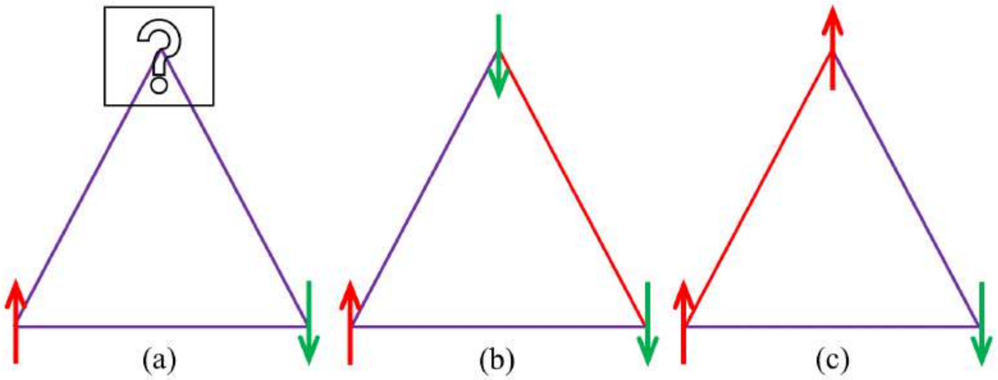

FIGURE 1.6: Geometrical frustration in the triangular lattice arrangement of an Ising antiferromagnet. The square with a ? symbol represents the flappable spins. Each configuration ((b) and (c)) has two satisfied (violet line) and one unsatisfied (red line) exchange interaction.

Thus, for each triangular lattice, one spin remains undetermined. Therefore, in the case of N Ising spins on triangular lattices, there will be minimum $2^{N/3}$ ground states with entropy $\frac{N}{3}\,k_{\mathrm{B}}\ln 2$. Extensive entropy at absolute zero temperature is a characteristic feature of frustrated systems. In such a system, the ground state has a large influence from perturbations such as lattice distortion, single-ion anisotropy, and magnetic interactions. As the degeneracy in the ground state is purely due to the geometry of the system, not by the symmetry of the Hamiltonian. Therefore, such perturbations also play a crucial role in defining the key features of frustrated systems, which can enhance the complexity of the magnetic structure of the system. Other examples of frustrated lattices are the kagome lattice and the pyrochlore lattice (Fig. 1.7) [43–46].

2. The magnetic frustration originates from the competitive magnetic interactions present in the system, so the ground state remains destabilized. It involves order-by-disorder phenomenon, which leads to quantum fluctuations in the system [47]. The magnetic ordering in these systems is suppressed to very low temperatures or may be absent. At sufficiently low temperatures, the quantum fluctuations are dominant over thermal fluctuations leading to a plethora of quantum magnetic phenomena. Thus, the quantum effects are most susceptible to such kinds of systems. Consider the case of a square lattice with nearest (J_1) and next nearest neighbor (J_2) coupling where J_2 is antiferromagnetic (Fig. 1.8). If we first look at the possibility of J_1 being antiferromagnetic, the problem can be treated as a

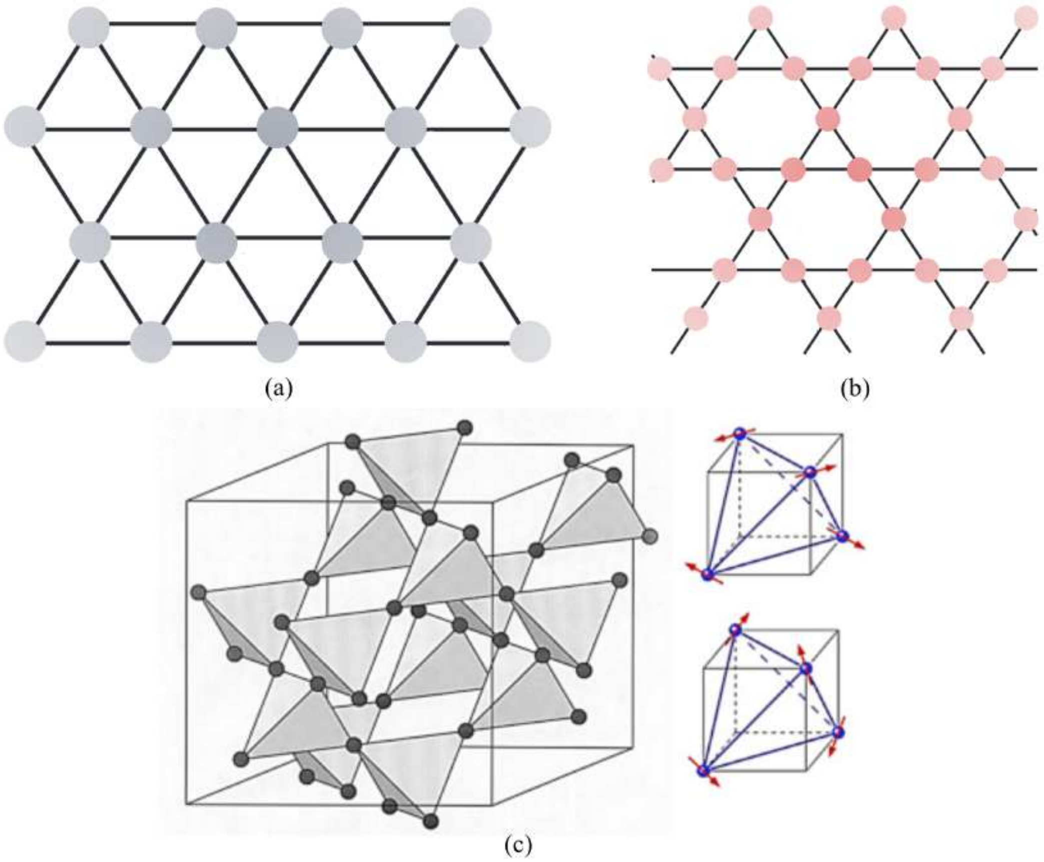
(a)
(b)
(c)

FIGURE 1.7: Frustrated lattice in two dimensions (a) Triangular (b) Kagome and three dimensions (c) Pyrochlore.

nested triangular lattice arrangement. When the two interactions are comparable ($J_1 \approx J_2$), the square lattice structure in Fig. 1.8 reaches the limit of triangular arrangement, thereby providing frustration in the system [48]. On the other hand, in the case of J_1 to be ferromagnetic, magnetic frustration can occur if $J_1 \approx$ -J_2. However, if we consider the J_2 to be ferromagnetic (Fig. 1.8), all the interactions can be satisfied simultaneously, which leads to long-range order and hence no frustration.

It is clear that the frustration in the system greatly suppresses the long-range order so that the critical temperature decreases up to some extent. For an ideal antiferromagnet, the ordering temperature T_N is supposed to be at $|\theta|$. However, for a frustrated Ising antiferromagnet, the T_N decreases much below $|\theta|$, and the ratio $\frac{|\theta|}{T_\mathrm{N}}$ is defined as frustration parameter f. It turns out that for $f > 5$, the inter-cluster interaction of short-range ordered spins dominates over long–range magnetic order, and a short-range

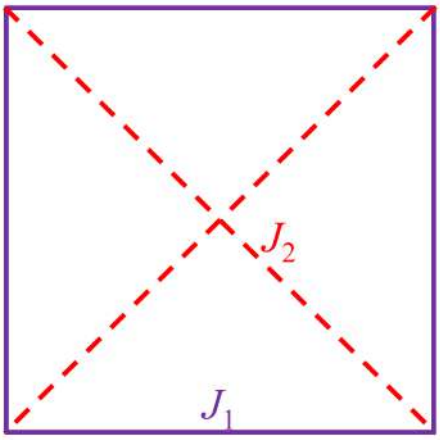

FIGURE 1.8: Square lattice arrangement considering nearest J_1 and next nearest neighbor J_2 interactions only. The solid violet line stands for J_1, and the red dashed line is for J_2.

spin-glass state is formed. In the pseudo-1D systems ($A_3BB'O_6$ type), the magnetic ions are arranged on a triangular lattice in the *ab* plane where the nearest and next nearest neighbor interaction is ferromagnetic and antiferromagnetic, respectively. Therefore in the context of $A_3BB'O_6$ type pseudo-1D systems, the magnetic frustration and hence short-range interacting spin clusters are important. The following section discusses the key features of the unusual spin-glass state.

1.4 Spin Glass

A consequence of frustrated geometry with degeneracy in the magnetic ground state is that the spins are frozen into random orientation so that a short-range spin-glass state is formed below a characteristic temperature called freezing temperature T_g. Although the glassy phase was experimentally discovered in 1966 by Violet [49], but it started picking up special attention after the susceptibility results by Mydosh [50]. It was found that most of the spectacular features of glassy systems were primarily due to the large number of anisotropic metastable states. The next subsection deals with the various unconventional features in the magnetization measurements arising due to the freezing of spins below T_g.

1.4.1 Basic features

The characteristic feature of spin-glass system is the peak in the susceptibility data at T_g (Fig. 1.9(a)). It is found that the peak is highly sensitive to the applied magnetic field (Fig. 1.9(b)) [50, 51]. Another most spectacular feature of the spin-glass system is the oscillating field frequency dependency of peak temperature. In the AC susceptibility measurement, the susceptibility χ is given by $\chi = \chi' + \mathrm{i}\chi''$, where χ' and χ'' are real and imaginary components, respectively. It is found that the cusp in the χ' data moves towards the right with increasing frequency (Fig. 1.10) [52]. On the other hand, the χ'' data shows a sharp anomaly in the vicinity of T_g (Fig. 1.10) [52]. It is also noted that the χ'' increases monotonically with increasing frequency. The dependence of AC susceptibility data (χ' and χ'') on the frequency of the oscillating magnetic field indicates a slow relaxation process in the spin-glass system, which arises due to the non-equilibrium nature of magnetic properties in this region. The relaxation time τ for this process is given by $\tau = 1/\omega$ where $\omega = 2\pi f$, and f is the frequency. Classification of the spin-glass system is based on the Mydosh parameter S given by $S = \frac{1}{T_\mathrm{g}}\frac{\Delta T_\mathrm{g}}{\Delta \log_{10} f}$, where $\Delta T_\mathrm{g} = (T_\mathrm{g})_{f_2}$ - $(T_\mathrm{g})_{f_1}$ and $\Delta \log_{10} f = \log_{10} f_2$ - $\log_{10} f_1$ [53]. Basically, it measures the sensitivity with the frequency of magnetic field oscillations, which is very robust to interacting magnetic entities. In the long-range ordered system, the interaction is strong; therefore, a large frequency field oscillation is required to produce a detectable shift in AC susceptibility.

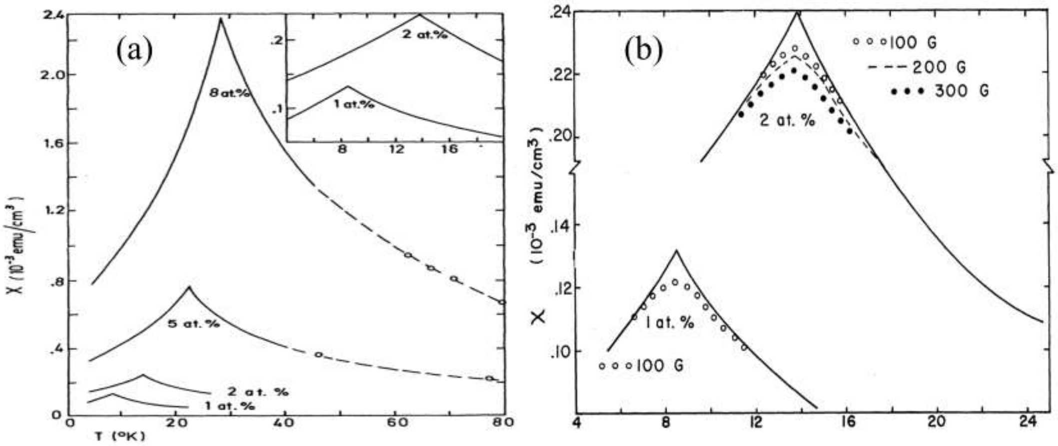

FIGURE 1.9: Susceptibility data of Gold-Iron alloys for different concentrations of Fe [50]. (a) Low field χ vs. T plot for varying concentrations of Fe (1% to 8%), where the inset shows the enlarged plot for lower Fe concentrations (1% and 2%). (b) χ vs. T plot at different magnetic fields (100 G to 300 G) for lower Fe concentrations, and the solid lines for the zero-field case.

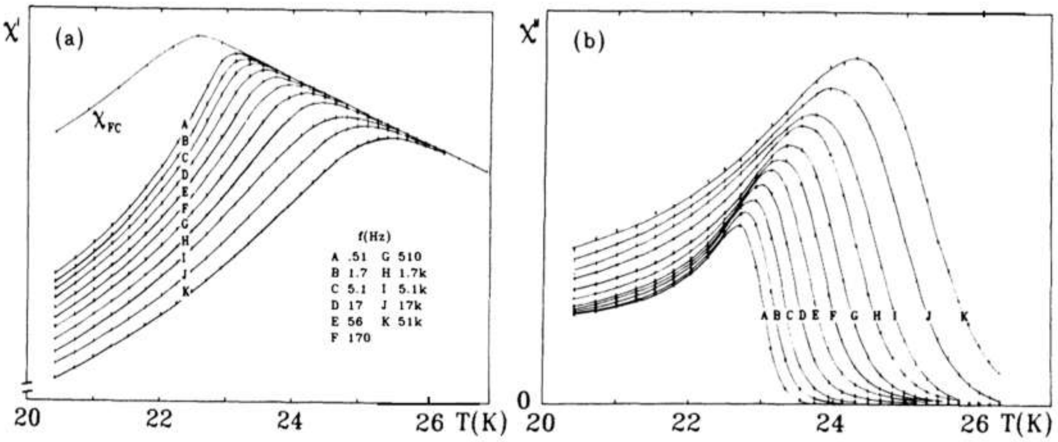

FIGURE 1.10: AC susceptibility vs. temperature at different frequencies of magnetic field oscillations [52]. (a) χ' vs. T, where the χ_{FC} denotes the field-cooled susceptibility under an applied magnetic field of 50 mG. (b) χ'' vs. T at selected frequencies.

On the other hand, for the spin-glass system, the magnetic entities are weakly interacting;

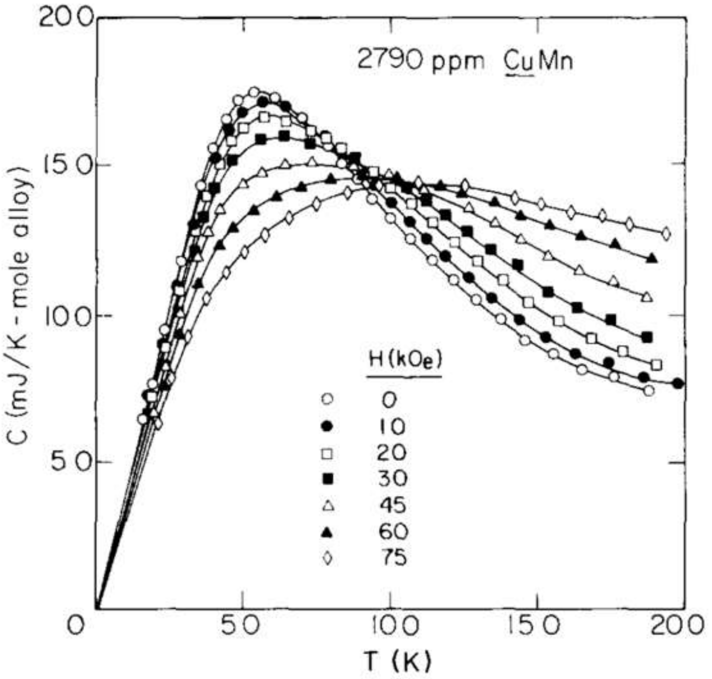

FIGURE 1.11: Specific heat vs. temperature at various magnetic field for CuMn system ($T_g = 3$ K) [55].

therefore, the shift in AC susceptibility is easily detectable. Usually, the value of S lies in the range 0.005 to 0.08 for spin-glass, while for the superparamagnetic system, it is around 0.2 [54]. The spin-glass systems are categorized into non-interacting spins/canonical spin-glass (S = 0.005-0.01) and interacting spin-clusters/cluster-glass (S = 0.02-0.08). For non-interacting magnetic entities, the relaxation time is given by Arrhenius law $\tau = \tau_0$

$\exp\left[\frac{E_{\mathrm{A}}}{k_{\mathrm{B}}T}\right]$, where τ_0 is the spin-flip time for a single spin or magnetic entity, and E_{A} is the activation energy required to separate adjacent magnetic entities. However, for the interacting spin-clusters, the dynamics is well described by the Vogel-Fulcher law $\tau = \tau_0 \exp\left[\frac{E_{\mathrm{A}}}{k_{\mathrm{B}}(T - T_0)}\right]$, where T_0 is the Vogel-Fulcher temperature. Dynamic scaling model, commonly known as power law often employed to examine the frequency dependence of freezing temperature. The slowing down of T_{g} is governed by the $\tau = \tau_0 \left[\frac{T - T_{\mathrm{g}}}{T_{\mathrm{g}}}\right]^{-z\nu}$, where $z\nu$ is the critical exponent. For the spin-glass system, the $z\nu$ lies between 4 and 12. In addition to the peak in the susceptibility data at T_{g}, no such anomaly was observed in the specific heat analysis in the vicinity of T_{g} (Fig. 1.11) [54, 55].

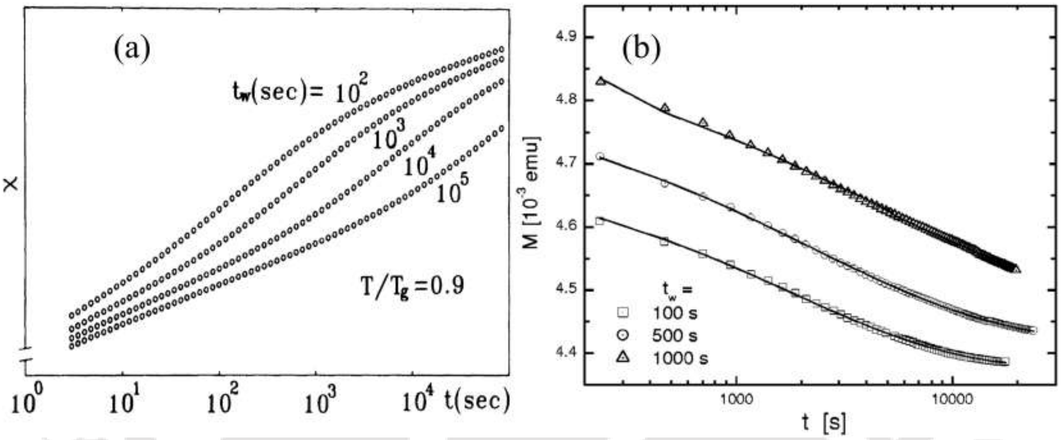

FIGURE 1.12: Magnetic relaxation measurements using different field cooling protocols for a set of waiting time t_{w}. (a) Zero-field-cooled magnetic relaxation for $(\mathrm{Fe}_{0.15}\mathrm{Ni}_{0.85})_{75}\mathrm{P}_{16}\mathrm{B}_6\mathrm{Al}_3$ (T = 20.3 K and T_{g} = 22.6 K) (b) thermoremanent magnetization relaxation for $\mathrm{RuSr}_2\mathrm{Gd}_{1.5}\mathrm{Ce}_{0.5}\mathrm{Cu}_2\mathrm{O}_{10-\delta}$ (T = 60 K and T_{g} = 72 K) [52,56].

Another crucial feature of the spin-glass system is the prolonged relaxation of magnetization [52, 56]. This non-equilibrium phenomenon of spin-glass systems can be studied when these systems are cooled from a temperature much above T_{g} to a temperature below T_{g} under different field cooling protocols. In the zero-field-cooled (ZFC) relaxation measurement, the system is cooled in the absence of external magnetic field down to the temperature below T_{g}. At the measuring temperature, an external magnetic field is applied, and the magnetization is recorded with time. For the thermoremanent magnetization relaxation measurements, the system is cooled from room temperature under an applied magnetic field. After a waiting time of t_{w} at the measuring temperature, the magnetization is recorded with time in zero field. It is found that the relaxation time strongly depends on the t_{w} (Fig. 1.12), the time for which the system is exposed to the external magnetic field. The time dependence of magnetization can be well described by the stretched exponential relaxation function. In addition, the memory and rejuvenation effects in the magnetic relaxation measurements are another most spectacular manifestation of non-equilibrium dynamics.

1.4.2 Edwards-Anderson model

The first theoretical model for understanding spin-freezing phenomena below a critical temperature was proposed by Edwards-Anderson [57–59]. It is based on the classical Hamiltonian

$$\mathcal{H} = -\sum_{ij} J_{ij} S_i S_j \tag{1.22}$$

on a simple magnetic system considering the nearest neighbor interactions only. The frustration in such systems has been introduced by taking random coupling J_{ij} among spins specified by the probability distribution of J_{ij}. In the Edwards-Anderson model, usually, the J_{ij} has a Gaussian distribution

$$P(J_{ij}) = \frac{1}{\sqrt{2\pi\sigma^2}} e^{-\frac{J_{ij}^2}{2\sigma^2}} \tag{1.23}$$

where σ^2 is the variance. Therefore, it is a finite-dimensional spin model (coupling among nearest neighbors only) with quenched disorder. Edwards-Anderson used the 'replica method' which greatly simplified the problem of averaging over free energy (logarithm of partition function Z) to average of Z^{n}. It is similar to averaging over n replicas of the system hence known as the replica trick. The vanishing magnetization below T_{g} ensures that no long-range order is possible in the spin glass phase. On the other hand, the non-zero value of the order parameter

$$Q = \frac{1}{N}\sum_{i} \langle S_{\mathrm{i}} \rangle^2 \tag{1.24}$$

below T_{g} signifies the freezing of spins into intermediate metastable states, while for $T > T_{\mathrm{g}}$, the Q becomes zero. Further optimization of free energy ***w.r.t.*** Q leads to a cusp-like feature in magnetization at T_{g}, and at this temperature, the Q attains a non-zero value. Thus, the bond disorder introduced by the Gaussian distribution of J_{ij} was successful in predicting a short-range spin-glass state below T_g. In addition, this model also predicts the cusp-like feature in the specific heat at the same temperature T_g which is contrary to experiments [60–62].

1.4.3 Sherrington–Kirkpatrick model

Like the Edwards-Anderson model, it also assumes the same distribution for J_{ij} (Eq. 1.23) [63–65]. The choice of variance $\left(\sigma^2 = \frac{1}{N}\right)$ in Eq. 1.23 makes the free-energy density independent of total spins N. However, in this model, each spin can interact with all other spins in the system so that the number of neighbors is infinite. Thus, the Sherrington-Kirkpatrick model is an extension of the Edwards-Anderson model [63]. The key feature of this model is a phase transition below T_g. On the other hand, the replica symmetric ansatz used by Sherrington and Kirkpatrick turns out to be unstable and yields negative entropy below the AT line, which is unphysical [66]. These undesirable outcomes of the replica symmetric ansatz suggested the researchers to use different assumptions to facilitate the solution [67–69]. In this manner, several attempts have been made to break the replica symmetry [70–73], and the solution was given by Parisi, commonly known as the Replica symmetry breaking solution [74–76]. It was thoroughly proved that the infinite-steps Replica symmetry breaking provides the accurate solution for free energy in the mean-field Sherrington-Kirkpatrick model.

1.5 Cluster Glass Model

Using the mean-field theory, Soukoulis *et al.* [77–79] proposed the cluster-mean-field theory in which the fundamental entity is interacting spin clusters rather than the single spin. In this approach, the clusters are identical, with equal number of spins in each cluster. The Hamiltonian for such a system is written as

$$\mathcal{H} = -\sum_{i,j=1}^{N_{\text{spin}}} \sum_{\nu,\lambda=1}^{N_{\text{cluster}}} J_{i\nu j\lambda}\, S_{i\nu}\, S_{j\lambda} \tag{1.25}$$

where N_{cluster} is the total number of clusters in the system, and N_{spin} represents the number of spins in each cluster. Eq. 1.25 is simplified to

$$\mathcal{H} = -\sum_{\nu<\lambda} J^{\text{inter}}_{\nu\lambda}\, S_\nu\, S_\lambda - \sum_{\nu}\sum_{i<j} J^{\text{intra}}_{ij}\, S_{i\nu}\, S_{j\nu}. \tag{1.26}$$

Here J^{intra}_{ij} and $J^{\text{inter}}_{\nu\lambda}$ are the intracluster and intercluster exchange constants, respectively. The intracluster interaction is assumed to be much stronger than the intercluster interaction. As in Eq. 1.22, the $J^{\text{inter}}_{\nu\lambda}$ is a random variable with Gaussian distribution $\left(P(J^{\text{inter}}_{\nu\lambda}) = \frac{1}{\sqrt{2\pi J^2}}\, e^{-\frac{J^2_{\nu\lambda}}{2J^2}}\right)$, while the intracluster interaction is treated exactly. Using the replica trick, one can obtain the free energy

$$\begin{aligned} F = -k_{\text{B}}\, T \lim_{n\to 0} \frac{1}{n}\Bigg[\text{Tr}_{\text{n}} \exp\Bigg(\sum_{\nu<\lambda} \frac{J^2}{2(k_{\text{B}}\, T)^2} \sum_{\alpha} S^\alpha_\nu\, S^\alpha_\lambda \sum_{\beta} S^\beta_\nu S^\beta_\lambda \\ - \frac{1}{k_{\text{B}}\, T} \sum_{\alpha}\sum_{\nu} \mathcal{H}^{\alpha\nu}_{\text{cluster}} \Bigg) - 1\Bigg] \end{aligned} \tag{1.27}$$

where $\mathcal{H}^{\alpha\nu}_{\text{cluster}}$ = - $\sum_{i<j} J^{\text{intra}}_{ij}\, S^\alpha_{i\nu}\, S^\alpha_{j\nu}$, is the intracluster Hamiltonian for the α^{th} replica and $[S^\alpha_\nu\, S^\alpha_\lambda, S^\alpha_{i\nu}\, S^\alpha_{j\nu}] = 0$. It introduces two variational parameters

$$\begin{aligned} q &= \langle S^\alpha_\nu\, S^\beta_\nu \rangle, \qquad \alpha \neq \beta \\ M &= \langle S^\alpha_\nu\, S^\alpha_\nu \rangle. \end{aligned} \tag{1.28}$$

The q is analogous to the Edwards-Anderson spin-glass order parameter where S_ν represents the cluster spin, and M denotes the total spin within a cluster. The free energy per cluster is given as

$$F = -k_{\text{B}}\, T\left(\frac{\bar{\text{J}}^2}{12(k_{\text{B}}\, T)^2}\,(q^2 - M^2) + \frac{1}{(2\pi)^{3/2}} \int d^3 r\, e^{-r^2/2} \ln \text{Tr} \exp(-\beta \mathcal{H}^{\text{cluster}}_{\text{eff}}) \right) \tag{1.29}$$

where $\bar{\text{J}} = \sqrt{z}J$, z is the total number of nearest neighbor clusters of a given cluster. The effective cluster Hamiltonian $\mathcal{H}^{\text{cluster}}_{\text{eff}}$ is given by

$$-\mathcal{H}^{\text{cluster}}_{\text{eff}} = \sum_{i<j} J^{\text{intra}}_{ij}\, S_{i\nu}\, S_{j\nu} + \bar{\text{J}}\sqrt{\frac{q}{3}}\, r.S_\nu + \frac{\bar{\text{J}}^2}{6k_{\text{B}}\, T}(M - q)\, S_\nu.S_\nu. \tag{1.30}$$

The M and q are derived using variational conditions $\left(\frac{\partial F}{\partial q}\right)_M = 0$ and $\left(\frac{\partial F}{\partial M}\right)_q = 0$. It leads to

$$M = \frac{1}{(2\pi)^{3/2}} \int d^3 r\, e^{-r^2/2}\, \mathrm{Tr}\left(S_\nu . S_\nu\, e^{-\beta \mathcal{H}_{\mathrm{eff}}^{\mathrm{cluster}}}\right)/Z \tag{1.31}$$

and

$$M - q = \frac{1}{(2\pi)^{3/2}} \int d^3 r\, r\, e^{-r^2/2} \sqrt{\frac{3}{q}}\, \frac{k_{\mathrm{B}} T}{\bar{\mathrm{J}}}\, \mathrm{Tr}\left(r . S_\nu\, e^{-\beta \mathcal{H}_{\mathrm{eff}}^{\mathrm{cluster}}}\right)/Z. \tag{1.32}$$

The susceptibility (χ) and specific heat (C_{m}) per cluster can be given in terms of M and q,

$$\begin{aligned} \chi &= \frac{g^2 \mu_{\mathrm{B}}^2}{3 k_{\mathrm{B}} T} (M - q) \\ C_{\mathrm{m}} &= C_{\mathrm{m}}^{\mathrm{inter}} + C_{\mathrm{m}}^{\mathrm{intra}} \end{aligned} \tag{1.33}$$

where $C_{\mathrm{m}}^{\mathrm{inter}}$ and $C_{\mathrm{m}}^{\mathrm{intra}}$ are intercluster and intracluster contributions, respectively. The $C_{\mathrm{m}}^{\mathrm{inter}}$ and $C_{\mathrm{m}}^{\mathrm{intra}}$ are given by

$$C_{\mathrm{m}}^{\mathrm{inter}} = \frac{d}{dT}\left(\frac{\bar{\mathrm{J}}^2}{6 k_{\mathrm{B}} T}(q^2 - M^2)\right) \tag{1.34}$$

and

$$C_{\mathrm{m}}^{\mathrm{intra}} = \frac{d}{dT} \int d^3 r\, e^{-r^2/2}\, \mathrm{Tr}\left(\mathcal{H}_{\mathrm{cluster}}^{\alpha\nu}\, e^{-\beta \mathcal{H}_{\mathrm{eff}}^{\mathrm{cluster}}}\right)/Z. \tag{1.35}$$

Similar to the Edwards-Anderson model, the χ attains a sharp cusp at T_{c}, while the C_{m} attains a maximum value much above T_{c}. Further study revealed that dynamic quantities such as correlation function and magnetization decay much slower when the clusters are present [80].

1.6 $Ca_3Co_2O_6$

So far, the fundamental aspects of magnetism, such as long-range order, short-range order, geometrical frustration, magnetic frustration, and spin-glass systems, along with the theoretical low-dimensional, spin-glass, and cluster-glass (CG) models, have been discussed. All these features and models are essential in the context of pseudo-1D $Ca_3Co_2O_6$

system because the novel magnetic phenomena in this compound result from the interplay between them. The following subsections deal with the characteristic features of the compound.

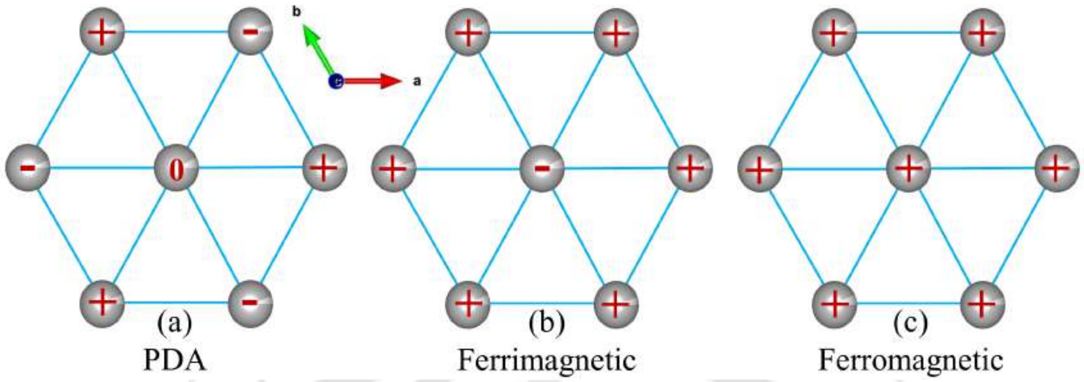

FIGURE 1.13: Experimentally proposed magnetic structures in the triangular lattice arrangement of $Ca_3Co_2O_6$. Here +, -, and 0 represent ferromagnetic, antiferromagnetic, and disordered spin chains, respectively.

1.6.1 Crystal structure

Materials belonging to the $A_3BB'O_6$ family crystallize in the rhombohedral structure having space group $R\bar{3}c$ (*cf.* Fig. 1.1). In the $Ca_3Co_2O_6$, the crystal structure consists of an infinite number of magnetic chains of alternating CoO_6 octahedra and CoO_6 trigonal prisms running along the *c*-axis, separated by non-magnetic Ca ions. These chains are arranged on a triangular lattice in the *ab*-plane (*cf.* Fig. 1.1). In the triangular lattice arrangement, geometrical frustration is expected if the inter-chain coupling is antiferromagnetic and spins are Ising type. The intra-chain separation between magnetic ions (2.59 Å) is approximately half of the inter-chain separation (5.31 Å) [81]; therefore, one could also expect the 1D character in magnetic properties. The different crystalline electric field at the octahedral (OCT) and trigonal prismatic (TP) geometry lead to different spin states of Co ions (low spin S = 0 at the OCT site and high spin S = 2 at the TP site) [28, 29, 82, 83]. The electronic state of Co ion at the OCT (Co1) and TP (Co2) sites was remained mystery for long time. Initially, first-principles-based density functional theory calculations by Vidya *et al.* predicted that the Co1 and Co2 corresponds to low spin Co^{4+} and high spin Co^{2+}, respectively [84]. Later, magnetic circular dichroism and soft-X-ray absorption spectroscopy results cleared that both the Co1 and Co2 ions are trivalent [82].

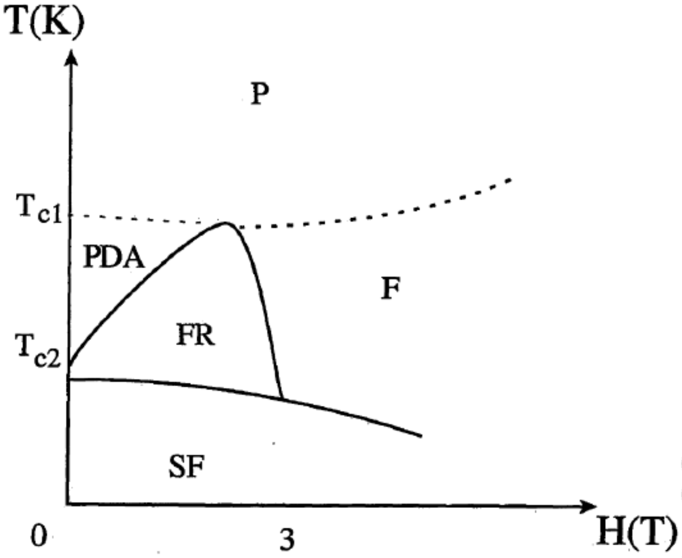

FIGURE 1.14: Magnetic phase diagram of $Ca_3Co_2O_6$. Here F, FR, PDA, SF, and P corresponds to ferromagnetic, ferrimagnetic, partially disordered antiferromagnetic, spin-freezing, and paramagnetic states, respectively [85].

1.6.2 Magnetic structure

The $Ca_3Co_2O_6$ exhibits a very rich magnetic phase diagram with temperature and magnetic field. Therefore, magnetization, neutron diffraction, and NMR studies have been done to obtain the true magnetic ground state features of the system. Initially, it was proposed by Kageyama *et al.* [85] that at low fields, the system undergoes a partially disordered antiferromagnetic (PDA) phase below T_{c1} (25 K), followed by spin-freezing phenomena below T_{c2} (10 K). In the PDA structure (↑↑ 0), 2/3 of the chains are antiferromagnetically coupled, while the 1/3 remains disordered (Fig. 1.13) [85–87]. Furthermore, with magnetic field, the magnetization plateau at 1/3 of saturation value corresponds to ferrimagnetic (↑↑↓) configuration followed by a field-induced ferromagnetic (↑↑↑) transition (Fig. 1.13). Based on these results, the magnetic phase diagram proposed by Kageyama *et al.* is shown in Fig. 1.14. The PDA phase of $Ca_3Co_2O_6$ remained questionable for years [23, 88]. Neutron diffraction study by Agrestini *et al.* [30] cleared that the magnetic structure below T_{c1} is an incommensurate amplitude-modulated PDA (spin density wave) with wave propagation vector k = (0, 0, 1.01)

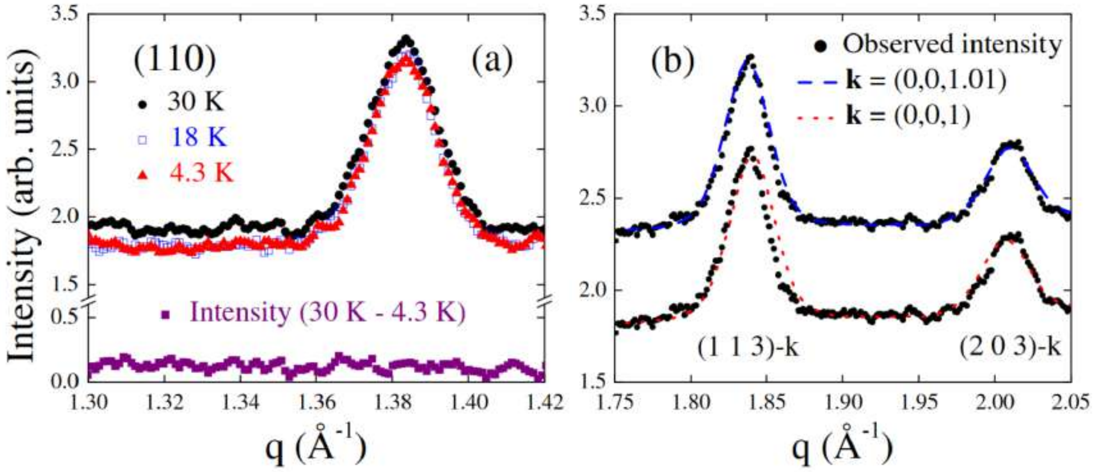

FIGURE 1.15: (a) Neutron intensity for (110) reflection at different temperatures (b) Neutron diffraction pattern at 18 K and refinement for two values of k = (0,0,1) and (0,0,1.01) [30].

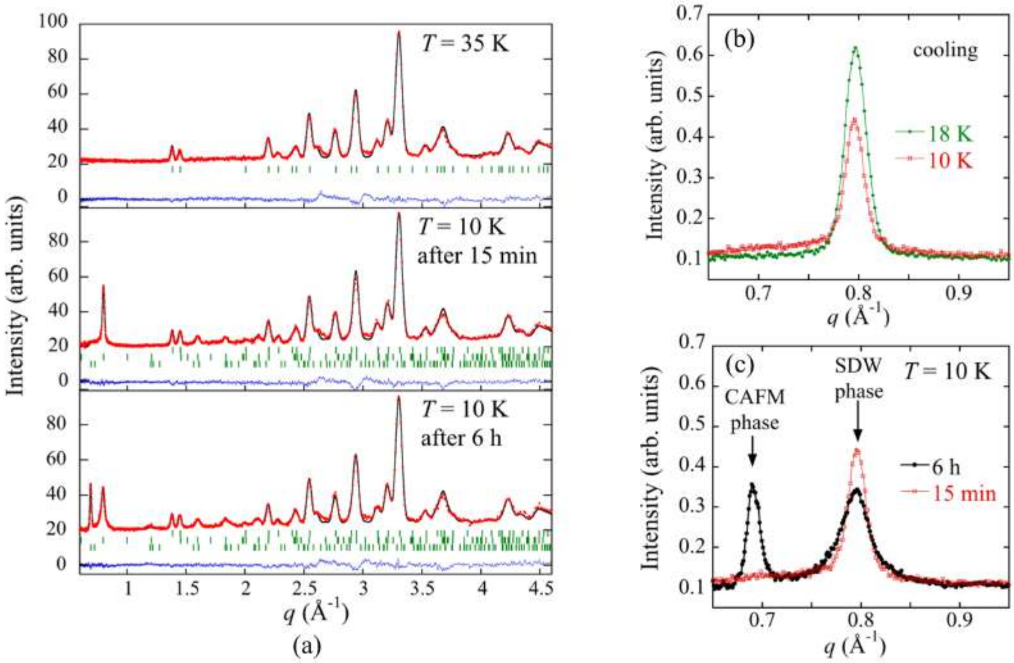

FIGURE 1.16: (a) Neutron diffraction pattern taken after different waiting time at fixed temperatures T = 35 and 10 K [14]. (b) Decrease in the intensity of magnetic Bragg peak corresponding to spin density wave phase on decreasing temperature [14]. (c) Neutron diffraction pattern at 10 K collected after different waiting time [14].

(Fig. 1.15). Their study also revealed the coexistence of long-range magnetic order with short-range order [30]. Another observation on the time dependence of magnetic Bragg reflections has shown that the peaks related to the spin density wave phase slowly lose intensity (Figs. 1.16(a) and (c)), suggesting that the spin density wave phase is not a stabilized structure [14]. Simultaneously, new Bragg reflections, which can be indexed

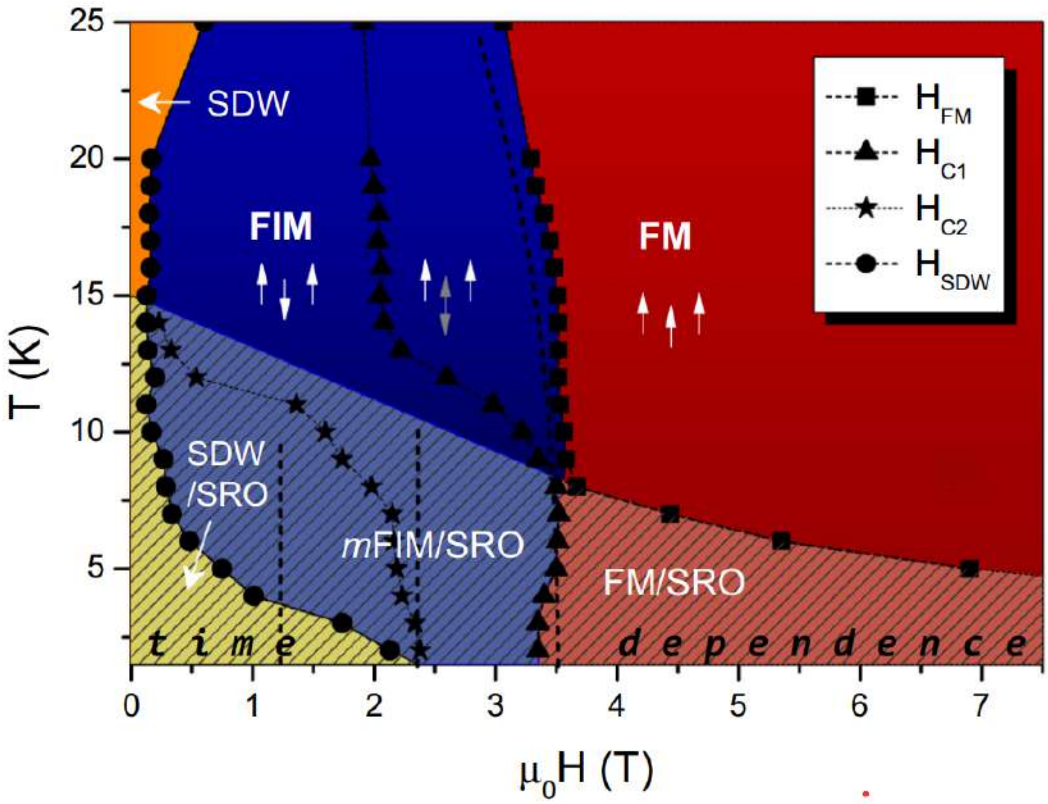

FIGURE 1.17: Magnetic phase diagram of $Ca_3Co_2O_6$ proposed by Lampen *et al.* [90]. Here FM, FIM, Mfim, SRO, and SDW stand for ferromagnetic, ferrimagnetic, metastable ferrimagnetic, short-range-order, and spin-density wave structure, respectively.

by k = (0.5,-0.5,1) that correspond to commensurate antiferromagnetic (CAFM) structure, begin to appear (Fig. 1.16(c)) [14]. Furthermore, suppression of spin density wave phase and stabilization of commensurate antiferromagnetic structure were also observed in the pressure-dependent neutron diffraction study at high-pressure $P = 2.1$ GPa [89]. Based on the critical points obtained from the change in magnetic entropy calculations by Lampen *et al.* [90], Fig. 1.17 shows the phase diagram of the $Ca_3Co_2O_6$ system.

In addition to the de-stabilized magnetic phases with decreasing temperature, the isothermal M-H curves also change drastically with temperature (Fig. 1.18). In the temperature range $T_{c2} \leq T \leq T_{c1}$, the magnetization curve exhibits a ferrimagnetic plateau with moment 1/3 of the saturation value followed by a field-induced step to saturation value, which suggests the ferromagnetic phase [25]. On lowering the temperature, the M-H curve exhibits a large hysteresis, and magnetization steps in the regular magnetic field

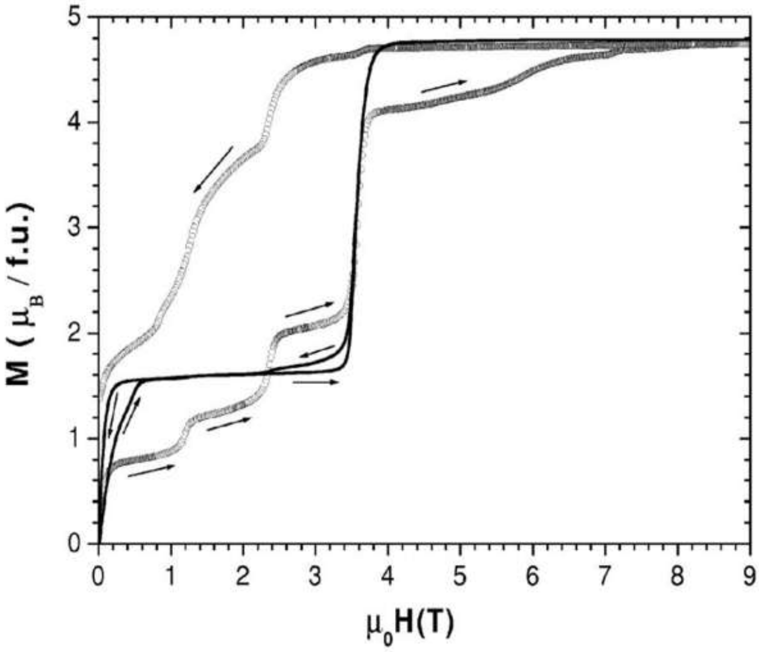

FIGURE 1.18: Isothermal M-H curves recorded at 2 K (open circle) and 10 K (solid line) where the arrow shows the direction of magnetic field [25].

interval (1.2 T) appeared (Fig. 1.18) [27]. These results are indicative of quantum tunneling of the magnetization in $Ca_3Co_2O_6$. Thus, this system provides a different class of materials other than molecular magnets to study the quantum effects. On the other

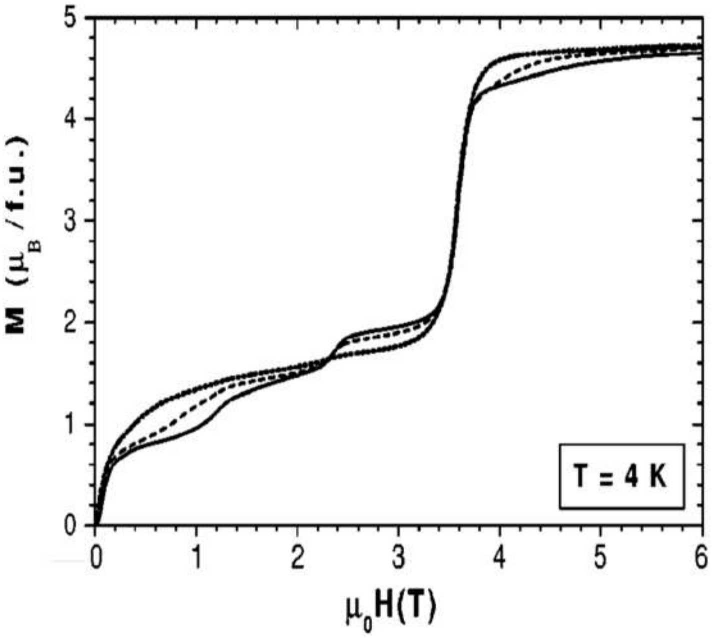

FIGURE 1.19: Virgin M-H curves recorded at 4 K for different magnetic field scanning rates: 0.01 T/min (dotted line), 0.1 T/min (dashed line), and 1 T/min (solid line) [25].

hand, it was also observed that these steps are most prominent for a fast magnetic field sweep rate (1 T/min) and completely smoothen out for a slow scan (0.01 T/min) (Fig. 1.19) [25]. Thus, in addition to the neutron diffraction results, the time dependence of magnetic phases was also observable with the magnetic field. Furthermore, detailed discussions on the magnetic structure of the system by experimental and theoretical results can be found in refs. [91–104].

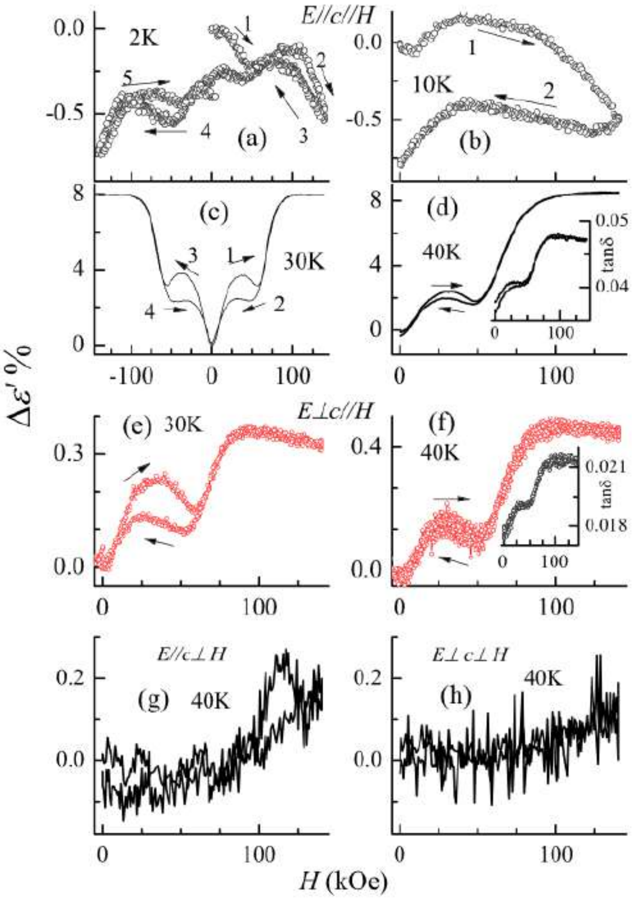

FIGURE 1.20: Change in the dielectric constant ($\Delta\epsilon'$) of $Ca_3Co_{1.4}Rh_{0.6}O_6$ with magnetic field (H) [110]. (a), (b), (c), and (d) shows $\Delta\epsilon'$ vs. H for $E \parallel c \parallel H$ at different temperatures. (e) and (f) shows $\Delta\epsilon'$ vs. H for $E \perp c \parallel H$ at different temperatures. (g) and (h) shows $\Delta\epsilon'$ vs. H for $E \parallel c \perp H$ and $E \perp c \perp H$, respectively, at 40 K.

1.6.3 Magneto-dielectric behavior

The Co spin-chains in the rhombohedral structure of $Ca_3Co_2O_6$ are arranged on a triangular lattice (*cf.* Fig. 1.1) and couple through a weak antiferromagnetic interaction, which leads to geometrical frustration in the system. It is well known that the frustrated geometry breaks the inversion symmetry leading to magneto-electric coupling in the ordered state [105, 106]. Magneto-dielectric coupling in $Ca_3Co_2O_6$ was first observed by Bellido *et al.* [107]. The steplike magnetocapacitance and dielectric relaxation in this system further lead to potential applications in sensors and memory devices [108]. On the other hand, Basu *et al.* [9] reported the magneto-electric coupling effect in this system well above T_{c1}, that is primarily due to spin chain ordering. Such a unique feature of magneto-electric coupling in the magnetically isolated spin chains is essential to enable spin-controllable electric effects. The dielectric properties of the system were further improved by the elemental substitution. The Gd substitution in $Ca_3Co_2O_6$ leads to complex dielectric relaxation and ferroelectric-relaxor-like behavior [109]. On the other hand, the Rh substitution leads to anisotropic magneto-dielectric coupling with improved dielectric constant and loss factor in this system (Fig. 1.20) [110]. A more detailed investigation on the magneto-dielectric behavior of $Ca_3Co_2O_6$ and its substituents can be found in refs. [111–117].

1.7 Motivation

It is clear that the $Ca_3Co_2O_6$ system exhibits a complex magnetic structure due to the reduced dimension of spin interactions and competing lattice, spin, electric, and orbital degrees of freedom. Additionally, the magnetic structure of the system is extremely sensitive to external perturbations such as temperature, pressure, and magnetic field. The unconventional features and the dynamic magnetic structure of the system are indicative of degeneracy in the magnetic ground state; therefore, the $Ca_3Co_2O_6$ system is ideal for a thorough understanding of the low-dimensional magnetic system, which is a topic of enormous interest from condensed matter physics point of view.

In addition to the external perturbation effects, the flexibility of the $A_3BB'O_6$ structure in accompanying a wide range of elements provides additional degree of freedom in modifying the magnetic structure of the system by an appropriate amount of lower/higher valence ions substitution. An earlier report by Basu *et al.* [109] suggested the modification in the oxidation state of both Co1 and Co2 ions by the partial replacement of Ca^{2+}

ions by Gd^{3+} ions. On the other hand, the Dy and Lu substitution leads to the stabilization of spin density wave phase and modification in the oxidation state of Co2 ions only [118]. These features further enable us to study the stable phases of low-dimensional systems. Further evidence of modification in the magnetic and electronic structure of the system by rare earth ions substitution can be found in refs. [84, 119–122]. In addition to the rare earth ion substitution effects, the doping of transition metals at the Co2 site offers opportunities to modify the magnetic structure of the system by the imbalance of intra-chain and inter-chain coupling. As it is well known that the exotic magnetic feature of this system is a consequence of reduced dimensionality effects and frustration, therefore, it became essential to maintain the pseudo-1D character of the system while influencing the magnetic structure with different doping content. In this way, attempts have been made to tune the magnetic structure of the system by Fe substitution [123–130], which has an ionic radius comparable to Co ions anticipating that there will be no strong lattice distortion. However, the Fe substitution leads to a decrease in the magnetic ordering temperature and deviation from 1D character [124], which is primarily due to the reduced strength of intra-chain ferromagnetic interaction with the Fe content. Similar to the effects of Fe substitution, the magnetic ordering temperature also decreases with Mn and Cr substitution [131–135]. The chemical disorder effect due to Mn substitution in this system enhances the glassy feature of the system [131]. Furthermore, the Mn substitution leads to ferroelectricity in this system, which is a result of inversion symmetry breaking [111, 136–138]. In contrast to the Fe, Mn, and Cr substitution effects, the magnetic ordering temperature increases for Ir and Rh substitution, and the intra-chain ferromagnetic interaction gets enhanced [21, 110, 139, 140]. Thus, it is concluded that depending on the alignment of dopant ion moment with Co ion moment, the dominant interaction is antiferromagnetic for Fe, Cr, and Mn substitution and ferromagnetic for Ir and Rh substitution. Due to the dominance of ferromagnetic/antiferromagnetic interaction with substitution, the ground state degeneracy is lifted, and the exotic magnetic features of the system are gradually suppressed.

As it is clear that the transition metals substitution in this system leads to a strong magnetoelectric coupling which has potential applications but dramatically influences the characteristic feature of the system. Thus modifying the magnetic structure of this system with magnetic dopants no longer be a good choice from condensed matter physics point of view, and strongly suggested to look for non-magnetic dopants, which may have little effect on the intra-chain and inter-chain interactions so that the key features remain unaltered. As suggested by Ruan *et al.* [141], the non-magnetic Sc substitution for Co2 ions (up to 60 %) does not influence the intra-chain ferromagnetic interaction. However, the doping effects of other non-magnetic ions in this system are still unexplored.

Considering all these ideas, this system is ideal for exploring the novel aspects of magnetism and provides an ideal platform to play around with the metastable phases of the system. In addition, the Co ion in this system has the possibility of spin state transition when a higher/lower valence ion is substituted. Thus, the magnetic and electronic structure of the system is extremely sensitive to external perturbation and doping content. This thesis is focused on understanding the complex magnetic and electronic structure of $Ca_3Co_2O_6$ and the substituted (magnetic/non-magnetic) compound through experimental results and theoretical predictions. The experimental part involves the characterization of structural, magnetic, and electronic states of these samples by X-ray diffraction, Raman, magnetization, and X-ray photoelectron spectroscopy measurements. On the other hand, these features were theoretically predicted by first-principles-based density functional theory calculations results.

Chapter 2

Experimental and Computational methods

This chapter discusses the experimental technique used for sample synthesis, characterization, and various magnetic measurements. It also provides important insight into the working principle of the experimental tools used for these measurements. In addition, a brief description of the operating condition of various instruments is also provided. First, the sample synthesis technique with necessary precautions during the synthesis process is discussed in section 2.1. The following sections 2.2 and 2.3 briefly describe the phase identification techniques (X-ray diffraction and Raman spectroscopy) of the prepared samples. The powder X-ray diffraction method and the diffractometer used for recording diffraction patterns are discussed in section 2.2. Basics of the microstructure analysis, along with a brief description of the Field Emission Scanning Electron Microscope (FESEM), is given in section 2.4. Section 2.5 describes the surface-sensitive X-Ray Photoelectron Spectroscopy (XPS) technique used for the chemical composition analysis. It also provides essential information about the X-ray photoelectron spectrometer and its mode of operation. Magnetization measurements of this thesis are performed on Physical Property Measurement System (PPMS) outlined in section 2.6. In addition, the computational methods used in this work are also discussed in this chapter.

2.1 Sample Preparation

The solid-state reaction route is the most commonly used method for synthesizing polycrystalline oxide samples. Throughout this thesis, the samples were prepared by this method. The basic principle is quite simple, two or more solids react with each other under some extrinsic conditions to form the desired compound, which separates them [142, 143]. Reactions in the solid form are extremely slow since the mixed reactants are inhomogeneous at the atomic level. However, if the reactants are chemically reactive or contain interacting ions, the reaction in the solid form may happen easily. Therefore, the atoms of constituent elements can bring together by solid-state diffusion to obtain the desired product [144]. At ambient temperature, the diffusion process is closely related to the defect in the crystal. In crystalline solids, the defects can be either point (interstitial or vacancy) or extended (grain-boundaries or dislocations) [142]. The atoms have much higher mobility along the defect; therefore, the defects act as a high-diffusivity path in the crystal. In addition, the diffusion process in crystalline solids depends rather strongly on thermodynamic variables (temperature and pressure). Thus, the diffusion process in solids generally occurs due to the thermally activated movement of atoms or molecules.

In the solid-state reaction route, the stoichiometry of required reagents is grounded in an acetone medium using an agate mortar pestle. It requires several hours of grinding to ensure better contact between the surfaces of constituting elements and homogeneity in the obtained mixture. In order to remove unwanted impurities such as carbonates, sulfates, and nitrides, the obtained mixture is calcined above room temperature. The calcined powder was then pressed in the form of disc-shaped pellets using a hydraulic press to improve the contact area between reactants. It is well known that most solids do not react at ambient temperature due to diffusion barriers. To overcome these barriers, heat treatment is necessary much above room temperature, which provides thermal activation energy for ions to diffuse across the energy barrier. A commercial tabletop furnace manufactured by Nabertherm, Germany (model HTCT 03/15) with a maximum operating temperature of 1773 K has been used for heat treatment. As the reaction rate in solid form is quite slow; therefore, it is best to re-sintered the samples with intermediate grinding to ensure homogeneity. Furthermore, the kinetics of these ions can be controlled by the heating and cooling rate, which is essential for the final sintering.

The major issues that can affect the reaction in the solid-state form are (1) Precursors (2) Container (3) Sintering. In addition, the evaporation of reactants during heat treatment may cause a potential loss.

1. **Precursors:** Starting materials should be of high purity and must be taken in stoichiometry. Problems can occur if the reactants contain mixed valence transition metals or are highly moisture/CO_2 sensitive. In order to avoid this, the reactants must be dried above room temperature. Furthermore, it is helpful to use reagents either in nitrate or carbonate form, which can decompose above room temperature. The decomposition step dramatically reduces the particle size, leading to better surface contact and increasing the reactivity. The exerted gases during the decomposition step can further boost the reaction rate.

2. **Container:** In the solid-state reaction route, the powder is kept inside a suitable container for heat treatment in air/medium. It becomes essential to use inert containers so the reactions may not get affected. Generally, the crucibles/boat of Au, Pt, and Al_2O_3 are used as a container. Out of these, the alumina crucibles are preferred for preparing oxide samples. Crucibles made up of alumina are cost-effective and have a high melting point; therefore can sustain at higher temperatures. Furthermore, the high-purity Al_2O_3 is inert so that contamination may be avoided.

3. **Sintering:** It is the trickiest part of solid-state reactions. For known compounds, the appropriate condition for reaction can be obtained from the literature. However, for new compounds, favorable conditions are obtained using a trial-and-error approach. Furthermore, it is worth mentioning that during the sintering process, necessary precautions are required to avoid excess frothing of reagents due to decomposition. The heat treatment should not be above the melting point of reactants. In general, there are three stages in the solid-state sintering process. The initial stage involves the formation of strong bonds between powder particles so that the density may increase. In the intermediate step, the grain boundaries are formed, and the porosity decreases while the pores are still connected. The reduced

porosity leads to a denser microstructure at the intermediate sintering. In the final stage, the pores are isolated from each other and slowly get eliminated.

2.2 X-ray Diffraction

X-rays were discovered in 1895 by German scientist Wilhelm Conrad Röntgen. It has a wavelength ranging from 100 to 0.1 Å, which is the order of lattice dimensions. Thus, the X-ray diffraction study plays a crucial role in determining the structural features of crystalline solids and can be considered the backbone of experimental condensed matter physics. The working principle is based on the constructive interference pattern obtained from the scattering of X-rays by the periodic arrangement of atoms in a lattice [145]. When a monochromatic beam of X-rays is incident on a crystalline solid, due to the comparable wavelength and interplanar spacing, the X-rays get diffracted (Fig. 2.1). The diffracted X-rays undergo constructive interference, and depending on the incident angle, several peaks appear in the diffraction pattern. Each peak in the diffraction pattern corresponds to a particular set of crystallographic planes (hkl). The condition for constructive interference is given by Bragg's law

$$2d\sin\theta = n\lambda \tag{2.1}$$

where d is the interplanar spacing, θ is the glancing angle, n is the diffraction order, and λ is the wavelength of the X-ray. Thus, in view of X-ray diffraction experiments, Bragg's condition can be satisfied by varying either θ or λ. Based on varying parameters and the nature of samples, the X-ray diffraction methods are mainly categorized into three categories (Table 2.1) [145].

TABLE 2.1: List of the main X-ray diffraction methods.

Method	Fixed Parameter	Variable
Laue method	θ	λ
Rotating-crystal method	λ	θ
Powder method	λ	θ

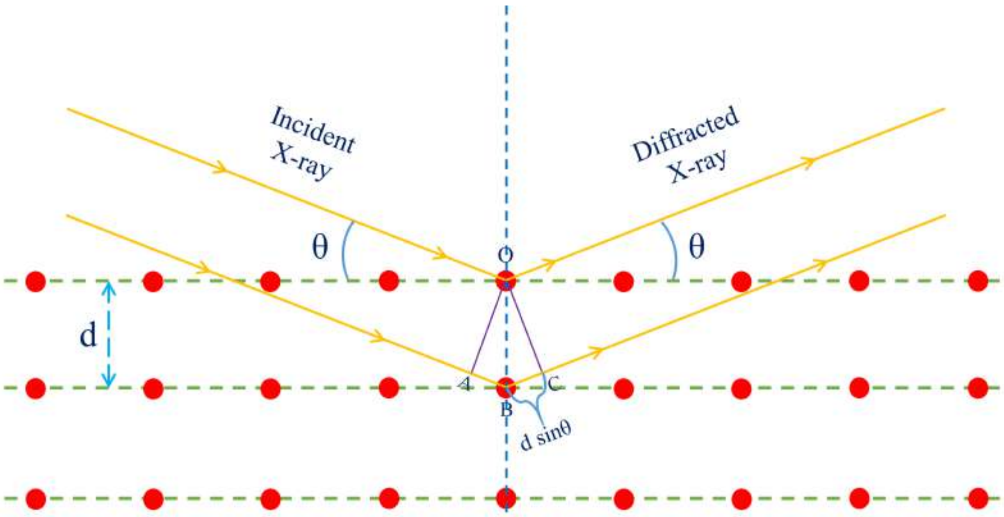

FIGURE 2.1: Schematic representation of diffraction of X-ray beam by periodically arranged atoms (red circle) in a lattice. The beam at the bottom traverses an additional path of AB + BC = $2d\sin\theta$.

Laue's method allows a beam of white radiation to fall on a fixed single crystal. Thus, θ is fixed while λ changes in this method, and each set of (hkl) planes diffract a particular wavelength which satisfies Eq. 2.1. Rotating-crystal method is used for the crystallographic study of single crystals. The single crystal is placed in such a way that one of its axes is normal to incident X-ray direction, and a cylindrical film surrounds it. Furthermore, it is rotated about the axis of the cylindrical film so that for a particular set of planes, Bragg's condition is satisfied. On the other hand, the powder diffraction method is the most widely used for the structural study of polycrystalline samples.

2.2.1 Powder diffraction method

In this method, the specimen is a very fine powder, where each particle is a tiny crystal with a random orientation [145]. Therefore, the whole assembly of particles can produce reflection corresponding to each set of (hkl) plane. If we consider the reflection from a particular set of planes, the plane is now rotated about the direction of the incident X-ray (θ is fixed). The reflected beam traverses a cone with axis along the direction of the transmitted beam. In this way, separate cones corresponding to each set of (hkl) planes are formed. Fig. 2.2 depicts a few such cones formed by the Debye-Scherrer powder diffraction method. It consists of a cylindrical camera curved by a narrow strip of film. The specimen (target) is placed on the axis of the cylinder while the X-ray beam

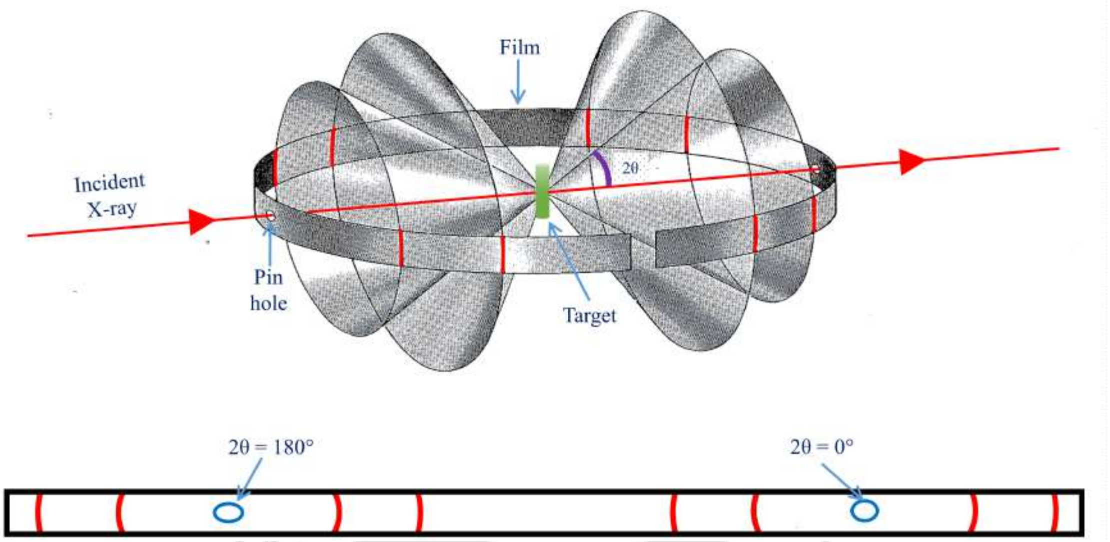

FIGURE 2.2: Diffraction of the X-ray beam by a polycrystalline sample (Target) using the Debye-Scherrer method [145]. The incident beam undergoes diffraction, and the diffracted beam traces a cone corresponding to each set of planes. The diffraction spots were obtained on a cylindrical film.

is directed transverse to this axis (Fig. 2.2). It is shown in Fig. 2.2 that the cones of diffracted X-ray beam intersect the cylindrical film in lines, and the diffraction pattern is obtained. With the help of diffraction spots, the θ corresponding to each line can be determined. As the λ is already known, it allows us to calculate the interplanar spacing. This method is often used for phase identification and accurately determining the lattice constants. Thus, using this method, one can determine the whole crystal structure of the system.

2.2.2 X-ray diffractometer

It is an instrument used for the structural study of crystalline or non-crystalline materials by understanding their way of diffracting a known wavelength X-ray beam. The X-ray diffraction patterns of the prepared polycrystalline samples were taken using a commercial Rigaku X-ray diffractometer (XRD) (TTRAX III) (Fig. 2.3(a)). It is equipped with a 9 kW rotating anode generator in a Bragg-Brentano geometry to generate the X-rays (Fig. 2.3(b)). Typical wavelengths of generated X-rays depend on the type of metal target used. The K_α radiations produced by the Cu target were used as a source (λ = 1.5406 Å). Furthermore, a high-accuracy theta-theta goniometer allows one to do the 2-theta scans where the sample is fixed horizontally. In the Bragg-Brentano geometry,

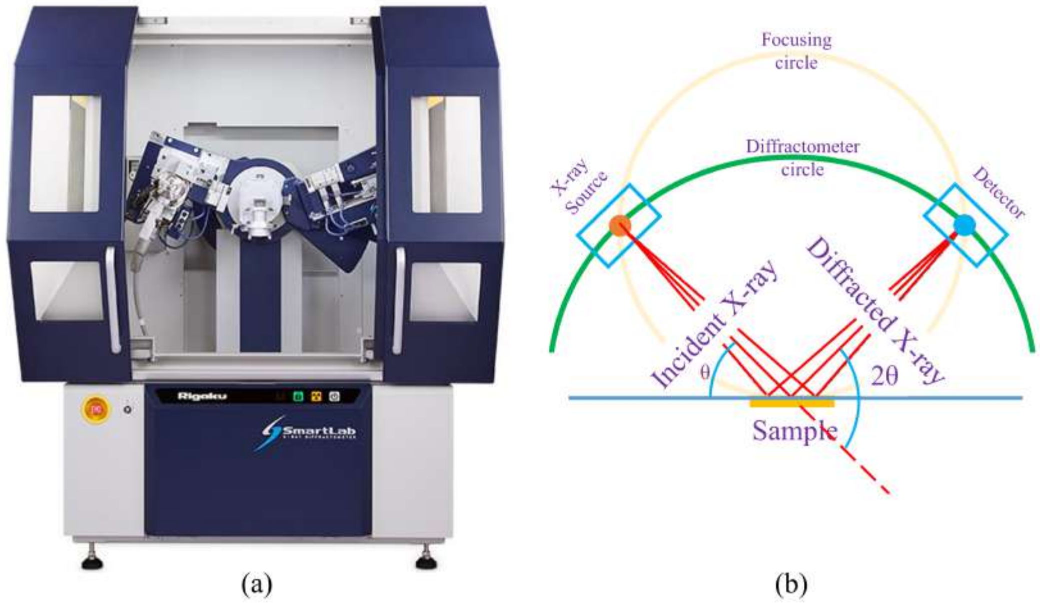

FIGURE 2.3: (a) Rigaku TTRAX III X-ray diffractometer (b) Bragg-Brentano diffraction geometry.

the X-ray source and detector are equidistant from the sample (Fig. 2.3(b)). Thus, the X-ray source and the detector moves in a circle (diffractometer circle) with its center at the sample, and the relationship between the incident angle (θ) and diffracted angle (2θ) is always maintained. It turns out that the focusing circles are always tangent to the sample and have a variable diameter with θ. The Bragg-Brentano geometry requires precise alignment to offer perfect focusing and high-resolution analysis.

The prepared samples were scanned in the range $2\theta = 10°$-$80°$ with a scan rate of 10 °/min having a step size 0.02°. Further analysis of X-ray diffraction data has been done by the Rietveld refinement method using the FULLPROF program [146, 147]. It confirms the phase purity of the samples and provides structural parameters such as lattice constants, site occupancy, and atomic positions. The refined structures were further analyzed by the VESTA software to extract bond lengths and bond angles.

2.3 Raman Spectroscopy

In addition to the crystallographic information from the X-ray diffraction analysis, Raman spectroscopy based on the Raman effect is also a versatile and adaptable tool for crystallographic studies, such as crystalline phases, orientation, bonding information, defects, strain, etc [148–150]. The Raman effect is an inelastic light scattering phenomenon based on photon-phonon interaction. When a beam of light is illuminated to a specimen (solid, liquid, or gaseous), the light may get absorbed, scattered, or not interact with the substance. If the energy of the incident photon is equal to the energy gap ($\mathit{\Delta} E_{\mathrm{V}}$) between the vibrational ground state and excited state of the molecule, the photon gets absorbed, and the molecule is promoted to the excited state. Such change in the energy of the radiation is studied in absorption spectroscopy. On the other hand, in Raman spectroscopy, a monochromatic beam of light is used, and the scattering of light due to the interaction of photons with the molecule is studied. Thus, in Raman spectroscopy, the energy of the scattered radiation differs from the incident radiation in vibrational units. Therefore, unlike absorption spectroscopy, no energy matching of incident photon to $\mathit{\Delta} E_{\mathrm{V}}$ is required in Raman spectroscopy [148]. Depending on the distortion induced by the interaction of light with the molecule, the scattering can be elastic (Rayleigh) or inelastic (Raman). The Rayleigh scattering involves distortion in the electron cloud only.

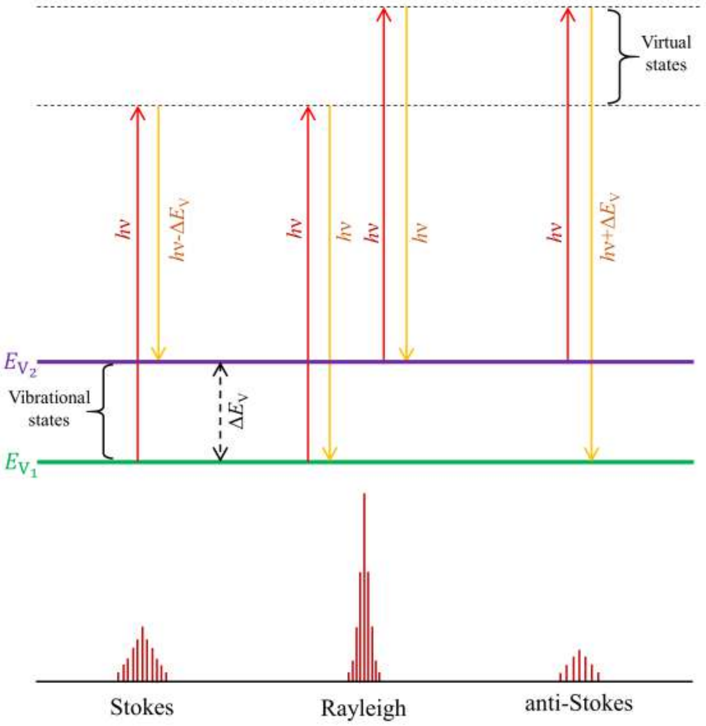

FIGURE 2.4: Principle of scattering process: light quanta of energy $h\nu$ interacts with the molecule which can be either in the vibrational ground (E_{V_1}) or excited (E_{V_2}) state.

Thus, the scattered photons have the same frequency as the incident radiation, and it is the dominant process in scattering. On the other hand, Raman scattering corresponds to the involvement of nuclear motion in the scattering process. Therefore, energy transfer occurs either from photon to molecule or from molecule to photon. Thus, depending on the vibrational state of the molecule, the scattered photon can have the energy either $h\nu$-$\varDelta E_{\mathrm{V}}$ (Stokes lines) or $h\nu+\varDelta E_{\mathrm{V}}$ (anti-Stokes lines), where h is the Planck's constant and ν is the frequency of the incident photon [148, 149]. Fig. 2.4 shows the schematic representation of the scattering process. Usually, at room temperature, most of the molecules are in their vibrational ground state (E_{V_1}), while due to thermal energy, only a few of them may present in the vibrational excited state (E_{V_2}). The virtual states are created when a high-energy photon interacts with the molecules and causes polarization. In the Rayleigh scattering, no energy change occurs, and the molecule returns to its original state; therefore, the scattered photon has the same frequency as the incident one (Fig. 2.4). On the other hand, the Raman scattering process leads to a change in the vibrational level of the molecule ($E_{\mathrm{V}_1} \rightarrow E_{\mathrm{V}_2}$ or $E_{\mathrm{V}_2} \rightarrow E_{\mathrm{V}_1}$). Molecules in the vibrational ground state are promoted to the excited state by absorbing energy, and photons with lower energy $h\nu$-$\varDelta E_{\mathrm{V}}$ are scattered. The corresponding Raman line of lower frequency is called the Stokes line. On the other hand, molecules in the vibrational excited state transfer their energy to the photon and de-excited to E_{V_1}. In this process, photons with energy $h\nu+\varDelta E_{\mathrm{V}}$ are scattered, and the corresponding Raman line of higher frequency is called the anti-Stokes line. As the E_{V_1} is much more populated than the E_{V_2} (Boltzmann's law) therefore, in the Raman spectra, the Stokes lines are appeared to be much stronger than the anti-Stokes line.

The room temperature Raman spectra were recorded in the wavenumber range of 100-1000 cm^{-1} using a micro-Raman spectrometer (LabRAM HR800, Horiba Jobin Yvon) with an excitation wavelength of 488 nm (Fig. 2.5(a)). In this micro-Raman spectrometer, the 800 mm focal length spectrometer equipped with two switchable gratings is confocally coupled to the microscope. Fig. 2.5(b) shows the schematic diagram of the working of the micro-Raman spectrometer. The incoming Ar-ion laser beam (λ = 488 nm and 514 nm) is reflected by the beam splitter, which splits it into two parts having the same wavelengths. This intense laser beam is illuminated over the sample through a

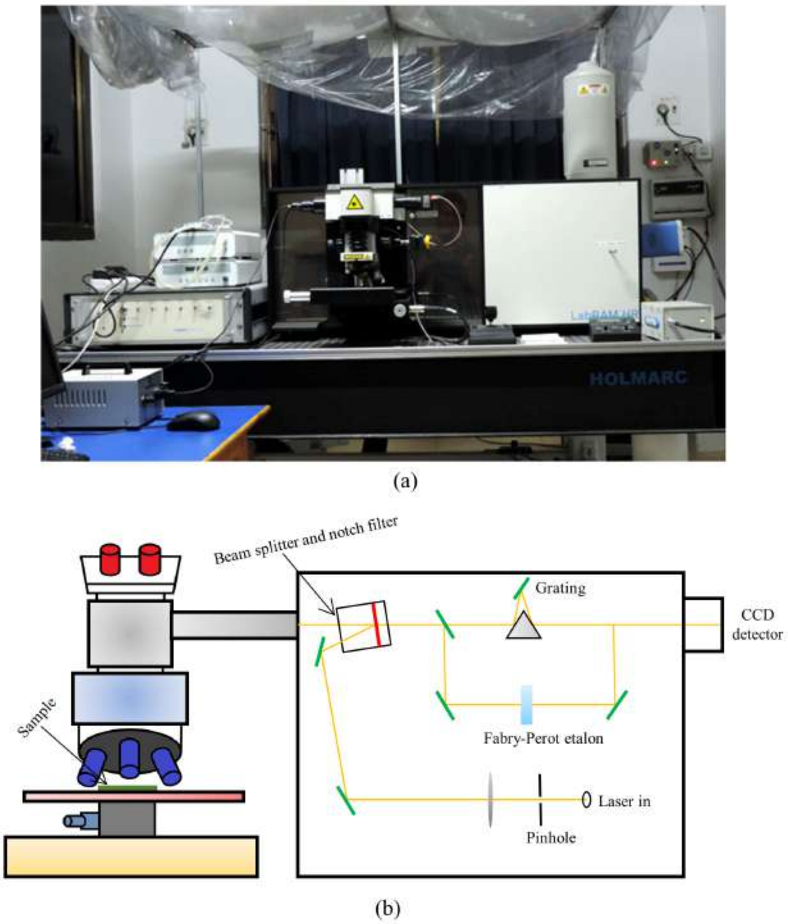

FIGURE 2.5: (a) Laser micro-Raman system (LabRAM HR800, Horiba Jobin Yvon) (b) Schematic diagram.

microscope with a spot size of a few microns, and the photons get scattered. From the scattered radiation, the notch filter allows only the Raman scattered wavelengths while it effectively blocks the Rayleigh scattered wavelengths. Further, the scattered radiation is allowed to pass through the grating and etalon, which resolve the weak Raman scattered wavelengths coming from the specimen. In order to obtain the Raman spectra, a charge-coupled device is used, which detects the change in the polarizability of the specimen from the change in the wavelength and converts it into the intensity.

2.4 Field Emission Scanning Electron Microscope

It is well known that the defects and grain size play a crucial role in determining various physical, mechanical, and chemical properties of the polycrystalline samples. Thus, after confirming the phase purity of the prepared samples, it became essential to have

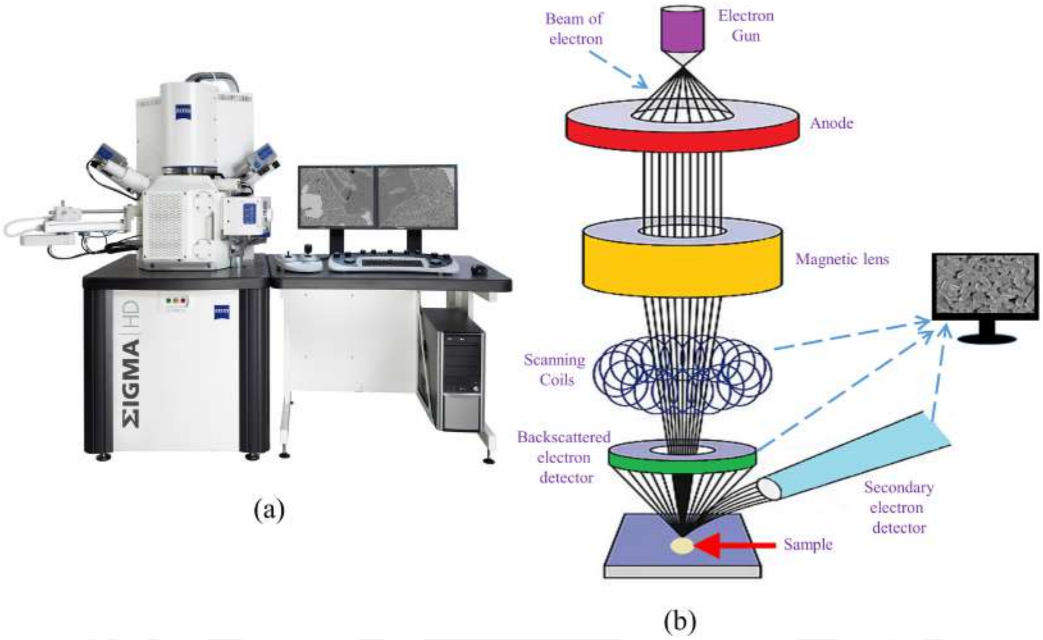

FIGURE 2.6: (a) Field Emission Scanning Electron Microscope (*Σ*IGMA) (b) Schematic diagram.

a thorough understanding of their microstructure. It involves a complete description of constituting particles (size, shape, and distribution of grains) and the composition analysis in polycrystalline materials. The microstructural study has been done using a ZEISS-made *Σ*IGMA Field Emission Scanning Electron Microscope equipped with energy dispersive X-ray spectroscopy (EDS) (Fig. 2.6(a)) [151]. It uses a focused beam of electrons to produce high-resolution images (1 nm) at magnifications 10× to 300,000×. The source is an electron gun with sharply pointed Schottky emitters (Zirconium oxide coated tungsten tip) held at a high negative potential relative to the anode to cause field emission under vacuum (Fig. 2.6(b)). Emitted electrons are confined to a narrower beam by electromagnetic lenses. Thus, the whole setup provides accelerated narrower beams of high as well as low electron energy leading to minimum sample damage and charging (accelerating voltage in the range 0.5 to 30 kV). Furthermore, the electron beam is focused on the sample by an objective lens, and electromagnetic scanning coils scan the surface of the specimen. When the electron beam strikes the specimen, it will penetrate it up to a certain depth. Thus, the electron beam interacts in many different ways with the surface and near-surface region of the sample, which will be discussed later. The impinging electrons have sufficient kinetic energy to produce signals in the form of ejected electrons or characteristic X-rays. The in-lens ac detectors gather these ejected electrons to produce the microstructure of the sample on a computer screen. However, Energy dispersive X-ray spectrometer equipped with the FESEM uses the characteristic X-rays for the composition analysis of the sample.

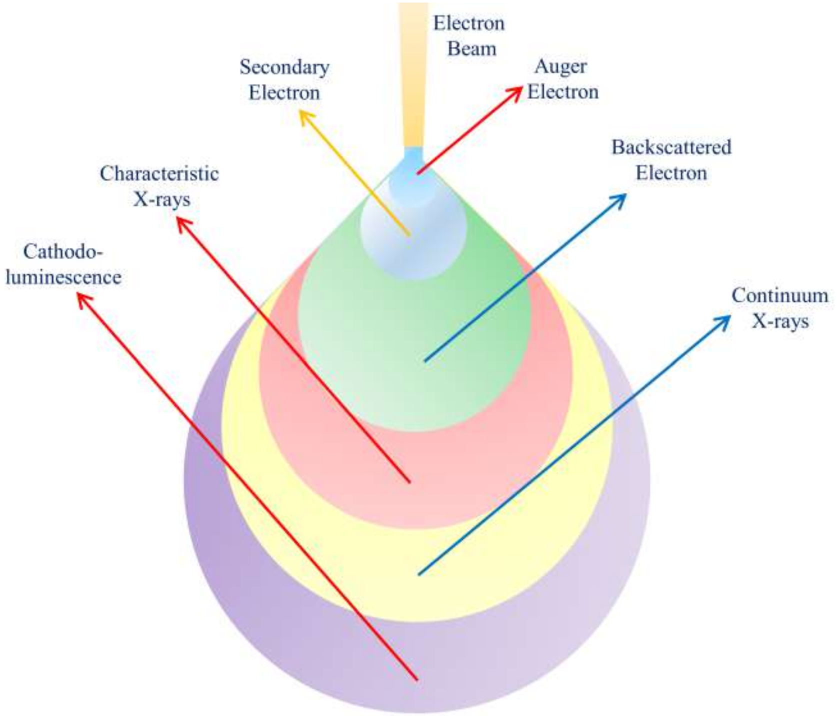

FIGURE 2.7: Signals from the drop-shaped interaction volume when an electron beam strikes the surface of the sample.

Generally, the incoming electrons have both elastic and inelastic interactions with the nuclei/electrons of the specimen [152]. In inelastic interactions, the primary electrons interact with the electric field of the shell electron. It leads to energy transfer from the primary electron to the shell electron. As a result, secondary electrons are emitted, which have energy less than 50 eV. The outer shell electrons fill the vacancy created by the emission of secondary electrons, and X-rays of characteristic frequencies are produced. However, instead of emitting photons, the energy can be transferred to another electron, which is then ejected. This is known as the Auger effect, and the released electron is called the Auger electron. On the other hand, in elastic interactions, the primary electrons interact with the nucleus of the specimen, and the direction of primary electrons changes without any change in the energy. If the deflected electrons come out of the specimen, they are called backscattered electrons. Therefore, based on the elastic and inelastic interactions of the incoming beam of electrons with the electron/nuclei of the specimen, the beam electrons are distributed (Fig. 2.7). Usually, the secondary electrons are emitted from a depth of 5-50 nm of the sample. The backscattered electrons escaped from a relatively more depth, while the characteristic X-rays are emitted from a much larger depth.

In order to take the micrographs of the sample, the solid samples were mounted on carbon tape and coated with a thin layer of gold. Furthermore, the particle size distribution was obtained using ImageJ software.

2.5 X-ray Photoelectron Spectroscopy

It is a surface-sensitive spectroscopic technique commonly used for the composition analysis, chemical state, empirical formula, and oxidation state of elements within the compound. In X-ray photoelectron spectroscopy, all the elements except hydrogen and helium can be detected with a detection limit in parts per thousand range [153]. XPS technique was developed by Siegbahn and his colleagues at the University of Uppsala, Sweden, and it is based on the photoelectric effect [154].

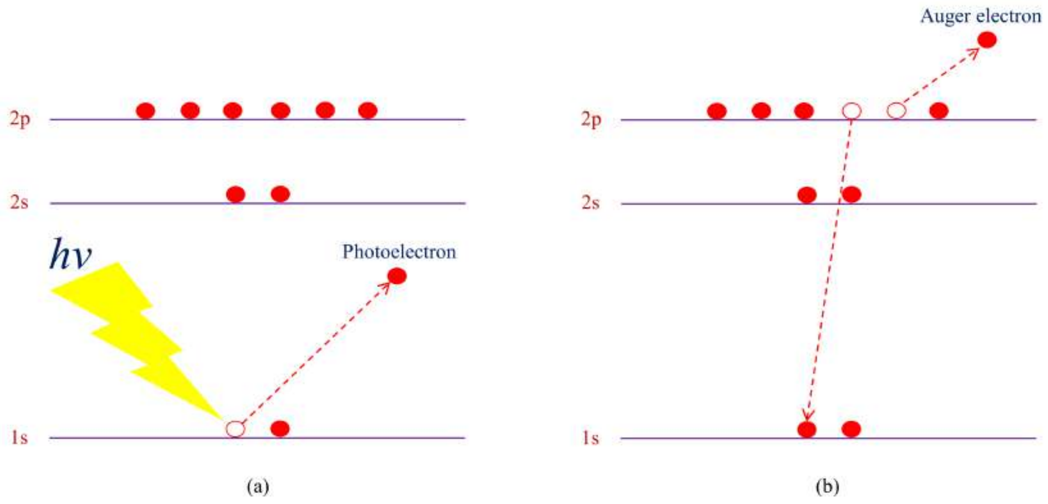

FIGURE 2.8: The XPS photoemission process (a) incoming photon of energy $h\nu$ emits a photoelectron from the specimen (b) relaxation process leads to emission of Auger electron.

The XPS analysis involves irradiating the specimen with a monoenergetic soft X-ray and analyzing the emitted electron. A typical XPS spectrum is a plot of the number of detected electrons vs. binding energy where each element in the specimen produces a set of characteristic peaks. The binding energy E_{BE} of the electron is given by the photoelectric effect equation

$$E_{\mathrm{BE}} = h\nu - E_{\mathrm{K}} - \phi \tag{2.2}$$

where the first, second, and third term on the right-hand side represents the photon energy of the X-ray, measured kinetic energy of the emitted electron, and spectrometer work function, respectively. In the photoemission process, the ions remain excited; therefore, Auger electrons could be emitted during the relaxation. The process of excitation and de-excitation during XPS operation is shown in Fig. 2.8.

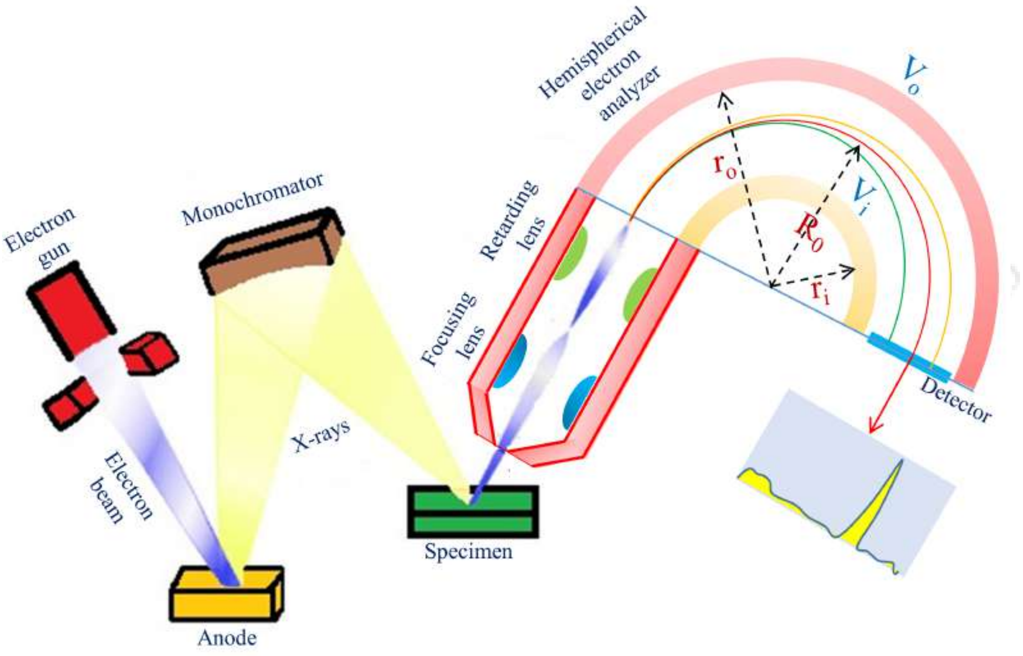

FIGURE 2.9: Schematic diagram of XPS spectrometer.

The XPS measurements were performed using a Thermo-Scientific ESCALAB Xi+ spectrometer which provides better resolution and high spectral sensitivity. The sample analysis chamber is made of 5 mm thick mu-metal (iron-nickel alloy) to provide efficient magnetic shielding. Fig. 2.9 shows the schematic diagram of the XPS spectrometer, and the main components of the XPS are as follows [155]:

1. **X-ray source:** The characteristic X-rays such as Al-K$_\alpha$ (1486.6 eV) and Mg-K$_\alpha$ (1253.6 eV) are used for photoelectron emission. Generally, the X-ray produced by the interaction of high-energy electrons with anode material is non-monochromatic.

Working with non-monochromatic X-rays may cause satellite peaks and poor resolution; for these reasons, monochromatic sources are prioritized. The twin crystal micro-focusing monochromator is used to obtain the monochromatic X-ray, and the monochromated beam can be focused to spot sizes of range 200 μm to 900 μm.

2. **Ultra-high vacuum:** XPS analysis requires ultra-high vacuum (10^{-7} Pa) conditions inside the chamber. Otherwise, the photoelectrons may lose their energy due to collision with gas molecules. The ultra-high vacuum inside the chamber is achieved using a titanium sublimation pump and a turbomolecular pump.

3. **Electron energy analyzer and lens:** The main function of an electron energy analyzer is to disperse the ejected electrons according to their kinetic energy. In XPS, a 180° hemispherical electron energy analyzer is often used for this purpose (Fig. 2.9). It consists of two concentric hemispherical electrodes held at voltages V_i and V_o, respectively. The V_i and V_o are chosen in such a way that the emitted electrons with energy equal to the pass energy E_0 follow a circular path of radius $R_0 = \frac{r_\mathrm{i}+r_\mathrm{o}}{2}$ where r_i and r_o are the radii of the inner and outer hemispheres, respectively. A point-like detector at the other end will detect only those electrons with energy equal to E_0. By changing the E_0, one can get the number of photoelectrons as a function of E_K. Furthermore, the electrostatic lens focuses the incoming photoelectrons, and the retarding lens is used to achieve high resolution. Thus, the combination of an electron analyzer with lens system provides ideal conditions for spectroscopy.

For the chemical composition analysis, the samples were taken in powder form. The XPS measurements were performed using an ESCALAB Xi+ (Thermo Fisher) spectrometer with a monochromatic Al-K$_\alpha$ X-ray source under ultra-high vacuum conditions. The photoelectrons are analyzed by the hemispherical electron energy analyzer operating in the constant analyzer energy (CAE) mode using the electromagnetic lens. For the survey scan and high-resolution spectra, the CAE was set at 200 eV and 50 eV, respectively.

2.6 Physical Property Measurement System

The Physical Property Measurement System (PPMS) is a sensitive, versatile, and non-destructive tool manufactured by Quantum Design to study the magnetic and electric transport properties of samples (solids/thin films) under a well-controlled temperature and magnetic field. The advanced version of this system (DynaCool) provides all the features of PPMS without the requirement of liquid cryogens (Fig. 2.10). It utilizes a pulse tube cryocooler (single two-stage) for the functioning of temperature control system and superconducting magnet. It leads to vibration-less environment for measurements and low maintenance cost. Sample environment is further controlled by evacuating the chamber to less than 10^{-4} Torr using the cryopump. The PPMS DynaCool system is operational in the magnetic field range -9 T to +9 T and temperature range 1.8 K to 1000 K. Fig. 2.10 displays the main components of the PPMS DynaCool system the cryostat assembly, pump cabinet, and module bay.

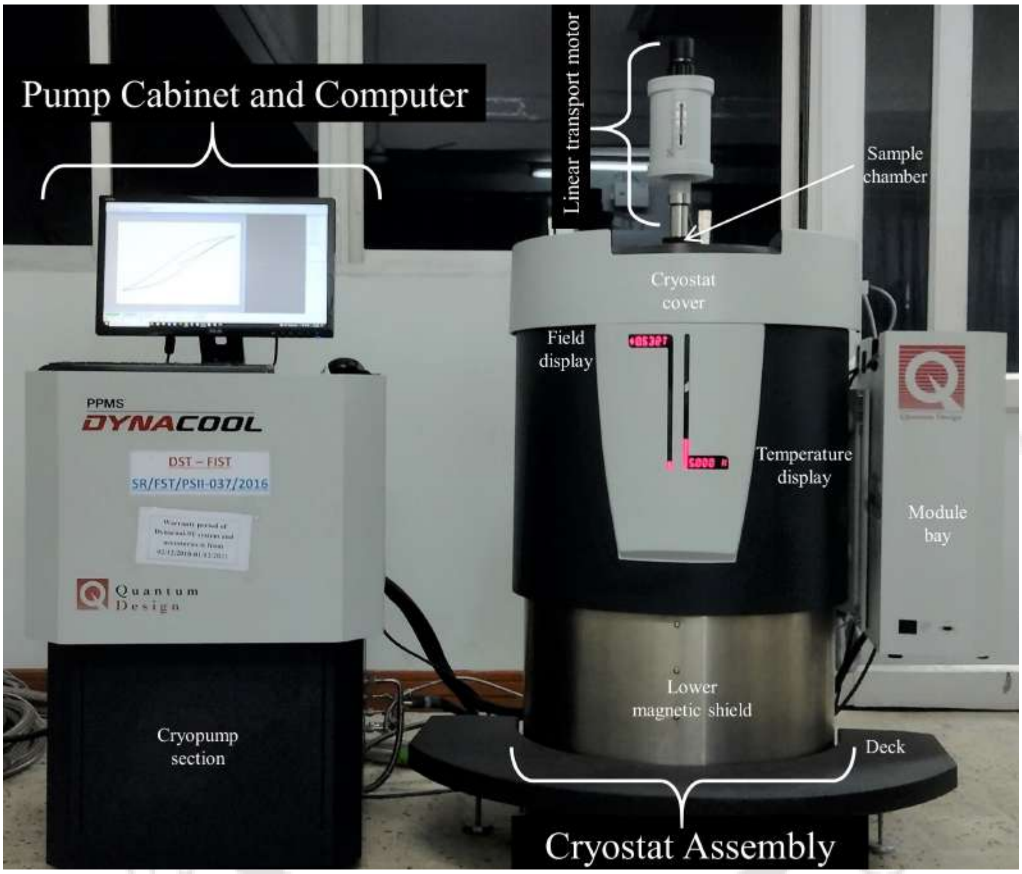

FIGURE 2.10: PPMS DynaCool system.

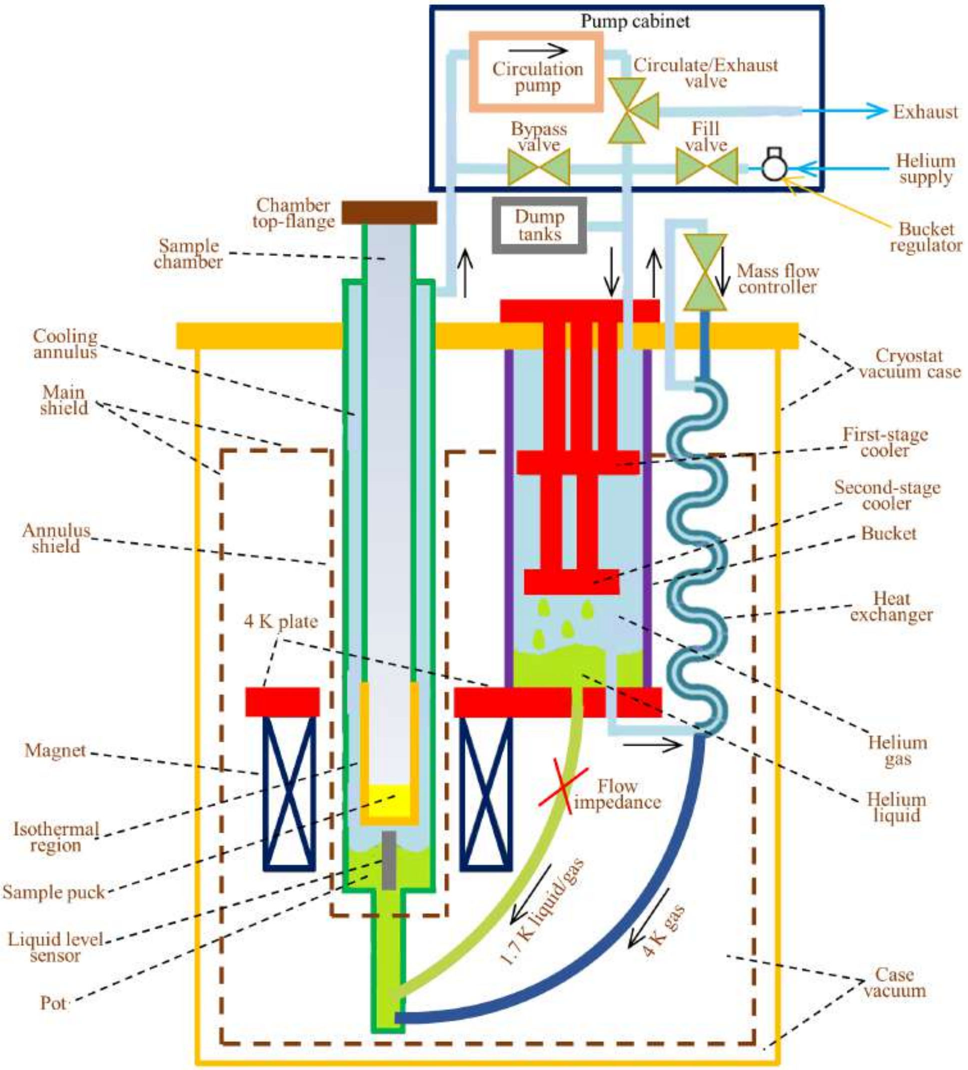

FIGURE 2.11: Schematic diagram of PPMS.

The cryostat assembly contains the conduction-cooled superconducting magnet, the cryocooler pulse-tube assembly, and the sample chamber. Fig. 2.11 shows the components of the controlling system of the cryostat, magnetic field, and chamber temperature. The superconducting magnet can generate a maximum vertical field of 9 T, and the value of current at this field is 55 A. In the DynaCool system, the cryocooler is mounted in a helium gas tank called bucket (Fig. 2.11). First-stage of the cryocooler is used for the cooling of the main shield, the first stage of the cryopump, the annulus shield, and the mechanical and electrical heat loads from room temperature. The second stage provides cooling for the sample chamber, superconducting magnet, 4 K plate, the second stage of cryopump, and the mechanical and electrical heat loads arising from the first stage of cooling. The components of the DynaCool system operate at different temperatures, ranging from room temperature to 1.8 K, and in order to maintain the temperature, thermal isolation between cryostat components is necessary. Cryostat case vacuum (evacuation up to 2 Torr) isolates those components which are not in mechanical contact. The main shield protects the second-stage components from room-temperature thermal radiation, and the annulus shield isolates the superconducting magnet from thermal radiation during high-temperature measurements. The isothermal region of high-conductivity copper provides a thermally uniform sample environment, and a puck interface is located at the bottom of it. A block heater and thermometer pair control the temperature of the puck. In addition, two other heater and thermometer pairs (neck and high neck) reduce the thermal gradient inside the chamber. Furthermore, the circulation loop enables the cooled helium flow inside the chamber, and the main components of the circulation loop are presented in Fig. 2.11. The common operating modes of the circulation loop are (i) Circulating, (ii) Pumping, (iii) Sealed, and (iv) Venting.

The CAN module bay located at the right of the cryostat (Fig. 2.10) hosts modules for system operations and measurements. For temperature control functions, the system is configured with Temperature Control Module. The other modules enable various magnetic and electric transport property measurements, and some of them are as follows:

1. **Vibrating sample magnetometer (VSM):** This option enables the PPMS DynaCool system to operate as a fast and sensitive DC magnetometer. It employs a linear transport motor for vibrating the sample and a puck-based first-order gradiometer coil set for detection. Using this configuration, a large oscillation amplitude (1-3 mm) and frequency (40 Hz) enable the system to detect a magnetization change of less than 10^{-6} emu [156]. In this mode, the DC magnetic moment can be measured as a function of temperature (1.8 K to 400 K), magnetic field (-9 T to 9T), and time. Furthermore, the VSM Oven option allows magnetic measurements much above room temperature (300 K to 1000 K). The magnetization data and results presented in this thesis were obtained using the PPMS DynaCool system operating in the VSM mode, and 2.6.1 discusses the VSM mode in detail.

2. **AC measurement system (ACMS II):** It employs an AC-drive coil set for alternating excitation field and a detection coil set for the determination of AC

susceptibility that enables the DynaCool system to operate as a versatile DC magnetometer and AC susceptometer. The AC-drive coil can generate alternating fields of amplitude 0.05 to 15 Oe in the frequency range of 10 Hz to 10 kHz.

3. **Thermal transport:** The thermal transport option (TTO) enables the users to measure the thermal transport properties such as thermal conductivity, electrical resistivity, Seebeck coefficient, and thermoelectric figure of merit. In the TTO operation, the sample under a high vacuum is subjected to a heat pulse, and the temperature and voltage drop along the sample is recorded. Sophisticated software based on a thermal circuit model dynamically extracts the thermal transport properties from these curves.

4. **Heat capacity:** It uses the puck-based microcalorimeter to measure the heat capacity of the sample across the accessible range of field and temperature of the DynaCool system. In this option, the sample under a high vacuum is subjected to a heat pulse, and its temperature response is recorded. Sophisticated software based on a thermal circuit model extracts the heat capacity from these curves.

2.6.1 Vibrating sample magnetometer

The basic principle of VSM operation is that a time-varying magnetic flux (ϕ) through the pickup coil induces a voltage (V_{PC}) in the coil (Faraday's law) given by

$$V_{\mathrm{PC}} = -\frac{d\phi}{dt} = -\left(\frac{d\phi}{dZ}\right)\left(\frac{dZ}{dt}\right) \tag{2.3}$$

where t is the time and Z is the vertical position of the specimen with the pickup coil. In the case of sinusoidally oscillating specimen position, it is simplified to

$$V_{\mathrm{PC}} = 2\pi f A M K_{\mathrm{c}} \sin(2\pi f t) \tag{2.4}$$

where f is the frequency of the oscillation, A is the amplitude, M is the DC magnetic moment, and K_{c} is a coupling constant. The magnetization measurements involve measuring the coefficient of the sinusoidal term in Eq. 2.4, and Fig. 2.12 shows a schematic representation of the procedure.

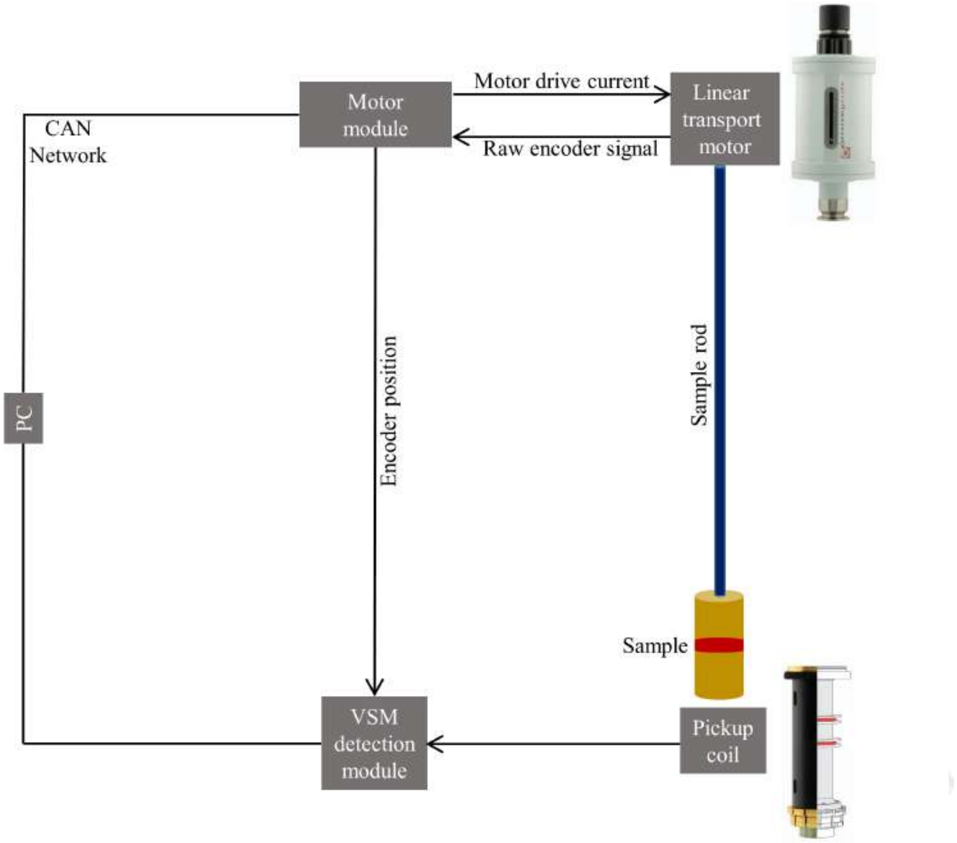

FIGURE 2.12: Block diagram of working principle of VSM.

In the VSM option, the sample attached at the end of the rod is driven sinusoidally inside a gradiometer pickup coil by using a linear motor transport (LMT). The position, amplitude, and frequency of the oscillation is adjusted from the motor module using an encoder signal readback from the LMT (Fig. 2.12). The induced $V_{\rm PC}$ in the coil due to the change in the magnetic flux is amplified and lock-in detected using the detection module. The raw encoder signal from the LMT is interpreted by the motor module, which provides position encoder signal (reference signal) for synchronous detection. Detection module detects the in-phase and quadrature-phase signals from the amplified $V_{\rm PC}$ and from the encoder. The VSM application on the PC handles all the control of detection module via the CAN network (Fig. 2.12).

2.7 Computational Methods

Having outlined the importance of experimental tools to have a thorough understanding of the structure and magnetism of complex systems, it became relevant to re-investigate the bulk systems from a theoretical point of view to establish a concordance between experimental and theoretical results. Over the decades, Density Functional Theory (DFT) has been one of the most powerful tools to have an important insight into many-body systems at the microscopic level. DFT became most popular among people working in condensed matter physics because it requires only a few structural parameters to determine various properties of the system. It allows us to do calculations of ground state energies, lattice structure, density of states, band structure, Fermi surface, magnetic moments, magnetic anisotropy, etc. In DFT, these properties are functionals (functions of another function) of spatial and spin-dependent electron density distribution, $n(\mathbf{r})$. Therefore, for an N-body system, the number of degrees of freedom reduces from $3N$ to 3 by its electron density. The foundation of DFT is based on Hohenberg-Kohn theorem, which states that the properties of a system are functionals of ground state electron density. An exact solution from DFT calculation has been made by taking together Born-Oppenheimer approximation, Kohn-Sham ansatz, and approximation for the exchange-correlation potential. The term exchange-correlation potential introduces the effects of Coulomb potential and Pauli principle beyond electrostatic interaction of homogeneous electron gas. Local Density Approximation (LDA) is the simplest approximation that locally substitutes the exchange-correlation energy density of an inhomogeneous system with that of a homogeneous electron gas evaluated at the local density. Further improvements in LDA have been made by gradient corrections, commonly known as Generalized Gradient Approximation (GGA). This chapter describes the theoretical methods used in the electronic structure determination of many body systems.

2.8 The Many-body Problem and Born-Oppenheimer Approximation

The Hamiltonian for a many-body system can be written as

$$\mathcal{H} = -\frac{\hbar^2}{2}\sum_{I}\frac{\nabla^2_{R_I}}{M_I} - \frac{\hbar^2}{2}\sum_{i}\frac{\nabla^2_{r_i}}{m_e} + \frac{e^2}{2}\sum_{I\neq J}\frac{Z_I Z_J}{|R_I - R_J|} \\ + \frac{e^2}{2}\sum_{i\neq j}\frac{1}{|r_i - r_j|} - e^2\sum_{I,i}\frac{Z_I}{|R_i - r_i|}. \tag{2.5}$$

The indexes i, j (I, J) run on electrons (nuclei), the r_i (R_i) and m_i (M_i) represent the position and mass of the i^{th} (I^{th}) electron (nuclei), and Z_I and Z_J represent the atomic number of nuclei I and J, respectively. Here the first and second terms are kinetic energies of nuclei and electrons, respectively. The third, fourth, and fifth terms are the potential energy of nucleus-nucleus, electron-electron, and electron-nucleus Coulomb interactions, respectively. In order to determine the electronic structure of the system, one needs to solve the many-body Schrödinger equation given by

$$\mathcal{H}\Psi = E\Psi \tag{2.6}$$

where E is the total energy of the system and Ψ is the wavefunction of the form,

$$\Psi = \Psi(r_1, r_2, ..., r_i, ..., R_1, R_2, ..., R_I, ...). \tag{2.7}$$

However, it is difficult to solve it in practice for large systems, and approximations are required to reduce the number of terms in Eq. 2.5. Since the relative masses of nuclei are much larger than the electrons; therefore, the motion of nuclei is much slower than (two orders of magnitude) that of electrons and the kinetic energy term corresponding to the nuclei in Eq. 2.5 can be neglected. Based on these facts, the nuclei are considered fixed, and the wavefunctions of electrons and nuclei are treated separately, commonly known as the Born-Oppenheimer approximation [157]. The wavefunction under this approximation can be written as

$$\Psi = \chi(R_1, R_2, ..., R_I, ...)\,\Phi(r_1, r_2, ..., r_i, ..., R_1, R_2, ..., R_I, ...) \tag{2.8}$$

where χ stands for the nuclei and Φ for the electrons. Thus, under the Born-Oppenheimer approximation, the motion of electrons is separated from nuclei, and it is considered that the electrons are moving under a constant potential formed by nuclei.

2.9 Thomas-Fermi-Dirac Approximation

Despite the simplification introduced by the Born-Oppenheimer approximation, the task of solving the Schrodinger equation for an N-body system with $3N$ degrees of freedom is still difficult. To sort out this problem, Thomas, Fermi, and Dirac used electron density as a fundamental variable [158–160]. In this model, the total energy of the system under an external potential is given by

$$\begin{aligned} E_{\mathrm{TFD}}[n(\mathbf{r})] = A_1 \int n(\mathbf{r})^{5/3}\,d\boldsymbol{r} \; + \int n(\mathbf{r})\,V_{\mathrm{ext}}(\mathbf{r})\,d\boldsymbol{r} \; + \; \frac{1}{2}\iint \frac{n(\mathbf{r})\,n(\mathbf{r}')}{|\mathbf{r}-\mathbf{r}'|}\,d\boldsymbol{r}\,d\boldsymbol{r}' \\ + \; A_2 \int n(\mathbf{r})^{4/3}\,d\boldsymbol{r}. \end{aligned} \tag{2.9}$$

Here the first term is the kinetic energy of the electrons with $A_1 = \frac{3}{10}\,(3\pi^2)^{2/3}$. The second, third, and fourth terms are classical nucleus-electron Coulomb interaction, Hartree energy, and electron correlation. Although this semi-classical approach was the first step towards describing the ground state properties by electron density, however; it suffers miserable difficulties in addressing exchange and correlation effects. Later, in 1964, Hohenberg and Kohn proved the DFT to be the exact theory for many-body systems, and their approach is the main pillar of modern-day DFT [161].

2.10 Density Functional Theory

2.10.1 Hohenberg–Kohn theorems

It applies to system consisting of interacting particles moving under an external potential, and their approach is summarized in the following two theorems [162].

Theorem I: For any interacting electron system under the influence of external potential V_{ext}, the electron density $n(\mathbf{r})$ uniquely determines the V_{ext}, except for a constant. Thus the total energy is a unique functional of $n(\mathbf{r})$.

Theorem II: The energy functional $E[n(\mathbf{r})] = F[n(\mathbf{r})] + \int n(\mathbf{r})\, V_{\text{ext}}(\mathbf{r})\, d\boldsymbol{r}$ is minimized by the true ground state density $n_0(\mathbf{r})$ of the system, and the exact ground state energy is the global minimum value of $E[n(\mathbf{r})]$. Here $F[n(\mathbf{r})]$ is the universal functional independent of $V_{\text{ext}}(\mathbf{r})$, and it represents the kinetic and interaction energy of the electrons.

Although the Hohenberg-Kohn approach provides a different perspective to solve the many-body problem; however, the exact calculations of various properties of the system is still difficult because the $F[n(\mathbf{r})]$ is unknown. To overcome this difficulty, Kohn and Sham mapped the many-body problem onto a single-body problem by an auxiliary non-interacting electron system constrained to the fact that the two systems have the same ground state density [163].

2.10.2 Kohn–Sham formalism

Kohn-Sham approach of treating the many-body system as a single-body was the first step toward the practical use of Hohenberg-Kohn theorems [163]. It makes the DFT the most powerful tool to describe various ground state properties of the system. This approach maps the interacting electron system under real external potential onto a pseudo-non-interacting system where the electrons move under a single-particle Kohn-Sham potential $V_{\text{KS}}(\mathbf{r})$. For this fictitious non-interacting system, the Hamiltonian is given by

$$\mathcal{H}_{\text{KS}} = -\frac{1}{2}\nabla^2 + V_{\text{KS}}(\mathbf{r}) \qquad (\textit{in Hartree units}). \tag{2.10}$$

The ground state for this independent N electron system is obtained by solving the N one-electron Schrodinger-like eigenvalue equations,

$$(\mathcal{H}_{\text{KS}} - \epsilon_{\text{i}})\, \Psi_{\text{i}}(\mathbf{r}) = 0 \tag{2.11}$$

where $\Psi_{\mathrm{i}}(\mathrm{r})$ are the single particle orbitals with corresponding eigenvalues ϵ_{i}, and i run from 1 to N. The density of this auxiliary single-electron system is obtained from

$$n(\mathbf{r}) = \sum_{i=1}^{N} |\Psi_{\mathrm{i}}(\mathbf{r})|^2 \tag{2.12}$$

where $\int n(\mathbf{r})\, d\boldsymbol{r} = N$. In Kohn-Sham formalism, the ground state energy of the system is obtained by minimizing the

$$E_{\mathrm{KS}}\left[n(\mathbf{r})\right] = T_{\mathrm{S}}\left[n(\mathbf{r})\right] + E_{\mathrm{Hartree}}\left[n(\mathbf{r})\right] + E_{\mathrm{XC}}\left[n(\mathbf{r})\right] + \int n(\mathbf{r})\, V_{\mathrm{ext}}(\mathbf{r})\, d\boldsymbol{r} \tag{2.13}$$

where the total electrons (N) are fixed. Here $T_{\mathrm{S}}\left[n(\mathbf{r})\right]$ is the Kohn-Sham kinetic energy given by,

$$T_{\mathrm{S}}\left[n(\mathbf{r})\right] = -\frac{1}{2}\sum_{i=1}^{N}\int \Psi_{\mathrm{i}}^{*}(\mathbf{r})\, \nabla^2 \Psi_{\mathrm{i}}(\mathbf{r})\, d\boldsymbol{r}. \tag{2.14}$$

The second term in Eq. 2.13 is the Hartree energy,

$$E_{\mathrm{Hartree}}\left[n(\mathbf{r})\right] = \frac{1}{2}\iint \frac{n(\mathbf{r})n(\mathbf{r}')}{|\mathbf{r}-\mathbf{r}'|}\, d\boldsymbol{r}\, d\boldsymbol{r}' \tag{2.15}$$

and the third term $(E_{\mathrm{XC}}\left[n(\mathbf{r})\right])$ represents the exchange-correlation functional. Using the Hohenberg-Kohn theorems, the ground state energy can be calculated by minimizing Eq. 2.13, and the obtained Kohn-Sham potential is

$$V_{\mathrm{KS}}(\mathbf{r}) = V_{\mathrm{ext}}(\mathbf{r}) + \frac{\delta E_{\mathrm{Hartree}}\left[n(\mathbf{r})\right]}{\delta n(\mathbf{r})} + \frac{\delta E_{\mathrm{XC}}\left[n(\mathbf{r})\right]}{\delta n(\mathbf{r})} \tag{2.16}$$

where the second term is Hartree potential $V_{\mathrm{Hartree}}(\mathbf{r})$ expressed as

$$V_{\mathrm{Hartree}}(\mathbf{r}) = \int \frac{n(\mathbf{r}')}{|\mathbf{r}-\mathbf{r}'|}\, d\boldsymbol{r}' \tag{2.17}$$

and the third term is exchange-correlation potential $V_{\mathrm{XC}}(\mathbf{r})$. The Eq. 2.11, 2.12, and 2.16 together are called Kohn-Sham equations. These equations need to be solved self-consistently because the single-particle potential $V_{\mathrm{KS}}(\mathbf{r})$ depends on the density. The ground state energy E_0 is given by,

$$E_0 = \sum_{i=1}^{occ} \epsilon_{\mathrm{i}} - \frac{1}{2}\iint \frac{n(\mathbf{r})n(\mathbf{r}')}{|\mathbf{r}-\mathbf{r}'|}\, d\boldsymbol{r}\, d\boldsymbol{r}' + E_{\mathrm{XC}}\left[n\right] - \int n(\mathbf{r})\, V_{\mathrm{XC}}(\mathbf{r})\, d\boldsymbol{r}. \tag{2.18}$$

Since $E_{\mathrm{XC}}[n]$ is unknown in Eq. 2.18, therefore approximations are required to calculate the ground state properties. The commonly used approximation for exchange and correlation term is the LDA [163].

2.10.3 Local density approximation

It is the most straightforward approach that replaces the exchange-correlation energy per electron for this inhomogeneous system at a point $\mathbf{r}$ by the same for a homogeneous electron gas of the same density evaluated at the same point $\mathbf{r}$. For a non-spin-polarized system, the $E_{\mathrm{XC}}[n]$ under LDA is expressed as

$$E_{\mathrm{XC}}^{\mathrm{LDA}}[n] = \int n(\mathbf{r})\, \epsilon_{\mathrm{XC}}^{\mathrm{hom}}(n(\mathbf{r}))\; dr \tag{2.19}$$

where $\epsilon_{\mathrm{XC}}^{\mathrm{hom}}(n(\mathbf{r})) = \epsilon_{\mathrm{X}}^{\mathrm{hom}}(n(\mathbf{r})) + \epsilon_{\mathrm{C}}^{\mathrm{hom}}(n(\mathbf{r}))$, is the sum of the exchange $\epsilon_{\mathrm{X}}^{\mathrm{hom}}(n(\mathbf{r}))$ and correlation $\epsilon_{\mathrm{C}}^{\mathrm{hom}}(n(\mathbf{r}))$ energy per electron for a homogeneous system of density $n(\mathbf{r})$. However, for spin-polarized systems, the exchange and correlation terms cannot be treated separately. The $\epsilon_{\mathrm{X}}^{\mathrm{hom}}(n(\mathbf{r}))$ can be calculated analytically using the Hartree-Fock method and expressed as [164, 165]

$$\epsilon_{\mathrm{X}}^{\mathrm{hom}}\left(n(\mathbf{r})\right) = -\frac{3}{4}\left(\frac{3}{\pi}\right)^{1/3}\left(n(\mathbf{r})\right)^{1/3}. \tag{2.20}$$

However, the $\epsilon_{\mathrm{C}}^{\mathrm{hom}}(n(\mathbf{r}))$ is the most difficult to estimate except for high and low-density limits [166, 167]. Therefore, to calculate the exact $\epsilon_{\mathrm{C}}^{\mathrm{hom}}(n(\mathbf{r}))$ for intermediate densities, quantum Monte Carlo simulations have been performed for the energy of the homogeneous system [168]. Based on these simulations for the approximation of $\epsilon_{\mathrm{C}}^{\mathrm{hom}}(n(\mathbf{r}))$, several LDA methods were proposed [169, 170]. In spite of the ignorance of the contribution from inhomogeneous electron density in $\epsilon_{\mathrm{XC}}^{\mathrm{hom}}(n(\mathbf{r}))$, the success of LDA is remarkable because it satisfies the sum rule for the exchange-correlation hole [171]. The LDA results are satisfactory for the geometrical parameters of small molecules; however, it suffers massive failure in predicting the band gap. These drawbacks lead to the approximation of $E_{\mathrm{XC}}[n]$ beyond LDA by adding gradient corrections on the electron density [172–174].

2.10.4 Generalized gradient approximation

In spite of the success of LDA in describing the structural parameters (bond lengths, particle densities, vibrational frequencies) for atoms or simple molecules, the ignorance of inhomogeneities in electron density produces errors in predicting the ground state energies and band gap for semiconductors. It leads to density gradient corrections on the electron density [172–174], which provides much more satisfactory results than LDA in many cases. The $E_{\mathrm{XC}}\,[n]$ under gradient corrections is expressed as

$$\begin{aligned} E_{\mathrm{XC}}^{\mathrm{GGA}}[n] &= \int n(\mathbf{r})\, \epsilon_{\mathrm{XC}}^{\mathrm{GGA}}(n(\mathbf{r}), |\nabla n(\mathbf{r})|)\ d\boldsymbol{r} \\ &= \int n(\mathbf{r})\, \epsilon_{\mathrm{X}}^{\mathrm{hom}}(n(\mathbf{r}))\, F_{\mathrm{XC}}(n(\mathbf{r}), |\nabla n(\mathbf{r})|)\ d\boldsymbol{r} \end{aligned} \tag{2.21}$$

where F_{XC} is dimensionless and can be written as a sum of exchange F_{X} and correlation F_{C} contribution ($F_{\mathrm{XC}} = F_{\mathrm{X}}+F_{\mathrm{C}}$). Several forms of F_{X} in terms of density gradient ($\nabla n(\mathbf{r})$) have been proposed, which are widely used as B88 (Becke) [173], PW91 (Perdew and Wang) [175], and PBE (Perdew, Burke, and Enzerhof) [174]. In general, for systems having rapidly varying electron density, the GGA method works better than the LDA; however, in the case of ionic crystals, the GGA overcorrects the LDA results. Thus, depending on the nature of atoms and molecules, these two methods can be used as alternatives. However, for strongly correlated electron systems such as transition-metal oxide and rare-earth elements, both methods work poorly. The DFT results using LDA/GGA method predict the metallic nature of NiO, which is in general a Mott insulator with localized d electrons [176]. In view of these drawbacks, additional orbital-dependent interaction needs to be coupled with these methods.

2.10.5 DFT+U method

There are numerous approaches, such as self-interaction correction (SIC) [177], DFT (GGA/LDA) + U [178–180], and Hartree-Fock (HF) [181], to include the correlation effects in the localized orbitals. Out of these methods, the GGA/LDA + U is the most common and widely used to deal with this problem. Throughout this thesis, all the calculations were performed using GGA + U functionals. The term GGA + U stands for the method that involves GGA along with the on-site orbital-dependent interaction. This additional orbital-dependent term $\left(\frac{1}{2}\mathrm{U}\sum_{\mathrm{i}\neq\mathrm{j}} n_{\mathrm{i}}\, n_{\mathrm{j}}\right)$ is considered only for Coulomb interaction between highly localized orbital (d or f) electrons, where n_{i} and n_{j} are orbital occupancies. If we remove the double-counted averaged GGA/LDA energy of these localized orbital electrons (ignoring the non-sphericity and exchange also), the energy functional under this approximation is simplified to [179]

$$E_{\mathrm{DFT+U}} = E_{\mathrm{DFT}} + \frac{1}{2}\,U\sum_{\mathrm{i}\neq\mathrm{j}} n_{\mathrm{i}}\, n_{\mathrm{j}} - \frac{1}{2}\,U N_{\mathrm{d/f}}\,(N_{\mathrm{d/f}} - 1) \tag{2.22}$$

where $N_{\mathrm{d/f}}$ is the total number of d or f electrons ($N_{\mathrm{d/f}} = \sum n_{\mathrm{i}}$), and the orbital energies (ϵ_{i}) are the derivatives of Eq. 2.22 **w.r.t.** n_{i}

$$\epsilon_{\mathrm{i}} = \frac{\partial E}{\partial n_{\mathrm{i}}} = \epsilon_{\mathrm{DFT}} + \mathrm{U}\left(\frac{1}{2} - n_{\mathrm{i}}\right). \tag{2.23}$$

This simplest approach shifts the orbital energy by $+U/2$ for unoccupied orbitals and $-U/2$ for occupied orbitals, leading to upper and lower Hubbard bands with energy separation U for strongly correlated transition metal oxides. In spite of the success of on-site Coulomb interaction in predicting the correct results for Mott insulators, a general form of orbital basis set is required to properly account for the direct and exchange Coulomb interactions in partially filled localized orbitals. Thus a generalized version of this method is defined in terms of density matrix $\{n_\sigma\}$ as

$$E^{\mathrm{DFT+U}}_{\mathrm{total}}\,[\rho_\sigma(\mathbf{r}), \{n_\sigma\}] = E^{\mathrm{DFT}}[\rho_\sigma(\mathbf{r})] + E^{\mathrm{U}}[\{n_\sigma\}] - E_{\mathrm{dc}}[\{n_\sigma\}] \tag{2.24}$$

where $\rho_\sigma(\mathbf{r})$ is the charge density for spin-σ electrons, and the second term is the d-d or f-f electron Coulomb interaction energy

$$\begin{aligned} E^{\mathrm{U}}[\{n\}] = \frac{1}{2}\sum_{\{m\},\sigma}\Big\{ &\langle m, m''|\,V_{\mathrm{ee}}\,|m', m'''\rangle\, n_\sigma^{mm'}\, n_{-\sigma}^{m''m'''} - \Big(\langle m, m''|\,V_{\mathrm{ee}}\,|m', m'''\rangle \\ &- \langle m, m''|\,V_{\mathrm{ee}}\,|m''', m'\rangle\Big)\, n_\sigma^{mm'}\, n_\sigma^{m''m'''}\Big\} \end{aligned} \tag{2.25}$$

where V_{ee} are the screened Coulomb interactions between d or f electrons, and m is the magnetic quantum number. The third term corrects the double-counted averaged

GGA/LDA energy in Eq. 2.24 and expressed as

$$E_{\mathrm{dc}}[\{n_\sigma\}] = \frac{1}{2}UN_{\mathrm{d/f}}(N_{\mathrm{d/f}}-1) - \frac{1}{2}J\left[N^{\uparrow}_{\mathrm{d/f}}(N^{\uparrow}_{\mathrm{d/f}}-1) + N^{\downarrow}_{\mathrm{d/f}}(N^{\downarrow}_{\mathrm{d/f}}-1)\right]. \tag{2.26}$$

Here $N_{\mathrm{d/f}} = N^{\uparrow}_{\mathrm{d/f}} + N^{\downarrow}_{\mathrm{d/f}}$, $N^\sigma = \mathrm{Tr}\left(n^{\mathrm{mm}'}_\sigma\right)$, and U and J are Coulomb and exchange parameters, respectively. In constructing the effective single-particle Hamiltonian $\mathcal{H}_{\mathrm{eff}}$, an additional single-particle potential $V^\sigma_{\mathrm{mm}'}$ was used with the usual GGA/LDA potential as

$$\mathcal{H}_{\mathrm{eff}} = \mathcal{H}_{\mathrm{DFT}} + \sum_{m,m'} |inlm\sigma\rangle\, V^\sigma_{\mathrm{mm}'}\, \langle inlm'\sigma| \tag{2.27}$$

where

$$\begin{aligned} V^\sigma_{\mathrm{mm}'} = \sum_{\{m\}} \Big\{ &\langle m, m''|\, V_{\mathrm{ee}}\, |m', m'''\rangle\, n^{m''m'''}_{-\sigma} - \Big(\langle m, m''|\, V_{\mathrm{ee}}\, |m', m'''\rangle \\ &- \langle m, m''|\, V_{\mathrm{ee}}\, |m''', m'\rangle \Big)\, n^{m''m'''}_{\sigma} \Big\} - U\left(N_{\mathrm{d/f}} - \frac{1}{2}\right) + J\left(N^\sigma - \frac{1}{2}\right). \end{aligned} \tag{2.28}$$

In Eq. 2.27, i is the site, n is the principal quantum number, and l is the orbital quantum number. Furthermore, the matrix elements of V_{ee} are expressed as

$$\langle m, m''|\, V_{\mathrm{ee}}\, |m', m'''\rangle = \sum_{k=0}^{2l} \mathrm{a}_k\,(m, m', m'', m''')\, F^k \tag{2.29}$$

where F_k is the effective Slater integrals and

$$\mathrm{a}_k\,(m, m', m'', m''') = \frac{4\pi}{2k+1} \sum_{q=-k}^{k} \langle lm|\, Y_{kq}\, |lm'\rangle\, \langle lm''|\, Y^*_{kq}\, |lm'''\rangle \tag{2.30}$$

here Y stands for spherical harmonics. The U and J for 3d or 4f electrons are related to Slater integrals as

$$\begin{aligned} U &= F^0;\ J = \frac{F^2+F^4}{14} && (\text{for } 3d) \\ U &= F^0;\ J = \frac{286F^2+195F^4+250F^6}{6435} && (\text{for } 4f) \end{aligned} \tag{2.31}$$

where the ratio $F^4/F^2 \approx 0.625$ (0.667) for 3d (4f) elements, and the $F^6/F^2 \approx 0.5$ for 4f elements [182]. Furthermore, there are two different approaches, the fully localized limit (FLL) and the around mean field (AMF) [183, 184], for determining the double-counting term E_{dc}. The main advantage of the DFT + U method is that the Hubbard correction term is applied to the specific electrons (d or f), while the others are treated by the standard GGA/LDA. Furthermore, the inclusion of on-site Coulomb interaction in standard GGA/LDA not only tunes the band gap for transition metal oxides but also provides qualitative improvement for ground-state properties.

2.11 DFT Implementation

In calculating the ground state properties, one needs to solve the Kohn-Sham equations. Since the V_{KS} in Eq. 2.16 is closely related to $n(\mathbf{r})$ therefore, these equations need to be solved self consistently. Fig. 2.13 shows the step-by-step process to achieve the self-consistent convergence criteria. Initially, with an arbitrary value of $n(\mathbf{r})$, the V_{KS} is calculated, and the Eq. 2.11 is solved to get the single-particle wavefunctions. Using the obtained wavefunctions, the new electron density is calculated from Eq. 2.12. The self-consistent condition is checked after calculating the new electron density. If the convergence criteria is achieved, the various properties are calculated. Otherwise, the same process will restart with a new density, a mixture of density for the previous iteration and the newly calculated one. This process runs until self-consistency is achieved.

The major difficulty in following the above procedure is to solve the Kohn-Sham equation with a given V_{KS}; therefore, developing an accurate and less time-consuming method for solving these equations is the biggest challenge from condensed matter physics point of view. There are several methodologies to overcome these issues, which are broadly classified into three categories: the plane wave basis set, the localized atomic orbitals [185, 186], and the atomic sphere methods [187]. In this thesis, we employed a generalized plane wave-based approach called Projector Augmented Wave (PAW) [188].

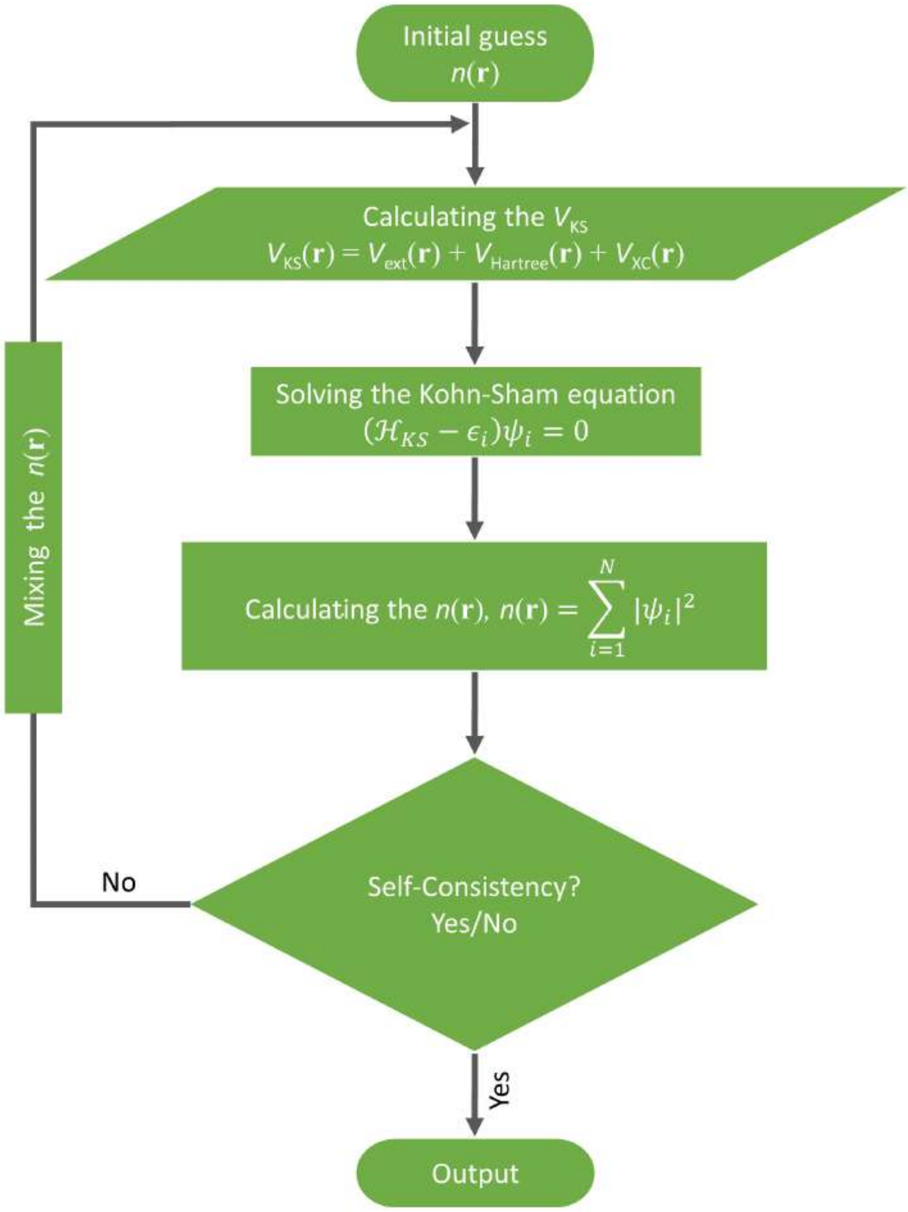

FIGURE 2.13: Flowchart for solving the Kohn-Sham equations.

2.12 Plane Wave Basis

In the periodic crystal structure, there is a regular arrangement of atoms; therefore, the atoms are considered to move under an effective periodic potential $V_{\text{eff}}(\mathbf{r})$ expressed as

$$V_{\text{eff}}(\mathbf{r}+\mathbf{T}) = V_{\text{eff}}(\mathbf{r}) \tag{2.32}$$

where **T** is the translation vector of the lattice ($\mathbf{T} = n_1\mathbf{a}_1 + n_2\mathbf{a}_2 + n_3\mathbf{a}_3$, where n_1,n_2, and n_3 are integers and $\mathbf{a}_1$, $\mathbf{a}_2$, $\mathbf{a}_3$ are the Bravais lattice vectors). Under this condition, Bloch's theorem states that the electron wavefunctions can be expanded in a discrete set of plane waves

$$\Psi_{\boldsymbol{k}}(\mathbf{r}) = \mathrm{e}^{i\boldsymbol{k}.\mathbf{r}} u_{\boldsymbol{k}}(\mathbf{r})\,. \tag{2.33}$$

Here $\boldsymbol{k}$ is the wave vector, and $u_{\boldsymbol{k}}$ is the periodic function of periodicity same as the lattice. Thus, the expansion of electronic wavefunctions under an effective periodic potential is quite simple and a breakthrough point from condensed matter physics perspective. However, it requires a large number of plane waves to expand the wavefunctions for tightly bound core electrons. In addition, this method is poorly suited for dealing with the rapid oscillations of wavefunctions for valence electrons. Thus, the Bloch's theorem alone can't be sufficient for the proper description of the system. So pseudopotentials method that removes the wiggles in the wavefunctions for valence electrons, providing smooth pseudo-wavefunctions with a reasonable number of plane waves in the core region, has been introduced. The most widely used plane wave-based pseudopotentials are Norm-Conserving Pseudopotentials (NCPP) and Ultrasoft Pseudopotentials (USPP) [189, 190]. In spite of the success of the pseudopotentials method in making the calculations cost-effective for large systems, the results were less accurate; therefore, a generalized modern-day approach known as Projector Augmented Wave has been introduced [188]. The following subsections deal with the evolution of the plane wave basis method.

2.12.1 Norm-conserving pseudopotentials

Basically, it replaces the effects of the motion of core electrons and nuclei with pseudopotentials such that the valence electron states in the core region can be represented by smooth pseudo-wavefunctions with fewer plane waves, and the core states are eliminated. The NCPP are determined using atomic reference states subject to the following constraints:

1. Beyond the core cut-off radius r_c, the pseudo-valence eigenstates should have the same amplitude and energies as that of the all-electron eigenstates.

2. Inside the r_c, the norm of each pseudo wavefunction Ψ_{PV} should be the same as that of the corresponding all-electron wavefunction Ψ_{AE}. It can be mathematically expressed as

$$\int_0^{r_c} \Psi^*_{PV}(\mathbf{r})\,\Psi_{PV}(\mathbf{r})\,r^2\,\mathrm{d}\mathbf{r} = \int_0^{r_c} \Psi^*_{AE}(\mathbf{r})\,\Psi_{AE}(\mathbf{r})\,\boldsymbol{r}^2\,\mathrm{d}\mathbf{r}. \tag{2.34}$$

This most straightforward approach of plane wave basis with pseudopotentials significantly reduced the computational cost and worked well with the s and *p* shell case, where the wavefunctions can be represented by a limited number of plane waves. However, this method becomes intractable for the localized *d* and *f* shells where a large number of plane waves are required. The success of this method depends on the appropriate selection of r_c, which should be around the outermost maximum of the Ψ_{AE}.

2.12.2 Ultrasoft pseudopotentials

Under norm-conservation criteria, it is unrealistic to make smooth pseudo-wavefunctions inside r_c. Thus, the approach of NCPP in solving Kohn-Sham equations demands a large number of plane waves, making the process time-consuming. In 1990, Vanderbilt proposed a new and radical approach known as USPP to achieve much smoother pseudo-wavefunctions than NCPP, leading to low cut-off energy for plane waves [190–192]. The norm-conserving condition is no longer required in this method; therefore, a charge deficit described by local augmentation charges exists between Ψ_{PV} and Ψ_{AE}. Thus, the method of ultrasoft pseudopotentials arises with inherent complications such as non-normalized wavefunctions, which leads to the eigenvalue problem. In addition, the charge density can not be governed by simple rules. However, the pseudopotentials generated by this approach are transferable and cost-effective, and their wide range of use in the calculations for larger systems is sufficient to prove their reliability in solid-state physics.

2.12.3 Projector augmented wave

It combines the linearized augmented-plane wave [188, 193, 194] with the pseudopotentials approach and turns out to be one of the most precise and transferable methods for calculations. In this approach, the system is divided into the augmentation region and the interstitial region. The augmentation region consists of non-overlapping spheres ($|\mathbf{r} - \mathbf{r}^i| < \mathrm{r}^i_{\mathrm{cut}}$, where $\mathbf{r}^i$ is the position of the i^{th} atom and $\mathrm{r}^i_{\mathrm{cut}}$ is the cut-off radius) enclosing each atom of the system, and the interstitial region has the remaining part. In the augmentation region, the wavefunction is obtained by partial wave expansion in a sphere around the atom, while in the interstitial region, it is expanded in terms of plane waves.

In this method, the pseudo wavefunction $\tilde{\Psi}_n$ is directly connected to the all-electron wavefunction Ψ_n by a linear transformation

$$|\Psi_n\rangle = \hat{\mathrm{T}}\,|\tilde{\Psi}_n\rangle. \tag{2.35}$$

As the Ψ_n and $\tilde{\Psi}_n$ differ only in the core region, therefore, the $\hat{\mathrm{T}}$ can be written as

$$\hat{\mathrm{T}} = \mathbb{1} + \sum_i \hat{\mathrm{T}}^i \tag{2.36}$$

where $\hat{\mathrm{T}}^i$ acts only inside that augmentation region which encloses the i^{th} atom. The $\tilde{\Psi}_n$ in the augmentation region is expanded as pseudo partial waves

$$\left|\tilde{\Psi}_n\right\rangle = \sum_{i,j} C^i_{nj}\,|\tilde{\chi}^i_j\rangle\,. \tag{2.37}$$

Since the $\hat{\mathrm{T}}$ is linear, therefore the C^i_{nj} must be the inner product with a set of projector operators $\tilde{p}^i_j$,

$$C^i_{nj} = \langle\tilde{p}^i_j|\tilde{\Psi}_n\rangle. \tag{2.38}$$

The $\hat{\mathrm{T}}$ can be written as

$$\hat{\mathrm{T}} = \mathbb{1} + \sum_{i,j}\left(|\chi^i_j\rangle - |\tilde{\chi}^i_j\rangle\right)\langle\tilde{p}^i_j|. \tag{2.39}$$

Substituting the $\hat{\mathrm{T}}$ in Eq. 2.35 provides the all-electron wavefunction expressed as

$$|\Psi_n\rangle = |\tilde{\Psi}_n\rangle + \sum_{i,j}\left(|\chi^i_j\rangle - |\tilde{\chi}^i_j\rangle\right)\left\langle\tilde{p}^i_j|\tilde{\Psi}_n\right\rangle. \tag{2.40}$$

Thus, using the PAW approach, the wavefunctions can be separated into smooth auxiliary wavefunctions and atom-centered contribution (sum over the difference of one-centered all electron contribution and one-centered pseudo part).

2.13 Vienna Ab initio Simulation Package

It is a material modeling program based on first principles commonly known as VASP. The computational code of VASP was written by Jürgen Furthmüller and Georg Kresse. The VASP has four input files:

1. INCAR
2. POSCAR
3. KPOINTS
4. POTCAR.

2.13.1 INCAR

The INCAR file specifies the input parameters that determine what to perform and how to do it. It also includes the key parameters for the calculations, such as the convergence criteria, plane wave cut-off energy, and smearing parameters. The VASP has default values for input parameters, which works well for most of the standard calculations. However, a few parameters need to be modified for specific calculations, such as the density of states, band structure, spin-orbit coupling, Fermi surface, and phonon dispersion. The details of such parameters is given below.

```
INCAR file
System = A2BC          ! Comment line
PREC = NORMAL          ! Precession: HIGH/MEDIUM/LOW/NORMAL/ACCURATE
ENCUT = 600            ! Kinetic Energy Cutoff in eV
EDIFF = 1.0E-06        ! Energy convergence criteria in eV
```

```
ICHARG = 2          ! 0|1|2|11|12    to construct or fixed initial charge density
ISTART = 0          ! 0|1|2    determines whether to read the WAVECAR or not
ISPIN = 2           ! Spin polarized calculations: 1-No    2-Yes
LREAL = .TRUE.      ! TRUE/FALSE   Real-space projection or in reciprocal space
EDIFFG = 1.0E-03    ! Stopping criteria for ionic relaxation
IBRION = 2          ! Ionic relaxation: 0-MD   1- RMM-DIIS   2-CG
ISIF = 1            ! 0|1|2|3|4|5|6    Calculations of Stress tensor and Relaxation
SIGMA = 0.10        ! determines smearing width in eV
ISMEAR = 0          ! -1 Fermi smearing, 0 Gaussian smearing, -5 tetrahedron
```

2.13.2 POSCAR

It is an essential file that contains the necessary information about crystal structure and atomic positions to run the VASP calculations. The usual format for POSCAR file is as follow

POSCAR file

```
A2BC                ! Comment line
1.0                 ! lattice scaling factor
4.0500001907    0.0000000000    0.0000000000
0.0000000000    4.0500001907    0.0000000000
0.0000000000    0.0000000000    4.0500001907
A    B    C
8    4    4
Direct
0.250000000    0.250000000    0.250000000    A
0.750000000    0.750000000    0.750000000    A
0.750000000    0.750000000    0.250000000    A
0.250000000    0.250000000    0.750000000    A
0.750000000    0.250000000    0.750000000    A
0.250000000    0.750000000    0.250000000    A
```

```
0.250000000    0.750000000    0.750000000    A
0.750000000    0.250000000    0.250000000    A
0.000000000    0.000000000    0.000000000    B
0.000000000    0.500000000    0.500000000    B
0.500000000    0.000000000    0.500000000    B
0.500000000    0.500000000    0.000000000    B
0.500000000    0.500000000    0.500000000    C
0.500000000    0.000000000    0.000000000    C
0.000000000    0.500000000    0.000000000    C
0.000000000    0.000000000    0.500000000    C
```

Here the first line is the comment line, and usually, it is preferable to write the system name. The universal lattice scaling factor, which is used to scale the atomic coordinates and lattice vectors, is given in the second row. Unit cell of the current system is defined by the three lattice vectors (x y z) given in the third, fourth, and fifth lines. The sixth row provides the list of elements present in the system, and the seventh row specifies the total number of species of each element. The eighth row specifies whether the atomic positions are given in direct (fractional) coordinates or Cartesian coordinates, and the following lines specify the position of each atom sequentially.

2.13.3 KPOINTS

The KPOINTS file contains the number of k-points used to perform a calculation. The simplest way to specify the k-points is to choose a gamma-centered mesh, as given below.

KPOINTS file

```
Automatic generation
0                    ! 0 stands for Automatic generation scheme.
G                    ! G stands for gamma centered grid
6    6    6          ! Subdivisions along the reciprocal lattice vectors
0    0    0          ! Optional shift of the mesh
```

However, for the band structure calculation, the k-point integration was performed along the high symmetry path in the first Brillouin zone.

2.13.4 POTCAR

It contains the pseudopotentials for each element used in the VASP run. It also includes the basic information of elements such as valence, mass, electronic configuration, and energy in the reference configuration for which pseudopotential was generated.

Chapter 3

$Ca_{3-x}Dy_xCo_2O_6$: Evidence of Cluster-Glass-like Freezing

---

Spin-glass behavior in a system is mainly associated with geometrical frustration marked by numerous properties such as slow relaxation, memory effect, aging effect, and quantum tunneling of magnetization [27, 54, 195, 196]. The geometrical frustration in a system is a result of degeneracy in the magnetic ground state, due to which a non-uniform interaction develops. In some cases, the resulting non-uniform interaction can freeze the cluster of spins, and a cluster-glass state is formed [197, 198]. $Ca_3Co_2O_6$ is one of the geometrically frustrated compounds which belongs to the family of quasi 1D spin-chain compound of structure $A_3BB'O_6$ [23, 85, 199–202]. It crystallizes in the K_4CdCl_6 (rhombohedral) type structure with space group $R\bar{3}c$. The crystal structure of $Ca_3Co_2O_6$ consists of an infinite number of chains of alternating face-sharing CoO_6 octahedra (Co1) and CoO_6 trigonal prisms (Co2), which is running along the c-axis (*cf.* Fig. 1.1). These chains are separated by non-magnetic Ca^{2+} cations and surrounded by six other equally spaced chains, forming a triangular lattice in the ab plane [81]. The Co^{3+} ions located at the octahedral site are in the low spin ($S = 0$) state, while in the trigonal prism site, they are in the high spin ($S = 2$) state [28, 29]. It possesses an Ising-like character with spins parallel to the chain, while the intra-chain and inter-chain couplings are ferromagnetic and antiferromagnetic, respectively, which give rise to frustration and peculiar magnetic behavior [28, 201, 202]. The 1D character in the magnetic properties is expected because the distance between the magnetic ions along the chain is approximately half that of the inter-chain distance [81]. At low temperature, the combination of geometric frustration with 1D character makes it quite complicated and of considerable interest. Initially, it was proposed that the system undergoes a partially disordered antiferromagnetic phase below 25 K (T_{c1}), and a short-range glassy state is formed below 10 K (T_{c2}) [85]. However, the neutron diffraction study suggested that the transition corresponds to an incommensurate amplitude-modulated PDA (spin density wave) structure with a wave propagation vector k = (0, 0, 1.01) [30]. On lowering the temperature, the spin density wave structure became more destabilized, and over a time scale of several hours, new Bragg reflections corresponding to commensurate antiferromagnetic structure with wave propagation vector k = (0.5, -0.5, 1) began to appear [14, 30]. Furthermore, the pressure-dependent neutron diffraction study suggested the suppression of spin-density wave structure and stabilization of CAFM structure at pressure P = 2.1 GPa [89]. In addition to the pressure-induced effects, the system exhibits a complex magnetic phase diagram with temperature and magnetic field. At 10 K, the system exhibits a single in-field ferrimagnetic to ferromagnetic transition [200]; however, for the low temperature, successive regularly spaced steps have appeared in the M-H curves, which are related to QTM [25, 27]. Furthermore, the complicated dynamics of in-field transitions have drawn considerable interest from low-temperature magnetism point of view [25, 27, 203]. The frozen spin-state starts below 10 K, is highly frustration related, and its dynamics strongly depend on field sweep rate and thermal activation [25].

Irrespective of the 1D character in $Ca_3Co_2O_6$, there are significant chances of tuning the magnetic structure by elemental substitution to make it useful for application purposes. From the first-principles calculation for $Ca_{3-x}Y_xCo_2O_6$, the ground states were predicted to be a half-metallic ferromagnet and an unusual insulating ferromagnet [84]. It has been reported that it exhibits ferroelectric-relaxor-like behavior for $Ca_{3-x}Gd_xCo_2O_6$ [109]. The time-dependent spin density wave order in $Ca_3Co_2O_6$ has been stabilized for $Ca_{2.75}R_{0.25}Co_2O_6$ (R = Dy and Lu) [118]. Thus, Dy based rare-earth-ion substitution greatly influences the structural and magnetic properties of $Ca_3Co_2O_6$ [119]. However, the nature of magnetic ordering in these rare earth substituted compounds is still unclear. Hence, exploring their properties will be exciting and may unravel new magnetic states. This chapter deals with the structural and magnetic properties of Dy-doped $\mathrm{Ca_{3-x}Dy_xCo_2O_6}$ samples by analyzing X-ray diffraction, FESEM, RAMAN, XPS, and DC magnetization measurement data.

Here in this chapter, the structural and magnetic properties of $\mathrm{Ca_{3-x}Dy_xCo_2O_6}$ (x = 0, 0.1, 0.2, and 0.3) samples were discussed. The polycrystalline $\mathrm{Ca_{3-x}Dy_xCo_2O_6}$ samples were synthesized using the conventional solid-state route method, and evidence of Cluster-glass-like freezing phenomena was found in these samples. Isothermal magnetization curve depicts step-like change indicative of the first-order transition, which decreases with the increase of substitution. The Brillouin function was used to determine the 'spins'participating at this first-order transition $\left(\mathrm{J}\left(\frac{1}{2}\right) \rightarrow \mathrm{J}\left(\frac{3}{2}\right)\right)$. Relaxation measurements revealed the existence of short-range cluster-glass-like behavior. Analyzing the results using Vogel-Fulcher law shows that the Vogel-Fulcher temperature (T_0) and the relaxation time is around 10 K and 10^4 s, respectively.

3.1 Experimental Details

Polycrystalline samples of $\mathrm{Ca_{3-x}Dy_xCo_2O_6}$ (x = 0, 0.1, 0.2, and 0.3) were prepared by the solid-state reaction method. The required amount of reagents $\mathrm{CaCO_3}$, $\mathrm{Co_3O_4}$, and $\mathrm{Dy_2O_3}$ were mixed using an agate mortar pestle and preheated at 900 °C for 24 h. The obtained mixtures were pressed in the form of pellets and sintered at 1000 °C for 48 h.

Powder X-ray diffraction measurements were performed on all the samples at room temperature using a Rigaku X-ray diffractometer (TTRAX III) with Cu-Kα (λ = 1.5406 Å) radiation from scattering angle (2θ) 10° to 80°. Microstructural images and particle size were analyzed using ZEISS made Field Emission Scanning Electron Microscope. Room temperature Raman spectra were obtained using micro-Raman spectroscopy (LabRam HR, Jobin Yvon) with an excitation wavelength of 488 nm. The chemical composition of samples was analyzed by ESCALAB Xi+ (Thermo Fisher) X-ray photoelectron spectroscopy instrument. The magnetization data were taken using a vibrating sample magnetometer probe installed in a quantum design physical property measurement system. We have followed two protocols known as zero field cooled and field cooled (FC) for the magnetization measurements. In the ZFC protocol, the samples were cooled from room temperature to 3 K in the absence of an external magnetic field, and then external magnetic field was switched on at this temperature, and data were taken during the warming up cycle in the presence of the external magnetic field. For the FC protocol, the samples were again cooled from room temperature to 3 K under the same applied magnetic field used in ZFC measurements, and magnetization data were taken during the warming up cycle.

3.2 Results

3.2.1 Structure

The X-ray diffraction patterns of all the samples were taken at room temperature and analyzed by the Rietveld refinement technique using the FULLPROF program. Rietveld refinement confirms the single-phase formation, and the compound crystallizes in the rhombohedral structure (space group $R\bar{3}c$). Fig. 3.1 shows the Rietveld refined data with associated Bragg position. The refined crystal structure of $Ca_3Co_2O_6$ containing alternating CoO_6 octahedra and CoO_6 trigonal prisms is presented in Fig. 3.2.

The lattice parameters 'a' and 'c' were directly obtained from the refinement. Table 3.1 contains the refined lattice parameters 'a', 'c', and the 'c/a' ratio, which are plotted with the Dy concentration in Fig. 3.3. From Fig. 3.3, we can see that as we increase the Dy content, the lattice parameter 'a' decreases while 'c' increases and the overall 'c/a' ratio increases (Table 3.1). The intra-chain bond length (Co1-Co2) increases with the Dy concentration, while the inter-chain bond length (Co2-Co2) decreases (Table 3.1). Thus, the substitution of Dy results in the elongation of the c-axis. For x = 0.1 sample, the volume of the cell (V) decreases, but for x = 0.2 and 0.3, it increases (Table 3.1). The lower ionic radius of the Dy^{3+} ion (1.05 Å) compared to the Ca^{2+} ion (1.14 Å) suggested that the Dy substitution should result in the shrinkage of the lattice. It supports the result for x = 0.1 sample but is different for the x = 0.2 and 0.3 samples. The doping

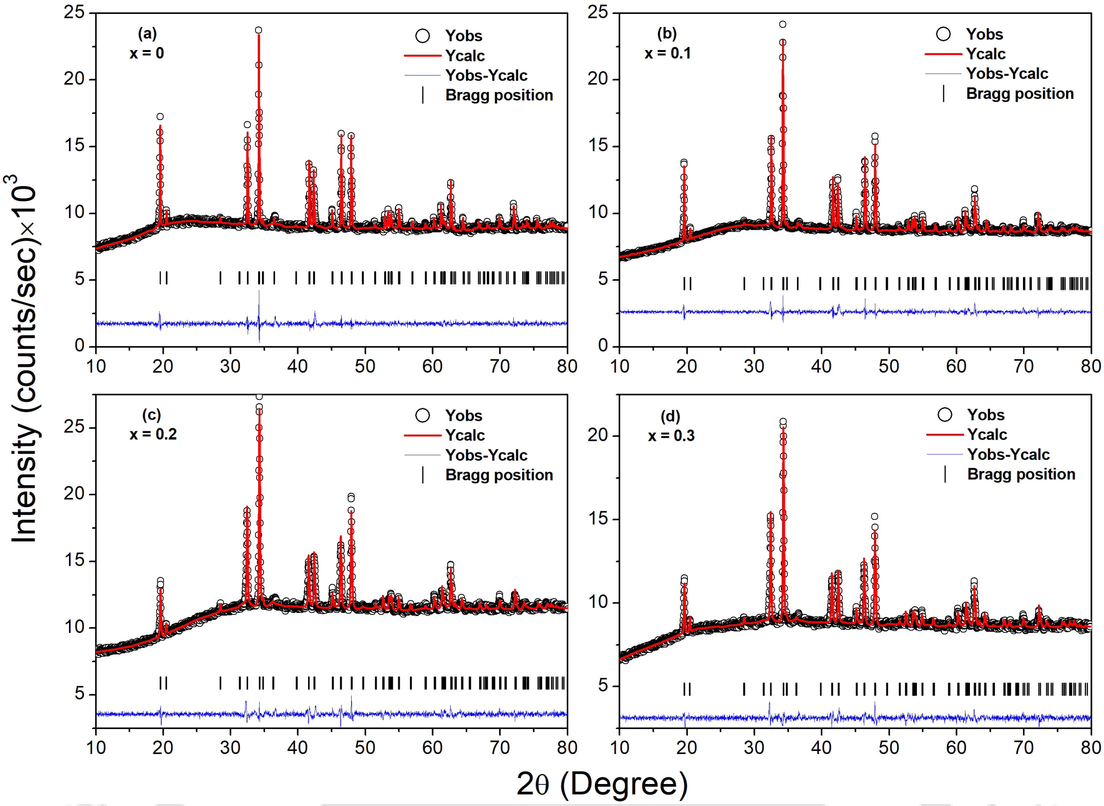

FIGURE 3.1: Rietveld refined X-ray diffraction patterns of $Ca_{3-x}Dy_xCo_2O_6$ (x = 0, 0.1, 0.2, and 0.3) at room temperature (open circle). The red solid line represents the calculated data, and the black vertical line represents the position of Bragg peaks. At the bottom of each figure, the blue solid line shows the difference between the observed and calculated patterns.

of Dy^{3+} ions for Ca^{2+} ions will possibly lead to a reduction of Co^{3+} to Co^{2+} ions to maintain charge neutrality, which is earlier reported by Jain *et al.* [118]. The Co^{2+}(HS) and Co^{2+}(LS) ions have ionic radius 0.745 Å and 0.65 Å, respectively, which is higher than the ionic radius of Co^{3+}(HS) ion (0.61 Å). For x = 0.1 sample, the lattice shrinks due to a small ionic radius of Dy^{3+} ion. As the Dy concentration increases, a greater number of Co^{2+} ions were induced, due to which the lattice expands for x = 0.2 and 0.3 samples. It also suggested that the effect of induced Co^{2+} ions arises significantly for x ≥ 0.2.

The FESEM micrographs are shown in Fig. 3.4. It can be seen that the grains are spherical for all the samples, and their distribution is relatively uniform over the entire region. Using ImageJ software, we have calculated the average particle size, which decreases from 3 μm for the parent compound to 1.8 μm for the x = 0.3 doped sample.

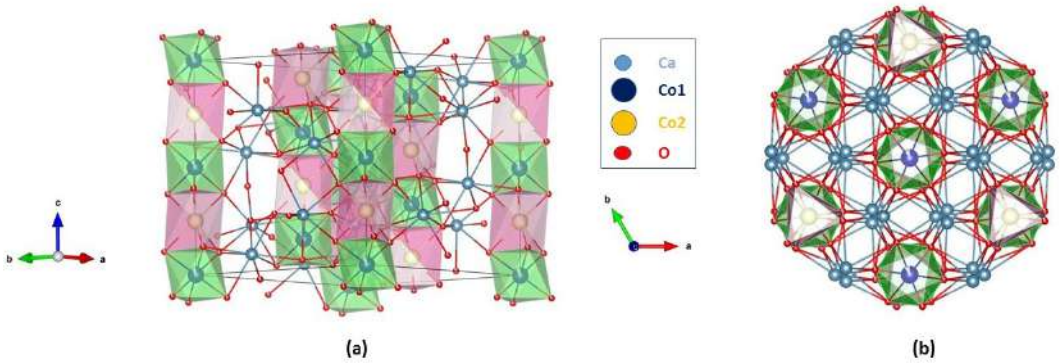

FIGURE 3.2: (a) Crystal structure of $Ca_3Co_2O_6$, showing alternating CoO_6 octahedra (shown in green) and CoO_6 trigonal prisms (shown in pink) (b) projection along the *c*-axis.

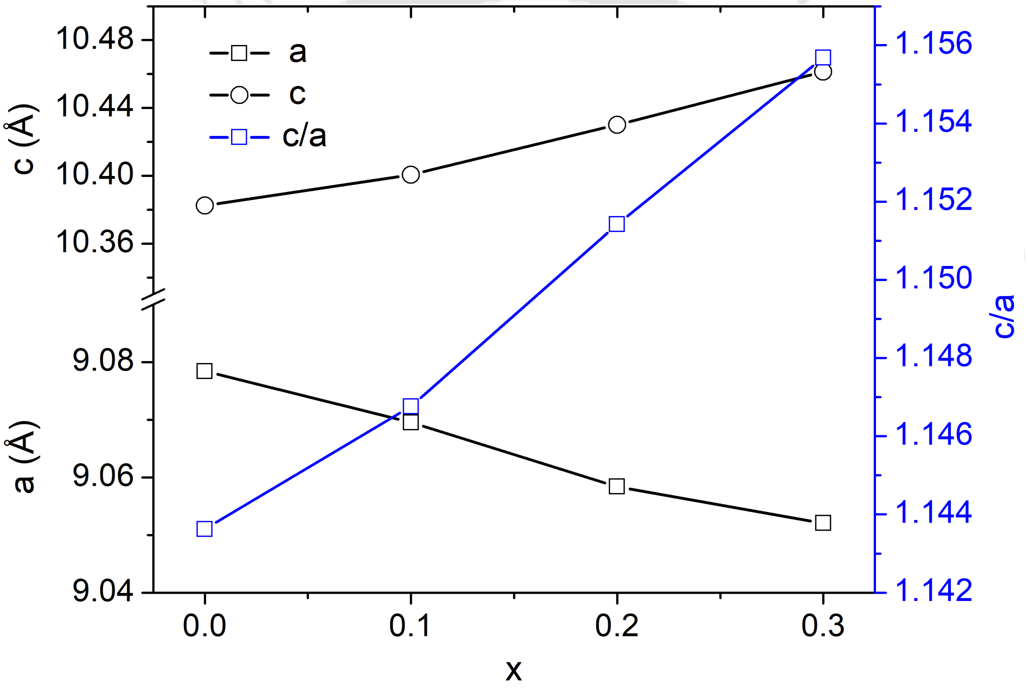

FIGURE 3.3: Variation of lattice parameter a, c, and c/a ratio with the doping concentration of Dy (x = 0, 0.1, 0.2, and 0.3).

3.2.2 Raman spectroscopy

Fig. 3.5 depicts the observed room temperature Raman spectra of $Ca_{3-x}Dy_xCo_2O_6$ (x = 0, 0.1, 0.2, and 0.3) in which four modes are visible in the range of 500 cm^{-1} to 750 cm^{-1}. These four modes are at 540 cm^{-1}, 571 cm^{-1}, 639 cm^{-1}, and 691 cm^{-1}. Group theoretical analysis for rhombohedral structure with $R\bar{3}c$ space group predicts 24 Raman active modes having A_{1g} and E_g symmetries ($4A_{1g}+10E_g$) [204, 205]. The E_g mode is 2-fold degenerate (E_{1g} and E_{2g}). According to the crystallographic site symmetries,

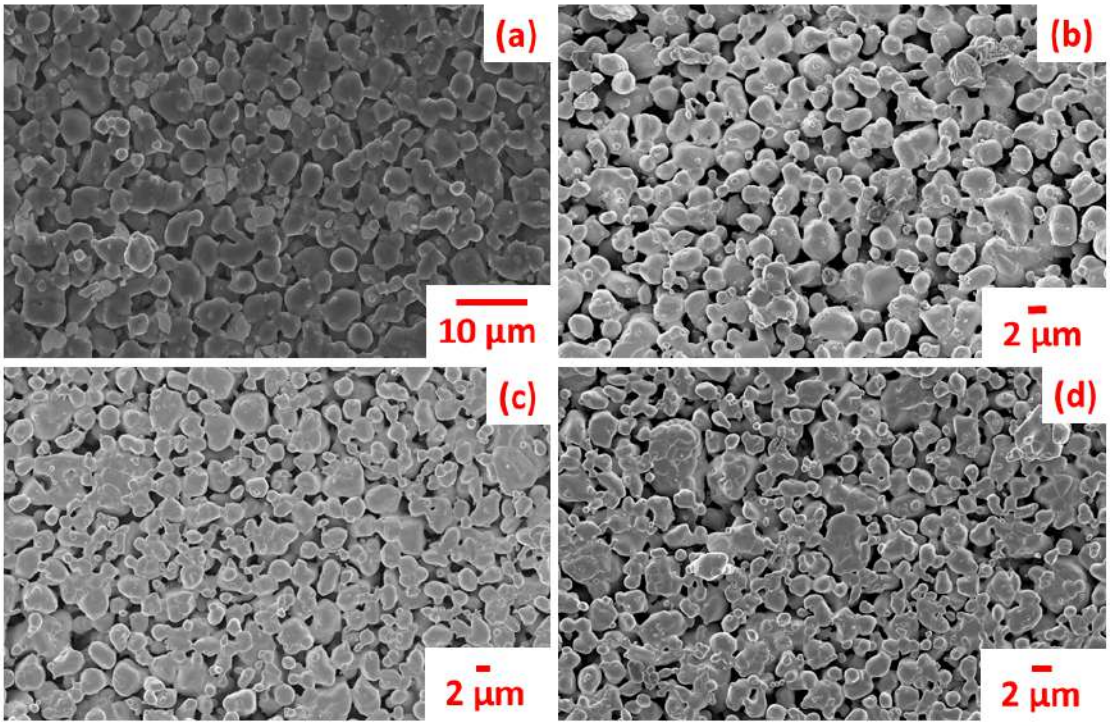

FIGURE 3.4: FESEM micrographs for $Ca_{3-x}Dy_xCo_2O_6$ (a) x = 0 (b) x = 0.1 (c) x = 0.2 (d) x = 0.3.

TABLE 3.1: Lattice parameters a, c, c/a ratio, volume of the cell (V), intra-chain (Co1-Co2), and inter-chain (Co2-Co2) bond lengths of $Ca_{3-x}Dy_xCo_2O_6$ (x = 0, 0.1, 0.2, and 0.3).

x	a(Å) (± 0.001 Å)	c(Å) (± 0.001 Å)	c/a	V (Å^3)	Co1-Co2 (Å)	Co2-Co2 (Å)
0	9.078	10.382	1.144	741.05	2.596	5.520
0.1	9.070	10.401	1.147	740.90	2.600	5.516
0.2	9.058	10.430	1.151	741.17	2.608	5.511
0.3	9.052	10.461	1.156	742.87	2.615	5.510

both the Co1 and Co2 ions sites are stationary for the Raman active A_{1g} mode, while for the E_g mode, only the Co1 ions site is stationary. The intense peak at 639 cm^{-1} was assigned to E_{1g} symmetry, and the broad modes at 540 cm^{-1}, 571 cm^{-1}, and 691 cm^{-1} were set to E_{2g}, E_{1g}, and A_{1g} symmetry, respectively [205]. No additional peaks related to Dy or its oxide phases were detected in the Raman spectra of Dy doped samples, which is consistent with the X-ray diffraction results (Fig. 3.5). The observed modes were shifted towards the lower frequency side as the concentration of Dy increases (Fig.

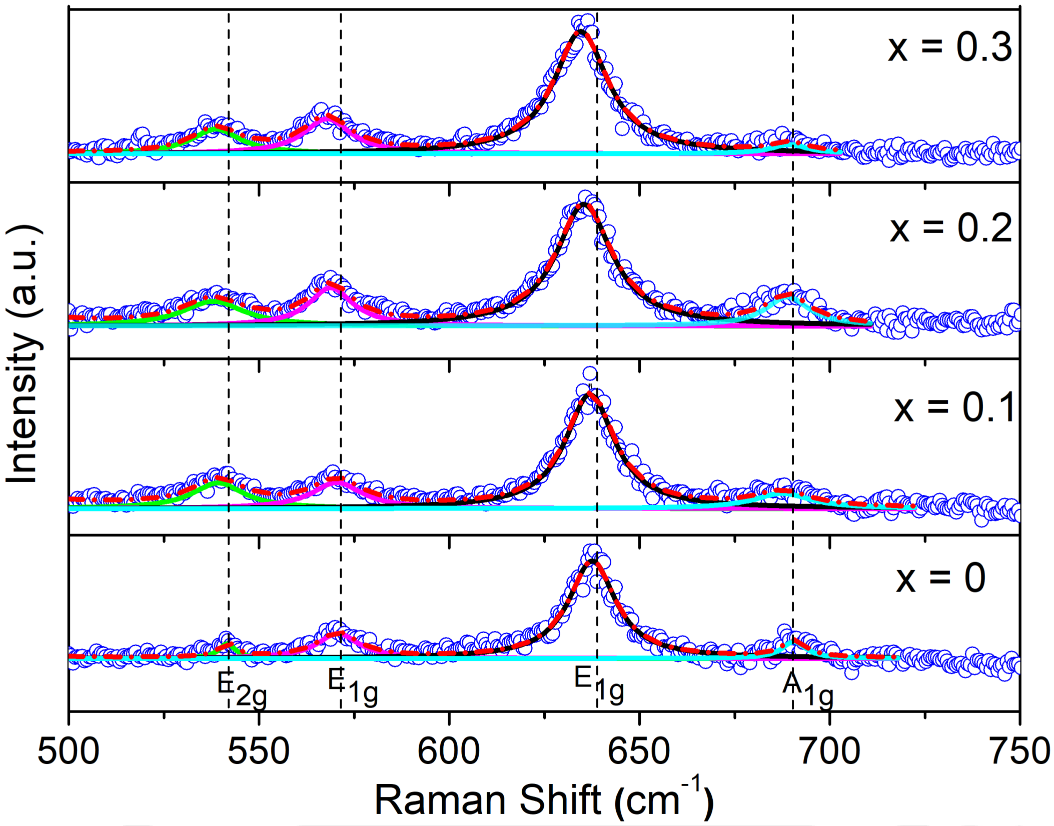

FIGURE 3.5: Room temperature Raman spectra (open circle) for $Ca_{3-x}Dy_xCo_2O_6$ (x = 0, 0.1, 0.2, and 0.3). Solid green, violet, black, and sky-blue lines correspond to the individual Lorentzian fitting, and the red dashed line is their sum.

3.5). Mode frequency depends on force constant and ionic mass, and is proportional to $(k/\mu)^{1/2}$, where k is the force constant and μ is the reduced mass. The force constant decreases due to the increase in the lattice constant 'c' and cell volume (V) for the Dy doped samples (Table 3.1). Irrespective of the force constant, the reduced mass (μ) increases due to the heavier atomic weight of the Dy^{3+} ion. So, the mode frequency decreases due to the combination of both.

3.2.3 XPS analysis

Structural analysis of the prepared samples using X-ray diffraction data strongly suggested the reduction in the oxidation state of Co ions. Therefore, to clarify it, the Co 2p core-levels of the prepared samples have been studied using X-ray photoelectron spectroscopy. Fig. 3.6(a) shows the survey spectra of the parent compound, which confirms

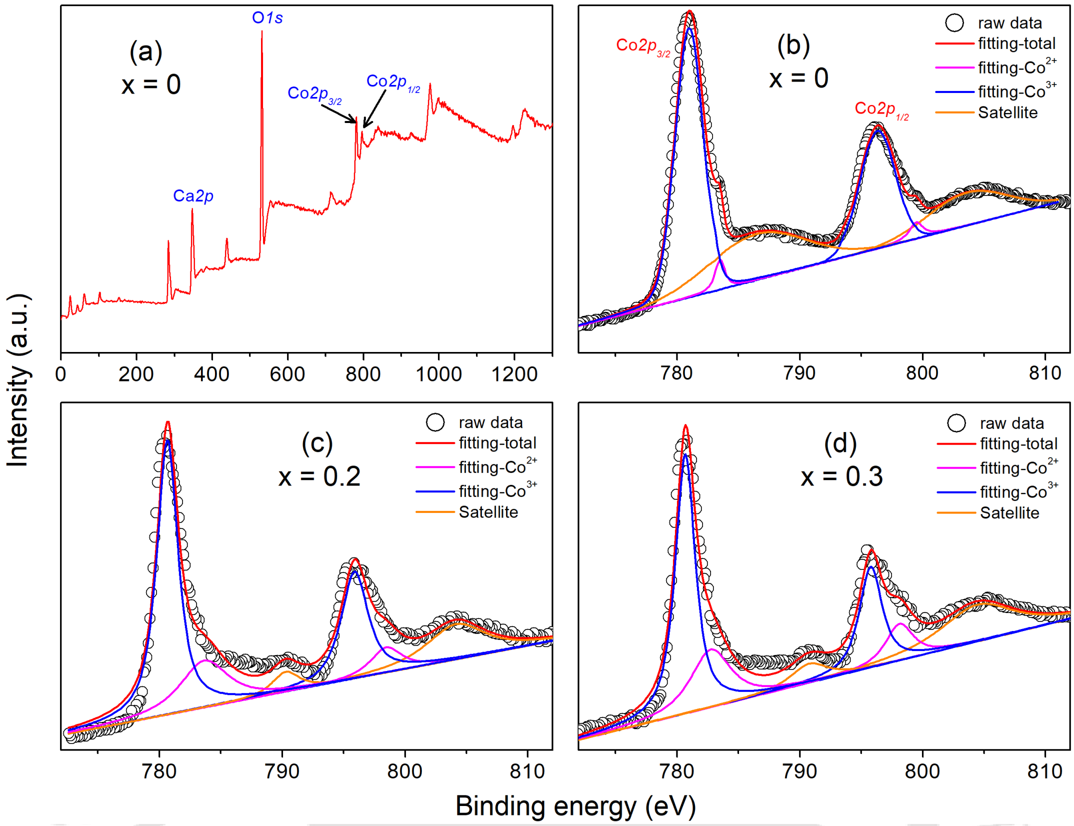

FIGURE 3.6: XPS results for $Ca_{3-x}Dy_xCo_2O_6$ (x = 0.0, 0.2, and 0.3) (a) survey spectra for $Ca_3Co_2O_6$, which shows the presence of Ca, Co, and O atoms. Deconvoluted results of $Co2p_{1/2}$ and $Co2p_{3/2}$ for samples with (b) x = 0, (c) x = 0.2, and (d) x = 0.3.

the presence of constituent atoms (Ca, Co, and O). The broad asymmetric peaks corresponding to Co $2p$ core-levels confirm the mixed valence of Co ions (Figs. 3.6(b), (c), and (d)). For all the compositions, the Co $2p$ core-levels were deconvoluted into two peaks of $2p_{1/2}$ (795.82 and 797.93 eV), two peaks of $2p_{3/2}$ (780.63 and 782.26 eV), and two weak satellite peaks (786.54 and 803.65 eV). The peaks of $2p_{1/2}$ and $2p_{3/2}$ at 795.82 and 780.63 eV, respectively, are attributed to the existence of Co^{3+} (S = 2) ion, while the peaks of $2p_{1/2}$ and $2p_{3/2}$ at 797.93 and 782.26 eV, respectively, is attributed to the existence of Co^{2+} (S = 3/2) ion. Both experimental and theoretical studies for the parent compound suggested trivalent states for Co ions at the octahedral and trigonal prism sites; however, the peak corresponding to Co^{2+} ions is due to the oxygen non-stoichiometry arising during sample preparation [206]. The area under each peak was taken to calculate the percentage of Co^{3+} and Co^{2+} ions, and the estimated content is given in Table 3.2. It is important to note that the area under deconvoluted fitting curves of Co^{3+} and Co^{2+}

indicates that the percentage of Co^{2+} ions increases with an increase in Dy concentration. Thus, the observed XPS results corroborate the experimental finding from X-ray diffraction data.

3.2.4 Temperature variation of magnetization

Magnetization as a function of temperature is measured under both zero field cooled and field cooled conditions in an applied magnetic field of 1000 Oe. Fig. 3.7 shows the M-T curves for $Ca_{3-x}Dy_xCo_2O_6$ (x = 0, 0.1, 0.2, and 0.3). As seen from Fig. 3.7, the ZFC-FC magnetization curves takes an upturn below 25 K. The slope of the upturn decreases with the increase in Dy concentration, and it gets smoothed for x = 0.3 sample. In the ZFC curves, the magnetization attains a maximum for x = 0, 0.1, and 0.2 samples while the peak gets diminished for x = 0.3 sample. On the other hand, the FC magnetization increases continuously with decreasing temperature. It is hard to identify the transition temperatures directly from the ZFC curve, so we did the temperature derivative of ZFC magnetization data (inset Fig. 3.7). For parent compound, the $\frac{dM}{dT}$ is constant before reaching the first transition at 25 K due to magnetic ordering (inset Fig. 3.7(a)). It is a transition from paramagnetic to an incommensurate amplitude-modulated PDA state, and the transition temperature is denoted by T_{c1} [30]. The magnetization increases sharply below T_{c1}, and the M-T ZFC-FC curves split up at around 16 K. It is called splitting temperature, marked by T^* (Fig. 3.7(a)). The bifurcation of the ZFC-FC curves is a signature of an irreversibility phenomenon occurring in glasses. However, in contrast to the spin-glasses, where this irreversibility feature generally occurs below the cusp of the transition, here, the splitting occurs relatively away from the two transition temperatures. Interestingly, the ZFC curve attains a maximum below T^*, and the system again enters into a disordered glassy state [25, 85, 91]. We have identified the transition temperature from $\frac{dM}{dT}$ vs. T plot where the derivative becomes zero, and it is denoted by T_{c2}. The observed values of T_{c1} and T_{c2} (Table 3.2) are consistent with the earlier reported value [28, 85]. Like the parent compound, we have identified the transition temperatures T_{c1} and T_{c2} for Dy doped samples by the same process (inset Fig. 3.7(b)). The transition temperatures T_{c1} and T_{c2} shift to the low-temperature side with Dy content (Table 3.2). The decrease in T_{c2} suggests that the glassy behavior

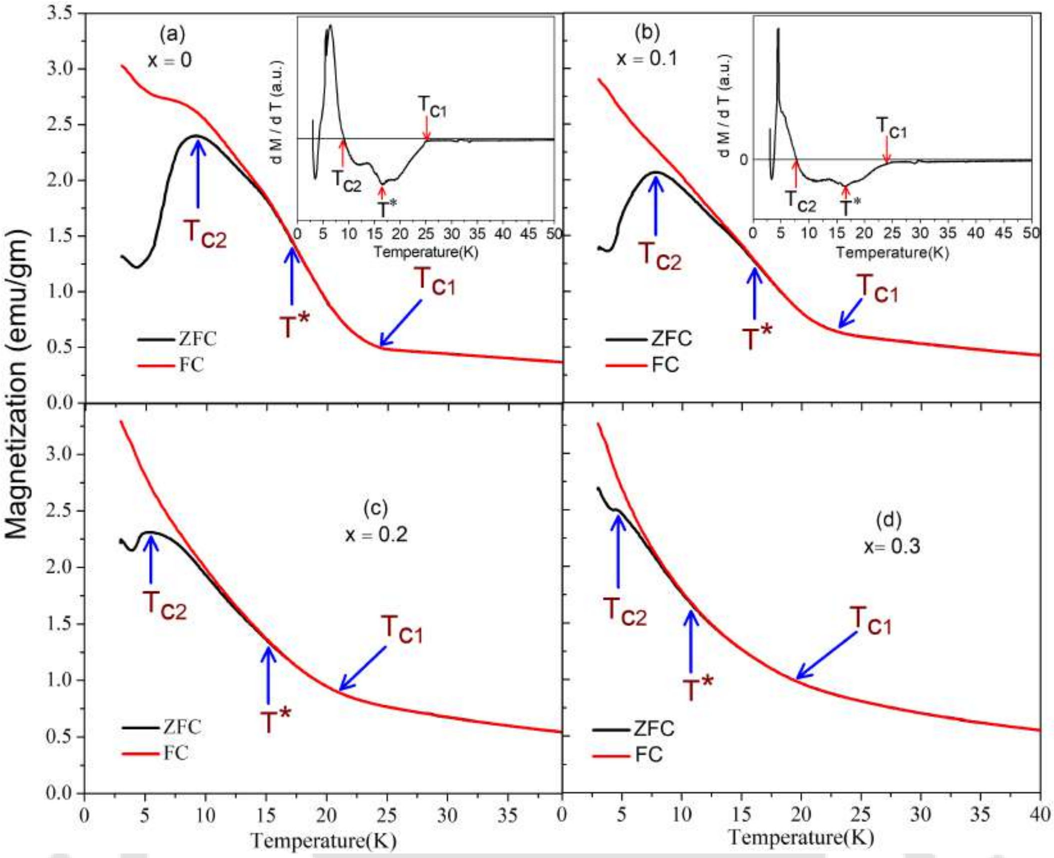

FIGURE 3.7: DC magnetization vs. temperature curve of $Ca_{3-x}Dy_xCo_2O_6$ (x = 0, 0.1, 0.2, and 0.3) in an applied magnetic field of 1000 Oe under ZFC (black line) and FC (red line) condition. Inset shows the $\frac{dM}{dT}$ vs. temperature plot.

is gradually suppressed with Dy concentration, and to understand its dynamics, the temperature-dependent magnetic relaxation below T_{c2} is necessary.

Fig. 3.8 depicts the inverse susceptibility behavior for $Ca_{2.7}Dy_{0.3}Co_2O_6$. The DC susceptibility in the paramagnetic region (175 K – 300 K) obeys the Curie-Weiss law,

$$\chi = \frac{C_{\mathrm{mol}}}{T - \theta} \tag{3.1}$$

where C_{mol} is molar Curie constant, and θ is Curie-Weiss temperature. The effective magnetic moment (μ_{eff}) was calculated by using the relation $\mu_{\mathrm{eff}} = (3C_{\mathrm{mol}}k_{\mathrm{B}}/N_{\mathrm{A}}\mu_{\mathrm{B}}^2)^{1/2}$, where k_{B} is the Boltzmann constant, and N_{A} is the Avogadro number. Table 3.2 contains the value of effective magnetic moment (μ_{eff}) and Curie temperature (θ) for all samples. For the parent compound, the value of $\mu_{\mathrm{eff}} = 5.6\ \mu_{\mathrm{B}}$ and $\theta = 31$ K are consistent with the earlier reported value [28]. The Lande g-factor was calculated from these results, and the 'g' value comes out to be 2.3. Large value of 'g' is mainly due to the highly

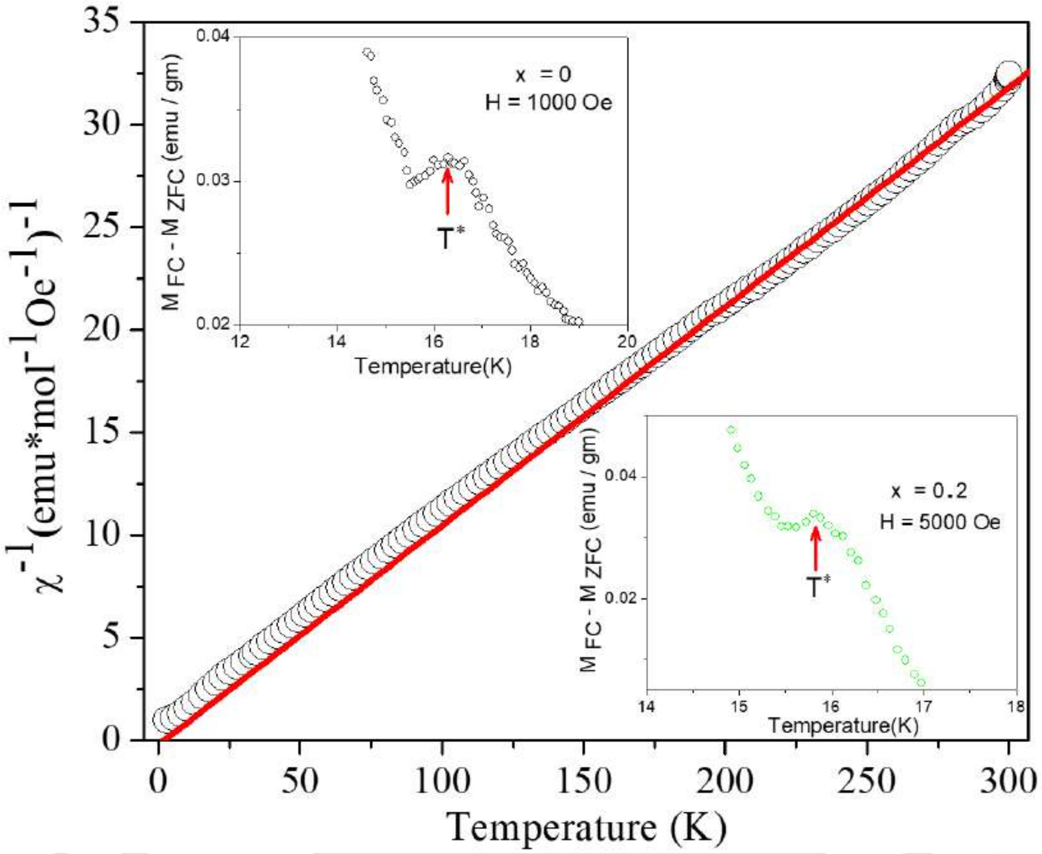

FIGURE 3.8: The inverse susceptibility vs. temperature data (open circle) fitted to the Curie-Weiss law (red line) for $Ca_{2.7}Dy_{0.3}Co_2O_6$. Inset shows the M_{FC} - M_{ZFC} vs. temperature curves for x = 0 and 0.2 samples.

anisotropic magnetic character and a possible reason for the strong Ising-like property of Co spins [18, 82, 202]. Inset Fig. 3.8 shows the difference between magnetizations measured under field cooled condition (M_{FC}) and zero field cooled condition (M_{ZFC}) for x = 0 and 0.2 samples in an applied magnetic field of 1000 Oe and 5000 Oe, respectively. The difference between the magnetizations M_{FC} and M_{ZFC} increases and attains a maximum at 16 K (T^*). Below this, there is a dip in the curve, and then it increases continuously. Generally, the deviation between M_{FC} and M_{ZFC} changes monotonically if the metastable states do not occur in any of the branches. Hence such an effect of the difference reaching a maximum value indicates the non-equilibrium nature of the magnetic properties in this region, which is later on studied through the relaxation measurements. The non-equilibrium magnetization is a result of the strong anisotropic nature of the spin structures in this system [207].

The effective magnetic moment increases continuously with the concentration of Dy due

TABLE 3.2: Percentage of Co^{3+} and Co^{2+} ion in $Ca_{3-x}Dy_xCo_2O_6$. The value of transition temperatures (T_{c1} and T_{c2}), Curie temperature (θ), effective magnetic moment (μ_{eff}), μ_{eff}(cal), critical field (H_c), relaxation time (τ), and critical exponent (n) for $Ca_{3-x}Dy_xCo_2O_6$.

x	Co^{3+} (%)	Co^{2+} (%)	T_{c1} (K)	T_{c2} (K)	θ (K)	μ_{eff} (μ_B)	μ_{eff}(cal) (μ_B)	H_c (T)	τ (sec)	n
0	94.9	5.1	25	9.1	31	5.6	5.6	3.4	1366	0.52
0.1	81	19	23	7.8	25	6.6	6.5	3.2	1043	0.54
0.2	71.4	28.6	20	5.3	14	7.5	7.2	3	680	0.56
0.3	69	31	18	4.5	2	8.5	7.9	2.8	512	0.62

to the combined effect of the large paramagnetic moment of Dy and the mixture of Co^{3+} (S = 2) and Co^{2+} (S = 3/2) spins [118]. The value of the calculated effective magnetic moment (μ_{eff}(cal)) is given by

$$\mu_{eff}(\mathrm{cal}) = \sqrt{xg^2 J(J+1) + 2.3^2\left(x \times \frac{3}{2} \times \frac{5}{2} + (1-x) \times 2 \times 3\right)} \tag{3.2}$$

where x is the doping concentration of Dy^{3+} ion, and J is the total angular momentum quantum number. Table 3.2 contains the μ_{eff}(cal) for all the samples. There is a good match between the experimentally determined value of μ_{eff} and the calculated value μ_{eff}(cal) for x = 0.1 sample. However, higher experimental value of μ_{eff} is observed for x = 0.2 and 0.3 samples. The μ_{eff} for all the compositions was estimated using the calculated value of g = 2.3, which is derived from the experimental data of the parent compound. Our results suggested that the x = 0.1 compound exhibits similar features as the parent compound with the value of g = 2.3; however, the results for x = 0.2 and 0.3 samples are considerably different (higher) from that for the parent compound. Therefore, the possible reasons for the large difference between estimated and calculated data are large magnetic anisotropy and partial quenching of the orbital moment of Co^{3+} ion. The θ decreases from 31 K for the parent compound to 2 K for x = 0.3 doped samples (Table 3.2). The decrease in the 'θ' value is mainly due to the reduced ferromagnetic coupling along the c-axis. Thus, the substitution of Dy suppresses the Ising ferromagnetic character of the compound by introducing the antiferromagnetic

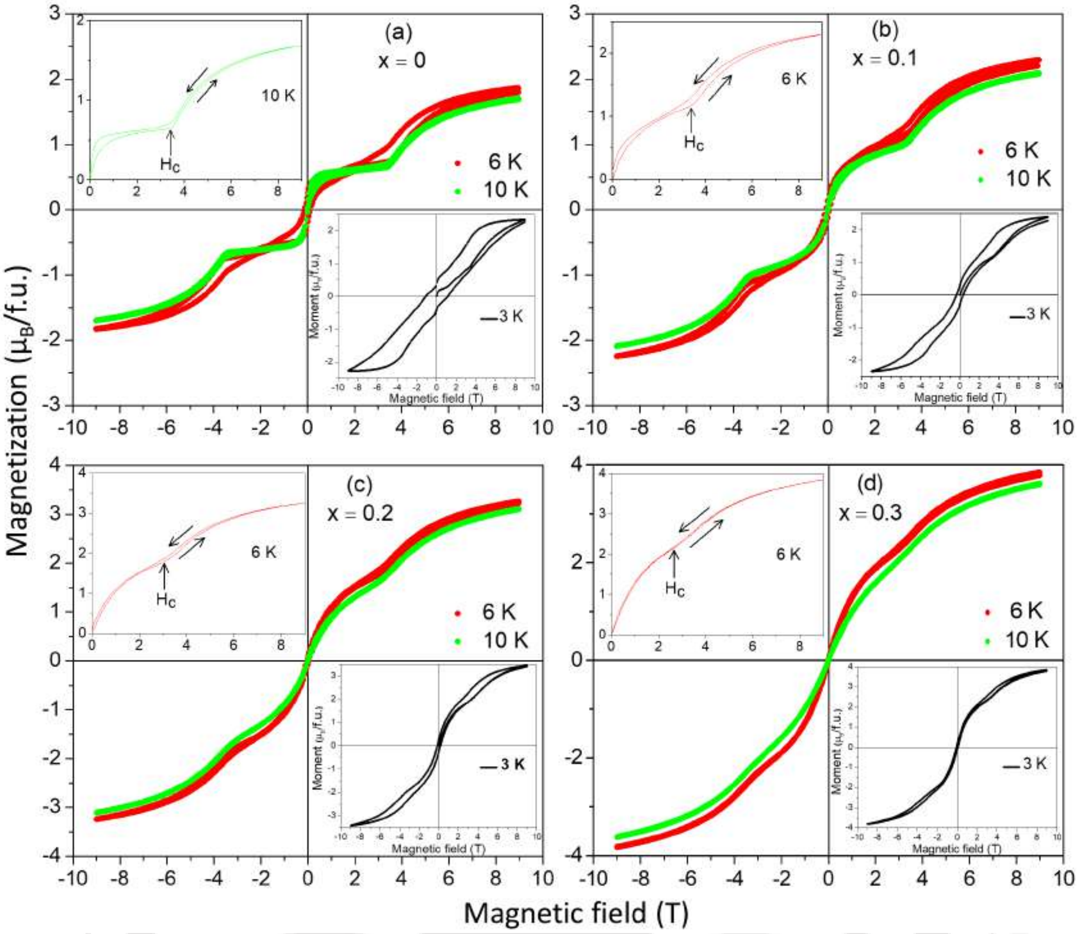

FIGURE 3.9: Isothermal M-H curves at temperature T = 6 K (red), and 10 K (green) for $Ca_{3-x}Dy_xCo_2O_6$ (x = 0, 0.1, 0.2, and 0.3). The inset shows the enlarged view of the first quadrant M-H curves for both field increasing and decreasing branches, and at the bottom, the full cycle M-H at 3 K is plotted.

coupling of induced Co^{2+} ions with the Co^{3+}(HS) ions.

3.2.5 Field dependence of magnetization

Fig. 3.9 shows the M-H curves of $Ca_{3-x}Dy_xCo_2O_6$ (x = 0, 0.1, 0.2, and 0.3) measured at various temperatures. To explain the magnetization process in the samples, the first quadrant M-H curve for both field increasing and decreasing branches are included in the inset Fig. 3.9. It can be seen from the inset Fig. 3.9(a) that the magnetization curve for the parent compound at 10 K increases sharply at low fields ($H < 1$ T) and tends to saturate with the increase in field, characterizing the ferrimagnetic ground state of the compound [85, 200]. Further increase in the magnetic field leads to a transition from ferrimagnetic to ferromagnetic state [199–201]. The transition field is called critical field

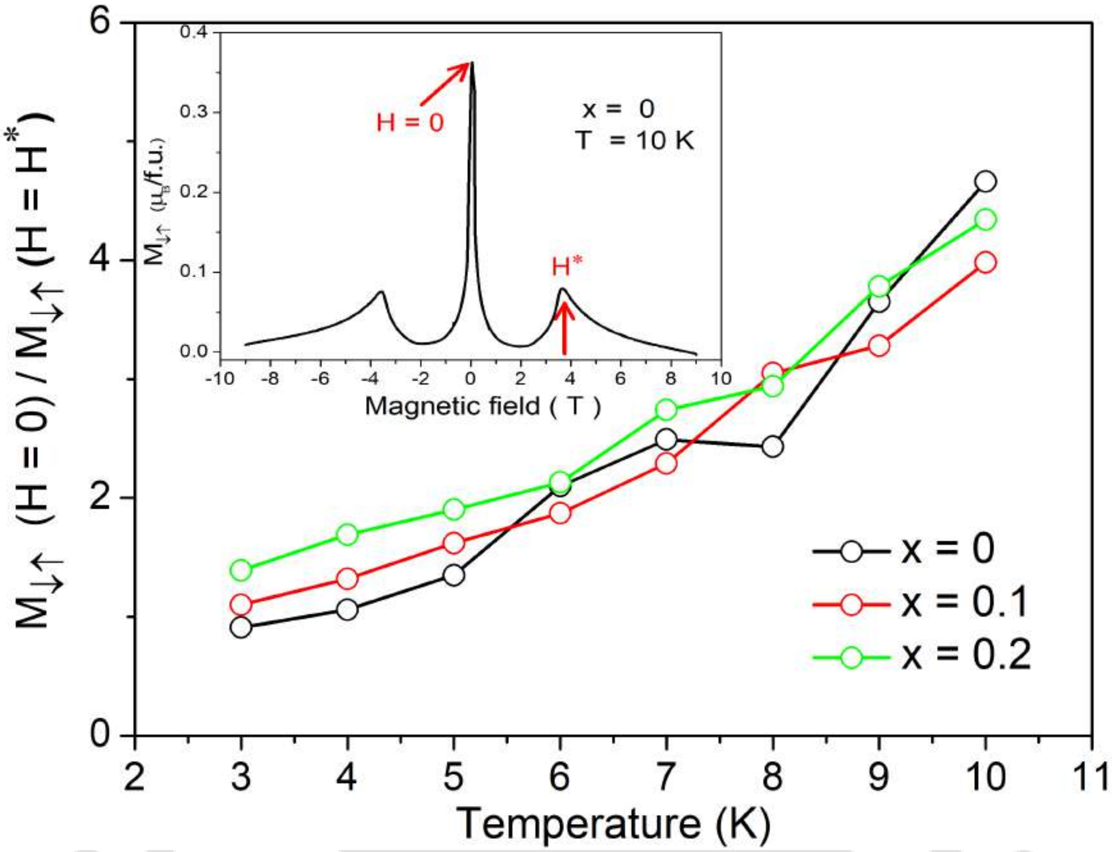

FIGURE 3.10: $\frac{M_{\downarrow\uparrow}(\text{at} H=0)}{M_{\downarrow\uparrow}(\text{at} H=H^*)}$ vs. temperature curve for $Ca_{3-x}Dy_xCo_2O_6$ (x = 0, 0.1, and 0.2). Inset shows the $M_{\downarrow\uparrow}$ vs. magnetic field plot for the parent compound at 10 K.

H_c, above which the magnetization increases, followed by hysteresis in the demagnetization process. A sharp rise in magnetization accompanied by hysteresis is attributed to the first-order phase transition. At 10 K and 6 K, the M-H curves exhibit similar features (Fig. 3.9(a)). The M-H curve changes its shape drastically at 3 K and attains a large hysteresis (inset Fig. 3.9(a)). Inset Figs. 3.9(b), (c), and (d) contains the enlarged view of the first-quadrant M-H for both field increasing and decreasing branches of Dy doped samples at 6 K. In the low-field region ($H < 1$ T), the magnetization rises more sharply than the parent compound, but it doesn't tend to saturate. In addition, the essential H_c to induce the ferrimagnetic to ferromagnetic transition decreases as the Dy concentration increases (Table 3.2). The decrease in H_c indicates the weakening of the intra-chain ferromagnetic interaction with Dy substitutions. Another notable feature is that the M-H curve at 3 K became less hysteric for Dy doped samples (inset Figs. 3.9(b), (c), and (d)).

In order to analyze this complex magnetic behavior, we have calculated the difference between magnetization for ramping down (+9T to -9T) ($M_\downarrow$) and ramping up (-9T to +9T) cycles ($M_\uparrow$). Inset Fig. 3.10 depicts the variation in $M_\downarrow$ - $M_\uparrow$ ($M_{\downarrow\uparrow}$) with magnetic field for the parent compound at 10 K. This difference is proportional to the remanent magnetization at $H = 0$ if there was a single ferromagnetic like transition. However, the ferromagnetic transition for this sample lies at a non-zero magnetic field ($H = H_c$). So, it is obvious that the difference ($M_{\downarrow\uparrow}$) at $H = H_c$ should replicate the remanent magnetization of this ferromagnetic transition. We observed from the inset Fig. 3.10 that the difference ($M_{\downarrow\uparrow}$) picks up at H^*, which is very close to the value of the transition field (H_c). Hence the value of $M_{\downarrow\uparrow}$ at $H = H^*$ is proportional to the remanent magnetization of this transition, along with the conventional remanent magnetization $M_{\downarrow\uparrow}$ (at $H = 0$) marked in Fig. 3.10. It will be informative if we compare the remanent magnetization for these two transitions by taking a ratio as $\frac{M_{\downarrow\uparrow}(\mathrm{at}H=0)}{M_{\downarrow\uparrow}(\mathrm{at}H=H^*)}$. In the main panel of Fig. 3.10, we have plotted the $\frac{M_{\downarrow\uparrow}(\mathrm{atH=0})}{M_{\downarrow\uparrow}(\mathrm{at}H=H^*)}$ with temperature for all the samples. We observed that this ratio increases monotonically as a function of temperature. This implies that the metastability effects at higher temperatures for the in-field transition (H_c) decreases faster compared to that of the ferrimagnetic transition at $H = 0$.

Similar to the analysis which we have performed using $M_{\downarrow\uparrow}$ for constant H, we have tried to look for $|H_\downarrow - H_\uparrow|$ ($|H_{\uparrow\downarrow}|$) for constant values of magnetization (M). In the hysteretic region, there are two values of applied magnetic field ($H_\downarrow$ and $H_\uparrow$) for each value of constant magnetization (M). The difference ($|H_{\uparrow\downarrow}|$) indicates the softness or hardness of a ferromagnetic material around $H = 0$. For a highly anisotropic ferromagnetic material, this $|H_{\uparrow\downarrow}|$ also provides us information about the strength of anisotropy [39]. Inset Fig. 3.11 is a plot of $|H_{\uparrow\downarrow}|$ as a function of the applied magnetic field (H). The applied magnetic field corresponding to the maximum value of $|H_{\uparrow\downarrow}|$ is marked as H^{**}. As $|H_{\uparrow\downarrow}|$ is indicative of the strength of anisotropy, so for a ferromagnetic transition occurring at a finite field H_c, the difference between H^{**} and H_c will provide us the information about the softness or hardness of the material. The main panel of Fig. 3.11 is a plot of the difference between the transition field H_c and H^{**} vs. temperature for all the samples. As H_c is almost constant for all the samples as a function of temperature so the decrease

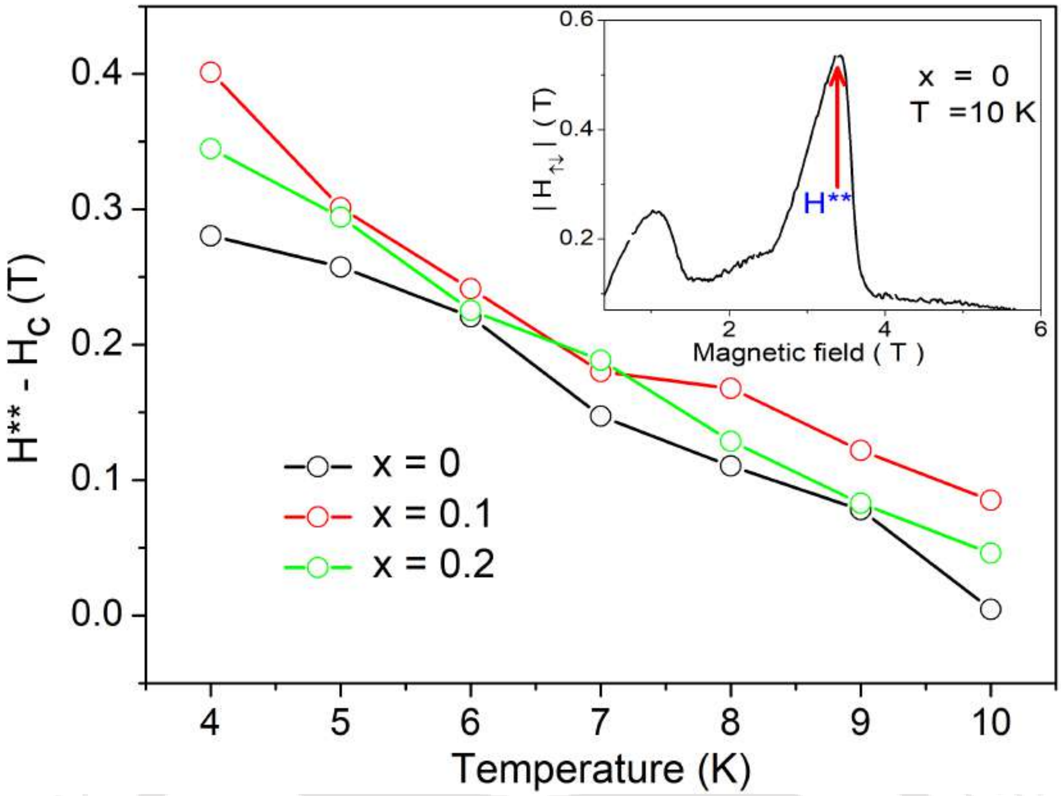

FIGURE 3.11: Temperature dependence of H^{**}-H_c for $Ca_{3-x}Dy_xCo_2O_6$ (x = 0, 0.1, and 0.2). Inset shows the variation in $|H_{\uparrow\downarrow}|$ with magnetic field for the parent compound at 10 K.

in the value of H^{**} - H_c can be totally attributed to the value of H^{**}. It indicates the strength of the anisotropy associated with this transition decreases similarly with the increase of temperature for all the samples, depicting that the substitution has little effect on this phenomena.

In order to understand the spin contribution below and above H_c, the virgin curves at various temperatures (Fig. 3.12) were fitted to the Curie–Brillouin law,

$$M = NgJ\mu_B B_J(x). \tag{3.3}$$

Here N is the number of atoms per unit volume, μ_B is Bohr magneton, and $B_J(x)$ is the Brillouin function given by,

$$B_J(x) = \left[\frac{2J+1}{2J}\coth\left(\frac{2J+1}{2J}x\right) - \frac{1}{2J}\coth\left(\frac{1}{2J}x\right)\right] \tag{3.4}$$

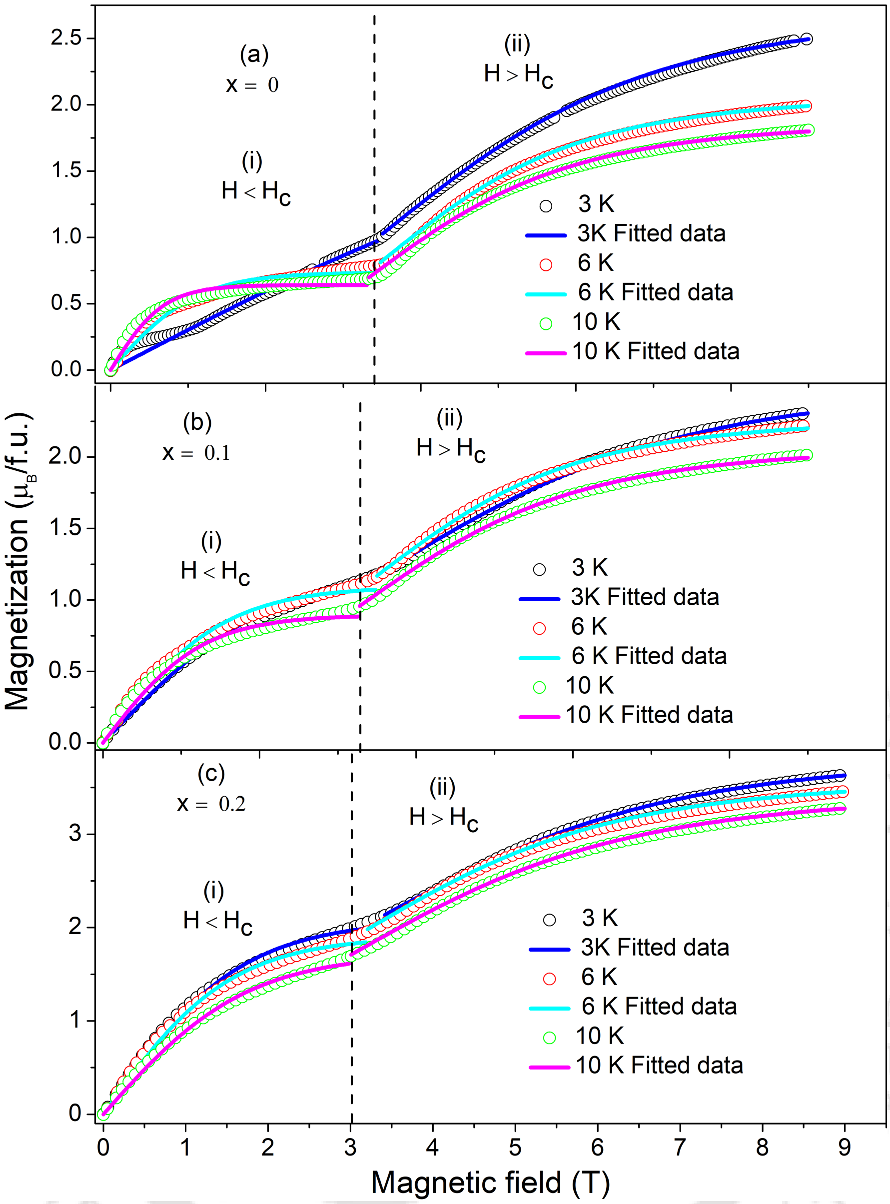

FIGURE 3.12: Curie–Brillouin law fitting (solid line) in the isothermal M-H curves (open circle) obtained at temperature T = 3 K, 6 K, and 10 K for $Ca_{3-x}Dy_xCo_2O_6$ (x = 0, 0.1, and 0.2). The dashed line divides the M-H curve into two regions (i) $H < H_c$ (ii) $H > H_c$.

where $x = \frac{gJ\mu_B(H+\lambda M)}{k_B T}$ and λ is the mean field coefficient. Using the expansion coth(y) = $\frac{1}{y} + \frac{y}{3} - \frac{y^3}{45}$, the magnetization can be written as [208]

$$M = \left[\frac{H}{\alpha\beta\gamma} + \sqrt{\frac{H^2}{4(\alpha\beta\gamma)^2} + \frac{1}{27}\left(\frac{1}{\alpha\beta\gamma} - \frac{1}{\beta}\right)^3}\right]^{\frac{1}{3}} - \left[\frac{\left(\frac{1}{\alpha\beta\gamma} - \frac{1}{\beta}\right)}{3\left[\frac{H}{\alpha\beta\gamma} + \sqrt{\frac{H^2}{4(\alpha\beta\gamma)^2} + \frac{1}{27}\left(\frac{1}{\alpha\beta\gamma} - \frac{1}{\beta}\right)^3}\right]^{\frac{1}{3}}}\right] \tag{3.5}$$

where $\alpha = \frac{N(g\mu_B)^2(J^2+J)}{3k_B T}$ and $\beta = \frac{(g\mu_B)^2\left(J^2+J+\frac{1}{2}\right)}{9(k_B T)^2}$. In Fig. 3.12, the first-quadrant M-H curves are divided into two regions. The regions (i) and (ii) correspond to $H < H_c$ and $H > H_c$, respectively. We have fitted two individual Brillouin functions in these regions to obtain 'J' values. Eq. 3.5 fits well in the experimental data for x = 0.1 and 0.2 samples due to the large paramagnetic moment of Dy, while it deviates for the parent compound because of the presence of strong coupling between spins. The obtained 'J' values are $\frac{1}{2}$ and $\frac{3}{2}$ for the region (i) and (ii), respectively. The jump in the 'J' value $\left(\frac{1}{2} \rightarrow \frac{3}{2}\right)$ is not unusual, which will be explained later in the discussion.

3.2.6 Magnetic dynamics

The dynamics of $Ca_{3-x}Dy_xCo_2O_6$ (x = 0, 0.1, 0.2, and 0.3) samples were studied through ZFC magnetic relaxation measurements. In this process, the samples were cooled from room temperature to the desired temperature ($T < T_{c2}$) in the absence of an external magnetic field. The samples were magnetized for a short-time (60 sec) in an external magnetic field of 9 T, and then external magnetic field was switched off, and the decay in the remanent magnetization was measured with time for 10,000 sec. Usually, for the long ranged ordered systems, the remanent magnetization remains independent of time. The prolonged decay in the magnetization should be attributed to the glassy feature. Thus, the time response of DC magnetization is important to reveal the spin dynamics of the glassy system. Fig. 3.13 depicts the magnetic relaxation behavior of $Ca_{3-x}Dy_xCo_2O_6$ (x = 0 and 0.1) measured at various temperatures. The observed logarithmic relaxation behavior indicates the presence of a large number of intermediate anisotropic metastable states due to the clusters of spins. The magnetization relaxes slowly at temperatures $T \ll T_{c2}$ while it saturates after a short-time-interval for temperatures close to the T_{c2} (T = 8 K) (Fig. 3.13). Fig. 3.14 depicts the magnetic relaxation behavior of both compounds around their T_{c2}. The magnetization relaxes in a short-while and then saturates for x = 0 and 0.1 samples at temperatures 10 K and 8 K, respectively. These results suggested that the magnetic relaxation and glassy behavior are most prominent for temperatures much below T_{c2}.

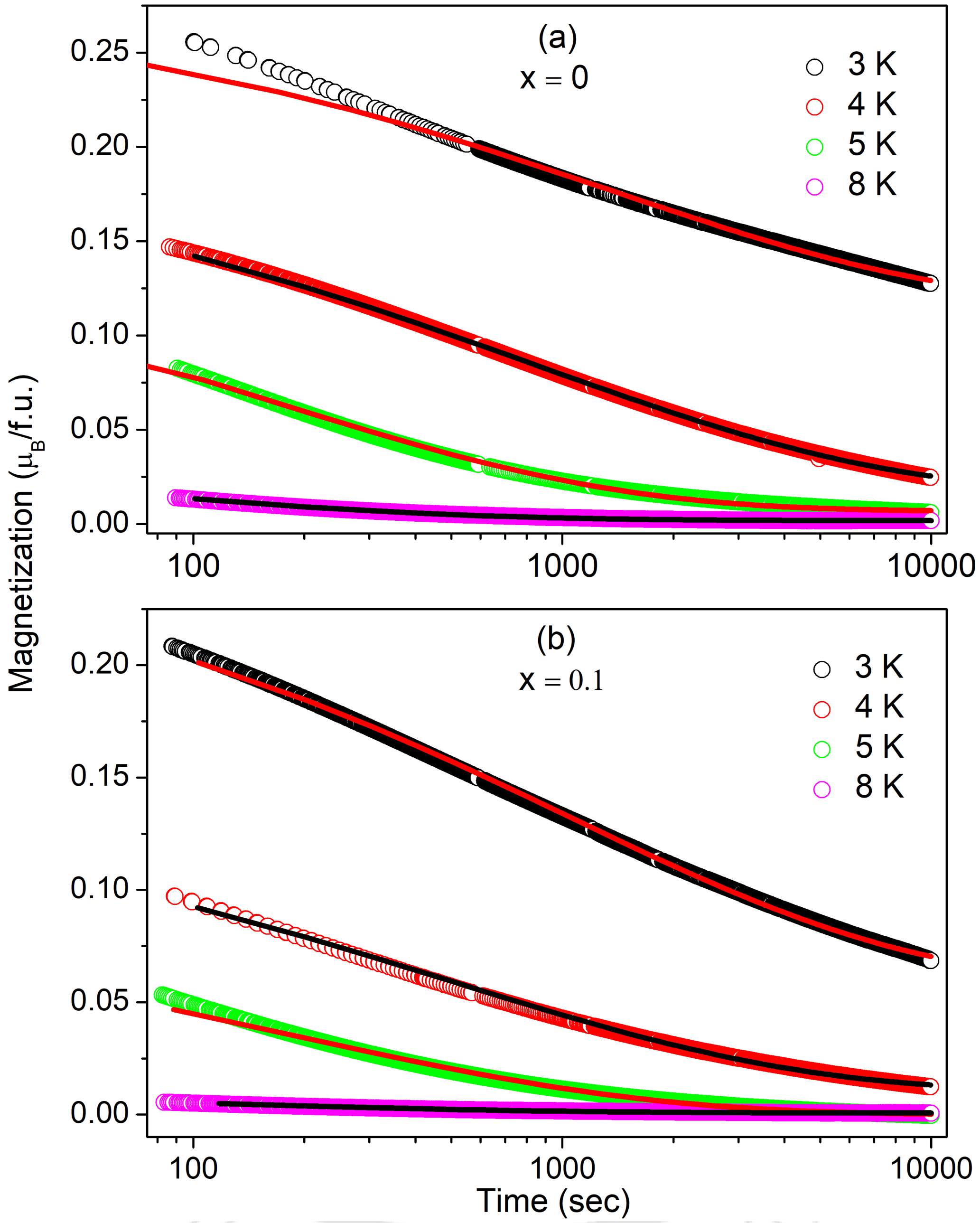

FIGURE 3.13: Remanent magnetization as a function of time (open circle) at temperatures T = 3 K to 8 K for $Ca_{3-x}Dy_xCo_2O_6$ (a) x = 0 and (b) x = 0.1. The solid line corresponds to the fitted data in Eq. 3.6.

In the glassy systems, the time dependence of magnetization can be described by stretched exponential relaxation function [131, 195],

$$M = M_0 + M_1 \exp\left[-\left(\frac{t}{\tau}\right)^{1-n}\right] \tag{3.6}$$

where M_0, M_1, τ, and n are spontaneous magnetization, glassy component, relaxation

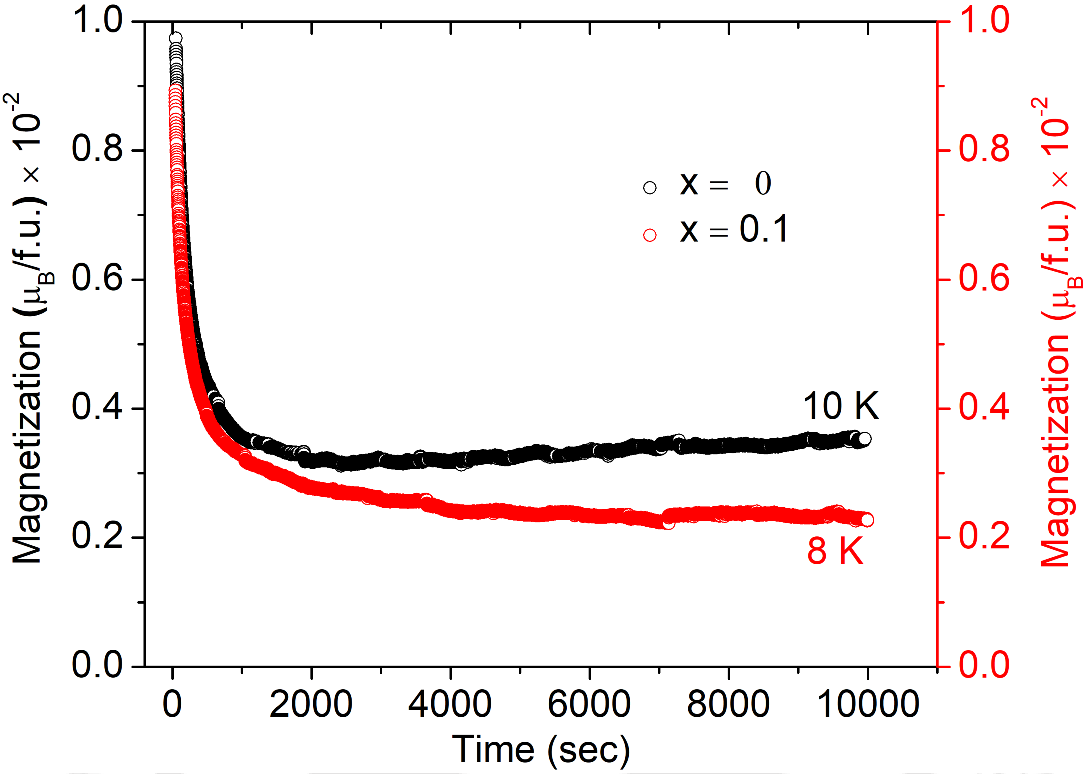

FIGURE 3.14: Magnetization relaxation curve at respective temperature for $Ca_3Co_2O_6$ (black open circle) and $Ca_{2.9}Dy_{0.1}Co_2O_6$ (red open circle) samples.

time, and critical exponent, respectively. The relaxation time (τ) and the critical exponent (n) are associated with the relaxation rate. For $n = 0$, the magnetization relaxes exponentially, and if $n = 1$, there is no relaxation. The magnetic relaxation curves for both compounds (Fig. 3.13) were fitted to Eq. 3.6 by varying the parameter M_0, M_1, τ, and n, and the fitted parameters have been tabulated in Table 3.3. A slight deviation from the fitted data was observed up to 100 sec. As the glassy feature gradually suppressed with temperature, the increased value of n and decreased value of τ with temperature supports this result (Table 3.3). The thermal activation energy releases the energy barrier, which affects the glassy feature, and the magnetization relaxes back quickly [131].

The dynamics of prolonged relaxation in this system was studied using the stretched exponential relaxation function. However, the origin of extremely slow relaxation remains unclear because both conventional glass and interacting spin-clusters might give rise to this feature. To elucidate this, we use the Vogel-Fulcher model of relaxation for interacting spin-clusters with uniaxial anisotropy, where the dynamical behavior is not

TABLE 3.3: The fitted parameters: spontaneous magnetization (M_0), glassy component (M_1), relaxation time (τ), and critical exponent (n) obtained by fitting the magnetic relaxation data at temperature T = 3 K to 8 K for $Ca_3Co_2O_6$ and $Ca_{2.9}Dy_{0.1}Co_2O_6$ in Eq. 3.6.

T	$x = 0$				$x = 0.1$			
(K)	M_0 (μ_B/f.u.)	M_1 (μ_B/f.u.)	τ (sec)	n	M_0 (μ_B/f.u.)	M_1 (μ_B/f.u.)	τ (sec)	n
3	0.117	0.16	1366	0.52	0.058	0.20	1043	0.54
4	0.006	0.19	708	0.55	0.010	0.14	489	0.55
5	0.007	0.16	313	0.56	0.007	0.10	198	0.56
6	0.004	0.09	113	0.57	0.004	0.06	67	0.56
7	0.002	0.06	53	0.57	0.002	0.03	38	0.57
8	0.001	0.04	34	0.58	0.001	0.01	27	0.58

only due to the spin-flip but also from the interacting short-range magnetic clusters. The Vogel-Fulcher equation for relaxation time is

$$\tau = \tau_0 \exp\left[\frac{T_A}{T - T_0}\right] \tag{3.7}$$

where τ_0 is an activation time, $T_A = E_A/k_B$ is an activation temperature, and T_0 is the Vogel-Fulcher temperature [54, 209]. For $T_0 = 0$ K, Eq. 3.7 converts to well known Arrhenius law, which is applicable for non-interacting magnetic entities. The activation temperature (T_A) defines potential barrier required separates to adjacent clusters in terms of activation energy (E_A). For temperatures between 3 K and 8 K, τ lies in the range of 1400 to 20 sec (Table 3.3). Fig. 3.15 depicts the temperature dependency of relaxation time (τ) for both x = 0 and x = 0.1 compounds. It is fitted to Eq. 3.7 by varying τ_0, T_A, and T_0. The fitted parameters are listed in Table 3.4 (Fig. 3.15). A non-zero value of T_0, 10.8 K and 9.3 K for x = 0 and 0.1 samples, respectively, confirms the presence of inter-cluster interaction and makes the system different from conventional glass. The decreased value of T_0 for x = 0.1 sample is also in good agreement with glassy transition temperature (T_{c2}) obtained from the DC M-T curves (Fig. 3.7). The obtained values of τ_0 for x = 0 and 0.1 samples are 5.5×10^4 and 3.4×10^4 sec, respectively, and it can be considered the limit of relaxation. Interestingly, the cluster separation parameter

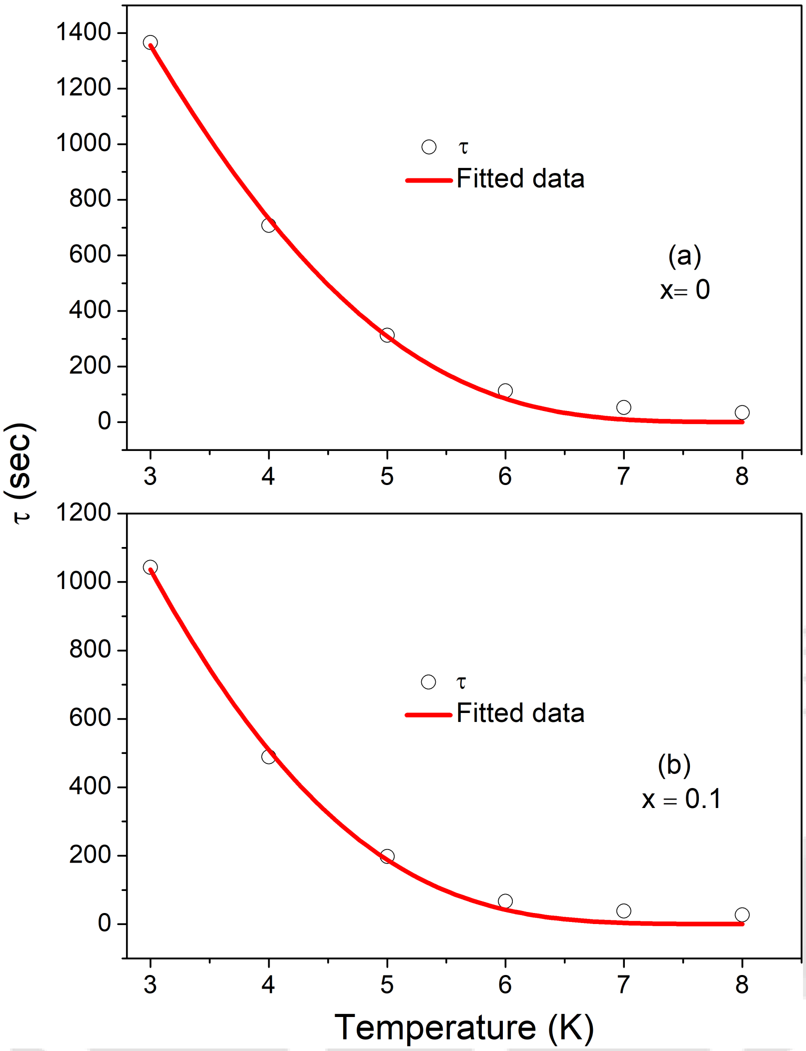

Figure 3.15: The relaxation time (τ) vs. temperature plot (open circle) for both (a) $Ca_3Co_2O_6$ and (b) $Ca_{2.9}Dy_{0.1}Co_2O_6$. The red solid line is fitted data in Eq. 3.7.

T_A decreases from 26 K for parent compound to 21 K for x = 0.1 sample. It suggests that these samples exhibit slow dynamics due to the formation of cluster-glass state, and with Dy substitution, this property is reduced.

Similar to the Vogel-Fulcher equation for relaxation time, the same model can be used to fit another parameter (ΔM) obtained from the relaxation data for x = 0 and 0.1 samples at various temperatures. The ΔM is defined as the total drop in the magnetization after the relaxation for 10,000 sec ($M_{t=0\text{sec}} - M_{t=10{,}000\text{sec}}$). The Vogel-Fulcher equation for ΔM is

$$\Delta M = M_A \exp\left[\frac{T_A}{T - T_0}\right] \tag{3.8}$$

where M_A is the limiting value of ΔM, and the rest of the parameters T_A and T_0 are

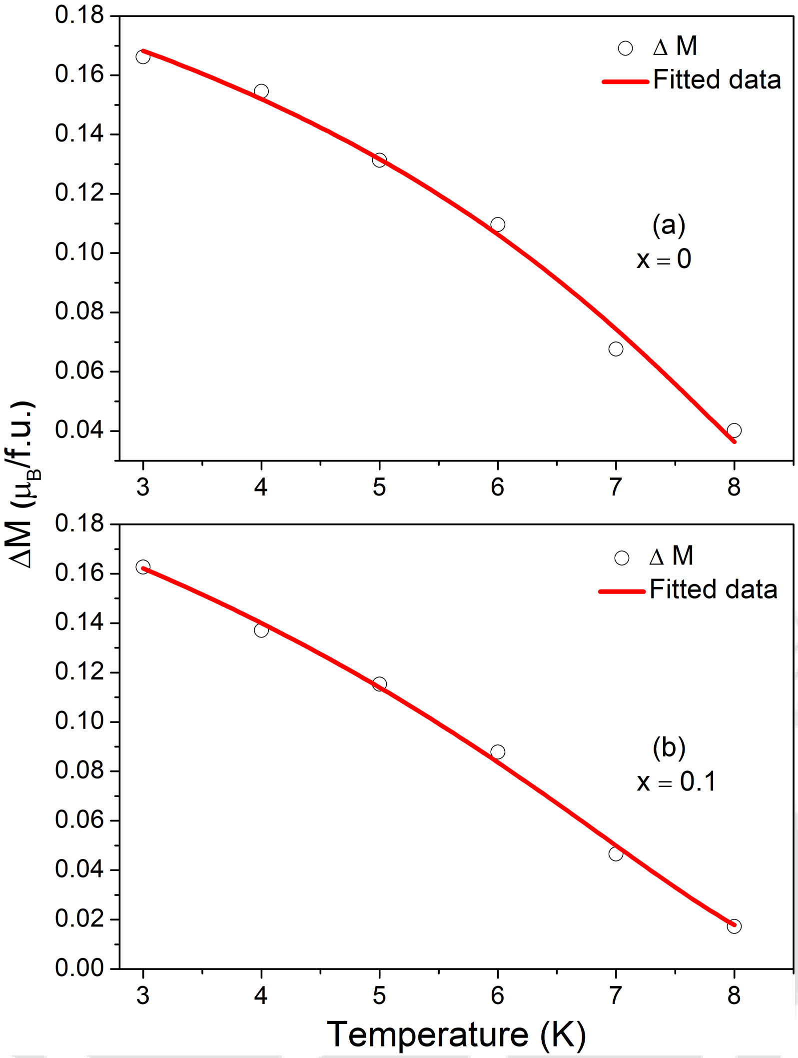

FIGURE 3.16: The ΔM vs. temperature plot (open circle) for both (a) $Ca_3Co_2O_6$ and (b) $Ca_{2.9}Dy_{0.1}Co_2O_6$. The red solid line is fitted data in Eq. 3.8.

the same as in Eq. 3.7. Fig. 3.16 shows the variation in ΔM with temperature for both x = 0 and 0.1 samples. It is fitted to Eq. 3.8, and the obtained parameters M_A, T_A, and T_0 are given in Table 3.4. The limiting parameter M_A increases from 0.31 for the parent compound to 0.39 for x = 0.1 sample. Large value of 'M_A' for x = 0.1 sample indicates the drop in the magnetization is more for a fixed time-interval than the parent compound. The obtained value of T_0 = 10.3 K and 9.4 K for x = 0 and 0.1 samples, respectively, are consistent with the Vogel-Fulcher equation fitting for relaxation time (τ); however, the T_A values are different (Table 3.4).

To make a comparative study of the dynamic behavior, the magnetic relaxation of x = 0.2 and 0.3 samples were also performed by the same procedure as for x = 0 and 0.1 samples.

TABLE 3.4: The value of activation time (τ_0), activation temperature (T_A), Vogel-Fulcher temperature (T_0), and the limiting value of ΔM (M_A) used in the fitting of relaxation time (τ) and ΔM (μ_B/f.u.) for $Ca_3Co_2O_6$ and $Ca_{2.9}Dy_{0.1}Co_2O_6$ to Vogel-Fulcher equations.

	Relaxation time (τ)			ΔM (μ_B/f.u.)		
x	$\tau_0 \times 10^4$ (sec)	T_A (K)	T_0 (K)	M_A (μ_B/f.u.)	T_A (K)	T_0 (K)
0	5.5	26	10.8	0.31	4.3	10.3
0.1	3.4	21	9.3	0.39	3.6	9.4

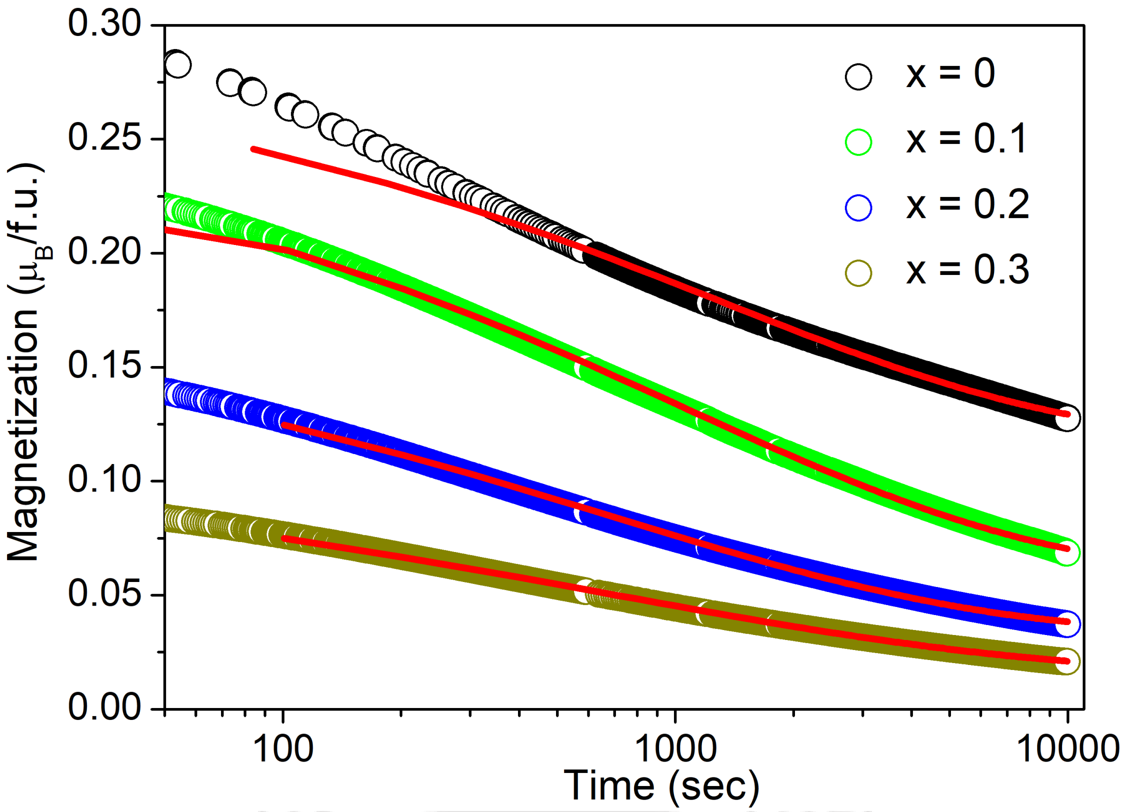

FIGURE 3.17: Remanent magnetization vs. time plot for $Ca_{3-x}Dy_xCo_2O_6$ (x = 0, 0.1, 0.2, and 0.3) at temperature T = 3 K. The solid line corresponds to the fitted data in Eq. 3.6.

Fig. 3.17 depicts the relaxation behavior of $Ca_{3-x}Dy_xCo_2O_6$ (x = 0, 0.1, 0.2, and 0.3) at 3 K. The remanent magnetization drops approximately 1/2, 1/3, 1/4, and 1/5 of its initial value ($M_{t=0sec}$) after 10,000 sec for x = 0, 0.1, 0.2, and 0.3 samples, respectively. Fast relaxation of remanent magnetization corresponds to reduced glassy features due to Dy substitution. To explain the time dependence of remanent magnetization, the relaxation data were fitted to Eq. 3.6 (Fig. 3.17). The fitted parameters n and τ are given in Table 3.2. As expected due to the weakening of glassy behavior for the Dy doped compounds, the n increases while τ decreases (Table 3.2).

3.3 Discussion

In the 1D chain of $\mathrm{Ca_3Co_2O_6}$, the Co ions along the chain are coupled through a strong ferromagnetic interaction while the inter-chain antiferromagnetic coupling is relatively weak. Here we are substituting the $\mathrm{Dy^{3+}}$ ions in the replacement of $\mathrm{Ca^{2+}}$ ions, which have an ionic radius lower than the $\mathrm{Ca^{2+}}$ ions. It is found that with the substitution of Dy in this system, the intra-chain separation of magnetic ions increases while their inter-chain separation decreases, which leads to reduced strength of ferromagnetic coupling along the chain. Furthermore, the super-exchange antiferromagnetic interaction path (Co2-O-Co2) for inter-chain Co2 ions in Dy substituted compound is comparatively much smaller than that for the parent $\mathrm{Ca_3Co_2O_6}$. In addition to it, the magnetic $\mathrm{Dy^{3+}}$ ions present in between the chain also provide a much shorter path (Co2-O-Dy) for the negative super-exchange interaction. The magnetization results for the series of $\mathrm{Ca_{3-x}Dy_xCo_2O_6}$ samples corroborate these findings.

It is evident from the M-T ZFC-FC results that the Dy substitution has a great influence on the magnetic properties of the system (Fig. 3.7). The magnetic ordering temperature (T_{c1}) and glassy transition temperature (T_{c2}) decreases with Dy concentration, and the glassy feature gets suppressed for x = 0.3 sample (Table 3.2). As mentioned in the literature, the glassy behavior is highly frustration related, which arises from the competitive ferromagnetic (intra-chain) and antiferromagnetic (inter-chain) coupling in the compound [28, 201, 202]. The ferromagnetic coupling originates from the overlap of d_{z^2} orbitals of intra-chain $\mathrm{Co^{3+}}$(HS) ions located at the trigonal prism site. Thus, the separation between magnetic ions along the chain has a large impact on this interaction. From the analysis of X-ray diffraction data (Table 3.1), it was found that, as we increase the Dy concentration, the c-axis gets enhanced. The enhancement of the c-axis leads to an increase in the intra-chain Co1-Co2 bond length, and as the bond-length increases (Table 3.1), it reduces the overlap in the d_{z^2} orbitals of intra-chain $\mathrm{Co^{3+}}$(HS) ions. Thus, the intra-chain ferromagnetic coupling along the c-axis gets weakened with Dy content.

In addition, the induced Co^{2+} ions due to the substitution of Dy^{3+} ions coupled antiferromagnetically with the Co^{3+}(HS) ions through a super-exchange antiferromagnetic interaction, and the strength of the interaction increases with Dy concentration [118]. As the intra-chain ferromagnetic coupling decreases and inter-chain antiferromagnetic interaction increases with Dy content, the size of magnetic clusters forming a frozen spin state gradually reduces, and hence the glassy features get suppressed. The considerable reduction in the θ for Dy doped samples also indicates the weakening of ferromagnetic character (Table 3.2). However, the positive value of θ for all the samples suggests that the ferromagnetic contribution is still dominant. Thus, we can say that the Dy-doped samples have glassy characteristics with weak ferromagnetic behavior.

We have seen clear evidence of large anisotropy in these samples by analyzing the M-H curves. At sufficiently low temperatures ($T \ll T_{c2}$), the anisotropy energy overcomes the Zeeman energy resulting in a complex hysteresis (inset Fig. 3.9). It is also noted from the Brillouin function analysis that the anisotropy effects reflect on the spin configuration of the system. Generally, for the Co^{3+} ion in trigonal prism environment, the energy orbital splits accordingly $d_{z^2} < d_{x^2-y^2} = d_{xy} < d_{xz} = d_{yz}$. Since the lower three orbitals are close to each other, the crystal field effect may alter their splitting, and there might be the possibility of modification in the ground state. In a recent report, it was found that the d_{xy} orbital occupies the lowest energy [83]. So we have concluded our Brillouin function fitting data from these results (Fig. 3.12). For the region $H < H_c$, only the lowest energy orbital (d_{xy} or d_{z^2}) is aligned, and we get the contribution $J = \frac{1}{2}$. In the region $H > H_c$, the rest of the orbitals are also aligned due to spin-flip, and we get $J = \frac{3}{2}$.

Slow decay of remanent magnetization for x = 0 and 0.1 samples (Fig. 3.13) confirms the presence of intermediate anisotropic metastable states. It is found that with a temperature above 10 K and 8 K for x = 0 and 0.1 samples, respectively, the glassy behavior gets suppressed (Fig. 3.14). The stretched exponential relaxation function (Eq. 3.6) was used to describe the time dependency of remanent magnetization. The fitted parameters n and τ strongly support the suppression of glassy feature with temperature (Table 3.3). At high temperatures, the thermal activation energy releases the energy barrier required to trap the system in intermediate metastable states [131], and the magnetization relaxes in quick time. As we decrease the temperature, the magnetization relaxes slowly due to the formation of a frozen spin-state. The significant effect of the glassy feature is seen below 5 K (Fig. 3.13).

The Vogel-Fulcher equation helps us to get meaningful results from the temperature-dependent relaxation measurements for x = 0 and 0.1 samples. The release of thermal activation energy due to the drop in T_A for x = 0.1 sample decreases the potential energy barrier required to separate the adjacent clusters, and the frozen spin state starts suppressing (Table 3.4). Activation time τ_0 in Eq. 3.7 sets a limit on relaxation time. The decrease in τ_0 for x = 0.1 sample indicates the magnetization relaxes for a shorter time as compared to the parent compound (Table 3.4). The matched value of T_0 (Table 3.4) with T_{c2} (Table 3.2) for x = 0 and 0.1 samples is an excellent agreement on the validity of this model for the cluster-glass system, and the fitted parameter strongly supports the suppression of glassy behavior with Dy substitution.

3.4 Conclusion

We have prepared polycrystalline samples of $Ca_{3-x}Dy_xCo_2O_6$ (x=0, 0.1, 0.2, and 0.3) by solid-state reaction method. The Rietveld refinement of X-ray diffraction data confirms the single-phase formation, and the compound crystallizes in the rhombohedral structure with space group $R\bar{3}c$. The DC magnetization and magnetic relaxation measurements were performed to illustrate the magnetic properties and spin dynamics of the system. M-T ZFC-FC data revealed that the system undergoes paramagnetic to an incommensurate amplitude-modulated PDA state (T_{c1}), followed by a glassy transition (T_{c2}). The magnetic properties were found to be sensitive to Dy substitution due to which the transition temperatures T_{c1} and T_{c2} decreases, and the glassy behavior gradually suppressed with Dy concentration. The higher experimental value of μ_{eff} for Dy doped samples indicates the strong anisotropic magnetic character identified from the non-equilibrium nature of magnetic properties. M-H curves depict the nature of in-field transition at H_c to be of first-order, and the spin contribution below and above the H_c were obtained from Curie–Brillouin law. Magnetic relaxation measurements confirm the presence of intermediate anisotropic metastable states due to spin-freezing phenomena.

Interestingly, the Vogel-Fulcher model provides evidence for this state to be formed from cluster of spins rather than a single spin.

Chapter 4

$Ca_3Co_{2-X}Mg_XO_6$: Spin-state transition of Co ion $\left(\boldsymbol{S} = 2 \rightarrow \boldsymbol{S} = \frac{5}{2}\right)$

Investigation of complicated magnetic structures and quantum magnetic phenomena in reduced spatial dimensions of spin interactions is an advanced field of research in magnetism. In systems with reduced dimensionality, the interplay of competing interaction, quantum fluctuation, and unusual spin give rise to various fascinating magnetic phenomena such as several quantum phases in $CoNb_2O_6$, magnetic field dependent spin density wave order in $BaCo_2V_2O_8$, and 1/3 saturation plateau in $Ca_3Co_2O_6$ [7, 15, 33]. In some low-dimensional systems, the magnetic ordering temperature is shifted to very low temperatures, and they acquire exotic in-field behavior, such as short-range glassy features and step-like transitions in magnetization [108, 210–212].

Chapter 3 clears that $Ca_3Co_2O_6$ is a magnetically rich compound, and the magnetic structure of the system can be significantly influenced by the substitution of magnetic ions so that the generality of the system is gradually suppressed. Therefore, it became essential to tune and analyze the peculiar features of this pseudo-1D system while maintaining the characteristic features of the system. However, the observed magnetization behavior of the system suggested that the magnetic dopant has a large impact on the intra-chain and inter-chain interactions, and the latter dominates over the former with the content of Dy. It releases the anisotropic energy barrier required to form the intermediate metastable states, and thus the puzzling features of the system are disappeared with the content of magnetic dopant. Other reports also suggested similar such features in the magnetic properties of the system when diluted with the magnetic ions [109, 118, 123–125, 131–133]. Therefore, it is clear that, so far, no effort has been given to prevent the 1D character of the compound with doping content. It motivated us to thoroughly understand the non-magnetic ions substitution effect in the net magnetism of the system that may have little influence on the intra-chain and inter-chain interactions. In addition, several reports are available for other compounds where substituting an appropriate non-magnetic ion in the replacement of a magnetic ion leads to frustration and exotic features in the magnetic properties [213, 214]. Considering these ideas, substituting a suitable non-magnetic ion of lower valence may open an additional degree of freedom with the possibility of spin-state transition for Co^{3+} ion to tune the magnetic structure. We have chosen Mg^{2+} ions, which are most likely to prefer magnetic Co2 site because of ionic radius matching with the possibility of creating a hole-like Fermi surface. We primarily embarked on the combined experimental and theoretical studies of this system, aimed at reduced dimensionality effects and pinning down the Fermi level by Mg substitution.

In this chapter, we discovered spin-state transition $\left(S = 2 \rightarrow S = \frac{5}{2}\right)$ of Co ions due to Mg substitution in the $Ca_3Co_2O_6$ apparent in the magnetic susceptibility, XPS, and first-principles study. We also examine the effect of Mg substitution on the magnetic and electronic structure of $Ca_3Co_2O_6$ by first-principles calculations. It involves generalized gradient approximation with Coulomb interaction (U) in exchange-correlation energy functional. Our study shows a reasonable agreement between effective magnetic moment determined from the Curie–Weiss fit with that from the XPS analysis and first-principles calculations study. The obtained results have shown unusual enhancement in magnetic moment due to non-magnetic ion substitution, which is further confirmed by DFT study. We also demonstrated that the step-like transitions, which is a characteristic feature of this one-dimensional system is very robust and is not affected with large Mg substitution. We have attributed the decrease in positive intra-chain exchange interaction constant

(J_1/k_B) to the antiferromagnetically coupled induced Co^{4+} ions $\left(S = \frac{5}{2}\right)$ arising from the Mg^{2+} ions substitution. The in-field metamagnetic transitions in the isothermal M-H curves below the critical field have been accurately mapped and successfully explained by the change in magnetic entropy (ΔS) calculations and Arrott plots. Electronic structure study reveals hole-type doping of Mg atom and the Fermi level shifts below. Density of state and band structure calculation indicates strong hybridization between partial states of Co-3d and O-2p orbitals for the Mg-doped compound, due to which the band crossing at Fermi level is observed, and a hole-type Fermi surface is formed.

4.1 Experimental Details

Bulk samples of polycrystalline $Ca_3Co_{2-x}Mg_xO_6$ (x = 0.05, 0.1, 0.15, and 0.2) were synthesized by the standard solid-state reaction method. The high purity reagents $CaCO_3$, Co_3O_4, and MgO in stoichiometric proportions were mixed using an agate mortar pestle until homogeneous mixtures were obtained. These mixtures were initially calcined at 900 °C for 24 h and then pressed in the form of cylindrical pellets. The pressed pellets were sintered at 1000 °C for 48 h.

The phase purity of these compounds was investigated using Rigaku X-ray diffractometer (TTRAX III) with a Cu-Kα ($\lambda = 1.5406$ Å) source over the scattering angle (2θ) range of 10°-80°. The chemical composition of samples was analyzed by ESCALAB Xi+ (Thermo Fisher) X-ray photoelectron spectroscopy instrument. Magnetic measurements of these compounds were carried out using vibrating sample magnetometer mode in Quantum Design made physical property measurement system. Two different protocols named zero field cooled and field cooled were followed for magnetic characterization. In the ZFC condition, the samples were cooled from 300 K to base temperature (2 K) without applying external magnetic field. After stabilizing the temperature at 2 K, the external magnetic field was switched on, and the data were taken from 2 K to 300 K in warming up cycle. In the FC condition, the samples were cooled (300 K to 2 K) under the same applied magnetic field used in ZFC measurements, and after stabilizing the temperature at 2 K, the magnetization data were taken while warming the samples from 2 K to 300 K.

4.2 Computational Details

The electronic structures of $Ca_3Co_{2-x}Mg_xO_6$ are calculated with the projector augmented wave method used within the DFT as implemented in the Vienna ab initio simulation package [161, 163, 215–217]. The Perdew-Burke-Ernzerhof function is used to account for the exchange-correlation energy in electron interaction [174]. A supercell of $Ca_3Co_2O_6$ having 66 atoms (18 Ca, 12 Co, and 36 O) is prepared for this work. Out of the twelve Co atoms, six atoms are in the low-spin state (Co1), and the other six are in the high-spin state (Co2). These calculations have been done by selecting structural parameters from Rietveld refinement of X-ray diffraction data. For the calculation of Mg-doped samples, the Co atoms were replaced from the Co2 site by Mg atoms. The exchange-correlation potential is treated by the combination of generalized gradient approximation and the method by Dudarev *et al.* [180]. The self-consistency runs were performed over a 4×4×4 Monkhorst-Pack k-point mesh in the irreducible Brillouin zone with cut-off energy of 600 eV, and it is considered to be converged when the total energy reaches the convergence accuracy of 10^{-6} eV. In order to improve the calculation precision of properties, a dense k-point grid (6×6×6) is used for electronic density of states. Tetrahedron method with Blöchl corrections was employed for performing the k-point integration [218]. The Hund's coupling parameter (J) and the strength of Coulomb interaction (U) for Co atoms were considered to be 0.0 eV and 2.0 eV, respectively. Furthermore, the electronic band structure calculation was done using high-symmetry k-points in the irreducible Brillouin zone.

4.3 Experimental Results

4.3.1 Structure

Powder XRD measurements were carried out on all the samples of $Ca_3Co_{2-x}Mg_xO_6$ (x = 0.05, 0.1, 0.15, and 0.2) at room temperature. Rietveld refinement method implemented in the FullProf Suite software was used in the analysis of XRD data. Fig. 4.1 displays the XRD patterns and the result of the Rietveld structural refinement for all the samples.

Rietveld refinement analysis reveals that the Bragg reflection obtained for these samples was indexed to the rhombohedral phase with space group $R\bar{3}c$. The refinement showed

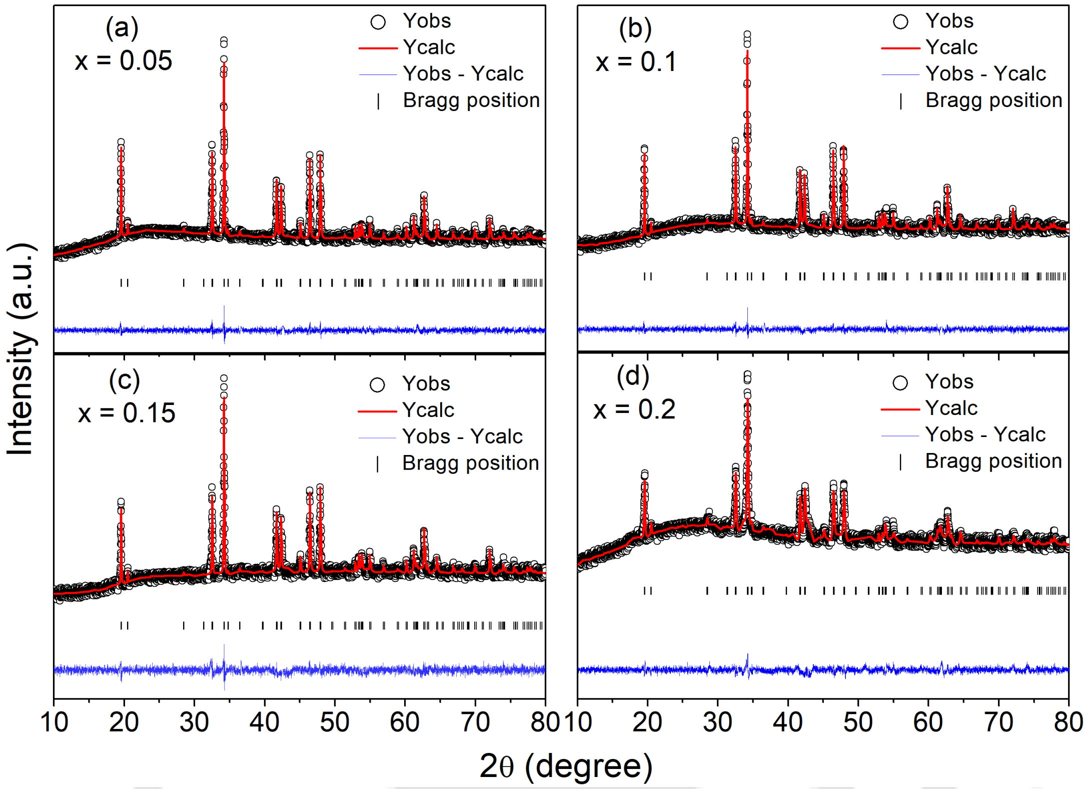

FIGURE 4.1: Rietveld refined XRD pattern of $Ca_3Co_{2-x}Mg_xO_6$ (x = 0.05, 0.1, 0.15, and 0.2) samples. The solid red and black vertical lines correspond to the calculated data and position of Bragg peaks, respectively. The solid blue line stands for the difference between observed and calculated data.

a good agreement between the observed and calculated patterns for all the samples. In the Rhombohedral setting $R\bar{3}c$, the Ca, Co1, Co2, and O were fixed at the 18e site (x, 0, 0.25), 6b site (0, 0, 0), 6a site (0, 0, 0.25), and 36f site (x, y, z), respectively. The refined site occupancies shown in Table 4.1 indicate that the Mg ions do not replace Co ions in both the sites (Co1 or Co2) but prefer to choose the spin up site (6a), and the site occupancy obtained from the refinement for all the atoms were close to the expected value. We did not observe any drastic change in the position coordinates of all the atoms with the increasing Mg concentration. Furthermore, the refinement results show only a slight decrease in lattice parameters 'a' and 'c' with the doping content of Mg. Trials have also been made to refine the XRD pattern by placing the Mg atoms on the 6b site, but the occupancy of Mg is negative, indicating the difficulty of Mg atoms to occupy the 6b site.

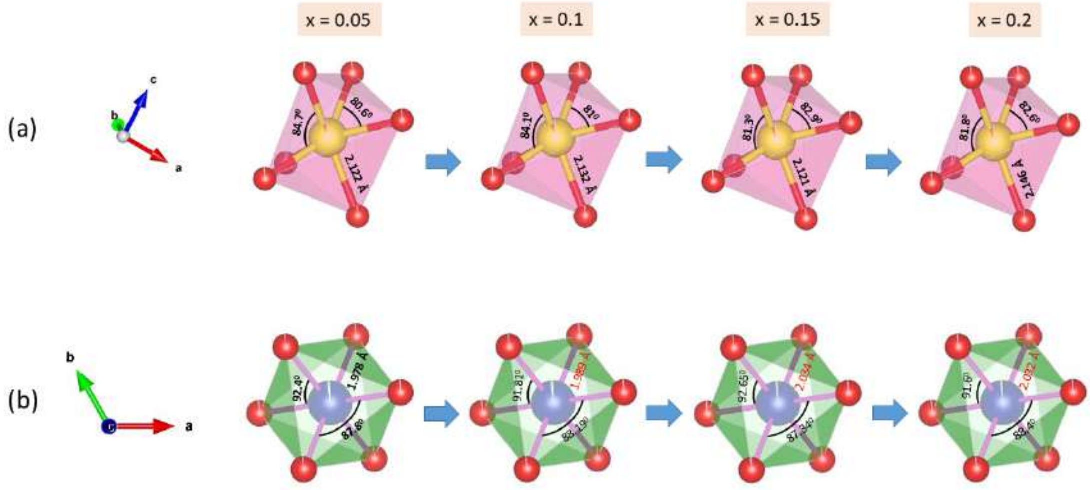

FIGURE 4.2: Polyhedral representation of CoO_6 (a) trigonal prism (b) octahedra for $Ca_3Co_{2-x}Mg_xO_6$ (x = 0.05, 0.1, 0.15, and 0.2) samples.

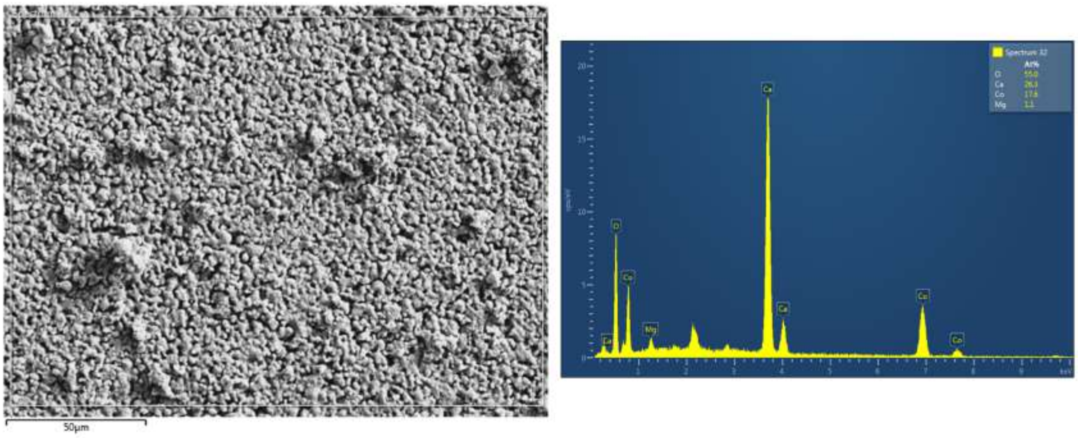

FIGURE 4.3: EDS spectra for $Ca_3Co_{1.9}Mg_{0.1}O_6$ sample.

It is evident from the Rietveld refinement results that the Mg ions successfully substituted for the lattice site of Co2 ions without altering the structure in a significant amount. So now, it became important to look at the effect of Mg substitution in the 1D character of the compound. The dimensionality in the spin-chain compound refers to the intra-chain and inter-chain separation between magnetic ions. For the 1D character to appear in the various property of the compound, the intra-chain separation between the magnetic ions should be approximately half of the inter-chain separation. In order to examine the 1D character of the compound, the structural visualization and bond distance analysis have been done using VESTA software. We have observed that the distance between the two nearest Co ions along the chain (Co1-Co2) and between the chain (Co2-Co2) are

TABLE 4.1: Atomic position, site occupancy, lattice parameters (a and c), and bond-distance (intra-chain Co1-Co2 and inter-chain Co2-Co2) for $Ca_3Co_{2-x}Mg_xO_6$ (x = 0.05, 0.1, 0.15, and 0.2) samples.

x	Atom	Site	x	y	z	Occupancy	a (Å)	c (Å)	Co1-Co2 (intra-chain) (Å)	Co2-Co2 (inter-chain) (Å)
0.05	Ca	18e	0.3700	0	0.25	0.510	9.077	10.381	2.596	5.519
	Co1	6b	0	0	0	0.165				
	Co2	6a	0	0	0.25	0.160				
	Mg	6a	0	0	0.25	0.009				
	O	36f	0.1874	0.0294	0.1141	1.020				
0.1	Ca	18e	0.3696	0	0.25	0.510	9.076	10.380	2.594	5.519
	Co1	6b	0	0	0	0.164				
	Co2	6a	0	0	0.25	0.154				
	Mg	6a	0	0	0.25	0.017				
	O	36f	0.1883	0.0277	0.1141	1.012				
0.15	Ca	18e	0.3691	0	0.25	0.508	9.075	10.381	2.595	5.518
	Co1	6b	0	0	0	0.165				
	Co2	6a	0	0	0.25	0.144				
	Mg	6a	0	0	0.25	0.025				
	O	36f	0.1899	0.0252	0.1182	1.006				
0.2	Ca	18e	0.3769	0	0.25	0.510	9.071	10.378	2.598	5.516
	Co1	6b	0	0	0	0.162				
	Co2	6a	0	0	0.25	0.141				
	Mg	6a	0	0	0.25	0.033				
	O	36f	0.2023	0.0316	0.1119	1.005				

comparable to the obtained values of these parameters for parent compound in Chapter 3 (Table 3.1). It is also found that these parameters remain independent of Mg substitution and hold the essential condition of 1D character to appear. The CoO_6 octahedral and the CoO_6 trigonal prism with associated bond lengths and bond angles are displayed in Fig. 4.2 for all the samples. It is clear from Fig. 4.2 that the incorporation of Mg ions does not alter the bond distances and bond angle for the Co1 ions at the octahedral site. However, these parameters varied slightly for the Co2 ions at the trigonal prism site but not significantly. Thus, from these results, we could expect an interplay of peculiar features of the 1D character with non-magnetic ion substitution induced disorder which may bring exotic magnetic properties in the substituted compound.

Fig. 4.3 depicts the energy dispersive spectra for the $Ca_3Co_{1.9}Mg_{0.1}O_6$ sample. It confirms the presence of Ca, Co, Mg, and O in the synthesized samples. No other traceable impurities were detected within the resolution limit of EDS. Further analysis confirmed that the obtained elemental percentages are comparable to their nominal values.

4.3.2 Temperature dependence of magnetization

In order to explore the magnetic properties of these systems, the magnetization measurement of powder samples of $Ca_3Co_{2-x}Mg_xO_6$ (x = 0.05, 0.1, 0.15, and 0.2) were performed after the ZFC and FC conditions in an applied magnetic field of 0.1 T. It reveals the important features of the complicated magnetic state of these compounds. Fig. 4.4 illustrates the temperature dependence of ZFC and FC magnetization for the studied $Ca_3Co_{2-x}Mg_xO_6$ samples. All the plots for these samples have shown similar characteristics. The magnetization increases sharply below the first transition at around 25 K, which remains independent of the doping content of Mg. Bifurcation between M-T ZFC-FC curves followed by a maximum in the ZFC curve is observed below this temperature. The cusp in the ZFC curve displayed for low temperature in all the samples is a characteristic behavior of disordered systems. On the other hand, the FC magnetization increases monotonically with decreasing temperature. For the parent compound $Ca_3Co_2O_6$, the sharp rise in the magnetization at 25 K (T_{c1}) corresponds to transition from paramagnetic to an incommensurate amplitude-modulated PDA state, and the cusp at 9 K (T_{c2}) has the place on the called spin-glass state [25, 30, 91]. The transition temperatures (T_{c1} and T_{c2}) were obtained by the procedure mentioned in Chapter 3 and marked by the arrow in Fig. 4.4. It is found that the T_{c1} and T_{c2} remain independent of the Mg ion concentration. In addition, as expected from the non-magnetic ion (Mg) substitution, the magnetization decreases.

Furthermore, we have characterized the magnetization data by plotting the inverse of dc magnetic susceptibility against the temperature for all the samples (inset Fig. 4.4). It exhibits a linear behavior above 150 K and follows the Curie-Weiss law (Eq. 3.1). In the inset of Fig. 4.4, the inverse dc susceptibility curves for all the samples were fitted to Curie-Weiss law to obtain C_{mol} and θ. The μ_{eff} was calculated from the fitted value of C_{mol} (Table 4.2) by using the relation $\mu_{\mathrm{eff}} = (3C_{\mathrm{mol}}k_B/N_A\mu_B^2)^{1/2}$, where k_B is the Boltzmann constant, N_A is the Avogadro number, and μ_B is Bohr magneton. Table

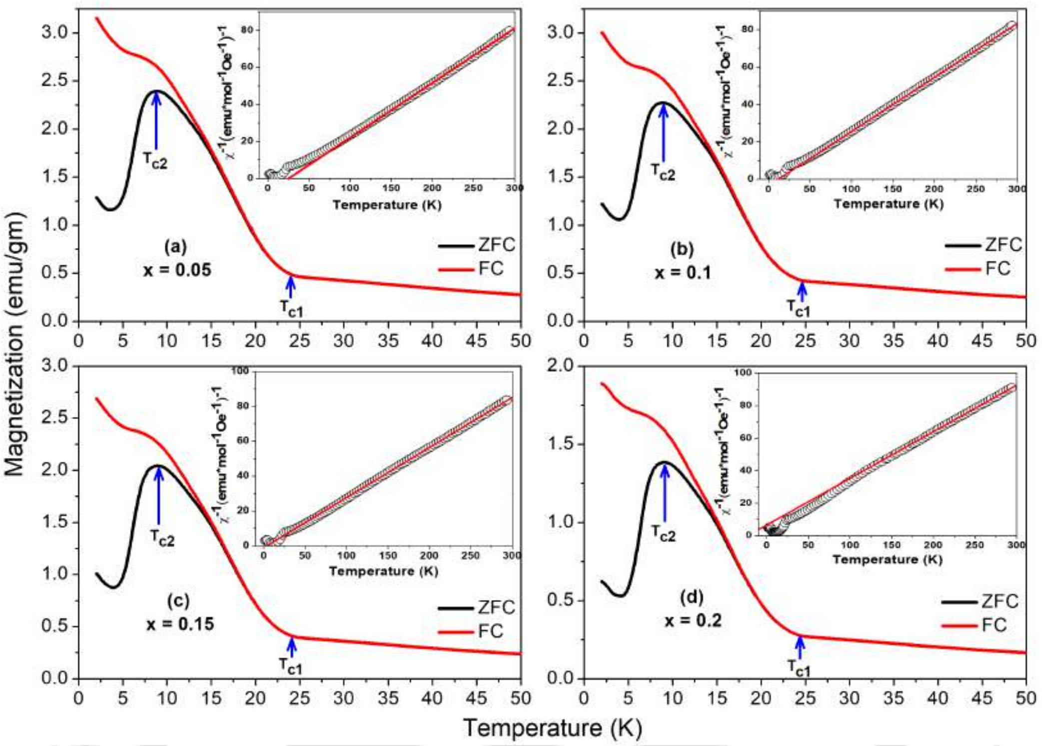

FIGURE 4.4: DC magnetization vs. temperature curves for $Ca_3Co_{2-x}Mg_xO_6$ (a) x = 0.05 (b) x = 0.1 (c) x = 0.15 (d) x = 0.2 under an applied magnetic field of 0.1 T. Inset shows the inverse susceptibility vs. temperature data fitted to the Curie-Weiss law for all the samples.

4.2 contains the obtained values of μ_{eff} and θ for all the samples. It is observed that the calculated values of μ_{eff} and θ for these samples are less than 5.6 μ_B and 31 K, respectively that for the parent compound (Table 3.2). As for the parent compound, the Co^{3+} ion in the octahedral environment is in the low spin state (S = 0), and in the trigonal prism environment, they are in the high spin state (S = 2). If the Mg^{2+} ions go to the octahedral site (S = 0) then to maintain the charge neutrality some of the Co^{3+} ion at the octahedral site (S = 0) partially transform into Co^{4+} ion $\left(S = \frac{1}{2}\right)$ or some of the Co^{3+} ion at trigonal prism site (S = 2) partially transform into Co^{4+} ion $\left(S = \frac{5}{2}\right)$, which should eventually lead to higher value of μ_{eff} for the Mg doped compound compared to parent compound; however, the experimental results are contrary to this, which clears that the Mg^{2+} ions sits at the Co2 (6*a*) site. In addition, the increased value of μ_{eff} with the doping content of Mg is unexpected. The theoretical value of μ_{eff} for these samples has been calculated by taking the μ_{eff} for the parent compound 5.6 μ_B, and it shows a decreasing trend with Mg concentration (Table 4.2). As the increase in the experimentally observed value of μ_{eff} with doping content of Mg is contrary to the theoretical prediction; therefore, we refer the increased value of μ_{eff} might be because of the induced Co^{4+} ions $\left(S = \frac{5}{2}\right)$ due to the substitution of Mg^{2+} ions for Co^{3+} ions (S = 2) to maintain the charge neutrality. The spin configuration of the system will be discussed in the next section. On the other hand, the θ decreases monotonously with Mg ion concentration and attains a negative value for x = 0.2 sample (Table 4.2). The decreased value of θ was mainly due to the combined effect of non-magnetic Mg^{2+} ion pairs and the super-exchange antiferromagnetic interaction developed by induced Co^{4+} $\left(S = \frac{5}{2}\right)$ ions along the chain.

TABLE 4.2: Molar Curie constant (C_{mol}), effective magnetic moment (μ_{eff}), Curie temperature (θ), theoretical value of μ_{eff}, exchange interaction constant (J_1/k_B), relaxation time (τ), and critical exponent (n) for $Ca_3Co_{2-x}Mg_xO_6$ (x = 0.05, 0.1, 0.15, and 0.2) samples.

x	C_{mol}	μ_{eff} (μ_B)	θ (K)	μ_{eff} (theory) (μ_B)	J_1/k_B (S = 2) (K)	J_1/k_B $\left(S = \frac{5}{2}\right)$ (K)	τ (sec)	n
0.05	3.38	5.20	25	5.45	6.84	1.54	373	0.53
0.10	3.45	5.25	12	5.31	6.15	1.08	384	0.53
0.15	3.48	5.27	4	5.16	4.35	0.75	375	0.54
0.20	3.51	5.32	-23	5.01	-2.75	-0.44	-	-

To elucidate the spin configuration of the system, we have used 1D spin-chain model for $S = 2$ and $S = \frac{5}{2}$ system. Since we are expecting the change in the spin configuration of the system $\left(S = 2 \rightarrow S = \frac{5}{2}\right)$ due to Mg ion substitution. So we have taken the parent compound $Ca_3Co_2O_6$ ($S = 2$) as our reference system and tried to analyze the susceptibility data of $Ca_3Co_{2-x}Mg_xO_6$ by using the 1D chain model for $S = 2$ and $S = \frac{5}{2}$ system. The crystal structure of $Ca_3Co_2O_6$ consists of an infinite number of chains of alternating CoO_6 octahedral and CoO_6 trigonal prisms. In this system, the intra-chain (Co2-Co2) and inter-chain (Co2-Co2) coupling are ferromagnetic and antiferromagnetic, respectively. The intra-chain interaction was expected to be stronger than inter-chain interaction because the former has shorter Co-Co bond distances (Table 4.1). Fig. 4.5 shows the χT vs. temperature plot for all the samples. The susceptibility relation for S

= 2 1D spin-chain system is given by [124]

$$\chi T = \frac{1}{3}\chi_{\parallel} T + \frac{2}{3}\chi_{\perp} T \tag{4.1}$$

where $\chi_{\parallel}$ and $\chi_{\perp}$ are the parallel and perpendicular susceptibilities, respectively given by

$$\chi_{\parallel} T = \frac{3}{4}g^2 \exp\left(\frac{8J_1}{k_B T}\right) \tag{4.2}$$

and

$$\chi_{\perp} T = \frac{3}{4}g^2. \tag{4.3}$$

Here g is the Lande factor, k_B is the Boltzmann constant, and J_1 stands for the intra-chain exchange interaction between two nearest Co2 ions. To extract the J_1 considering $Ca_3Co_{2-x}Mg_xO_6$ as $S = 2$ system, the high-temperature susceptibility data (above 50 K) were fitted to Eq. 4.1. The high-temperature χT curves exhibit asymptotic behavior, described by Eq. 4.1 (Fig. 4.5). These curves show good agreement with the theoretical model for x = 0.05, 0.1, and 0.15 samples; however, the curve gets deviated for the x = 0.2 sample (Fig. 4.5), which indicates the change in the spin configuration of the system for this sample. The best fits were obtained with the values of J_1/k_B given in Table 4.2. Positive value of J_1/k_B for x = 0.05, 0.1, and 0.15 samples suggested that the dominant intra-chain interaction is ferromagnetic, while the negative value of J_1/k_B for x = 0.2 samples indicates the coupling to be an antiferromagnetic type. These results are consistent with the negative value of θ for the x = 0.2 sample (Table 4.2).

Similar to considering the $Ca_3Co_{2-x}Mg_xO_6$ as $S = 2$ system, we have tried to fit our experimental high temperature (above 50 K) susceptibility data in the 1D chain model for $S = \frac{5}{2}$ system, assuming that the inter-chain interaction is considerably weak. The susceptibility relation for $S = \frac{5}{2}$ 1D spin-chain system is given by [219]

$$\chi = \frac{NS(S+1)}{3k_B T} g^2 \mu_B^2 \frac{1 + u(K)}{1 - u(K)} \tag{4.4}$$

where N is the total number of spins, $u(K)$=coth$K$ - $\frac{1}{K}$, and $K = \frac{2J_1 S(S+1)}{k_B T}$. It is clear from Fig. 4.5 that the reproducibility of χT data by $S = \frac{5}{2}$ model is qualitatively and quantitatively better than the $S = 2$ model in the wide temperature range. This

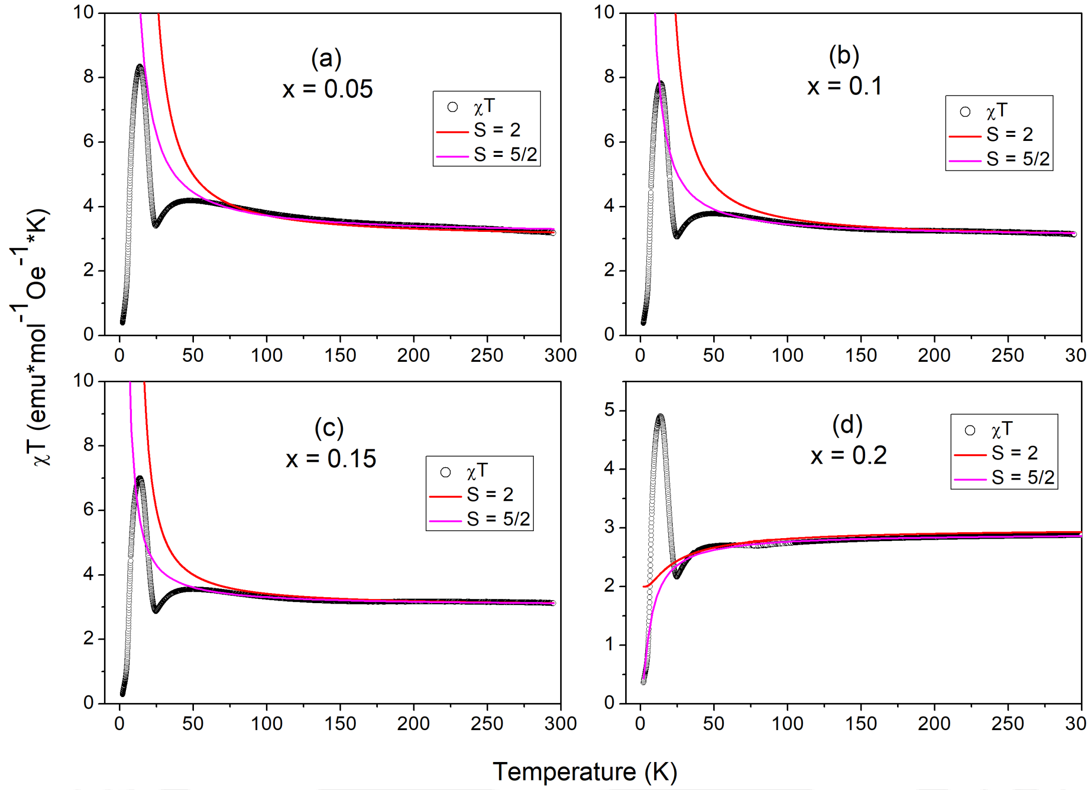

FIGURE 4.5: χT vs. temperature plot (open circle) for $Ca_3Co_{2-x}Mg_xO_6$ (a) x = 0.05 (b) x = 0.1 (c) x = 0.15 (d) x = 0.2. Solid line shows the fitted model S = 2 (red) and S = $\frac{5}{2}$ (pink).

finding revealed the evolution from the strongly 1D Ising-type anisotropic magnetism (S = 2) to 1D Heisenberg-type $\left(S=\frac{5}{2}\right)$ with Mg substitution in $Ca_3Co_2O_6$. Furthermore, a detailed investigation on this Mg substitution-induced spin-state transition has been done through XPS analysis. Table 4.2 contains the fitted value of J_1/k_B for $S=\frac{5}{2}$ model. It is observed that for $S=\frac{5}{2}$ model, the J_1/k_B value decreases from 1.54 K for x = 0.05 sample to 0.75 K for x = 0.15 sample, and attains a negative value for x = 0.2 sample. The negative value of J_1/k_B for x = 0.2 sample is also consistent with the negative value of θ for this sample (Table 4.2). In addition, the obtained values of J_1/k_B for $S=\frac{5}{2}$ model are quite different from that for $S=2$ model (Table 4.2). From the analysis of XRD data, it is found that the bond distance between intra-chain Co2 ions remains independent of Mg content (Table 4.1), so it eliminates the chances of decreased overlap of d_{z^2} orbitals of intra-chain Co2 ions. Thus, the decreased value of J_1/k_B with Mg ion concentration possibly because of the presence of Mg^{2+} ion pairs in the Co^{3+} ions chain, which reduces the intra-chain ferromagnetic coupling. Moreover, the Mg^{2+} ions substitution leads to the partial transform of Co^{3+} (S = 2) ions into Co^{4+} $\left(S=\frac{5}{2}\right)$

ions, due to which the μ_{eff} increases with the doping content of Mg, and a negative super-exchange antiferromagnetic interaction also develops between Co^{4+} ions along the chain. The strength of this interaction increases continuously with the concentration of Mg, and the negative value of J_1/k_B for x = 0.2 sample suggested that the intra-chain coupling is dominated by antiferromagnetic interaction above x ≥ 0.2.

4.3.3 Field dependence of magnetization

In order to understand the in-field behavior of these compounds, the field-dependent isothermal magnetization M-H measurements were performed on all the samples of $Ca_3Co_{2-x}Mg_xO_6$ (x = 0.05, 0.1, 0.15, and 0.2) at 2 K and 10 K, and are displayed in Fig. 4.6. The M-H curves of all the samples have similar characteristics; at temperature 10 K, the magnetization increases linearly for a small field region ($H < 1$ T) before reaching the saturation plateau. With further increasing magnetic field, a rapid jump in the magnetization is observed at around 3.6 T, indicating a field-induced magnetic transition. It is noted the magnetization doesn't get saturated for the highest applied field H = 9 T, indicating that the easy-axis of magnetization is randomly oriented with respect to the applied magnetic field. The M-H curve changes its behavior drastically at temperature T = 2 K and shows non-linear behavior having several intermediate inflection points (steps) followed by a large hysteresis in the demagnetization process. To gain further insight into the magnetization process, the $\frac{dM}{dH}$ vs. H curve at T = 2 K is included in the inset of Fig. 4.6. The inflection points are clearly visible in the $\frac{dM}{dH}$ vs. H plot for all the samples at around 1.2 T, 2.4 T, and 3.6 T, marked by H_{c2}, H_{c1}, and H_c, respectively (Fig. 4.6). This finding is in good agreement with the XRD results, and our samples acquire the striking feature in the magnetic properties of 1D materials, which is related to the quantum tunneling of magnetization [27, 196]. So far, no reports are available where the steps present in the M-H curve of the parent compound $Ca_3Co_2O_6$ are persists for doped samples. These results suggested that the Mg-doped samples have similar characteristics as the parent compound, and the Mg substitution does not alter the magnetic structure of the compound. For the parent compound, the saturation plateau at 10 K corresponds to the ferrimagnetic alignment, and the step-like

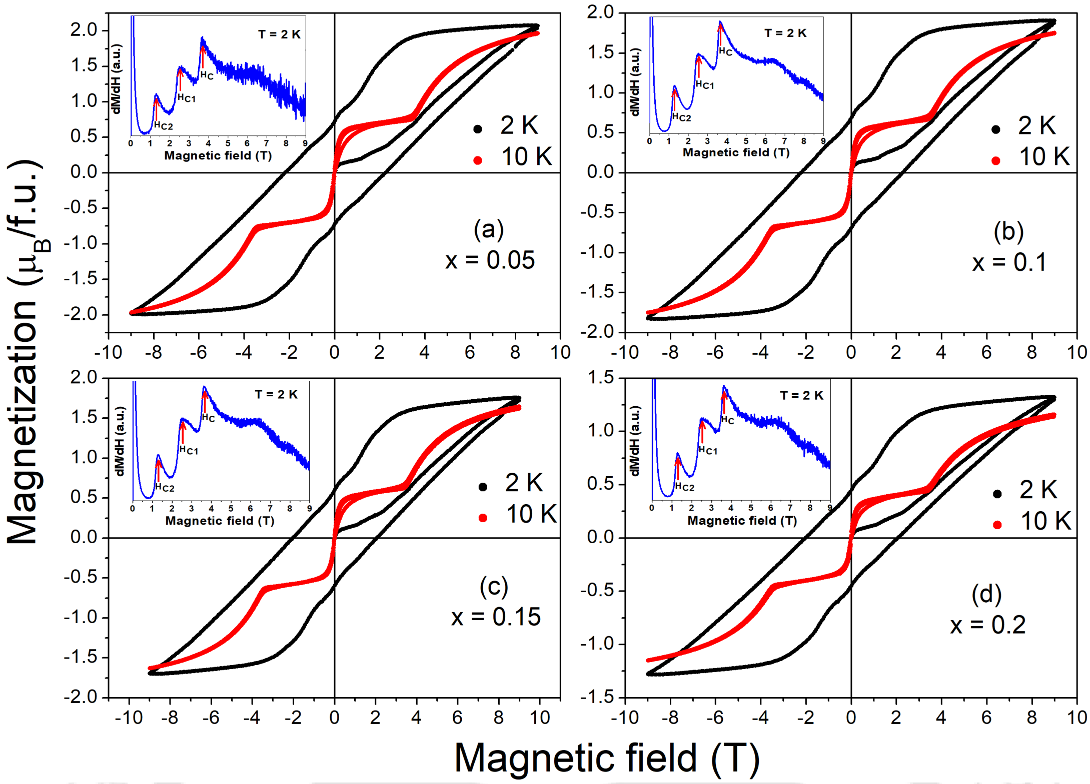

FIGURE 4.6: Isothermal M-H curves at temperature T = 2 K (black) and 10 K (red) for $Ca_3Co_{2-x}Mg_xO_6$ (x = 0.05, 0.1, 0.15, and 0.2). Inset shows the first-quadrant $\frac{dM}{dH}$ vs. H plot at T = 2K.

change at 3.6 T is a field-induced transition from ferrimagnetic state to ferromagnetic state [199–201].

To further explore the in-field behavior of the system, the magnetocaloric effect is an effective method for examining the field and temperature-dependent magnetic phase transition and is evaluated by calculating the magnetic entropy change (ΔS(T,H)) [220]. The ΔS can be extracted from the Maxwell relation $\frac{1}{\mu_0}\left(\frac{\partial S}{\partial H}\right)_{\mathrm{T}} = \left(\frac{\partial M}{\partial T}\right)_{\mathrm{H}}$ relating the change in magnetic entropy with respect to the magnetic field to change in magnetization with respect to temperature

$$\Delta S(\mathrm{T},\mathrm{H}) = \mu_0 \int_0^{\mathrm{H}} \left(\frac{\partial M}{\partial T}\right)_{\mathrm{H}} dH \tag{4.5}$$

where S, H, T, and M are entropy, magnetic field, temperature, and magnetization, respectively. For applying Eq. 4.5 and subsequently evaluating ΔS(T,H), the isothermal magnetization measurements were carried out with small steps for a range of temperatures in the vicinity of T_{c1} and T_{c2}. Fig. 4.7 displays the virgin curve for x = 0, 0.05,

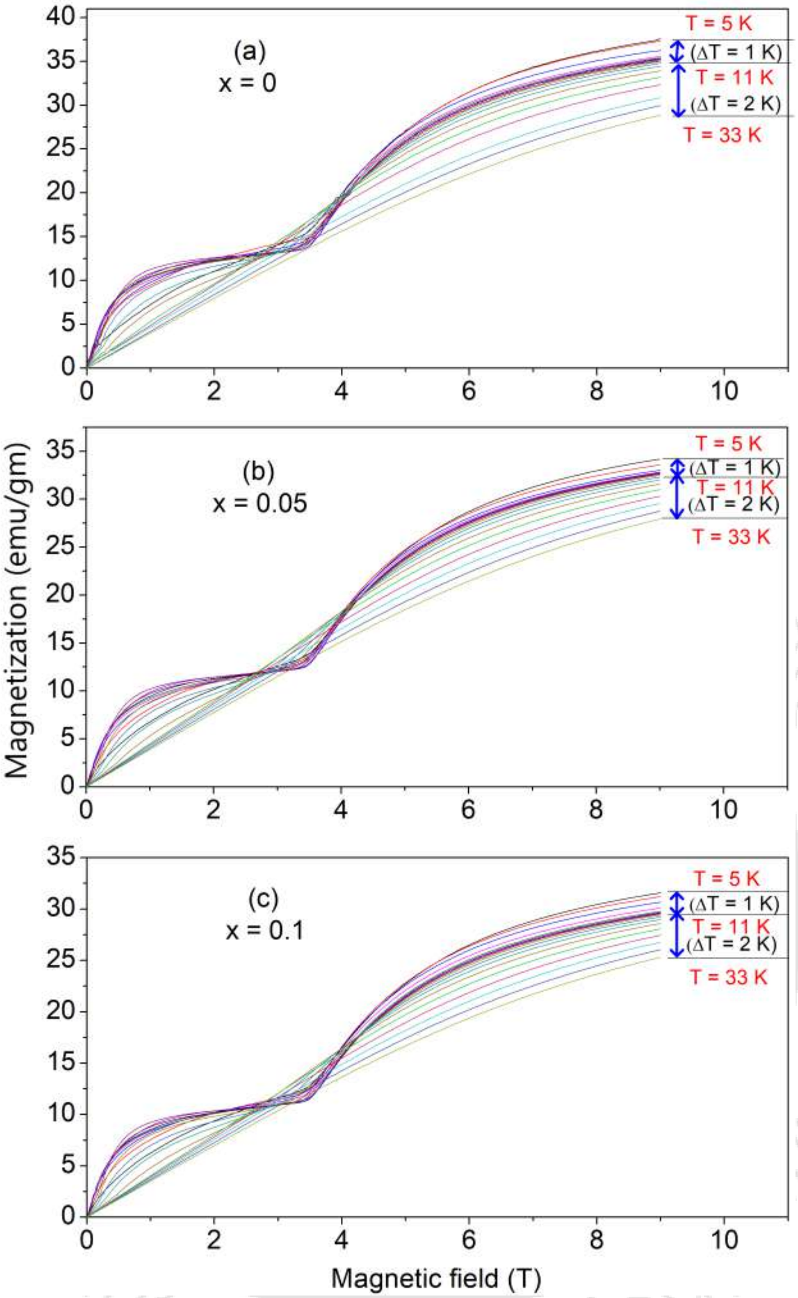

FIGURE 4.7: First-quadrant M-H curves for $Ca_3Co_{2-x}Mg_xO_6$ (x = 0, 0.05, and 0.1) samples in the temperature range T = 5 K to T = 33 K.

and 0.1 samples in the temperature range 5 K to 33 K. In the low-temperature region 5 to 11 K, the temperature step is 1 K. For the high-temperature region (11 to 33 K), the 2 K step is chosen. The aim of decreasing the temperature interval for 5 to 11 K was to better quantify the difference between the magnetization used in Eq. 4.5, as the curve changes its shape immensely in-between this region. Since to get an informative result from the ΔS calculation at higher magnetic fields ($H > 3$ T) for the parent compound, a series of isotherms were required up to temperature 100 K due to the presence

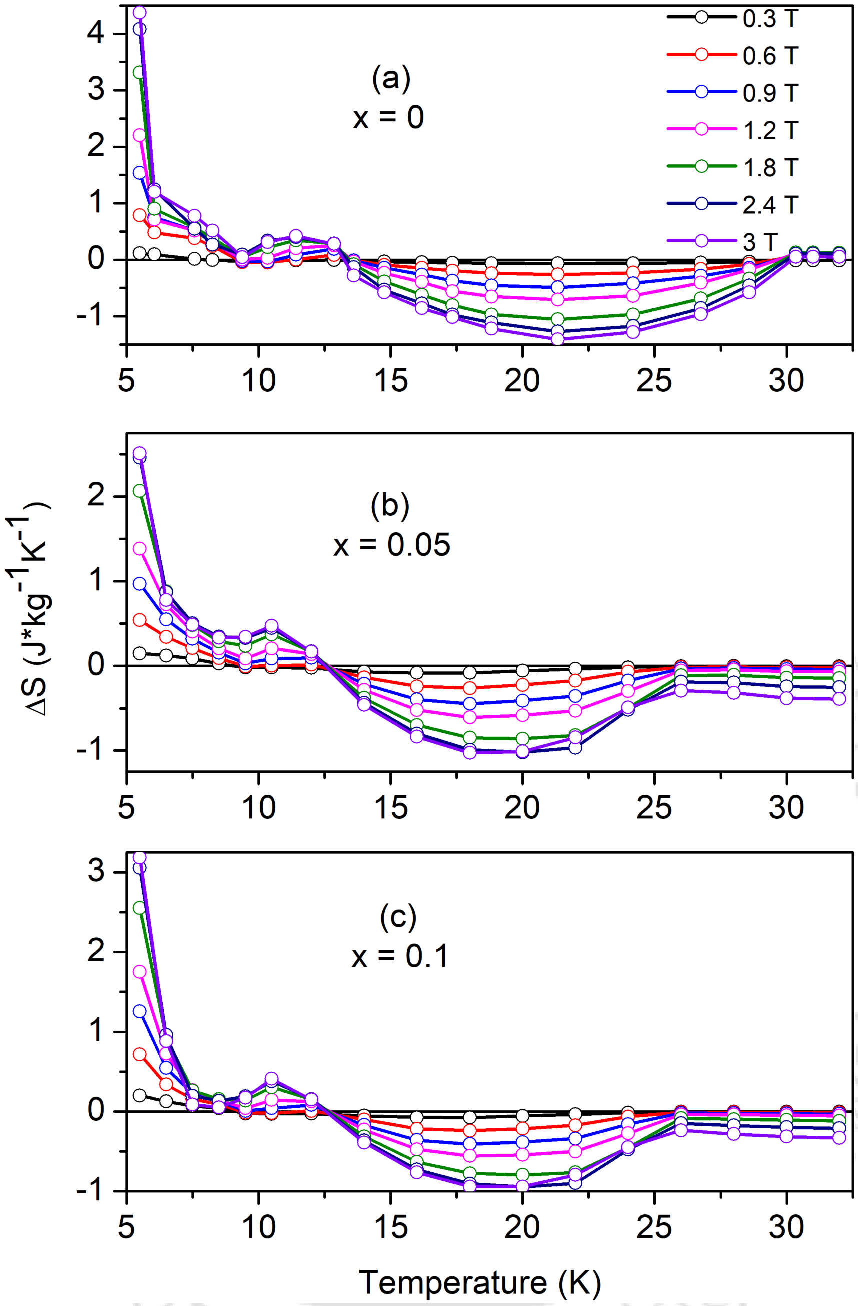

FIGURE 4.8: Change in entropy (ΔS) for $Ca_3Co_{2-x}Mg_xO_6$ (x = 0, 0.05, and 0.1) samples in the temperature range 5.5 K $\leq T \leq$ 32 K for field difference 0.3 T to 3 T.

of weak ferromagnetic correlations at high temperatures [90]. So we are restricted to do ΔS calculation up to field difference $H \leq 3$ T. Fig. 4.8 depicts the temperature dependence of ΔS for x = 0, 0.05, and 0.1 samples at different constant field difference. These curves present a characteristic shape with a minimum at $T \approx 22$ K for all the samples (Fig. 4.8), indicating an order-disorder transition. It is found that the value of ΔS for both the doped samples (x = 0.05 and 0.1) are in the same range, which is comparatively lower than the ΔS for x = 0 sample. For all the samples, the value of maximum entropy change $((\Delta S)_{\max})$ at $T \approx 22$ K increases with the magnetic field and reaches a value nearly -1.50 $Jkg^{-1}K^{-1}$, -1.00 $Jkg^{-1}K^{-1}$, and -0.95 $Jkg^{-1}K^{-1}$ for x = 0, 0.05, and 0.1 sample, respectively, for a field difference of 3 T. These values result into relative cooling power (RCP) of 19.1 J/kg, 10.7 J/kg, and 9.2 J/kg for x = 0, 0.05, and 0.1, respectively. It can be noted from Fig. 4.8 that there is a sign reversal in ΔS for temperature $T \leq 12$ K. A coexistence of the positive and negative magnetocaloric effect has been observed for the parent compound in the earlier report [90]. The temperature corresponding to the crossover from the negative to positive ΔS can be correlated with the coexistence of a short-range glassy state below T_{c2} with long-range order at zero field. The ΔS for x = 0.05 sample at T = 5.5 K is comparatively lower than the ΔS for x = 0 sample, indicating the disorder decreases with Mg substitution. Moreover, the increase in ΔS at low temperature for x = 0.1 sample is quite unusual.

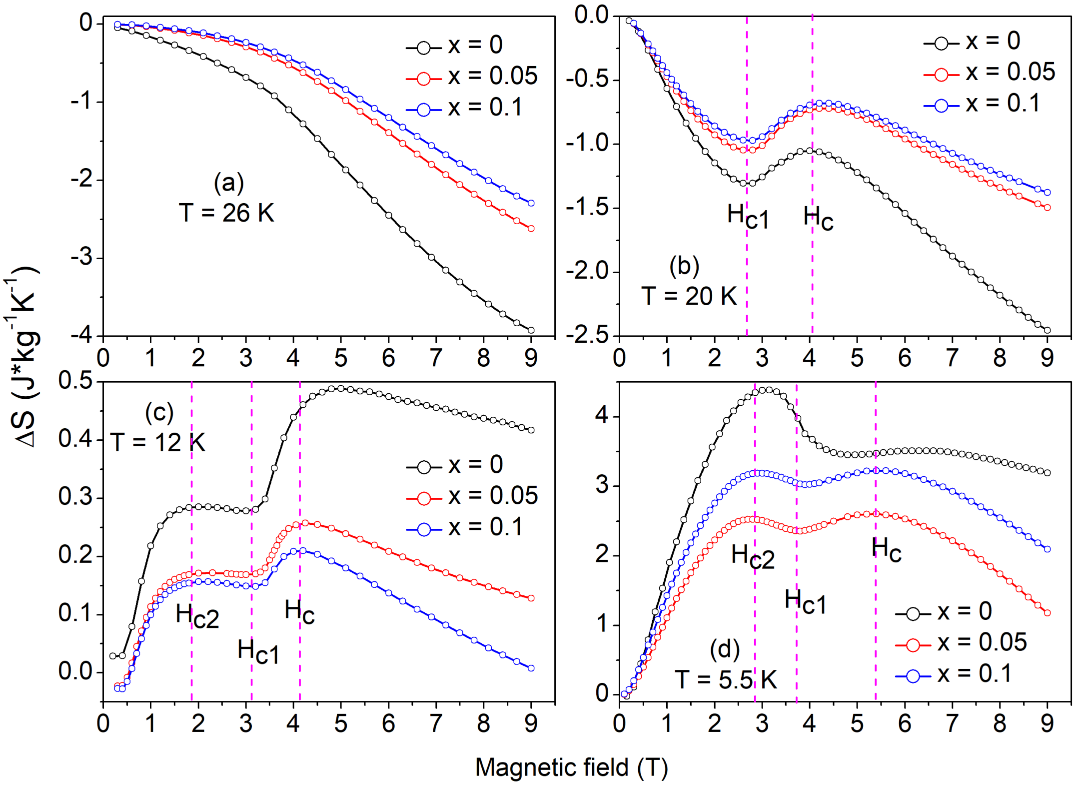

FIGURE 4.9: Change in entropy (ΔS) with magnetic field at various temperatures for $Ca_3Co_{2-x}Mg_xO_6$ (x = 0, 0.05, and 0.1) samples.

Furthermore, the ΔS calculation is also an important tool to identify the transition fields by examining its field dependence at constant temperature. Fig. 4.9 shows the field dependence of ΔS for x = 0, 0.05, and 0.1 samples at different temperatures. These curves exhibit similar features at constant temperature for all the samples except different values of ΔS and slight variation in transition fields. For the temperature region above T_{c1} (T = 26 K), the ΔS decreases monotonously (Fig. 4.9(a)) with the magnetic field for all the samples due to short-range ordering of ferromagnetic clusters present in the paramagnetic region by the application of magnetic field. As the temperature is decreased below T_{c1} (T = 20 K), the variation in ΔS with magnetic field becomes nontrivial (Fig. 4.9(b)). Upon reaching a local minimum, the ΔS begins to rise at $H \approx 2.6$ T ($H \approx H_{c1}$) and attains a maximum at $H \approx 4.2$ T ($H \approx H_c$), followed by a monotonous decrease with increasing magnetic field, characteristics of a ferromagnetic state. For the parent compound $Ca_3Co_2O_6$, the transition at H_{c1} corresponds to ferrimagnetic up-up-down ($\uparrow\uparrow\downarrow$) configuration of the spin-chains followed by a field-induced metamagnetic transition to ferromagnetic up-up-up ($\uparrow\uparrow\uparrow$) configuration above H_c [90, 199]. Thus, the increased value of ΔS in the field range $H_{c1} < H < H_c$ is attributed to the reversal of the third chain. In the low-temperature region ($T \leq 12$ K), the ΔS changes its sign from negative to positive for all the samples, and an additional entropy maximum at $H \approx H_{c2}$ emerges for $H < H_{c1}$ (Fig. 4.9(c)). These results are consistent with the three peaks obtained in the derivative plot of the 2 K M-H curve (see inset of Fig. 4.6). The entropy maximum at H_{c2} persists for the lowest measured temperature T = 5.5 K (Fig. 4.9(d)), and its value increases from 0.28 $Jkg^{-1}K^{-1}$ at 12 K to 4.45 $Jkg^{-1}K^{-1}$ at 5.5 K for x = 0 sample, pointing to the growing disorder due to the formation of the short-range glassy state. As the magnetic properties of the parent compound have shown the presence of a large number of intermediate anisotropic metastable states at low temperature, the maximum at H_{c2} may correspond to the transition from one of them to another. It is observed that the transition field H_{c1}, H_{c2}, and H_c shifted to the right side with lowering the temperature (T = 12 K to 5.5 K) (Figs. 4.9(c) and (d)). The increase in the H_{c1} and H_{c2} with decreasing temperature is consistent with the reported study of ΔS for the parent compound [90]. In addition, the ΔS maximum present at $H \approx H_c$ for T = 5.5 K (Fig. 4.9(d)) is absent in the earlier study of the parent compound at T = 5 K [90]. Thus, we are able to identify all three transitions from the magnetocaloric measurements in our samples. For the doped samples, the ΔS vs. magnetic field curves follows similar

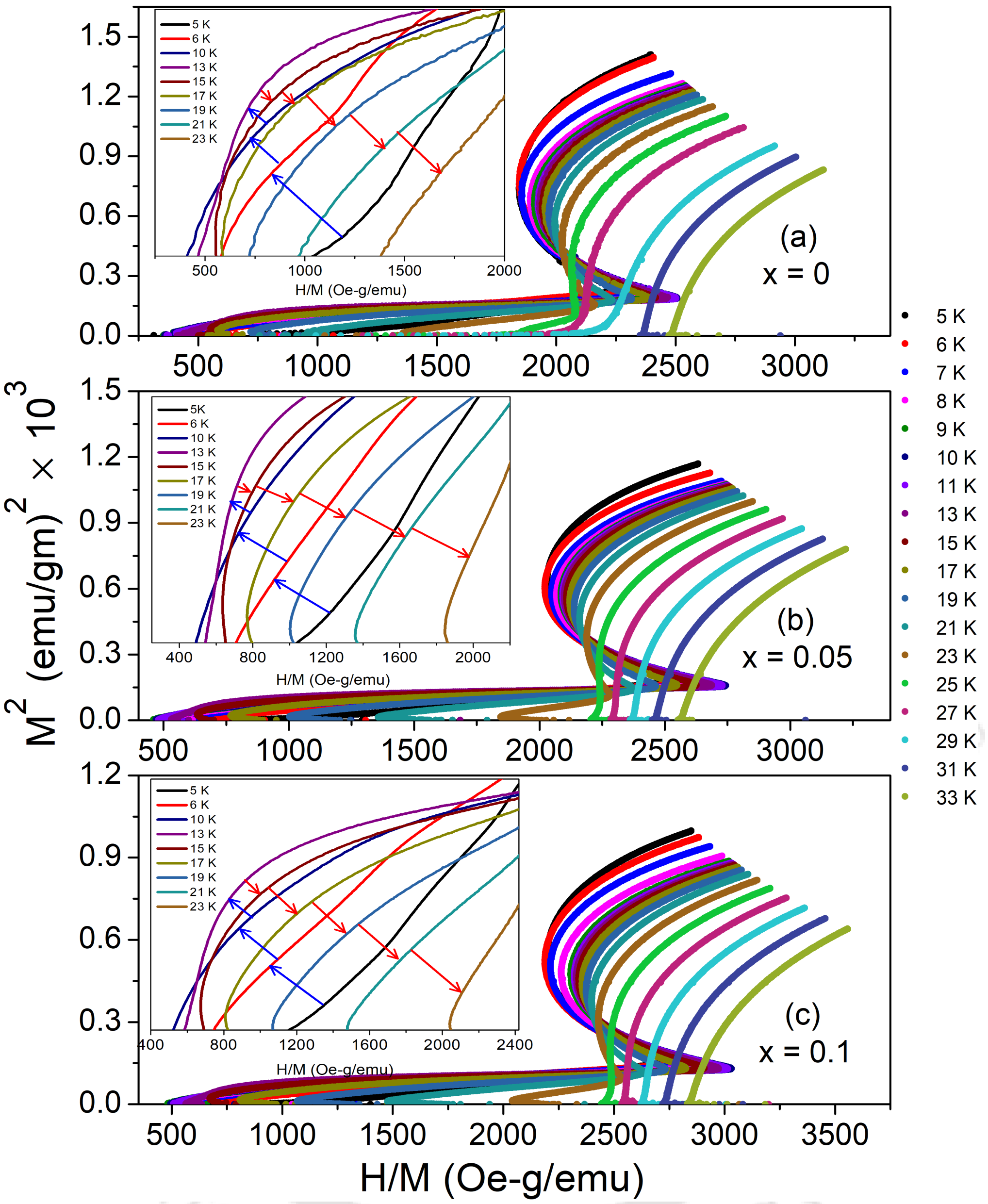

FIGURE 4.10: Arrott plots for $Ca_3Co_{2-x}Mg_xO_6$ (x = 0, 0.05, and 0.1) samples over a range of temperature 5 K $\leq T \leq$ 33 K. Inset shows the enlarged view of Arrott plot for some specific temperatures.

trend (Fig. 4.9). However, the decrease in ΔS for doped samples indicates the glassy feature reduces with Mg substitution.

In addition to the magnetocaloric effect, Arrott plots (M^2 vs. H/M) are also an important tool to examine the in-field behavior of the system, which are physically more transparent. Fig. 4.10 displayed the Arrott plots for x = 0, 0.05, and 0.1 samples. Above

T_{c1}, instead of being straight, these plots show some curvature which indicates the presence of weak ferromagnetic contribution in the paramagnetic region. In the temperature range 5 K $\leq T \leq$ 13 K, the plots are displaced to the left, while for 13 K $\leq T \leq T_{c1}$, plots start shifting to the right with temperature (inset Fig. 4.10). This anomalous behavior below T_{c1} is observed for low fields only, while for higher fields, these plots show concave curvature and shift continuously towards the right with increasing temperature (Fig. 4.10). These features can be related to the presence of strong coupling between ferrimagnetic ($\uparrow\uparrow\downarrow$) configuration among chains and intra-chain ferromagnetic interaction at low fields [90, 199]. As a result of this, the ferrimagnetic configuration renormalizes the ferromagnetic contribution in such a way that the ferromagnetic moment with field is reduced in comparison to the case when there is no ferrimagnetic order. In the low field region, the ferrimagnetic configuration among chains dominates, while for the high fields, the system switches from the predominantly ferrimagnetic configuration to the ferromagnetic configuration.

4.3.4 Magnetic dynamics

As the prominent magnetic features of the $Ca_3Co_2O_6$ system remain unaffected with the Mg substitution, while the magnetocaloric measurements suggested that the low-temperature disorder decreases with Mg content. So now it has become essential to look at the dynamic behavior of these samples at low temperatures, which is disorder-related. The dynamics of these samples have been studied through ZFC magnetic relaxation measurements. In this process, the samples were cooled in the absence of magnetic field (300 to 3 K). After stabilizing the temperature at 3 K, these samples were magnetized under an external field of 9 T for 60 sec. Then the external magnetic field was switched off, and the decay in the remanent magnetization was recorded for 3600 sec. Fig. 4.11 shows the drop in the remanent magnetization with time for x = 0.05, 0.1, and 0.15 samples. Unlike the parent compound, it was observed that the magnetization relaxes quickly for the Mg-doped samples. It indicates the release of the magnetic anisotropic energy barriers with Mg substitution. In order to get a detailed understanding of this, we have fitted the relaxation data in stretched exponential relaxation function (Eq. 3.6). The solid line in Fig. 4.11 shows the fitting of experimental data in Eq. 3.6, and the

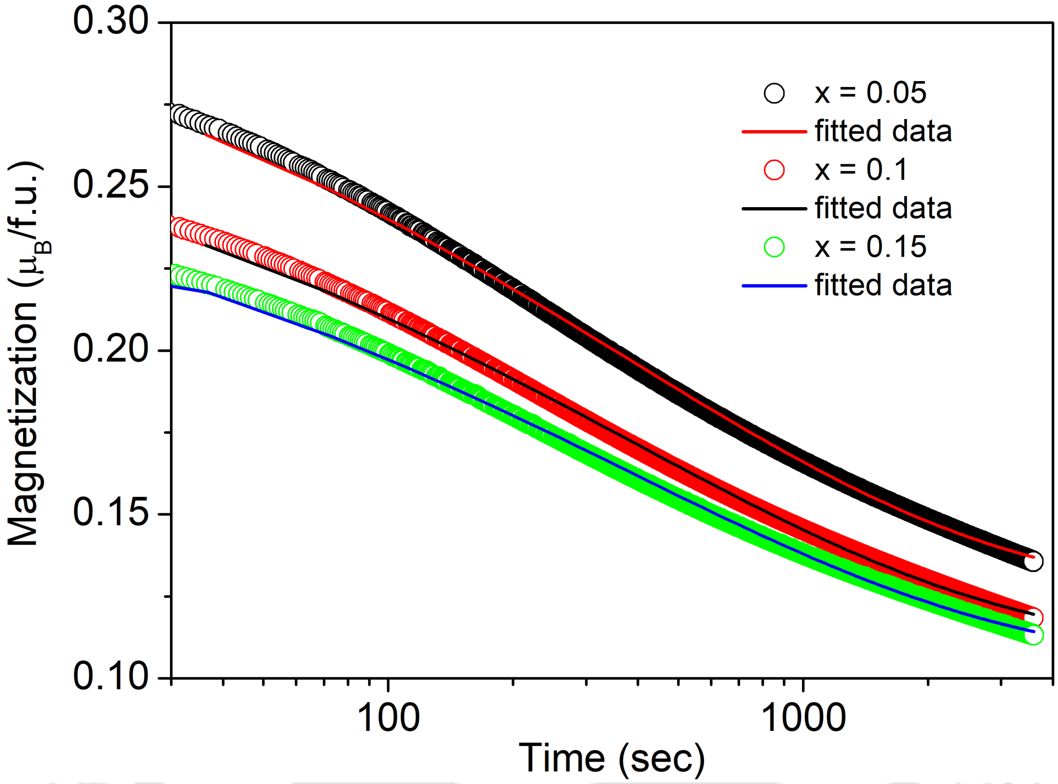

FIGURE 4.11: Drop in the remanent magnetization with time (open circle) at temperature T = 3 K for $Ca_3Co_{2-x}Mg_xO_6$ (x = 0.05, 0.1, and 0.15). Solid line shows the fitted data in Eq. 3.6.

obtained parameters τ and n are given in Table 4.2. It is found that the relaxation time for these samples is much smaller than for the parent compound (1366 sec), which indicates the reduced glassy feature with Mg substitution.

4.3.5 XPS analysis

As from the earlier susceptibility data analysis, we have expected an intermediate spin-state transition from Co^{3+} (S = 2) to Co^{4+} $\left(S=\frac{5}{2}\right)$ and a significant enhancement in the μ_{eff} due to Mg substitution. Thus, the relative percentage of Co^{3+} and Co^{4+} ions present in the system plays an important role in controlling its magnetic behavior. So in order to understand the role of different spins as well as valence states of Co ions in defining the magnetic properties of the system, we have measured core-levels of Co $2p$ for $Ca_3Co_{2-x}Mg_xO_6$ using X-ray photoelectron spectroscopy. Fig. 4.12 shows the Co $2p$ core-level spectra, consisting of broad peaks, which may arise due to spin-orbit coupling between $3d$ electron and $2p$ core of Co ions. The asymmetry of the peaks reveals the

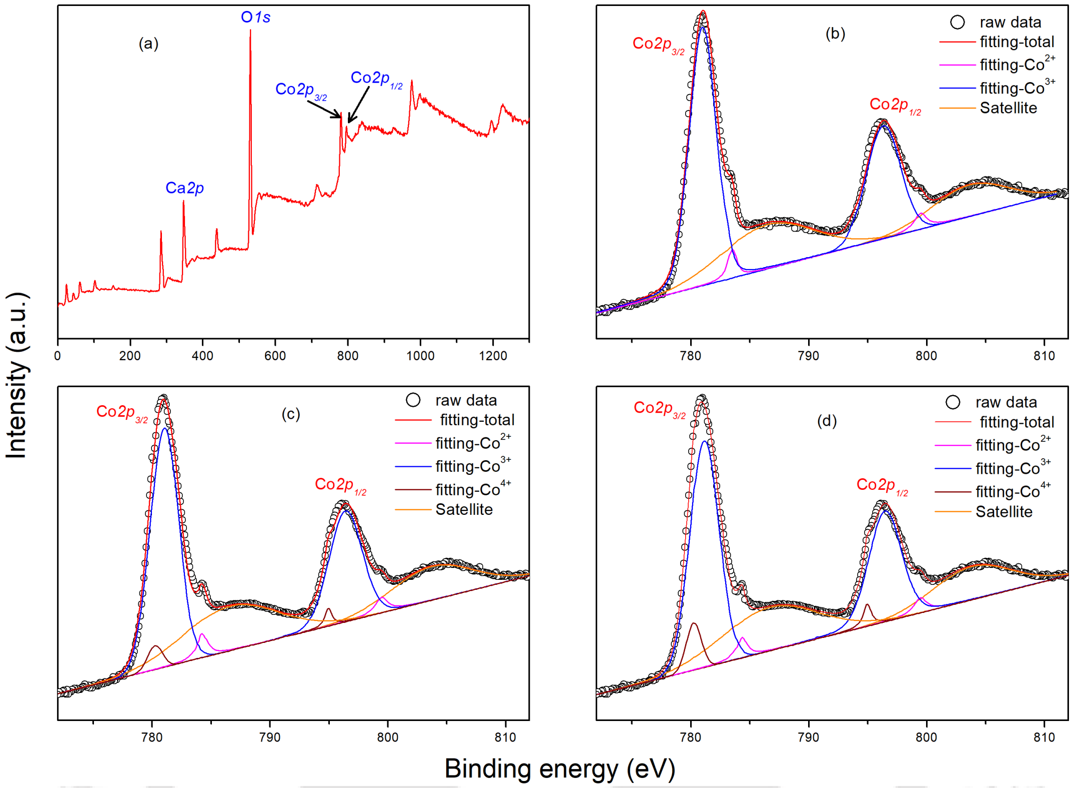

FIGURE 4.12: XPS results for $Ca_3Co_{2-x}Mg_xO_6$ (x = 0.0, 0.1, and 0.2) (a) survey spectra for $Ca_3Co_2O_6$ which shows the presence of Ca, Co, and O atoms. Deconvoluted results of Co $2p_{1/2}$ and Co $2p_{3/2}$ for samples with (b) x = 0, (c) x = 0.1, and (d) x = 0.2.

existence of mixed valences of the Co ion. For the parent compound, the spin-orbit of Co $2p$ peaks was deconvoluted into four peaks of $2p_{1/2}$ and $2p_{3/2}$, as well as two weak satellite peaks (Fig. 4.12 (b)). The peaks of $2p_{1/2}$ and $2p_{3/2}$ at 795.82 and 780.63 eV, respectively, is attributed to the existence of Co^{3+} ($S = 2$) ion, while the peaks of $2p_{1/2}$ and $2p_{3/2}$ at 797.93 and 782.26 eV, respectively, is attributed to the existence of Co^{2+} $\left(S = \frac{3}{2}\right)$ ion. Generally, the Co ions in both Co1 and Co2 sites are in the trivalent state; the presence of a small amount of Co^{2+} ion is due to the oxygen non-stoichiometry in the sample [206]. Unlike the parent compound, an additional valence state of Co ion (4+) has appeared for Mg substituted compound (Fig. 4.12 (c) and (d)), which governs the related magnetic properties. Notably, the substitution of Mg^{2+} ions causes the transfer of Co^{3+} ions ($S = 2$) into Co^{4+} ions $\left(S = \frac{5}{2}\right)$, due to which some of the Co ions prefer to stabilize in 4+ state along with the dominating 3+ state. From Fig. 4.12, the area under deconvoluted fitting curves of Co^{4+} and Co^{3+} indicates that the percentage of Co^{4+} ions increases with an increase in Mg concentration. To calculate the percentage Co ions in

TABLE 4.3: Percentage of Co^{2+}, Co^{3+}, and Co^{4+} ions in $Ca_3Co_{2-x}Mg_xO_6$ (x = 0, 0.1, and 0.2) samples calculated by taking area under Co $2p_{1/2}$ and $2p_{3/2}$ peaks.

x	Co^{2+} (%)	Co^{3+} (%)	Co^{4+} (%)
0	5.1	94.9	-
0.1	4.9	90.4	4.7
0.2	4.7	86.4	8.9

3+ and 4+ valence states, the area under each peak is taken, and the calculated content of Co^{2+}, Co^{3+}, and Co^{4+} ions is given in Table 4.3. The calculated μ_{eff} by considering relative percentage of Co^{3+} and Co^{4+} ions from XPS analysis for the x = 0.2 compound is 5.29 μ_B, which matches with the magnetization data (Table 4.2). Further, it shows a decreasing trend with increasing Mg concentration which corroborates the trend of μ_{eff} from the magnetization measurements.

4.4 Density Functional Theory Calculations

Having understood the role of Mg substitution in bringing unusual magnetism in $Ca_3Co_2O_6$ through experimental measurements, it became pertinent to investigate it from theoretical point of view. DFT is the most successful and extensively studied tool to insight into the structural, magnetic, and electronic properties in order to have a better understanding of the system from different perspectives. The first step towards that will be benchmark structural properties derived from DFT calculations against structural parameters derived from the analysis of XRD data by Rietveld refinement. It is well known that the transition metal oxide usually has strong Coulomb correlation; hence we introduced the Coulomb correlation effects through GGA+U method [180]. In order to select the appropriate U, the lattice parameter a and c were calculated with different U values between 0.0 to 4.0 eV. It is found that for U = 2.0 eV, the calculated values of a and c are most appropriate with the experimental findings. So for the entire DFT-based calculations, we have fixed the value of U to 2.0 eV.

TABLE 4.4: Calculated magnetic moments at each Ca, Co1, Co2, Mg, and O ion in $Ca_3Co_{2-x}Mg_xO_6$ (x = 0.0 and 0.167) samples.

x	Ca (μ_B)	Co1 (μ_B)	Co2 (μ_B)	Mg (μ_B)	O (μ_B)
0	0.02	0.06	2.90	-	0.14
0.167	0.01	0.04	2.96	0.0	0.13

In the next step, we calculated the magnetic moments at each site for both $Ca_3Co_2O_6$ and $Ca_3Co_{1.833}Mg_{0.167}O_6$ samples (Table 4.4). For the pristine $Ca_3Co_2O_6$, the calculated magnetic moments, 0.06 μ_B at Co1 site, 2.90 μ_B at Co2 site, and a rather large moment of 0.14 μ_B at the O site, are similar to the earlier report [18]. However, for the Mg substituted compound, we observed staggered magnetic moments for all the atoms. The average of the staggered magnetic moments are 0.04 μ_B, 2.96 μ_B, and 0.13 μ_B for Co1, Co2, and O site, respectively. For both samples, the magnetic moment of nearly 0.13 μ_B at O site is possibly a result of the hybridization between Co ($3d$) states with the O ($2p$) states, which can additionally enable the hybridization-mechanism-driven magnetism in these systems. Interestingly, the increase in the average magnetic moment on the Co2 sites from 2.90 μ_B for x = 0 sample to 2.96 μ_B for x = 0.167 sample, improving the agreement with the experimental results. It implies that the substitution of non-magnetic ion Mg in the replacement of magnetic ion Co can enhance the magnetic moment at the Co2 site and directly connected to the magnetism-related phenomena. However, in order to have a better understanding of such phenomena and interpretations with the experimental results, systematic study of the system is required at the microscopic level. Such understanding can be achieved if these systems are studied at microscopic level, that is, from electronic structure calculations. These calculations provide important insight into the hybridization mechanism, crystal field splitting, and in-site interactions and their effect on magnetic properties by total density of state (DOS), band structure, and Fermi surface analysis.

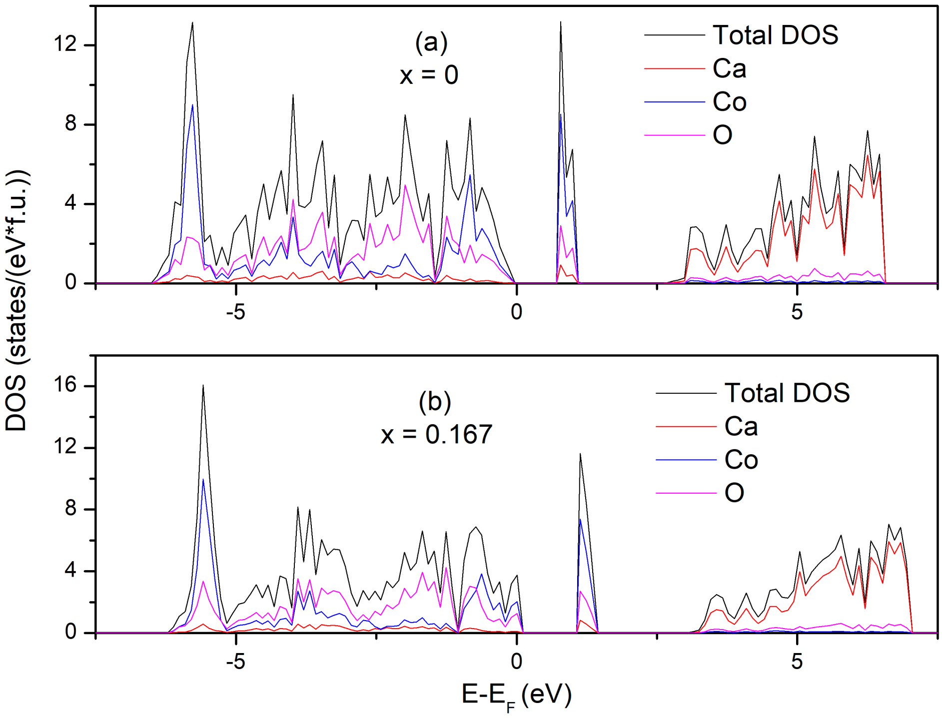

FIGURE 4.13: Total and site projected density of states for $Ca_3Co_{2-x}Mg_xO_6$ (x = 0 and 0.167). The total DOS is shown as black solid line, and the site projected DOS for Ca, Co, and O are indicated by solid red, blue, and magenta lines, respectively.

4.4.1 Electronic structure study

In the beginning, we attempt to understand the hybridization-mechanism and in-site interaction in these systems through density of state calculations. The total density of states per formula unit for $Ca_3Co_2O_6$ and $Ca_3Co_{1.833}Mg_{0.167}O_6$ samples has been calculated using GGA+U method (U = 2.0 eV). Fig. 4.13 shows the total electronic density of states along with the atom projected DOS in the energy interval -7.5 eV to +7.5 eV, where the Fermi energy (E_F) set at zero. The E_F for the parent compound is 5.6 eV, and as we move to Mg-doped compound, the E_F shifts to 5.0 eV. It is consistent with the fact that the Mg substitution creates holes in valence band, due to which Fermi level shifts below. In the DOS calculations for both systems, we observed band gap (ΔE) of nearly 1.0 eV, and the plot shows significant contribution from Ca atom above E_F (Fig. 4.13). However, for the Mg substituted compound, the Mg ion has no contribution to the electronic DOS. Apart from these results, the calculated density of state at E_F is not the same for both compounds. For the parent compound, the DOS at Fermi level is zero, whereas a non-zero value (3 states/(eV*f.u.)) is obtained for Mg-doped system.

It suggests that the overall profile of DOS for both the compounds are same; however, the substitution of Mg shifts the Fermi level below. Thus from these results, we could expect a similar band profiles for both the compound, whereas the number of bands crossing the Fermi level will not be the same. From Fig. 4.13, it is evident that the major contribution to DOS near the Fermi level (-1.2 eV to E_F) is dominated by Co-3d and O-2p states, and it is remarkable to note that the O atom contribution is nearly half that of Co atom contribution in the occupied state. Thus, these results show strong hybridization between Co-3d and O-2p orbital electrons in this energy range, which may lead to different crystal field splitting effects of 3d-orbitals and thus influences the electron occupancy. As the hybridization between Co-3d and O-2p orbital electrons is an important consequence of Co-O bond-length and bond-angle. Therefore, the structural changes in $Ca_3Co_2O_6$ due to Mg substitution can influence its electronic properties also. In the structural investigation, we observed that for CoO_6 trigonal prism environment, the Co-O bond-length is minimum for x = 0.15 sample (Fig. 4.2). Thus, the Co-O bond in Mg-doped compound is much stronger as compared with Co-O bond in $Ca_3Co_2O_6$. Consequently, the partial states of Co-3d and O-2p hybridize strongly for Mg-doped compound and cross the Fermi level in the electronic DOS.

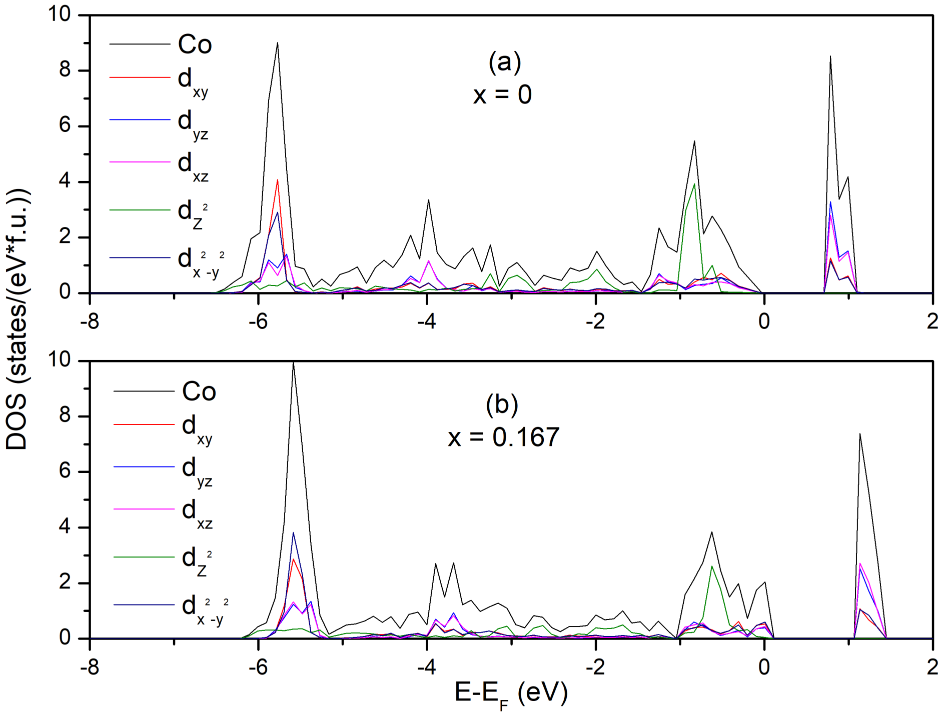

FIGURE 4.14: The contribution of d_{z^2}, $d_{x^2-y^2}$, d_{xy}, d_{xz}, and d_{yz} orbitals in the density of states for Co2 atom in $Ca_3Co_{2-x}Mg_xO_6$ (x = 0 and 0.167).

In order to lend insight into the spin structure and related magnetic properties of the systems discussed in the previous sections, the orbital-projected DOS for the Co-3d levels have been calculated. Fig. 4.14 shows the orbital-projected DOS for the Co-3d levels of $\mathrm{Ca_3Co_2O_6}$ and $\mathrm{Ca_3Co_{1.833}Mg_{0.167}O_6}$. It is observed that near the E_F, there is mixing of d_{z^2}, $d_{\mathrm{x}^2-\mathrm{y}^2}$, d_{xy}, d_{xz}, and d_{yz} spin-orbitals. Therefore, it would have an important consequence on the spin structure of the system, which is investigated in the previous chapter (Chapter 3). Generally, in the Co^{3+} ion trigonal prism environment, the energy orbital splits accordingly $d_{\mathrm{z}^2} < d_{\mathrm{x}^2-\mathrm{y}^2} = d_{\mathrm{xy}} < d_{\mathrm{xz}} = d_{\mathrm{yz}}$. In our calculation, we observed that the orbital projected DOS plot for $d_{\mathrm{x}^2-\mathrm{y}^2}$ orbit nearly overlaps with d_{xy} orbit plot. Similar to this, both the d_{xz} and d_{yz} orbitals contribute equally to the DOS. These results are consistent with the d-orbital splitting of Co^{3+} ion in trigonal prism environment. Our calculation also suggested that in this system, the $d_{\mathrm{x}^2-\mathrm{y}^2}$ and d_{xy} orbitals are very close to degenerate with d_{xz} and d_{yz} orbitals. We propose that the crystal field effect might be the origin of this splitting, and since the orbitals are close to degenerate in energy, which leads to the very large orbital contribution to the moment in these systems, as suggested from Chapter 3. Similar to this, the X-ray magnetic circular dichroism study shows a large orbital moment (1.7 μ_B) at Co2 site [221]. One of the surprising results from these calculations is the less contribution of d_{z^2} orbital in the DOS, and it appears only below the E_F. Thus, in addition to the experimental data, these results suggest an itinerant mechanism for the magnetic order in the form of strongly correlated electron systems.

To gain more insight into the physics of such complicated systems, we have calculated the band structure for both systems. The calculated band structure for $\mathrm{Ca_3Co_2O_6}$ and $\mathrm{Ca_3Co_{1.833}Mg_{0.167}O_6}$ compounds along the high symmetry k-points in the irreducible Brillouin zone are displayed in Fig. 4.15. For both the compound, the Fermi level is set at zero, which is represented by the solid black line. As predicted from DOS analysis, the top of valence band and the bottom of the conduction band (here the valence band and conduction band refers to the band below and above the Fermi level, respectively) are mainly originated from the strong hybridization between Co-3d and O-2p states, due to which the energy bands demonstrate dispersive character in the entire region of first Brillouin zone. Apart from this, there are multiple degenerate bands at high symmetry

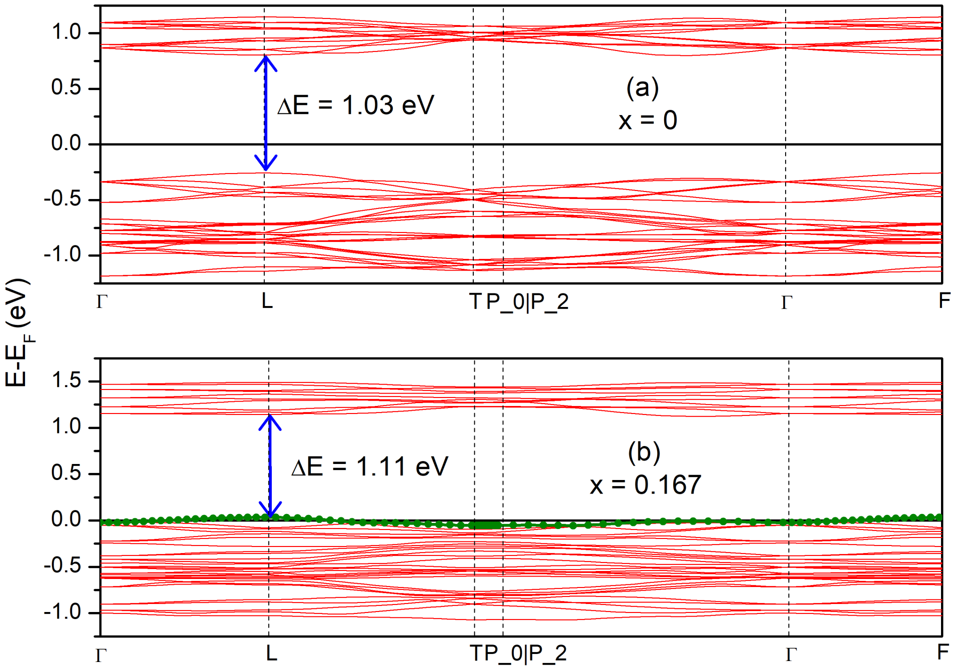

FIGURE 4.15: Calculated electronic band structure of $Ca_3Co_{2-x}Mg_xO_6$ (x = 0 and 0.167) along high-symmetry k-points. Zero energy indicated by the horizontal line refers to the position of the Fermi level. The olive dots correspond to the band crossing the E_F.

points. A direct band gap of nearly 1.0 eV is observed at the L point, and a second conduction band minimum occurs between the P_2 and Γ high-symmetry lines. For the parent compound, no energy band crosses the E_F (Fig. 4.15(a)), whereas, for the Mg-doped compound, one band crossing represented by olive dots in Fig. 4.15(b) is observed at E_F. The band across the Fermi level is from valence band to conduction band, indicating the hole nature, creating hole pockets at the Γ-point and electron pockets at the L point. This band shows dispersive nature along the Γ-L and Γ-F directions; however, it is almost flat for the T, P_0, and P_2 high symmetry points. Interestingly this band has multiple band crossing along with Γ-L, L-T, and Γ-F directions leading to complex nature of Fermi surface.

4.4.2 Fermi surface

The behavior of the compound at the Fermi level can be well understood by visualizing the Fermi surface and its shape. For being an insulator/semiconductor, we could not calculate the Fermi surface of $Ca_3Co_2O_6$. On the other hand, the Fermi surface at ambient conditions corresponding to the single energy band that crosses E_F for the

Mg-doped compound is shown in Figs. 4.16(a) and (b), where the empty region contains the holes and the shaded region for electrons. Generally, the shape of the Fermi surface is derived from the occupation of electronic energy bands, and the change in the color of Fermi surface is related to the electron velocity. The red and blue colors show fast and slow velocity of electrons, respectively, while the remaining colors show the intermediate velocity of electrons. It is clear that the first-principles study predicts a highly complex Fermi surface for $Ca_3Co_{1.833}Mg_{0.167}O_6$. The Fermi surface for $Ca_3Co_{1.833}Mg_{0.167}O_6$ in the first Brillouin zone is composed of six merged lobes, and these lobes are symmetrically away from the k_z-axis (Figs. 4.16(a) and (b)), which indicates the similar behavior of electrons about this direction. Out of these six lobes, four are connected, and two are opened at the surface of the first Brillouin zone. In the first-principles band structure calculation for $Ca_3Co_{1.833}Mg_{0.167}O_6$ along the high symmetry directions, we find that

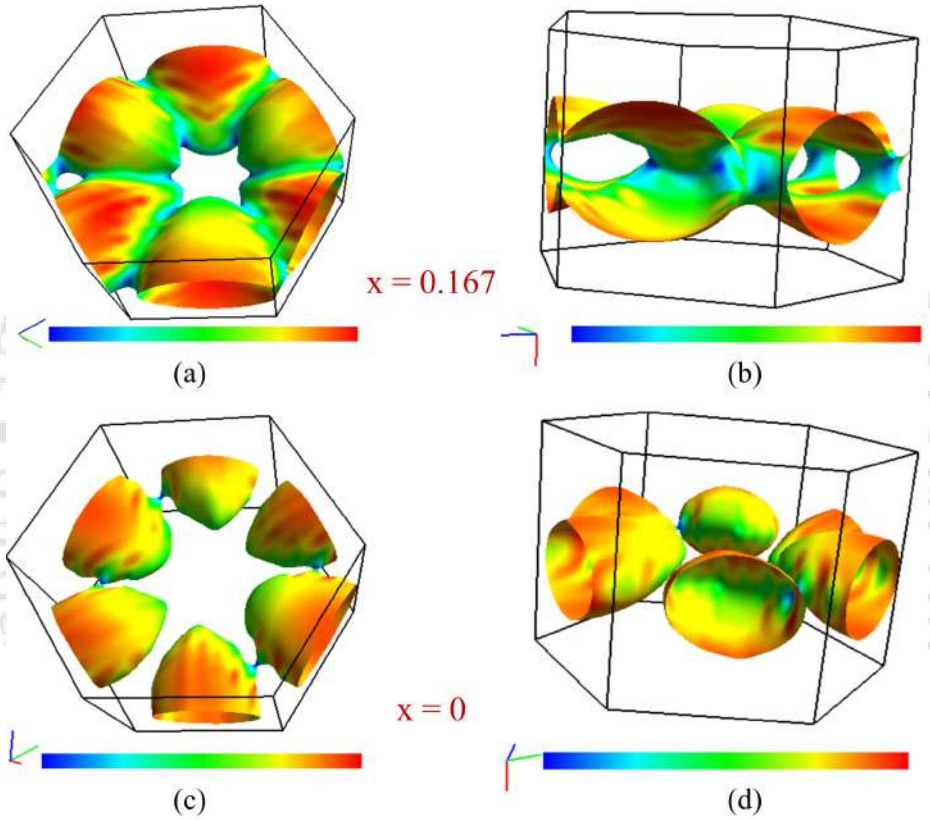

FIGURE 4.16: The Fermi surfaces of $Ca_3Co_{1.833}Mg_{0.167}O_6$ (a) and (b) in the first Brillouin zone for band crossing the Fermi-level. A representative Fermi surface for $Ca_3Co_2O_6$ (c) and (d), which emerges as the Fermi energy is shifted into the valence band.

the valence band gives rise to two well-separated hole pockets near Γ-L and Γ-F directions. Therefore, the Fermi surface topology displays a star-shaped empty region around Γ-point. Similar to this, far away from Γ point, another circular-shaped empty region around F-point corresponds to band crossing along the Γ-F direction. Thus, the momentum location and overall shape of Fermi surface agree well with the band structure plot.

In order to compare the Fermi surface topology of Mg-doped compound with parent compound, a representative Fermi surface of highest energy band in valence band, which emerges as the E_F is shifted to valence band for the parent compound is shown in Figs. 4.16(c) and (d). Similar to the Mg-doped compound, the Fermi surface of parent compound consists of six lobes that are symmetrically away from the k_z-axis, and at Γ point, there is no density. However, it is noticed from Figs. 4.16(c) and (d) that unlike the Fermi surface for the Mg-doped compound here, the lobes are separated from each other, and the hole like Fermi surface shrinks.

4.5 Discussion

Our study shows that the prominent features of $Ca_3Co_2O_6$ survive for the large Mg substitution, which is a signature of reduced dimensionality with additional hole-type substitution effects in the electronic structure of the system. Earlier studies have shown that the substitution at Co2 site has both positive and negative aspects [88, 124, 133, 135, 139]. The intra-chain ferromagnetic interaction dramatically increases for Ir and Rh doping [88, 139] while it decreases for Fe, Mn, and Cr substitution [124, 133, 135]. From our study, the obtained value of θ and J_1/k_B shows decreasing trend with Mg substitution, which is similar to that for the Fe, Mn, and Cr substitution at Co2 site, and it indicates the enhancement of antiferromagnetic interaction with substitution. In addition, the unaffected transitions (T_{c1} and T_{c2}) and step-like features in the M-H curves are quite different from earlier substitutions. Thus, from this point of view, this study is new to the literature, and the Mg^{2+} ion substitution brings two different aspects in the magnetic property of the system. The first one is key parameters in the magnetic property remain unaffected with Mg content. On the other hand, it suppresses the ferromagnetic contribution by introducing antiferromagnetic coupling of the induced Co^{4+} ions along the chain, which reduces the energy barrier required to form the short-range glassy state. The reduction in glassy feature is distinctly apparent from the $\varDelta S$ calculations. Thus, we can say that the key feature of the compound is its intrinsic property which remains unaffected as long as the dimensionality relation holds while the dynamic behavior is frustration-related. However, our DOS calculation results by taking experimental lattice parameters show insulator/semiconductor behavior for $Ca_3Co_2O_6$, which is contrary to the previously reported ferromagnetic half-metal behavior [84].

4.6 Conclusion

In this chapter, using the experimental tools of XRD, magnetization, and XPS, we study the structure and magnetism of $Ca_3Co_{2-x}Mg_xO_6$ (x = 0, 0.05, 0.1, 0.15, and 0.2) and try to establish a better concordance with theoretical predictions. We have prepared the polycrystalline samples by standard solid-state reaction method. Rietveld refinement of XRD data confirms that the doped Mg ion occupies the high spin trigonal prism site without altering its 1D character, which lefts its mark on the M-H curves. M-T ZFC-FC data reveal that the transition temperatures T_{c1} and T_{c2} remain unaffected with the doping content of Mg, whereas the μ_{eff} increases and θ decreases. The increase in μ_{eff} and decrease in θ are associated with the induced Co^{4+} $\left(S = \frac{5}{2}\right)$ ions arising due to the substitution of Mg^{2+} ions. XPS analysis, together with the first-principles study, confirms the enhancement in magnetic moment and provides sufficient evidence for spin transition from $S = 2$ to $S = \frac{5}{2}$ due to Mg substitution. The decreased value of J_1/k_B with Mg substitution has been attributed to the negative super-exchange interaction developed between induced Co^{4+} ions along the chain. Additionally, a detailed investigation on the electronic density of states and band structure provides an itinerant mechanism for the magnetic order and reveals hole-type doping of Mg atoms in this system. This hole-type doping leads to strong hybridization between partial states of Co-3d and O-2p orbitals, due to which the band crossing at E_F is observed for Mg-doped compound, and a hole-type Fermi surface is formed.

Chapter 5

$Ca_3Co_{2-x}Bi_xO_6$: Chemical disorder effect and Multilevel thermal memory cell

MEMORY devices based on heat flow and thermal rectification are in the limelight due to their excellent performance under harsh environments such as high temperatures, radiation flow, and external electric fields [222, 223]. These features make thermal memory devices most suitable for combustion engines, geothermal energy exploitation, and space exploration missions, as information writing, reading, processing, and storage are all by thermal manipulations [222]. Thus, thermal memory devices can be considered an alternative to electronic memory devices, which suffer performance degradation in harsh conditions [224]. The storage media in thermal memory devices can be phase-change materials or magnetically frustrated solids [223, 225]. In the frustrated magnets, the information storage is based on the principle of memory effect, a characteristic feature of ergodicity breaking in magnetic systems [222, 226]. However, the conventional route of data storage in the frustrated magnets is inefficient because it requires a long waiting time at interrupting points [222, 225, 226]. Therefore one has to look for alternative routes based on thermal manipulation that can contribute to the future development of thermal memory cell. In this context, spin cluster glass systems are the classic example, acquiring exotic features of frustrated systems [54]. Furthermore, the unconventional dynamics of these systems under cyclic temperature change experiments can be potentially used in the thermal memory cell to make it feasible [227].

It is clear from Chapter 3 and 4 that the pristine $Ca_3Co_2O_6$ exhibits characteristic features of glassy systems, and the unconventional dynamics of this system has the potential to contribute to the future development of thermal memory cell. However, as suggested by magnetic (Dy) and non-magnetic (Mg) dopant effects, the glassy feature is gradually suppressed with the doping content. Therefore, in order to make thermal memory cell feasible, the disorder in this system should be introduced in a different way other than the geometrical and magnetic frustration so that the glassy feature may enhanced. It is well known that the magnetic properties of glassy systems are affected by the relative strength of the competitive interactions. However, in an earlier report for $Ca_3Co_{2-x}Mn_xO_6$, the increased relaxation time for intermediate Mn-compositions has been attributed to the effect of chemical disorder [131]. Therefore, with impurity substitution in $Ca_3Co_2O_6$, the interplay of competing magnetic interactions and chemical disorder effects become crucial for glassy features [119, 125, 131, 133, 141]. The challenging issue in this compound is the single-phase synthesis of doped samples to explore the new mechanism of in-site originated disorder, which provides a plethora of anisotropy types. In this work, we have chosen Bi^{3+} ion in the replacement of the Co^{3+} ion, which has the same valence as the Co ions but a different ionic radius, due to which we could expect bond randomness effect. Here, we proposed an alternative route for thermal manipulation used in the thermal memory cell and compared it with the conventional ones. Our results suggested that multilevel data processing will become much more efficient and faster by using the proposed route. Furthermore, the enhanced glassy features with Bi substitution in this system will lead to a viable thermal memory cell.

We observed a low temperature glassy phase manifested through a clear memory effect and rejuvenation of magnetic relaxation under negative temperature cycle. Simultaneous Rietveld refinement of XRD data confirmed that the Bi^{3+} ion was doped at trigonal prism site, 6*a* (0, 0, 1/4) of Co. It is found that the glassy feature is robust over a wide range of Bi content, enabling the degeneracy in the magnetic ground state and large tunable ground state features. Additionally, the increment in glassy feature due to Bi substitution is attributed to the hybridization between the $Co^{3+}(3d)/Bi^{3+}(6s)$ orbital with the $O^{2-}(2p)$ orbital as a result of lattice distortion introduced by the random variation of Co1-O-Co2 bond-angle and Co1/Co2-O bond-lengths. We also depict here that the value of the relaxed magnetization follows a unique path for each temperature below the phase transition temperature (T_{c2}) for pristine $Ca_3Co_2O_6$ and its substituents. Here we propose a way to access these paths by cyclic thermal manipulations. Thus the magnetization corresponding to each temperature below T_{c2} can be utilized in multilevel data storage that has a potential application in the thermal memory cell. Furthermore, these results were compared with another route used in the thermal memory cell and were proven more efficient and faster than the latter one.

5.1 Experimental Details

The high purity $CaCO_3$, Co_3O_4, and Bi_2O_3 powders were taken in stoichiometric amounts to prepare the polycrystalline $Ca_3Co_{2-x}Bi_xO_6$ samples, followed by grinding these reagents using an agate mortar pestle to obtain a homogeneous mixture. The raw powders were heat treated at 1173 K for 24 h, then pelletized in cylindrical form having thickness 1 mm and diameter of 10 mm using a hydraulic press. These pellets were subjected to sintering at 1273 K for 48 h.

X-ray diffraction patterns of the prepared samples were obtained using a Rigaku X-ray diffractometer (TTRAX III) operating at 40 kV, 125 mA with CuK_α radiation (λ = 1.5406 Å) from scattering angle (2θ) 10 to 80°. Microstructural images were taken using ZEISS made Field Emission Scanning Electron Microscope. The magnetization measurements were performed using a PPMS DynaCool system that utilizes a vibrating sample magnetometer. We have followed zero-field-cooled and field-cooled protocols. In the ZFC protocol, the samples were cooled under zero field (300 to 2 K). The external magnetic field was applied at 2 K, and the data were taken during the warming-up cycle. In FC condition, the samples were cooled under the same applied field used for ZFC, and after reaching 2 K, the magnetization data were taken with increasing temperature.

5.2 Computational Details

The electronic and magnetic structures of $Ca_3Co_{1.833}Bi_{0.167}O_6$ have been explored by DFT calculations using the projector augmented wave method in VASP [161, 163, 215–217]. The exchange and correlation energy of electron interaction have been treated by the generalized gradient approximation method with the PBE potential [174]. Furthermore, a rotationally invariant formulation by Dudarev *et al.* (DFT+U) has been adopted to include on-site Coulomb interactions [180]. In the calculations, the Coulomb interaction term (U) and Hund's coupling parameter (J) for Co atoms are considered to be 2.0 eV and 0 eV, respectively.

In this work, we prepared a supercell consisting of 66 atoms (18 Ca, 6 Co1, 5 Co2, 1 Bi, and 36 O), and the basic structural parameters required to run these calculations were obtained from Rietveld refinement of XRD data. The plane wave cut-off energy was set to 600 eV, and self-consistency runs were performed over a gamma-centered k-point mesh (4×4×4) with total energy convergence criteria 10^{-6} eV. For the density of states calculations, we used a dense k-point mesh (6×6×6), and the k-point integration was performed using the tetrahedron method with Blöchl corrections [218]. Furthermore, the band structure of these systems has been calculated along the high symmetry k-point path in the irreducible Brillouin zone.

5.3 Experimental Results

5.3.1 Structure

The structural features of the synthesized powder samples were accessed through X-ray diffraction measurements. XRD data were analyzed by the Rietveld refinement technique implemented in the FullProf software. In the crystal structure of $Ca_3Co_2O_6$, the atomic positions of Co1 and Co2 are set to octahedral 6b and trigonal 6a sites, respectively. Rietveld refinement was carried out for these samples with substituted Bi atoms at the 6a site. Trials have also been made to refine the XRD pattern by placing the Bi atoms to the 6b site, but the occupancy of Bi is negative, indicating the difficulty of Bi atom to

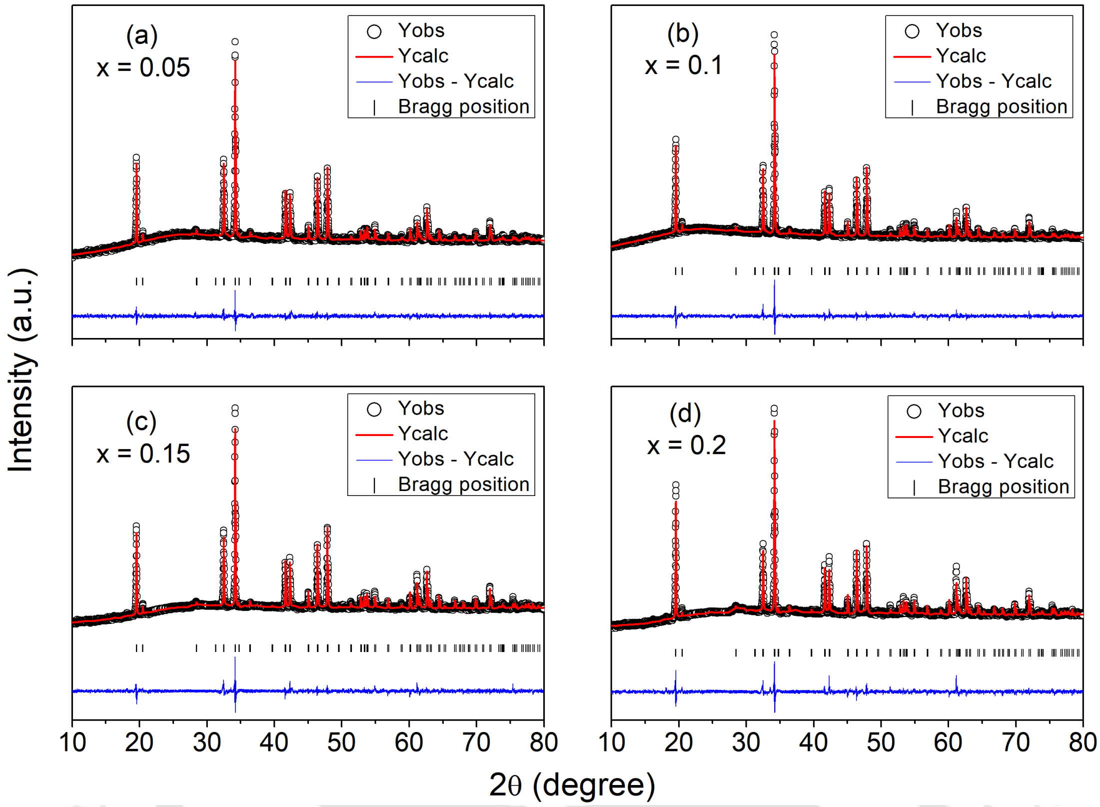

FIGURE 5.1: Room temperature X-ray diffraction patterns for $Ca_3Co_{2-x}Bi_xO_6$ samples Y_{obs}, refined by the Rietveld method. The solid red line represents the calculated intensity pattern (Y_{calc}).

occupy $6b$ site. Since the bond activation energy of Bi-O bonds is much higher than that of Co-O bonds due to the large size of Bi-ions. Thus, instead of occupying the $Co^{3+}(6a)$ site, some Bi-ions can enter the lattice at the interstitial sites. So, by substituting Bi^{3+} for $Co^{3+}(6a)$, we expect a bond-randomness effect because of the same valence and the different ion size. Fig. 5.1 presents the graphical output of the Rietveld refinement performed to the acquired XRD pattern of the $Ca_3Co_{2-x}Bi_xO_6$ (x = 0.05, 0.1, 0.15, and 0.2) samples. The obtained XRD patterns were well indexed within the rhombohedral Bravais lattices of space group $R\bar{3}c$ (Fig. 5.1), confirming a solid solution in the range $0 \leq x \leq 0.2$.

Crystallographic data derived from the Rietveld fitting and the reliability parameter of the refinement (R_{wp}, R_{exp}, and χ^2) are listed in Table 5.1. It was observed that the lattice parameters a and c increase with Bi content and attain a maximum value for x = 0.15 sample above this concentration; both of them decrease (Table 5.1). The monotonous increase in the lattice constant for the first three samples of the present

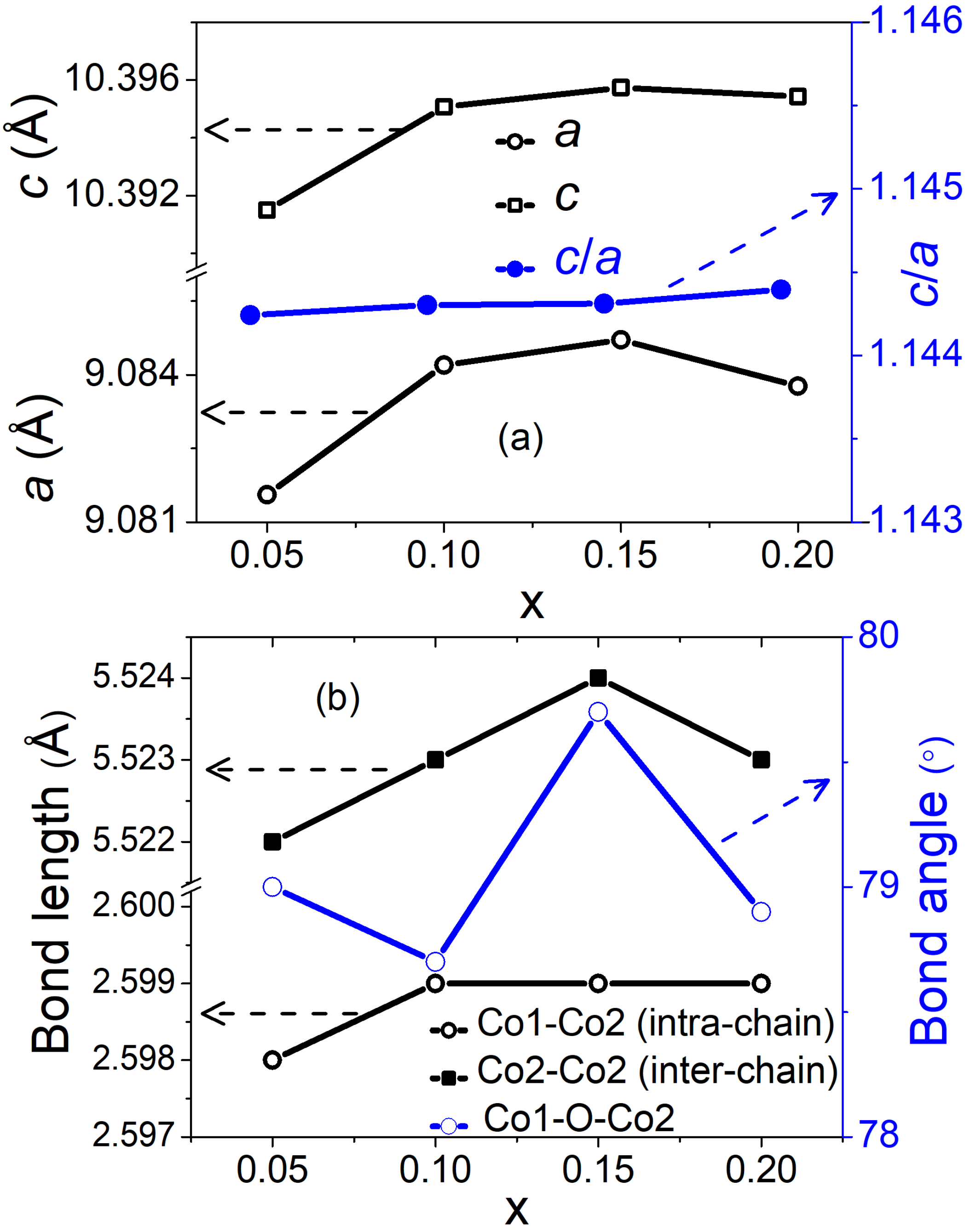

FIGURE 5.2: Variation in the (a) lattice parameters and associated (b) bond lengths and bond angles with the content of Bi for $Ca_3Co_{2-x}Bi_xO_6$ samples.

series is consistent with the large ionic radius of Bi^{3+} ion. However, the decreased value of both a and c for the $x = 0.2$ sample is quite unusual. To get a deeper insight into this, the bond-length and bond-angle analysis has been done using VESTA software. Table 5.1 contains the intra-chain (Co1-Co2) and inter-chain (Co2-Co2) bond-lengths and selected bond-angle for all the samples. Similar to the lattice constant, the intra-chain and inter-chain bond length has shown unusual dependence on Bi content (Fig. 5.2(b)).

TABLE 5.1: Lattice parameters a, c, intra-chain (Co1-Co2) and inter-chain (Co2-Co2) bond-length, bond-angle (Co1-O-Co2), and reliability parameter of the refinement for $Ca_3Co_{2-x}Bi_xO_6$ samples.

x	a (±0.001 Å)	c (±0.001 Å)	Co1-Co2 (±0.001 Å) (intra-chain)	Co2-Co2 (±0.001 Å) (inter-chain)	Bond-angle (°) (Co1-O-Co2)	R_{wp} (%)	R_{exp} (%)	χ^2
0.05	9.081	10.391	2.598	5.522	79	6.21	5.19	1.43
0.1	9.084	10.395	2.599	5.523	78.7	12.28	8.43	2.12
0.15	9.085	10.396	2.599	5.524	79.7	13.08	9.05	2.09
0.2	9.084	10.395	2.599	5.523	78.9	15.3	9.8	2.44

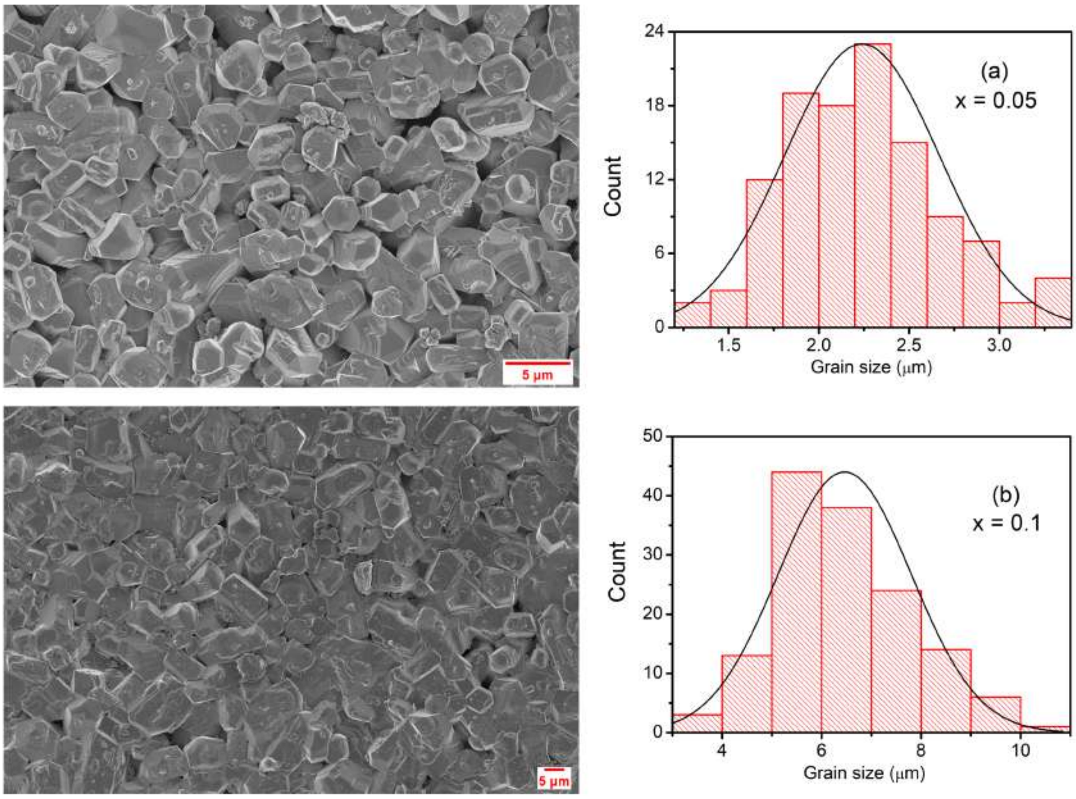

FIGURE 5.3: FESEM images for $Ca_3Co_{2-x}Bi_xO_6$ samples (a) x = 0.05 and (b) x = 0.1. The particle size histogram is shown on the right side and fitted to log-normal distribution (black curve).

The inter-chain bond length increases monotonously for the first three samples of the present series and decreases for x = 0.2. However, the intra-chain bond length remains independent of Bi substitution (Fig. 5.2(b)). Thus, these results indicate that with the Bi substitution, a relatively more significant distortion occurs along the *ab*-plane than the *c*-axis. One of the crucial findings from these results is that the intra-chain Co1-O-Co2 bond angle varies in an unusual manner with Bi-content (Fig. 5.2(b)), which indicates

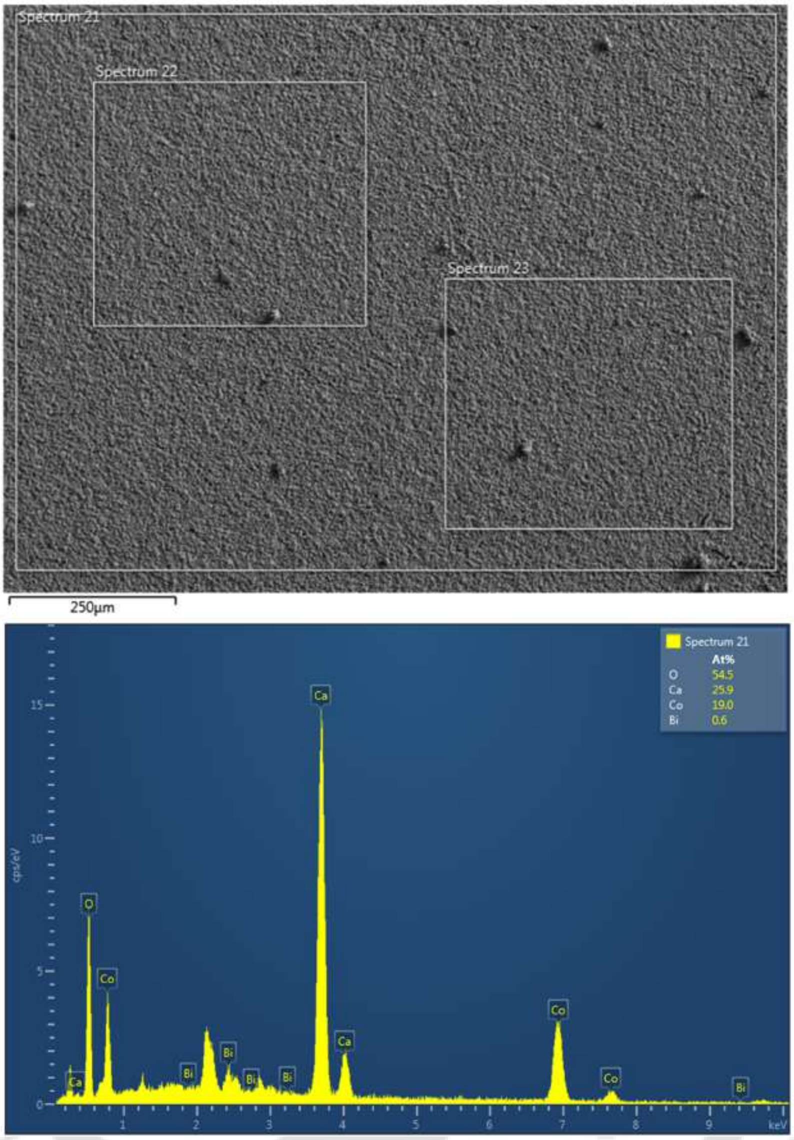

FIGURE 5.4: EDS spectra for $Ca_3Co_{1.9}Bi_{0.1}O_6$ sample.

the presence of broken or random bonds due to Bi substitution. So, bond-randomness effects should be anticipated by substituting Bi^{3+} for $Co^{3+}(6a)$ due to the same valence but a different ion size. The bond randomness effect may directly influence the exchange interaction mediated through oxygen atoms between the magnetic ions.

Fig. 5.3 displays the FESEM micrograph of the two members of the series (x = 0.05 and 0.1). For the parent compound, it was shown that the grains are spherical in shape, and their distribution is relatively uniform with a considerable amount of porosity (Fig. 3.4). However, it is clearly seen from Fig. 5.3 that the grain morphology and boundary have been changed with the substitution of Bi. The substituted samples have a relatively high-density microstructure, and they are almost void-free. The particle size distribution has been deduced from the FESEM micrograph, and it fits rather well with a log-normal function. From the particle size histogram shown in Fig. 5.3, it is found that the average particle size increases from 2.3 μm for x = 0.05 sample to 6.5 μm for x = 0.1 sample.

Fig. 5.4 depicts the energy dispersive spectra for the $Ca_3Co_{1.9}Bi_{0.1}O_6$ sample. It confirms the presence of Ca, Co, Bi, and O in the synthesized samples. No other traceable impurities were detected within the resolution limit of EDS. Further analysis confirmed that the obtained elemental percentages are comparable to their nominal values.

5.3.2 Temperature dependence of magnetization

Magnetization data were recorded with temperature using zero field-cooled and field-cooled conditions under an applied magnetic field of 1000 Oe (Fig. 5.5). These curves have a characteristic shape and exhibit similar features. The magnetization curves show an upward trend below 25 K, accompanied by the bifurcation of ZFC-FC curves at 16 K. The divergence of ZFC-FC curves for low temperatures indicates a history dependence on the magnetization process. Below 16 K, the ZFC curve attains a maximum, while the FC magnetization continues to rise with decreasing temperature, a characteristic feature of the glassy systems. The small magnetization response in the low-temperature ZFC curves demonstrates that the applied magnetic field is not strong enough to rotate the spins in the direction of field, which is indicative of a highly anisotropic system. For a homogeneous spin-glass, the FC curve is almost flat for $T < T_{c2}$, while for the interacting spin clusters (cluster-glass), the FC curve continues to rise with decreasing temperature [228]. Thus, for our systems, the magnetization differs from that for a homogeneous spin-glass (Fig. 5.5), and the increase in the FC magnetization below T_{c2} is due to the finite range of inhomogeneous states. It is also clear from Fig. 5.5 that the sharp peak in ZFC curves gets broadened with Bi-substitution and shifts towards higher temperatures. Transition temperatures T_{c1} and T_{c2} were obtained from dM/dT vs. T plot and listed in Table 5.2 (Fig. 5.6). The transition temperature T_{c2} increases with Bi substitution while the T_{c1} decreases (Table 5.2). The increased T_{c2} with Bi substitution in this system indicates the enhancement of glassy characteristics, while the decreased

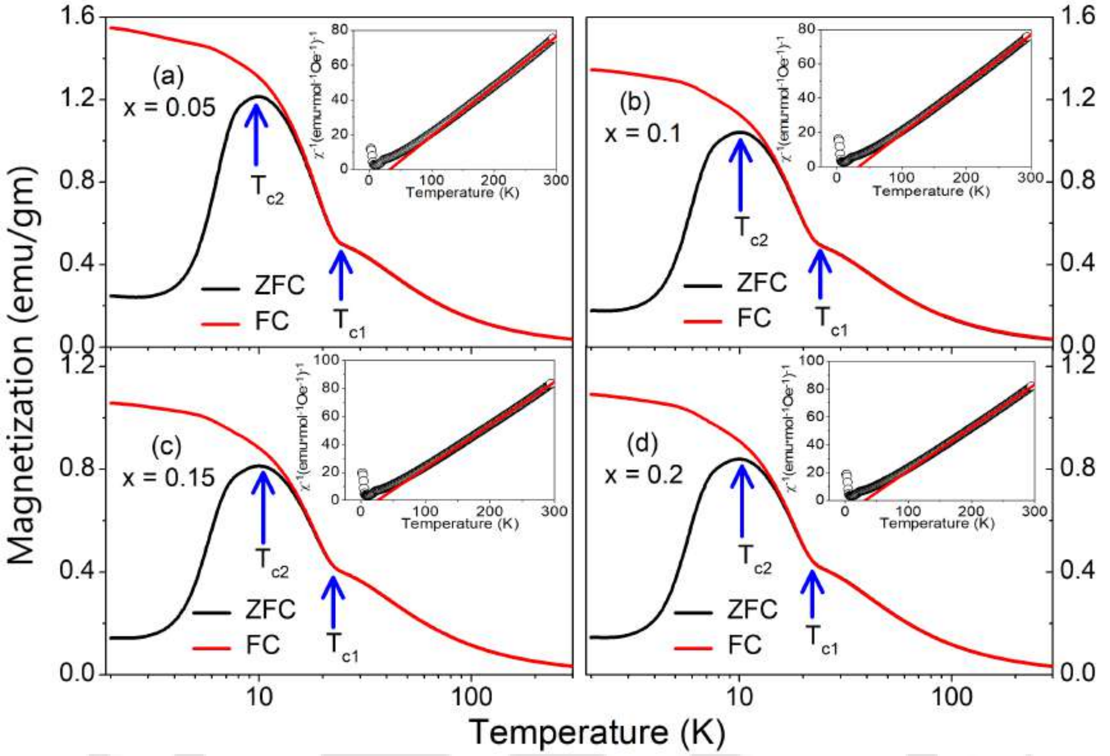

FIGURE 5.5: DC magnetization M-T curves under an applied magnetic field of 1000 Oe for $Ca_3Co_{2-x}Bi_xO_6$ samples. Inset shows the inverse susceptibility data fitted to the Curie-Weiss law.

value of T_{c1} indicates the reduced ferromagnetic coupling along the chain due to Bi substitution. We speculate that the bond-randomness effect arising from Bi substitution randomly imbalances the relative strength of competitive ferromagnetic (intra-chain) and antiferromagnetic (inter-chain) interactions in this system and might be the origin of this feature. Thus, the progressive Bi^{3+} ion in the Co^{3+} ions chain destabilized the magnetization along the chain, providing a way to short-range spin clusters, and to clarify it, magnetic relaxation measurements are necessary. The non-zero value of $d\mathrm{M}/d\mathrm{T}$ in the high-temperature region (25 K – 150 K) indicates the presence of weak ferromagnetic correlation in the paramagnetic region (Fig. 5.6).

Inset of Fig. 5.5 shows the plot of inverse susceptibility data as a function of temperature. In the high-temperature region (150 – 300 K), the susceptibility data obeys the Curie-Weiss law (Eq. 3.1). Based on the obtained value of molar Curie constant C_{mol}, the effective magnetic moment was calculated using $\mu_{\mathrm{eff}} = (3C_{\mathrm{mol}}k_{\mathrm{B}}/N_{\mathrm{A}}\mu_{\mathrm{B}}^2)^{1/2}$, where k_{B}, N_{A}, and μ_{B} are Boltzmann constant, Avogadro number, and Bohr magneton, respectively. The estimated values of μ_{eff} and θ are given in Table 5.2. The calculated

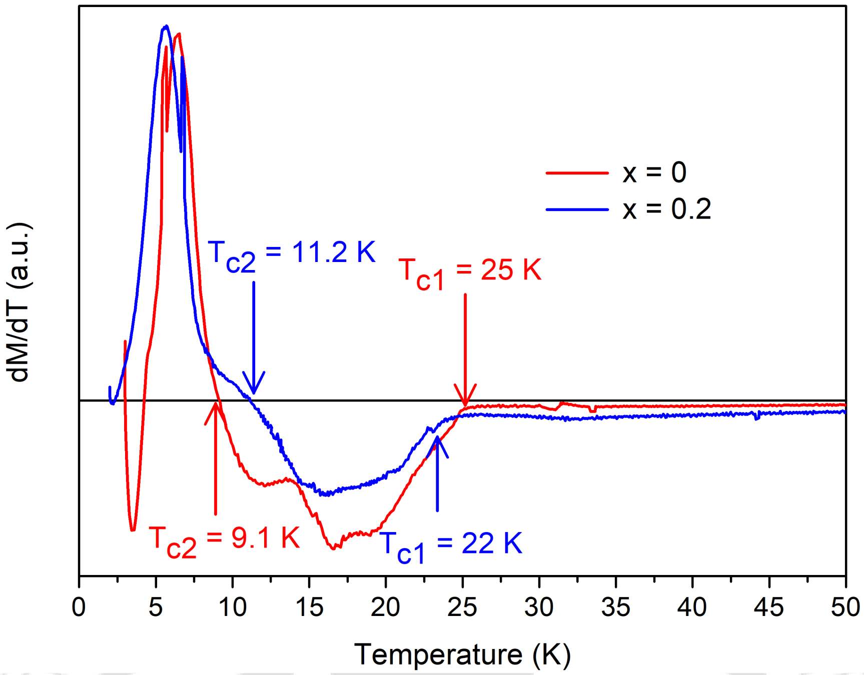

FIGURE 5.6: dM/dT vs. T plot for $Ca_3Co_{2-x}Bi_xO_6$ samples (x = 0 and 0.2) where the transition temperatures were marked by arrows.

value of μ_{eff} and θ for the parent compound are 5.6 μ_B and 31 K, respectively (Table 3.2). The positive value of θ suggested that the dominant interaction is ferromagnetic. As anticipated from Bi^{3+} substitution (non-magnetic), μ_{eff} decreases monotonously with the content of Bi (Table 5.2). On the other hand, the variation in Curie temperature has no systematic trend with the content of Bi. Initially, it decreases from 35 K for the x = 0.05 sample to 26 K for the x = 0.15 sample, and then it begins to rise with the Bi concentration. This complex behavior of θ typically arises due to the onset of ferromagnetic interaction in the paramagnetic matrix (Fig. 5.6).

5.3.3 Field dependence of magnetization

Fig. 5.7 shows the isothermal M-H curves of the $Ca_3Co_{2-x}Bi_xO_6$ samples measured at 2 K and 10 K. In the low-field region (10 K), the magnetization exhibits a nearly linear relation with the field and tends to saturate, characterizing the ferrimagnetic state [200]. With further increase in the magnetic field $H > H_c$, the magnetization takes a sharp upturn that corresponds to ferromagnetic configuration [200]. Moreover, the curves do not saturate for the maximum applied magnetic field of 9 T, indicating the random orientation of magnetization with respect to the field. It is worth noting that the

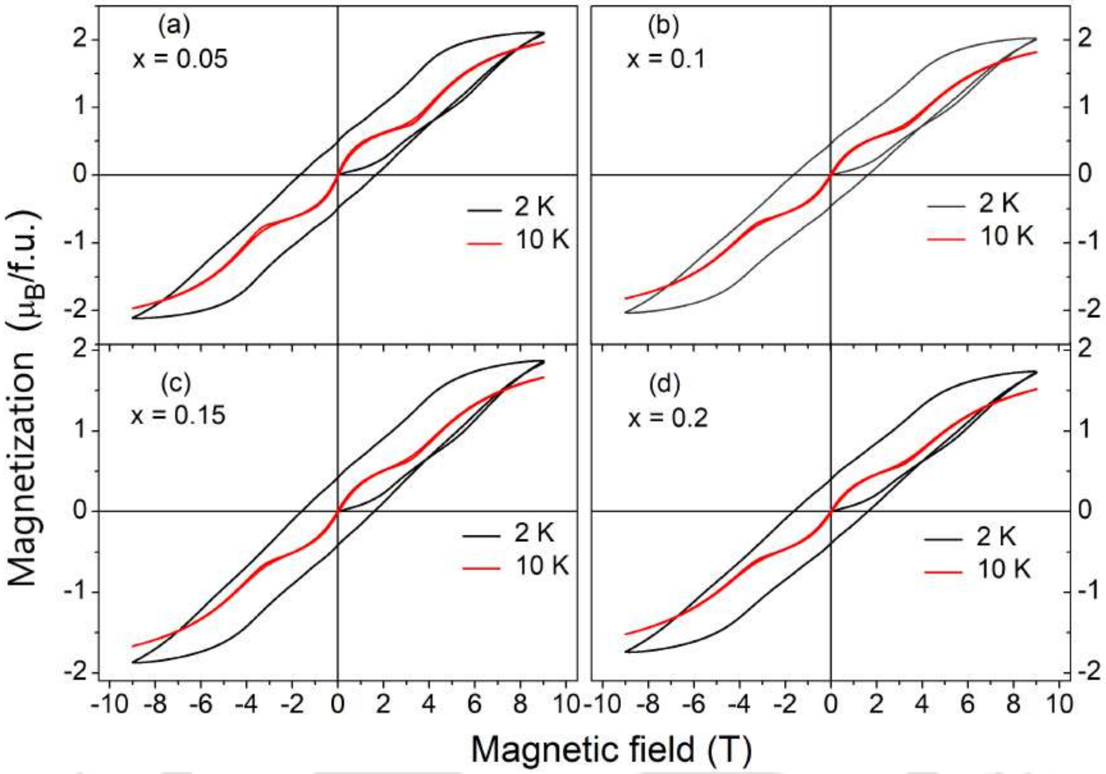

FIGURE 5.7: Isothermal M-H curves measured at 2 K (black line) and 10 K (red line) for $Ca_3Co_{2-x}Bi_xO_6$ samples.

transition at H_c accompanied by measurable hysteresis on decreasing the field confirms the first-order nature. This behavior is similar to that for the parent compound except for a slight difference in the H_c (3.4 T) and a relatively smooth transition compared to that for the parent compound. It was observed that the nature of curves remains unchanged across the series, and all the curves show significant hysteresis, which decreases with the increase in temperature.

In addition, it was also observed that the virgin curve (2 K) lies below the envelope curve for a field $H > 3.8$ T. It gives evidence for the metastability of the system related to the arrest of dynamics in a spin system. It usually occurs in the frustrated magnets having degeneracy in the ground state, so spins are rearranged with the application of an external magnetic field. Thus, the phenomenon of the virgin curve lying below the envelope for $H > H_c$ can be explained by the field-driven transition at $H = H_c$. In the isothermal field increasing cycle, the starting point is a ferrimagnetic (↑↑↓) configuration of spin chains. It is converted to a ferromagnetic (↑↑↑) configuration of spin chains when the system is exposed to a field $H > H_c$. On the field decreasing cycle (9 T to 0 T), the

TABLE 5.2: The transition temperatures (T_{c1} and T_{c2}), effective magnetic moment, Curie-temperature, relaxation time, and critical exponent for $Ca_3Co_{2-x}Bi_xO_6$ samples.

x	T_{c1} (K)	T_{c2} (K)	μ_{eff} (μ_B)	θ (K)	τ (sec)	n
0.05	24	9.6	5.3	35	1092	0.54
0.1	23	10.3	5.2	33	1120	0.53
0.15	23	10.6	5.1	26	1446	0.52
0.2	22	11.2	5.0	31	1422	0.53

initial configuration (↑↑↓) is not recovered due to the dynamic arrest of the ferromagnetic (↑↑↑) configuration. This state is carried over during the next isothermal field-increasing cycle giving rise to a higher magnetization value on the envelope curve.

5.3.4 Magnetic dynamics

We now discuss the non-equilibrium dynamics of these systems, which is decided by various measuring protocols. We first performed the ZFC magnetic relaxation to study the dynamic behavior of these samples. The samples were cooled from the paramagnetic region (300 K) to 3 K without applying an external magnetic field. Once the temperature was stabilized at 3 K, the samples were magnetized under an applied magnetic field of 9 T for a short duration (60 sec). After switching off the magnetic field, the drop in the remanent magnetization was recorded with time (Fig. 5.8). The relaxation behavior of these samples is logarithmically slow (Fig. 5.8), which suggests a slow approach of the system towards thermal equilibrium and broad distribution of spin-relaxation time. The stretched exponential relaxation function (Eq. 3.6) is most often used to describe the relaxation dynamics of glassy systems. The values of τ and n are associated with the nature of the energy barriers involved in the relaxation. Generally, for interacting spin clusters, n lies between 0 and 1. Moreover, for a fixed value of n, a larger value of τ means the magnetization relaxes slowly. The solid line in Fig. 5.8 shows the stretched exponential relaxation function fitting in the experimental data where a slight deviation was observed up to 100 sec. Above this, the relaxation behavior was well described by the stretched exponential relaxation function. The inset of Fig. 5.8 depicts the variation

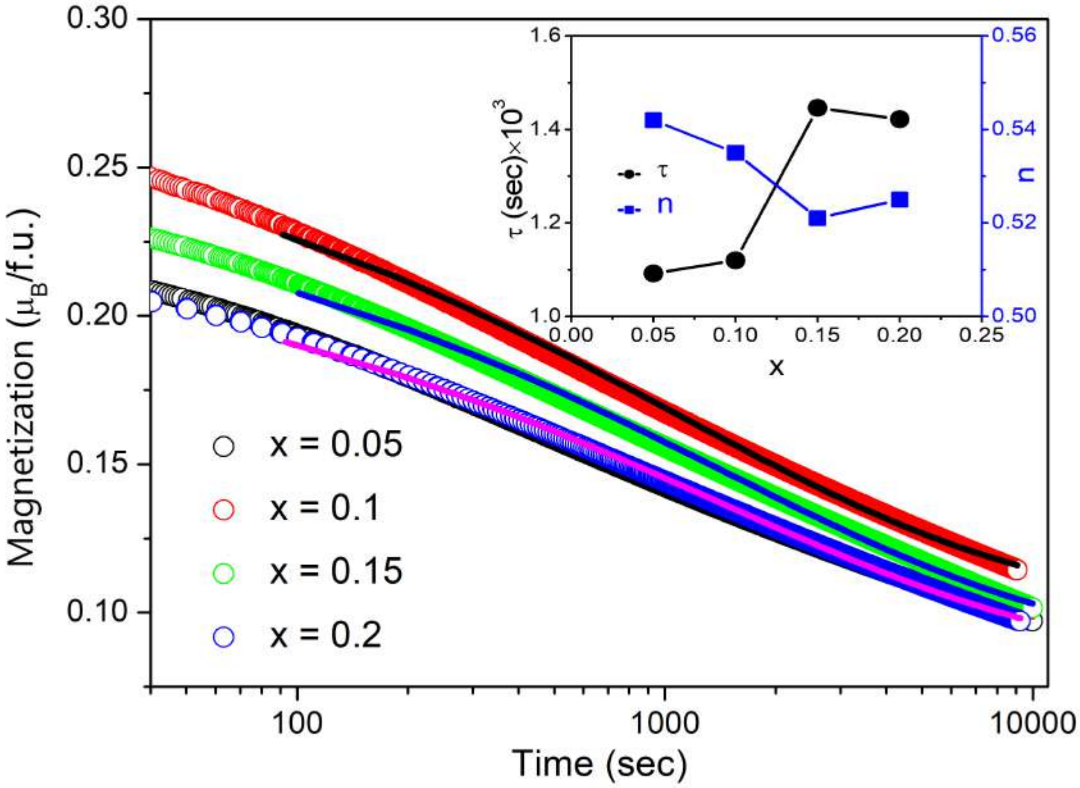

FIGURE 5.8: ZFC magnetic relaxation at 3 K for $Ca_3Co_{2-x}Bi_xO_6$ samples. The stretched exponential relaxation function fit to the experimental data is represented by the solid line. Inset shows the variation in τ and n with the content of Bi.

of fitted parameters relaxation time τ and critical exponent n with the content of Bi. The deduced value of n lies in the range of 0.52 to 0.55 (Table 5.2), indicating the system evolves through several intermediate metastable states. One of the important findings from these results is that the τ value for Bi-substituted compounds (x = 0.15 and 0.2) is higher than that for the pristine $Ca_3Co_2O_6$ (1366 sec), which confirms the enhanced glassy characteristics for Bi-substituted compounds. These results are consistent with the increased value of T_{c2} for Bi-doped samples; however, both the τ and n show an unusual relationship with the content of Bi (see inset of Fig. 5.8).

5.3.5 Memory and rejuvenation effects

Memory effect is another most spectacular manifestation of the non-equilibrium phenomenon occurring in frustrated spin systems studied by the FC aging protocol. The samples were field cooled (100 Oe) to 6 K, and the magnetization was measured with temperature. At this temperature, the cooling process was interrupted, and the systems

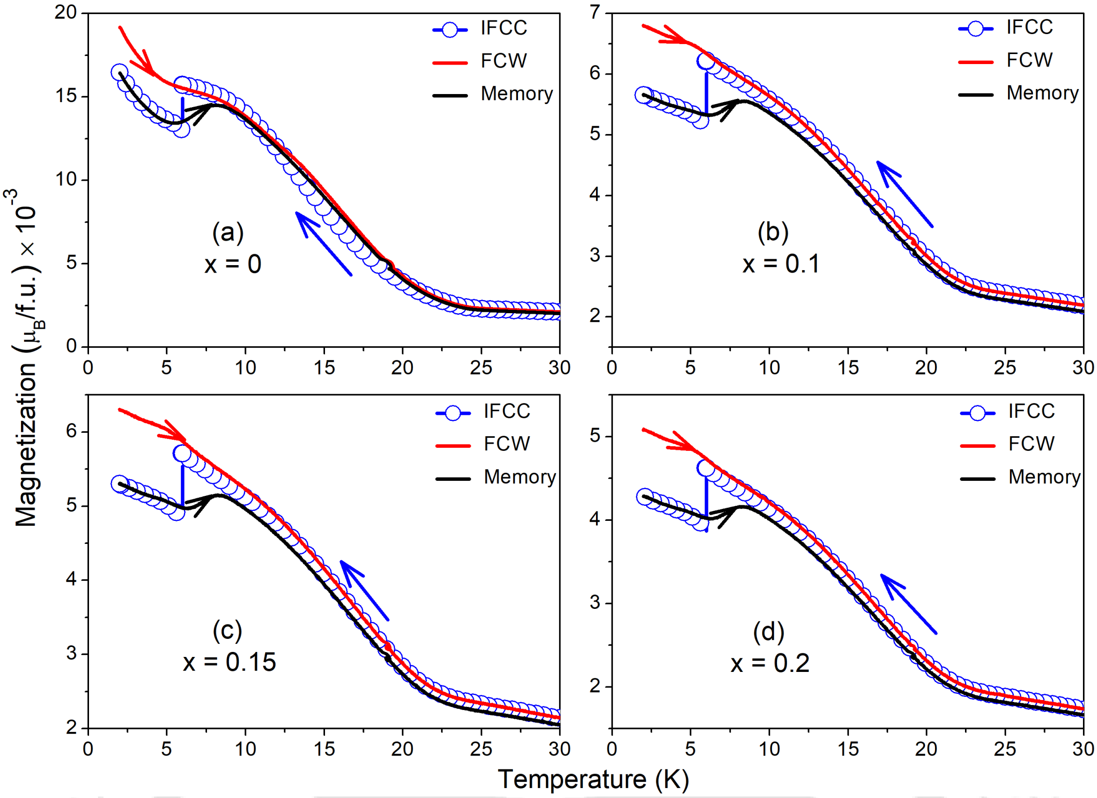

Figure 5.9: Temperature dependence of DC magnetization of $Ca_3Co_{2-x}Bi_xO_6$ samples measured under an applied field of 100 Oe in three different cycles as labeled in the plot. In the IFCC curve, the field was set to zero during the stop at T = 6 K for 5400 sec.

were allowed to relax by switching off the magnetic field for a duration t_s = 5400 sec. After the waiting time of 5400 sec, the same magnetic field was reapplied, and the FC process was resumed. The magnetization curve generated by following this procedure is called the interrupted field cooled cooling (IFCC) curve (Fig. 5.9). On reaching the base temperature (2 K), the magnetization data was re-recorded while warming the sample under the same field (100 Oe), denoted by the memory (Fig. 5.9). For reference, the field-cooled warming (FCW) curve under the same applied magnetic field was taken. The reproduced step on the memory curve at the interrupting point (6 K) demonstrates the memory of the system (Fig. 5.9). Such a phenomenon is associated with hindering magnetization recovery and is primarily attributed to the distribution of energy barriers. It is the conventional route used in thermal memory cell where aging is required for a long duration (5400 sec) at interrupting points to store the information [222]. Thus alternative ways of data storage based on thermal manipulation are necessary to make it feasible. We have performed these experiments for different magnetic field values and

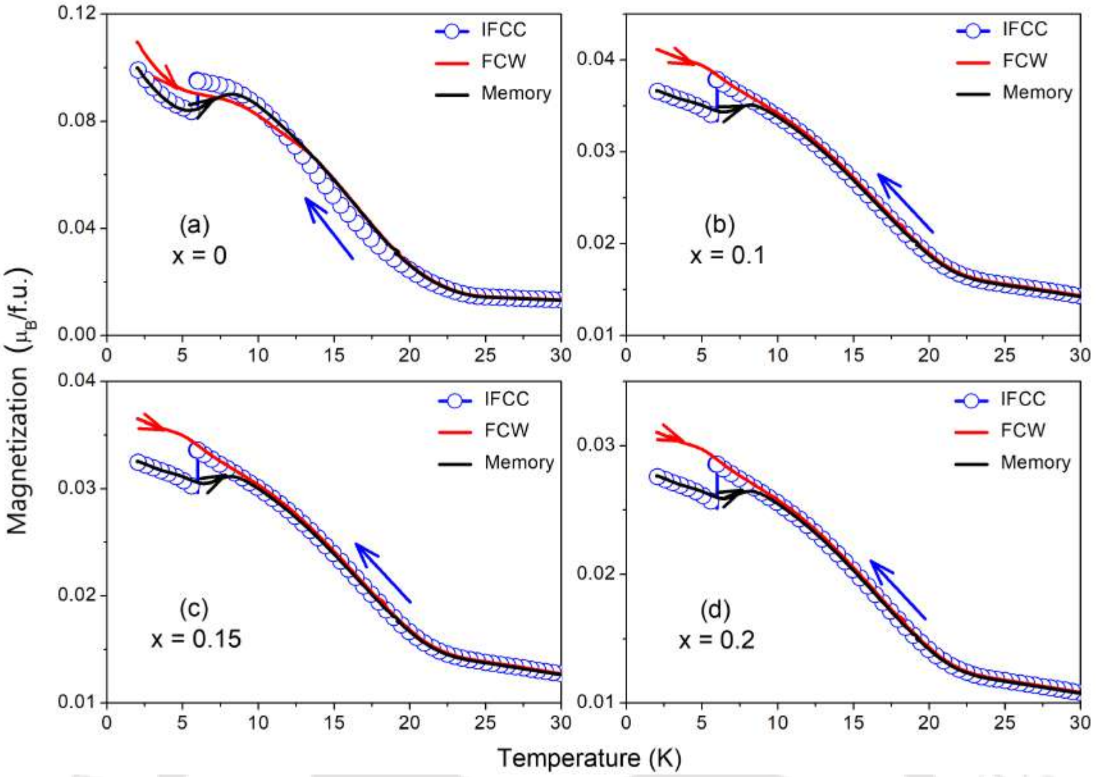

FIGURE 5.10: Demonstration of memory effect in the $Ca_3Co_{2-x}Bi_xO_6$ samples under an applied magnetic field of 500 Oe.

found that the memory intensity decreases with increasing field (Fig. 5.10).

In order to look for alternative routes of thermal manipulation, the magnetic relaxation measurements were performed under a negative temperature cycle. Initially, the samples were cooled to 6 K under a 100 Oe external magnetic field. The applied field was removed when the temperature stabilized at 6 K, and the magnetization data was taken with time for 5400 sec. The relaxation process was followed by a cyclic change of temperature (1 K/min temperature ramp rate) between 2 K and 6 K and taking the relaxation data at these temperatures for a time t_d (t_d = 900 sec for the parent compound and 450 sec for others) designated as memory in Fig. 5.11. It is evident from Fig. 5.11 that when the temperature was restored to the initial value (6 K), the relaxation curve was in continuance with its previous relaxation state at 6 K. Thus, the temporary cooling to 2 K does not erase the memory in FC relaxation for all the systems, demonstrating the rejuvenation phenomenon in magnetic relaxation. Furthermore, the rejuvenation phenomenon under negative temperature cycle was also shown for taking the relaxation measurement at a different temperature (8 K) and temporary cooling temperatures (6

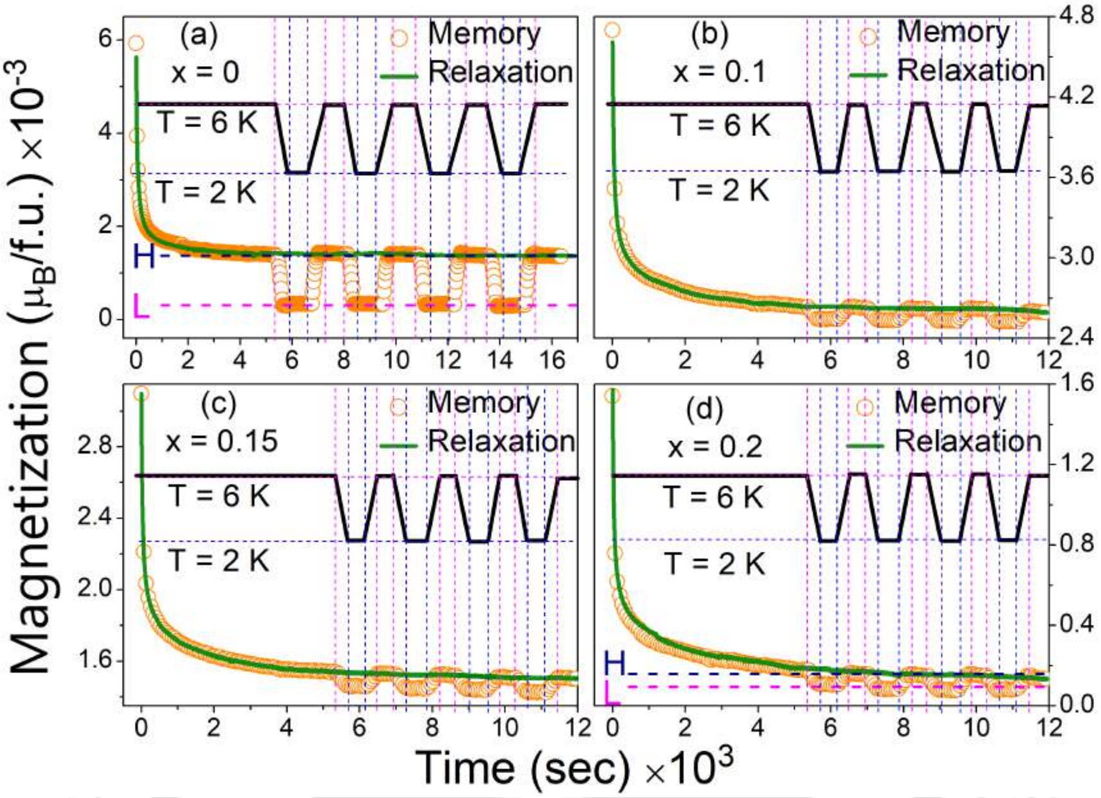

Figure 5.11: Magnetic relaxation experiments under negative temperature cycle for $Ca_3Co_{2-x}Bi_xO_6$ samples. The solid black line represents the temperature status with time during the measurement. The solid green line represents the uninterrupted magnetic relaxation curve at 6 K used for the reference. At the left corner of Figs. (a) and (d), the H and L represent the magnetization beyond 5400 sec for T = 6 K and 2 K, respectively.

K and 2 K) (Fig. 5.12(a)). In addition, this feature was further tested by changing the temperature ramp rate during the temperature cycle (Fig. 5.12(b)). The observed results show that the rejuvenation phenomenon in magnetic relaxation is robust against the change in the temporary cooling temperature and ramp rates (Figs. 5.12(a) and (b)).

Similar to the negative temperature cycle, the magnetic relaxation measurements were also performed for the positive temperature cycle, where the samples were field cooled (100 Oe) to 2 K. Magnetic relaxation data was taken with time after switching off the magnetic field at 2 K (Figs. 5.12(c) and (d)). In order to generate the memory curve, the same cyclic temperature protocol used in the negative temperature cycle was employed (2 K ↔ 6 K) (Figs. 5.12(c) and (d)). Unlike the negative temperature cycle, no rejuvenation and memory effects were observed for the first cycle in the magnetic relaxation experiments under positive temperature cycle.

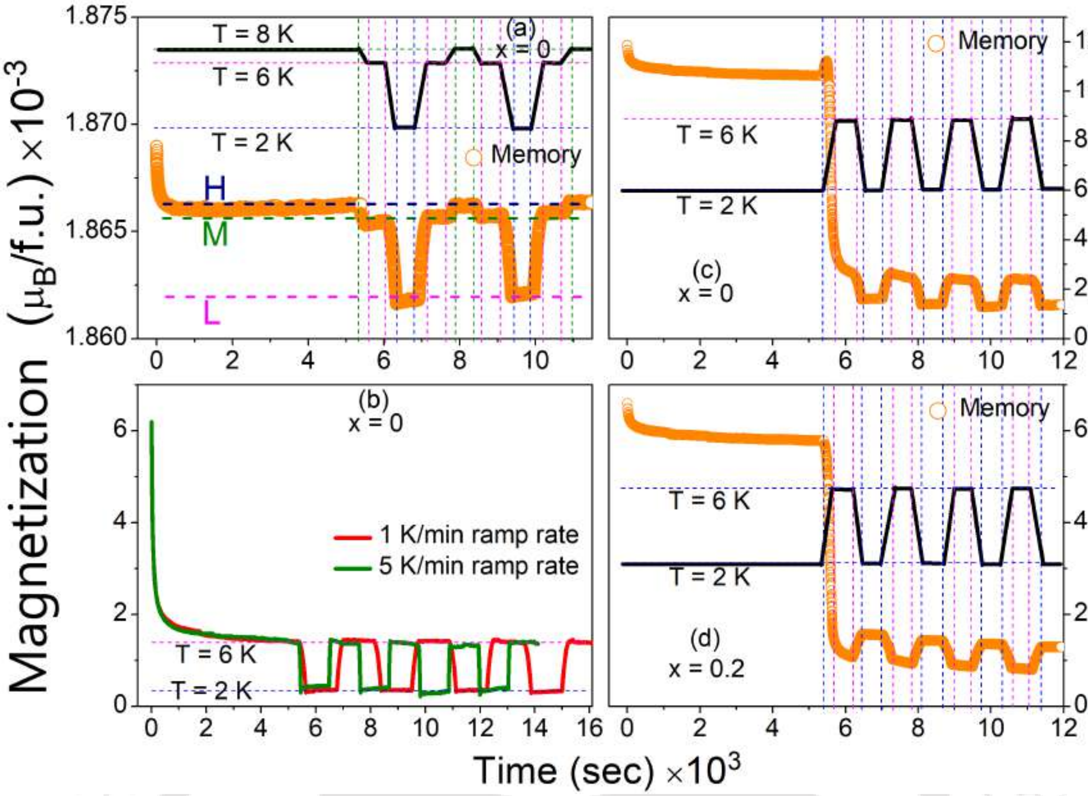

FIGURE 5.12: (a) Magnetic relaxation experiment under negative temperature cycle at different temporary cooling temperatures (8 K, 6 K, and 2 K) for $Ca_3Co_2O_6$, where the H, M, and L represent the magnetization beyond 5400 sec for T = 8 K, 6 K, and 2 K, respectively. (b) Relaxation experiments at different ramp rates during negative temperature cycle for $Ca_3Co_2O_6$. (c) and (d) Magnetic relaxation experiments under positive temperature cycle for $Ca_3Co_{2-x}Bi_xO_6$ samples.

The asymmetric relaxation nature below T_{c2} for negative and positive temperature cycles can be explained by the well-separated hierarchically organized temperature-dependent metastable states with equal magnetization, commonly known as the hierarchical glass model [229]. This model is based on the multi-valleyed nature of the free energy landscape below T_{c2}. The valleys in this landscape merges/splits into the new sub-valleys depending on the heating/cooling cycle of temperature (6 K $\leftrightarrow$ 2 K). In the negative temperature cycle (6 K $\rightarrow$ 2 K), the free energy landscape first splits into new sub-valleys (Fig. 5.13). The relaxations observed occur in the sub-valleys of this new scenario of the landscape. When the temperature is cycled back to its initial value (2 K $\rightarrow$ 6 K), the sub-valleys get merged, and the initial energy landscape is restored. Thus, the magnetization dynamics are recovered in this original landscape for the negative temperature cycle. Therefore, for this process, the energy barriers between the metastable states corresponding to the actual landscape are so high that the system cannot crossover the

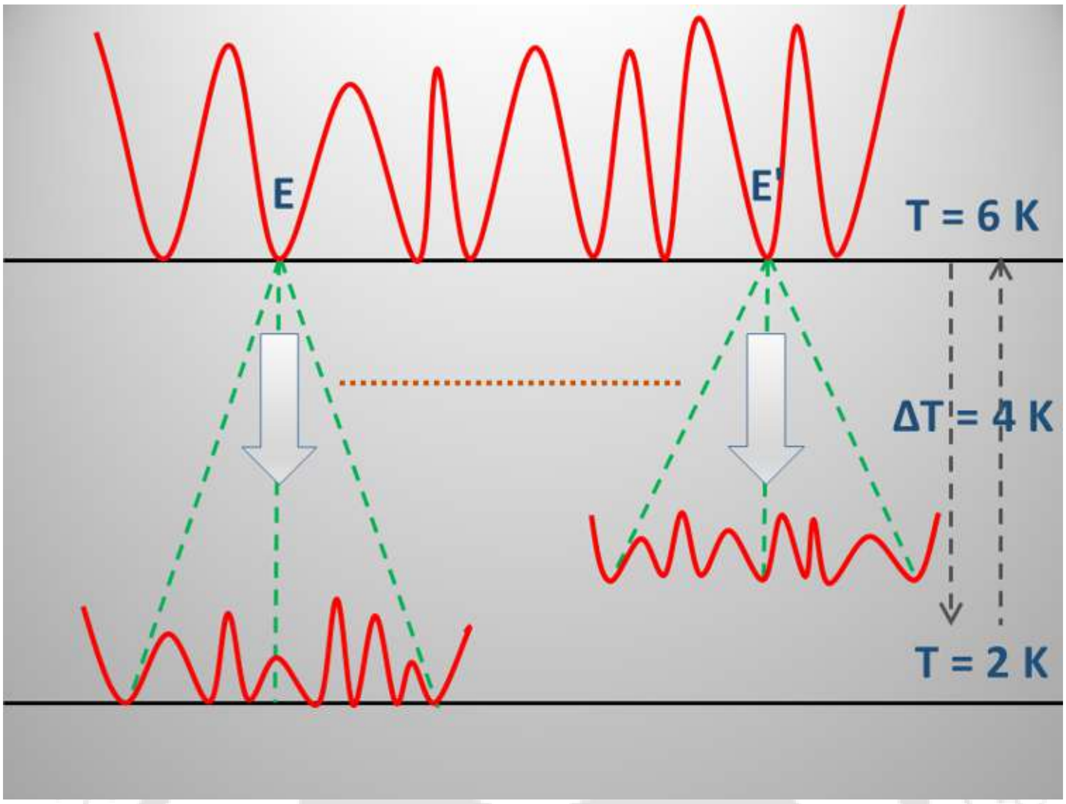

FIGURE 5.13: Splitting of two free-energy landscapes E and E′ according to hierarchical model of glassy phase under negative temperature cycle.

barrier during the time t_d. On the other hand, the first step for the positive temperature cycle (2 K → 6 K) corresponds to coalescing of multi-valleys in the energy landscape. When the temperature is restored (6 K → 2 K), although the free energy landscape is recovered, but the population of each valley does not remain the same as before. Therefore, there is an asymmetric nature of the cooling and heating cycles for large change in temperature.

5.4 Density Functional Theory Calculations

In view of the proposed magnetic structures from the experimental data, we have done a thorough understanding of spin and electronic structure of the Bi-substituted compound by first-principles-based DFT calculations. The computational and structural parameters used in these calculations are mentioned in Section 5.2. The experimentally proposed magnetic structures in the triangular lattice arrangement are PDA, ferrimagnetic, and ferromagnetic (see Fig. 1.13). In the PDA structure, the two chains are antiferromagnetically coupled, and the third chain remains disordered (see Fig. 1.13). The ferrimagnetic structure corresponds to the up-up-down (↑↑↓) configuration among chains, while the ferromagnetic structure corresponds to the up-up-up (↑↑↑) configuration. By comparing the energies corresponding to these configurations, we can predict the magnetic ground state. Our calculations suggested that the ferromagnetic up-up-up configuration is the most stable structure for our system, with a minimal difference between energies (ΔE_r) for PDA and ferrimagnetic configuration (Table 5.3).

5.4.1 Density of states

Fig. 5.14 depicts the total density of states for these compounds in the energy range -8.0 eV to +8.0 eV. The E_F for the Bi substituted compound is 5.4 eV. It is found that the Bi-substituted compound shows an insulator/semiconductor-type behavior, which is similar to that for the parent compound $Ca_3Co_2O_6$ (Fig. 4.13(a)). Further analysis from site projected DOS revealed that the near the E_F region is dominated by the Co-3d and O-2p electrons (Fig. 5.14). It is interesting to note that near the E_F, the contribution of O-2p electrons in the DOS is approximately equal to that for the Co-3d electrons. Thus, the hybridization of Co-3d electrons with O-2p electrons will be substantially large.

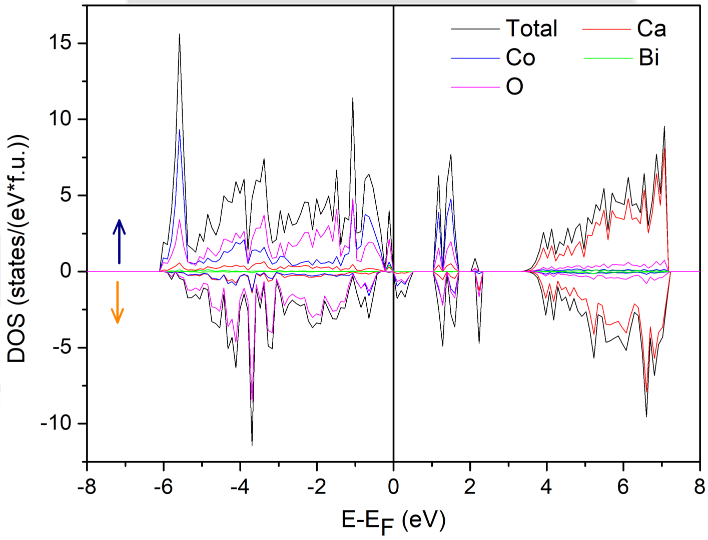

FIGURE 5.14: Calculated total DOS for $Ca_3Co_{1.833}Bi_{0.167}O_6$, where the E_F is set at zero. The ↑ and ↓ stand for the spin-up and spin-down states.

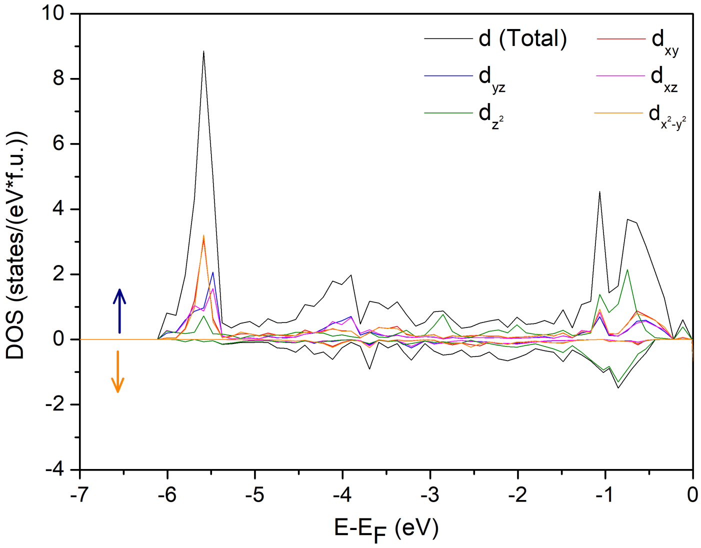

FIGURE 5.15: The *d*-orbital projected partial DOS of Co2 atom in $Ca_3Co_{1.833}Bi_{0.167}O_6$. The ↑ and ↓ stand for the spin-up and spin-down states.

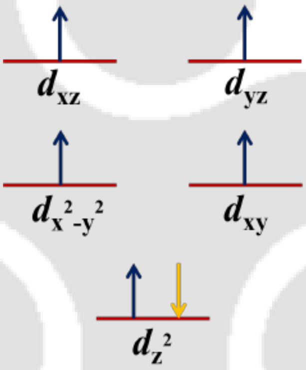

FIGURE 5.16: Schematic representation of *d*-orbital occupancy of Co2 atom for $Ca_3Co_{1.833}Bi_{0.167}O_6$.

In order to have a deeper insight into the spin structure of this system, we have calculated the spin-polarized orbital projected DOS of Co2 atoms, which confirms the high spin state of Co2 atom in trigonal prism environment (Fig. 5.15). Based on it, we propose the electronic configuration of the Co atom at the trigonal prism site (Fig. 5.16). The DOS results for spin up channel suggested that for Bi substitution, the first five electrons to be filled in d_{z^2} (↑), $d_{x^2-y^2}$ (↑), d_{xy} (↑), d_{xz} (↑), and d_{yz} (↑) spin-orbits, and the sixth electron occupies the d_{z^2} (↓) spin-orbit (Fig. 5.16). It confirms the high spin state of the Co^{3+} ion at the trigonal prism site. The calculated magnetic moment at each site is summarized in Table 5.3. These results indicate that the net magnetic moment of the

TABLE 5.3: Relative energies of different configurations among spin chains with respect to the ferromagnetic configuration. The calculated magnetic moment at each site of Co1, Co2, and O for $Ca_3Co_{1.833}Bi_{0.167}O_6$.

Relative energy (ΔE_r)		Magnetic moment	
Configuration	ΔE_r (meV)	Atom	Moment (μ_B)
Ferromagnetic	0	Co1	0.04
PDA	12	Co2	2.88
Ferrimagnetic	21	O	0.13

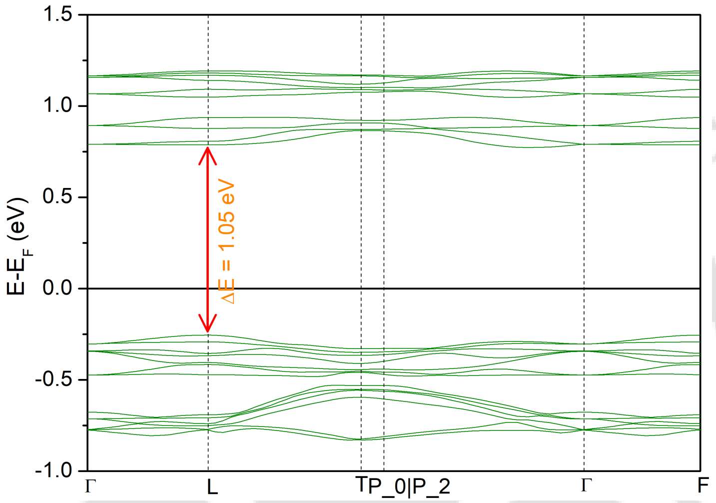

FIGURE 5.17: Band structure along the specified k-point direction in the first Brillouin zone for $Ca_3Co_{1.833}Bi_{0.167}O_6$.

system is mainly attributed to the high spin Co2 atoms. However, we observed a non-zero magnetic moment at the O site (Table 5.3), which is due to hybridization between Co-3d and O-2p states.

5.4.2 Band structure

It is clear from orbital projected DOS calculations that the magnetic and electronic structure remains unaltered with Bi substitutions. In order to have a deeper insight into the electronic structure of the system, we investigated the band structure of these systems. Fig. 5.17 shows the band structure of Bi substituted compound along high-symmetry direction of irreducible Brillouin zone. It consists of the conduction band and the valence band, where the Fermi level is set at zero (here the conduction band and valence band refer to the band above and below the Fermi level, respectively). We have found a direct band gap of 1.05 eV at L-point. Unlike the Mg substitution, no band crossing was observed for the Bi substitution, and the band profile looks similar to that for the parent compound (Fig. 4.15).

5.5 Discussion

In spin-frustrated systems, the characteristic features depend on lattice distortion, dipole-dipole interaction, crystal field effects, strength of exchange anisotropy, and surface spin disorder. It is evident from the XRD and magnetization results that the Bi-substitution has a considerable influence on the structural and magnetic properties, due to which the key parameters vary randomly. This behavior can be studied on the basis of two different aspects introduced by the Bi-ion substitution. The most common one is the reduced ferromagnetic character due to the presence of non-magnetic Bi-ions in the chain of Co1-Co2-Co1-Co2 ions. The reduced magnetization, T_{c1}, and decreased in-field transition strongly favor it. On the other hand, the increased value of T_{c2} and τ for intermediate Bi-substituted compounds is contrary to this (Table 5.2). Thus, to have a deeper insight into this, the second aspect of Bi-substitution, i.e., structural distortion, should be included. From the structural analysis, it is clear that the Bi-substitution led to increased crystallite size and lattice expansion, causing distortion of the lattice. In Bi-ion, the lone pair arises as a result of hybridization of $6s$ and $6p$ atomic orbitals with $6s^2$ electrons. The $6s^2$ lone pair of Bi^{3+} ions hybridize with O-$2p$ orbitals that lead to a covalent character of Bi-O bonds as well as change in Bi-O bond lengths, which can be seen from the random variation of bond-lengths and bond-angles with Bi-content (Table 5.1). Theoretical results based on first-principles calculations also suggested strong hybridization between Co-$3d$ and O-$2p$ electrons of the Bi-substituted compound (Fig. 5.14). The energy of this hybridization is much larger than the spin-orbit-coupling and coulomb correlation, due to which the variation of exchange interactions with Bi-substitution prevents the long-range ordered states in the system. Thus, the increased value of T_{c2} and τ with the content of Bi is likely a consequence of hybridization between the Co($3d$)/Bi($6s$) and O-$2p$ orbitals and increased magnetocrystalline anisotropy.

The observed results from the magnetization measurements suggested the origin of glassy feature in these systems is due to the combined effect of frustration, degeneracy in the ground state, and chemical disorder effects. Geometrical frustration in such systems is anticipated because of the triangular lattice arrangement, while magnetic frustration arises due to the competitive ferromagnetic (intra-chain) and antiferromagnetic (inter-chain) coupling. The unsaturated magnetic moment and large coercivity (≈ 1.6 T) confirm the frustration and random anisotropy. Moreover, the multi-steps in the isothermal M-H curves and the arrest of spin dynamics indicate the degeneracy in the magnetic ground state. On the other hand, the increased relaxation time for intermediate Bi compositions is attributed to the chemical disorder effect arising due to random variation of bond length and bond angle with Bi content. Thus, because of the complex origin of glassy features in these systems, the observed magnetization behavior for these systems is quite different from the conventional spin glass.

The memory and rejuvenation phenomena under cyclic temperature change indicate that the spin structure grown at a particular temperature does not irreversibly influence by the structure grown at different temperatures [230]. These features are associated with the inhomogeneous inter-cluster interactions among spins so that metastable states of significantly higher energies appear. In order to attain the ground state, the system has to overcome these anisotropic energy barriers. Thus, the initial state remains trapped for the negative temperature cycle (6 K $\rightarrow$ 2 K). In comparison, the system overcomes the energy barriers for the positive temperature cycle (2 K $\rightarrow$ 6 K); hence, no rejuvenation phenomenon was observed for the first cycle.

It is noticed from Fig. 5.11 that beyond the interrupting point (5400 sec), the magnetization corresponding to fixed temperatures 6 K and 2 K is almost constant, which is denoted by high (H) and low (L) levels, respectively. These states are easily recoverable in the temperature cycle experiments. Thus similar to the conventional route, the digital information can be coded corresponding to these levels [222, 226]. This information can be easily recovered by changing the temperature. Comparing with the previous route to achieve thermal memory, which is inefficient due to the long waiting time at the interrupting point (Fig. 5.9), the observed magnetization behavior for our systems has the potential to store the information in a short duration. Furthermore, from Fig.

5.12(a), it is clear that multiple levels L, H, and medium (M), can be created by taking relaxation measurements at three temporary cooling temperatures. It is important to note that the observed feature is not limited to three levels, but more levels can be made for multilevel data storage by including intermediate temperatures. The independence of this reversible phenomenon on the temperature ramp rate further makes the process faster (Fig. 5.12(b)).

In view of the technological importance, the viability of the storage media is one of the most crucial factors. A recent mean-field study of spin-glass for large system sizes suggested non-ergodicity in aging [231], indicating that the equilibrium will never be reached within the time window accessible by the experiments. The magnetic relaxation measurements under negative temperature cycle strongly favor these findings where the system does not overcome the trapped state even after changing the temperature (Fig. 5.11). Furthermore, Fig. 5.11 also depicts the non-volatility of the memory in these systems below T_{c2}. Therefore, the $Ca_3Co_2O_6$ system can be potentially used as a multilevel storage media based on thermal manipulation. Enhanced glassy feature with Bi substitution further makes the thermal memory cell more feasible.

5.6 Conclusion

We prepared polycrystalline samples of $Ca_3Co_{2-x}Bi_xO_6$ (x = 0, 0.05, 0.1, 0.15, and 0.2) by standard solid-state reaction method and proposed a new route of multilevel storage based on thermal manipulation that can be utilized in thermal memory cell to make it feasible. Rietveld refinement of XRD data confirms the single-phase formation, and the compound crystallizes in the rhombohedral structure with space group $R\bar{3}c$. The bond-length analysis indicates the interplay of reduced dimensionality and bond randomness effect. Magnetic properties were found to be sensitive to Bi-substitution, due to which the T_{c1} decreases while the T_{c2} increases. The μ_{eff} decreases monotonously with Bi-content, while θ shows unusual dependence on Bi-concentration. The phenomena of virgin M-H curves lying outside the M-H loop suggested the kinetic arrest of spin dynamics of the system. The cyclic temperature experiments have been performed to demonstrate the recurrence in the multilevels of the relaxed magnetization paths, which was not noticed earlier. The exquisite reproducibility of relaxed magnetization as a function of temperature under a non-equilibrium phase makes such a phenomenon unique. We showed that the information could be stored in terms of a constant magnetization value corresponding to each temperature below T_{c2}, which is easily recoverable with temperature cycling. Our results suggested that this new approach will be much more efficient than the reported ones and has the potential to make thermal memory devices faster and stable. This work will lead to the exploration in a variety of such materials having non-ergodicity as a possible route of thermal memory storage which should eventually lead a new outlook towards data storage.

Chapter 6

Summary and Conclusions

STUDY of the substitution effects of both magnetic and non-magnetic dopants in the various properties of the strongly correlated pseudo-1D spin chain compounds, including both theoretical and experimental aspects, to understand the underlying physics, is summarized in this chapter. Here we present the different aspects of magnetism and magnetic frustration arising due to magnetic and non-magnetic dopants in the spin structure, glassy behavior, and low dimensional characteristics of the system by a combined discussion on the structural features, static magnetic properties, dynamic magnetic behavior, and first-principles study. We also highlight the technological importance of the magnetically frustrated low-dimensional system in the thermal memory cell.

The present thesis discusses the structural, magnetic, and electronic properties of the substituted compounds $\mathrm{Ca_{3-x}Dy_xCo_2O_6}$ (x = 0, 0.1, 0.2, and 0.3), $\mathrm{Ca_3Co_{2-x}Mg_xO_6}$ (x = 0, 0.05, 0.1, 0.15, and 0.2), and $\mathrm{Ca_3Co_{2-x}Bi_xO_6}$ (x = 0.05, 0.1, 0.15, and 0.2). The $\mathrm{Dy^{3+}}$ ion has an ionic radius lower than the $\mathrm{Ca^{2+}}$ ion; therefore, with the substitution of Dy in this system, lattice shrinkage should be anticipated. However, the results obtained from the Rietveld refinement of X-ray diffraction data are contrary to this. The reduction of the $\mathrm{Co^{3+}}$ ion to $\mathrm{Co^{2+}}$ ion to maintain the charge neutrality with Dy substitution in this system may be the possible reason for this unusual trend because the $\mathrm{Co^{2+}}$ ion has a large ionic radius compared to the Co^{3+} ion. In addition, the Dy substitution leads to the increased separation of intra-chain magnetic ions while the inter-chain bond length decreases, which results in the reduced 1D character of the system. On the other hand, the characteristic features of the system remain preserved when the magnetic Co^{3+} site is doped with non-magnetic Mg^{2+} ions. The possible reason for such feature is the similar ionic radius of Mg^{2+} and Co^{3+} ions. However, the Mg^{2+} ion has a lower valence than the Co^{3+} ion; therefore, we could expect a hole-type substitution of Mg in this system. In addition to the higher (Dy^{3+}) and lower (Mg^{2+}) valence ion substitution in this system, we have also tried to influence its structural features by another non-magnetic dopant (Bi) of the same valence as the Co ion. The key advantage of Bi^{3+} ion substitution in this system is the bond randomness effect that arises due to the similar valence but a different ionic radius for both the elements (Co and Bi). Furthermore, the large ionic radius of Bi^{3+} ion compared to Co^{3+} ion leads to the increment in both a and c, which is dissimilar to the substitution effect of Dy and Mg. Thus, the structural analysis based on XRD results suggested three different aspects of substitution effects in the magnetic and electronic properties of the system, which requires a combined study to have a thorough understanding of such systems.

In order to clarify the electronic structure of the system, we combined the results from the X-ray photoelectron spectroscopy and the first-principle-based DFT calculations for all the samples. As anticipated from the Dy^{3+} ions substitution in the replacement of Ca^{2+} ions, the XPS results suggested that the relative percentage of Co^{2+} ions increases with the content of Dy. On the other hand, the replacement of Co^{3+} ions by Mg^{2+} ions leads to partial transform of Co^{3+} ions into Co^{4+} ions. In the first-principles-based DFT study, the parent compound $Ca_3Co_2O_6$ displays insulator/semiconductor behavior where no band crossing was observed at the Fermi level, and the band gap is 1.03 eV. The Bi-substituted compound exhibits a similar band profile with a band gap of 1.05 eV. On the other hand, band crossing at the Fermi level was observed for the Mg-substituted compound, and a hole-type Fermi surface was formed. The shifting of Fermi level towards the valence band also confirms the hole-type substitution of Mg in this system. Thus from these results, it is concluded that the Dy and Mg substitution in the $Ca_3Co_2O_6$ system leads to the electron and hole-type doping effects, respectively. On the other hand, the electronic structure remains unaltered with the substitution of Bi, which has the same valence as the Co ions.

Besides the substitution effect of electrons and holes in the electronic structure of the system, the Co^{3+} ions in this system have the possibility of spin state transition when doped with high or low valence ions. Understanding the electron and hole doping effects in the net magnetism of the pseudo-1D systems thus requires a combined discussion on the magnetic structures of these systems. The magnetization behavior for the parent compound $Ca_3Co_2O_6$ indicates highly anisotropic magnetic character and the significantly large value of g signifies the strong Ising-like features. For Dy substitution, the transition temperatures T_{c1} monotonically decreases with the content of Dy while the glassy feature is gradually suppressed. Such features originate from the reduced overlap of d_{z^2} orbitals of the intra-chain Co^{3+} (HS) ions that arise due to the elongation of the c-axis with the Dy content. On the other hand, the transition temperatures remain unaffected with the Mg content, primarily due to the unchanged structural parameters for the Mg substitution. The Bi substitution in this system leads to the bond-randomness effect, due to which the T_{c2} increases while the T_{c1} decreases. Such feature is attributed to the random variation of the bond length and bond angle with the content of Bi that randomly imbalances the inter-chain and intra-chain interactions, thereby providing frustration for the spin systems. In addition to the transition temperatures, the field-induced effects are highly susceptible to structural features. With Dy substitution, it is noticed that the H_c decreases, and the field-induced step at H_c smoothens out. Similar results were also observed for the Bi-substituted compounds. However, for the Mg substitution, the transition fields remain unchanged, and the step-like transitions, which is a characteristic feature of this pseudo-1D system, are robust and unaffected by large Mg substitution. Based on these results, it is concluded that the key features of the pseudo-1D systems remain unaltered as long as the low dimensionality relation holds. On the other hand, for the Dy and Bi substituted compounds where the lattice parameters vary drastically, the system loses its generality, and the characteristic low dimensional features are smoothened out. Furthermore, with Mg substitution in this system, the increased μ_{eff} with the content of non-magnetic ions is quite unusual. The increased value of μ_{eff} was referred to the spin-state transition of Co^{3+} ion $\left(\mathrm{S} = 2 \rightarrow \mathrm{S} = \frac{5}{2}\right)$ due to the hole-type substitution of Mg in this system, which was further confirmed by the XPS and first-principles-based results. It implies that substituting non-magnetic ions in the pseudo-1D systems can also enhance the magnetic moment and directly connected to the magnetism-related phenomena. However, for the Dy-doped systems, the large paramagnetic moment of Dy^{3+} ions suppresses the contribution from the induced Co^{2+} ions. On the other hand, the Bi ion has the same valence as the Co ion; therefore, μ_{eff} decreases monotonically with the content of Bi.

As the characteristic feature of this pseudo-1D system remains unaltered for Mg substitution, therefore for comparison, the magnetic structure of the parent and the Mg substituted compounds are also studied in the context of change in entropy calculations and Arrott plots. The obtained value of maximum entropy change and relative cooling power for a field difference of 3 T is nearly -1.5 $\text{Jkg}^{-1}\text{K}^{-1}$ and 19.1 J/kg, respectively. At the onset of the spin glass transition temperature (T_{c2}), there is a sign reversal of ΔS, indicating the coexistence of positive and negative magnetocaloric effect. Furthermore, to construct the magnetic structure of the system, the field dependence of ΔS at different constant temperatures has been used to map the transition fields. The Arrott plots further added the description of the magnetic structure of the systems.

Non-ergodicity in the frustrated materials leads to various fascinating features that are important from fundamental science and application perspectives. The dynamics of these systems based on magnetic relaxation measurements suggested ergodicity breaking for parent $Ca_3Co_2O_6$ and its Dy and Bi substituted compounds where the equilibrium is far away from the measurable time in experiments. On the other hand, for the Mg-substituted compound, the magnetization relaxes quickly. These results indicate different frustration mechanisms for the diluted spin chain systems. First of all, frustration occurs in both geometrical and magnetic manner for the pristine $Ca_3Co_2O_6$. The geometrical frustration occurs due to the triangular lattice arrangement, while the magnetic frustration originates from the competitive intra-chain ferromagnetic and inter-chain antiferromagnetic interactions. For the Dy-doped system, the decreased overlap of the d_{z^2} orbit of intra-chain Co^{3+} ions reduces the ferromagnetic magnetic coupling along the chain. Thus, the size of magnetic clusters forming the glassy state decreases. Similarly, substituting non-magnetic Mg ions also reduces the intra-chain ferromagnetic coupling due to the consequence of antiferromagnetically coupled induced Co^{4+} ions and the presence of non-magnetic Mg^{2+} ions in the chain of magnetic Co^{3+} ions. Thus, the non-ergodic $Ca_3Co_2O_6$ system switches to a weakly non-ergodic system by substituting Mg. On the other hand, the relaxation time for a few of the Bi-substituted compounds has been found higher than that for the parent $Ca_3Co_2O_6$. Such features are related to the intrinsic effects introduced by the substitution of Bi that produces in-site-originated disorder leading to a plethora of anisotropy. Therefore, in addition to the conventional geometrical and magnetic frustration, the chemical disorder effects arising due to Bi substitution enhance the glassy features of the system.

Owing to the out-of-equilibrium dynamics, the frustrated magnets have potential applications in the thermal memory cell. It can be considered a future alternative to electronic memory devices, which suffer performance degradation under harsh environments and electromagnetic radiation. The common thing among digital storage media is that the information is written in the memorizing medium with the help of an external field. For example, electric DRAM, magnetic hard disks, or electromagnetic laser light on CDs. Thus, magnetic storage can be affected under harsh environments and electromagnetic radiation. Furthermore, the magnetic storage media are sensitive to temperature and humidity and, therefore, can be influenced by thermal fluctuation. Here, in the case of the thermal memory cell, the information reading, writing, and processing are purely based on thermal manipulation, which is comparatively easily controllable. However, the conventional route used in the thermal memory cell based on memory effect experiment is inefficient because it requires long waiting at interrupting point. Thus, alternative methods based on thermal manipulation are necessary to make thermal memory cell feasible that can contribute to its future development. Here, we proposed a new route of multilevel storage based on the recurrence in the multilevel of the relaxed magnetization paths below T_{c2}. It is proven that this new route of multilevel storage will be much more efficient, faster, and stable than conventional ones. Thus this study will lead to the exploration in a variety of such materials having non-ergodicity as a possible route of thermal memory storage which should eventually lead a new outlook towards data storage.

Future Direction

Based on both the experimental and theoretical investigation of low dimensional frustrated magnets, this dissertation provides important insight into the tuneable magnetic and electronic structures of the diluted (magnetic/non-magnetic) spin-chain system and, using their non-equilibrium properties, lays the foundation of a new route of thermal manipulation used in thermal memory cell that can make multilevel storage faster and smoother. Thus this dissertation potentially opens up the scope for the further study of fundamental aspects in diluted pseudo-1D systems using X-ray magnetic circular dichroism and neutron diffraction. As the observed magnetization dynamics for parent and Bi-substituted samples have technological importance, but their operating temperature is quite low (6 K) therefore, the working temperatures need to be raised. Following are a few remarks that are underway to have a more detailed understanding of puzzling features of low dimensional magnets and can contribute to the future development of thermal memory cell.

- The first-principles-based DFT calculation performed in this thesis has been done using GGA + U approximation only. However, including the spin-orbit-coupling contribution may enhance our understanding of this complicated system.

- The spin dynamics of these systems can be studied by ac susceptibility measurements to understand the nature of energy barrier involved in the relaxation process.

- The observed results suggested semiconducting electron/hole-type doping for Dy/Mg in this system. In order to clarify it, transport experiments are necessary for conclusive evidence of semiconducting electron/hole-type behavior.

- The working temperature for cyclic thermal manipulation can be raised by the substitution of transition metals (Ir, Rh, and Mn) or by preparing the nano-composite of these samples.

Appendix A

List of Abbreviation

SDW	Spin-density Wave
LS	Low-spin
HS	High-spin
QTM	Quantum Tunneling of Magnetization
CG	Cluster-glass
PDA	Partially Disordered Antiferromagnetic
CAFM	Commensurate Antiferromagnetic
FESEM	Field Emission Scanning Electron Microscope
XPS	X-Ray Photoelectron Spectroscopy
PPMS	Physical Property Measurement System
XRD	X-ray Diffractometer
ΔE_{V}	Energy Gap
E_{V_1}	Vibrational Ground State
E_{V_2}	Vibrational Excited State
EDS	Energy Dispersive X-ray Spectroscopy
VSM	Vibrating Sample Magnetometer
ACMS II	AC Measurement System
TTO	Thermal Transport Option
LMT	Linear Motor Transport
DFT	Density Functional Theory
LDA	Local Density Approximation
GGA	Generalized Gradient Approximation
B88	Becke
PW91	Perdew and Wang
PBE	Perdew, Burke, and Enzerhof
LYP	Lee–Yang–Parr
SIC	Self-interaction Correction
HF	Hartree-Fock
FLL	Fully Localized Limit
AMF	Around Mean Field
PAW	Projector Augmented Wave
NCPP	Norm-Conserving Pseudopotentials
USPP	Ultrasoft Pseudopotentials
VASP	Vienna Ab initio Simulation Package
T_0	Vogel-Fulcher temperature
ZFC	Zero Field Cooled
FC	Field Cooled

$\boldsymbol{V}$	Volume of the Cell
$\boldsymbol{T}^*$	Splitting Temperature
$\boldsymbol{C}_{\mathrm{mol}}$	Molar Curie Constant
χ	DC Susceptibility
θ	Curie-Weiss Temperature
μ_{eff}	Effective Magnetic Moment
$\boldsymbol{k}_{\mathrm{B}}$	Boltzmann Constant
$\boldsymbol{N}_{\mathrm{A}}$	Avogadro Number
$\boldsymbol{g}$	Lande g-factor
$\boldsymbol{M}_{\mathrm{FC}}$	Magnetization Measured Under Field Cooled Condition
$\boldsymbol{M}_{\mathrm{ZFC}}$	Magnetization Measured Under Zero Field Cooled Condition
$\mu_{\mathrm{eff}}\mathbf{(cal)}$	Calculated Effective Magnetic Moment
$\boldsymbol{H}_{\mathrm{c}}$	Critical Field
$\boldsymbol{M}_{\downarrow}$	Magnetization for Ramping Down Cycle
$\boldsymbol{M}_{\uparrow}$	Magnetization for Ramping Up Cycle
μ_{B}	Bohr magneton
$\boldsymbol{B}_{\mathrm{J}}(\boldsymbol{x})$	Brillouin function
$\boldsymbol{T}_{\mathrm{c}}$	Critical Temperature
$\boldsymbol{M}_0$	Spontaneous Magnetization
$\boldsymbol{M}_1$	Glassy Component
τ	Relaxation Time
$\boldsymbol{n}$	Critical Exponent
τ_0	Activation Time
$\boldsymbol{T}_{\mathrm{A}}$	Activation Temperature
$\boldsymbol{E}_{\mathrm{A}}$	Activation Energy
$\boldsymbol{\Delta S}$	Change in Magnetic Entropy
$\boldsymbol{E}_{\mathrm{F}}$	Fermi Level
$\boldsymbol{J}$	Hund's Coupling Parameter
$\boldsymbol{U}$	Strength of Coulomb Interaction
$\chi_{\parallel}$	Parallel Susceptibility
$\chi_{\perp}$	Perpendicular Susceptibility
$\boldsymbol{J}_1$	Intra-chain Exchange Interaction Constant
$\boldsymbol{S}$	Entropy
$\boldsymbol{H}$	Magnetic Field
$\boldsymbol{T}$	Temperature
$\boldsymbol{M}$	Magnetization
$\boldsymbol{\Delta S}_{\mathrm{max}}$	Maximum Entropy Change
DOS	Total Density of State
$\boldsymbol{\Delta E}$	Band gap
IFCC	Interrupted Field Cooled Cooling Curve
FCW	Field-cooled Warming Curve

Bibliography

[1] E. Ising, "Beitrag zur theorie des ferromagnetismus," *Z. Phys.*, vol. 31, p. 0044, 1925.

[2] A. P. Petrović, D. Ansermet, D. Chernyshov, M. Hoesch, D. Salloum, P. Gougeon, M. Potel, L. Boeri, and C. Panagopoulos, "A disorder-enhanced quasi-one-dimensional superconductor," *Nat Commun.*, vol. 7, p. 12262, 2016.

[3] B. Bergk, A. P. Petrović, Z. Wang, Y. Wang, D. Salloum, P. Gougeon, M. Potel, and R. Lortz, "Superconducting transitions of intrinsic arrays of weakly coupled one-dimensional superconducting chains: the case of the extreme quasi-1D superconductor $Tl_2Mo_6Se_6$," *New J. Phys.*, vol. 13, p. 103018, 2011.

[4] J.-K. Bao, J.-Y. Liu, C.-W. Ma, Z.-H. Meng, Z.-T. Tang, Y.-L. Sun, H.-F. Zhai, H. Jiang, H. Bai, C.-M. Feng, Z.-A. Xu, and G.-H. Cao, "Superconductivity in Quasi-One-Dimensional $K_2Cr_3As_3$ with Significant Electron Correlations," *Phys. Rev. X*, vol. 5, p. 011013, 2015.

[5] K. Zhao, Q.-G. Mu, B. B. Ruan, T. Liu, B.-J. Pan, M.-H. Zhou, S. Zhang, G.-F. Chen, and Z.-A. Ren, "Synthesis and superconductivity of a novel quasi-one-dimensional ternary molybdenum pnictide $Cs_2Mo_3As_3$," *APL Mater.*, vol. 8, p. 031103, 2020.

[6] A. K. Bera and S. M. Yusuf, "Quantum phase transition from a spin-liquid state to a spin-glass state in the quasi-one-dimensional spin-*1* system $Sr_{1-x}Ca_xNi_2V_2O_8$," *Phys. Rev. B*, vol. 86, p. 024408, 2012.

[7] S. B. Lee, R. K. Kaul, and L. Balents, "Interplay of quantum criticality and geometric frustration in columbite," *Nat. Phys.*, vol. 6, p. 702, 2010.

[8] S. K. Upadhyay and E. V. Sampathkumaran, "Multiferroicity in a spin-chain compound, Tb_2BaCoO_5, with exceptionally large magnetodielectric coupling in polycrystalline form," *Appl. Phys. Lett.*, vol. 112, p. 262902, 2018.

[9] T. Basu, K. K. Iyer, K. Singh, and E. V. Sampathkumaran, "Novel dielectric anomalies due to spin-chains above and below Néel temperature in $Ca_3Co_2O_6$," *Sci. Rep.*, vol. 3, p. 3104, 2013.

[10] A. V. Koshelev, K. V. Zakharov, A. P. Pyatakov, L. V. Shvanskaya, A. A. Shakin, O. S. Volkova, D. A. Chareev, S. Kamusella, H.-H. Klauss, K. Molla, B. Rahaman, T. Saha-Dasgupta, and A. N. Vasiliev, "Spin-Order-Induced Ferroelectricity and Magnetoelectric Effect in $LiCuFe_2(VO_4)_3$," *Phys. Rev. Applied*, vol. 10, p. 034008, 2018.

[11] J. Y. Liu, J. Yu, J. L. Ning, H. M. Yi, L. Miao, L. J. Min, Y. F. Zhao, W. Ning, K. A. Lopez, Y. L. Zhu, T. Pillsbury, Y. B. Zhang, Y. Wang, J. Hu, H. B. Cao, B. C. Chakoumakos, F. Balakirev, F. Weickert, M. Jaime, Y. Lai, K. Yang, J. W. Sun, N. Alem, V. Gopalan, C. Z. Chang, N. Samarth, C. X. Liu, R. D. McDonald, and Z. Q. Mao, "Spin-valley locking and bulk quantum Hall effect in a noncentrosymmetric Dirac semimetal $BaMnSb_2$," *Nat. Commun.*, vol. 12, p. 4062, 2021.

[12] D. Hirobe, M. Sato, T. Kawamata, Y. Shiomi, K. Uchida, R. Iguchi, Y. Koike, S. Maekawa, and E. Saitoh, "One-dimensional spinon spin currents," *Nat. Phys.*, vol. 13, p. 30, 2017.

[13] S. Asai, T. Oyama, K. Nawa, A. Nakao, K. Munakata, K. Kuwahara, M. Hagihala, S. Itoh, Z. Hiroi, and T. Masuda, "Helical and collinear spin density wave order in the $S = \frac{1}{2}$ one-dimensional frustrated chain compound $NaCuMoO_4(OH)$ investigated by neutron scattering," *Phys. Rev. B*, vol. 101, p. 144437, 2020.

[14] S. Agrestini, C. L. Fleck, L. C. Chapon, C. Mazzoli, A. Bombardi, M. R. Lees, and O. A. Petrenko, "Slow Magnetic Order-Order Transition in the Spin Chain Antiferromagnet $Ca_3Co_2O_6$," *Phys. Rev. Lett.*, vol. 106, p. 197204, 2011.

[15] S. Kimura, M. Matsuda, T. Masuda, S. Hondo, K. Kaneko, N. Metoki, M. Hagiwara, T. Takeuchi, K. Okunishi, Z. He, K. Kindo, T. Taniyama, and M. Itoh, "Longitudinal Spin Density Wave Order in a Quasi-1D Ising-like Quantum Antiferromagnet," *Phys. Rev. Lett.*, vol. 101, p. 207201, 2008.

[16] S. E. Nikitin, S. Nishimoto, Y. Fan, J. Wu, L. S. Wu, A. S. Sukhanov, M. Brando, N. S. Pavlovskii, J. Xu, L. Vasylechko, R. Yu, and A. Podlesnyak, "Multiple fermion scattering in the weakly coupled spin-chain compound $YbAlO_3$," *Nat. Commun.*, vol. 12, p. 3599, 2021.

[17] J. Zeisner, M. Brockmann, S. Zimmermann, A. Weiße, M. Thede, E. Ressouche, K. Y. Povarov, A. Zheludev, A. Klümper, B. Büchner, V. Kataev, and F. Göhmann, "Anisotropic magnetic interactions and spin dynamics in the spin-chain compound $Cu(py)_2Br_2$: An experimental and theoretical study," *Phys. Rev. B*, vol. 96, p. 024429, 2017.

[18] H. Wu, M. W. Haverkort, Z. Hu, D. I. Khomskii, and L. H. Tjeng, "Nature of Magnetism in $Ca_3Co_2O_6$," *Phys. Rev. Lett.*, vol. 95, p. 186401, 2005.

[19] L. D. Sanjeewa, V. O. Garlea, R. S. Fishman, M. A. McGuire, J. Xing, H. Cao, J. W. Kolis, and A. S. Sefat, "Observation of a Large Magnetic Anisotropy and a Field-Induced Magnetic State in $SrCo(VO_4)(OH)$: A Structure with a Quasi One-Dimensional Magnetic Chain," *Inorg. Chem.*, vol. 59, p. 1029, 2020.

[20] W.-G. Yin, X. Liu, A. M. Tsvelik, M. P. M. Dean, M. H. Upton, J. Kim, D. Casa, A. Said, T. Gog, T. F. Qi, G. Cao, and J. P. Hill, "Ferromagnetic Exchange Anisotropy from Antiferromagnetic Superexchange in the Mixed 3d–5d Transition-Metal Compound Sr_3CuIrO_6," *Phys. Rev. Lett.*, vol. 111, p. 057202, 2013.

[21] E. V. Sampathkumaran and A. Niazi, "Superparamagnetic-like ac susceptibility behavior in the partially disordered antiferromagnetic compound Ca_3CoRhO_6," *Phys. Rev. B*, vol. 65, p. 180401, 2002.

[22] J. Singleton, J. W. Kim, C. V. Topping, A. Hansen, E.-D. Mun, S. Chikara, I. Lakis, S. Ghannadzadeh, P. Goddard, X. Luo, Y. S. Oh, S.-W. Cheong, and V. S. Zapf, "Magnetic properties of Sr_3NiIrO_6 and Sr_3CoIrO_6: Magnetic hysteresis with coercive fields of up to 55 T," *Phys. Rev. B*, vol. 94, p. 224408, 2016.

[23] A. Maignan, C. Michel, A. C. Masset, C. Martin, and B. Raveau, "Single crystal study of the one dimensional $Ca_3Co_2O_6$ compound: five stable configurations for the Ising triangular lattice," *Eur. Phys. J. B*, vol. 15, p. 657, 2000.

[24] P. Ding, L. Li, Y. J. Guo, Q. Y. He, X. S. Gao, and J.-M. Liu, "Influence of Co:Mn ratio on multiferroicity of $Ca_3Co_{2-x}Mn_xO_6$ around x 1," *Appl. Phys. Lett.*, vol. 97, p. 032901, 2010.

[25] V. Hardy, M. R. Lees, O. A. Petrenko, D. M. Paul, D. Flahaut, S. Hébert, and A. Maignan, "Temperature and time dependence of the field-driven magnetization steps in $Ca_3Co_2O_6$ single crystals," *Phys. Rev. B*, vol. 70, p. 064424, 2004.

[26] S. Toth, W. Wu, D. T. Adroja, S. Rayaprol, and E. V. Sampathkumaran, "Frustrated Ising chains on the triangular lattice in Sr_3NiIrO_6," *Phys. Rev. B*, vol. 93, p. 174422, 2016.

[27] A. Maignan, V. Hardy, S. Hébert, M. Drillon, M. R. Lees, O. Petrenko, D. M. Paul, and D. Khomskii, "Quantum tunneling of the magnetization in the Ising chain compound $Ca_3Co_2O_6$," *J. Mater. Chem.*, vol. 14, p. 1231, 2004.

[28] S. Aasland, H. Fjellvåg, and B. Hauback, "Magnetic properties of the one-dimensional $Ca_3Co_2O_6$," *Solid State Commun.*, vol. 101, p. 187, 1997.

[29] E. V. Sampathkumaran, N. Fujiwara, S. Rayaprol, P. K. Madhu, and Y. Uwatoko, "Magnetic behavior of Co ions in the exotic spin-chain compound $Ca_3Co_2O_6$ from ^{59}Co NMR studies," *Phys. Rev. B*, vol. 70, p. 014437, 2004.

[30] S. Agrestini, L. C. Chapon, A. Daoud-Aladine, J. Schefer, A. Gukasov, C. Mazzoli, M. R. Lees, and O. A. Petrenko, "Nature of the Magnetic Order in $Ca_3Co_2O_6$," *Phys. Rev. Lett.*, vol. 101, p. 097207, 2008.

[31] S. Agrestini, C. Mazzoli, A. Bombardi, and M. R. Lees, "Incommensurate magnetic ground state revealed by resonant x-ray scattering in the frustrated spin system $Ca_3Co_2O_6$," *Phys. Rev. B*, vol. 77, p. 140403, 2008.

[32] X. Y. Yao, S. Dong, and J. M. Liu, "Steplike magnetization of spin chains in a triangular lattice: Monte Carlo simulations," *Phys. Rev. B*, vol. 73, p. 212415, 2006.

[33] Y. B. Kudasov, "Steplike Magnetization in a Spin-Chain System: $Ca_3Co_2O_6$," *Phys. Rev. Lett.*, vol. 96, p. 027212, 2006.

[34] X. Yao, S. Dong, H. Yu, and J. Liu, "Monte Carlo simulation of magnetic behavior of a spin-chain system on a triangular lattice," *Phys. Rev. B*, vol. 74, p. 134421, 2006.

[35] L. Onsager, "Crystal Statistics. I. A Two-Dimensional Model with an Order-Disorder Transition," *Phys. Rev.*, vol. 65, p. 117, 1944.

[36] B. M. McCoy, "Encyclopedia of mathematical physics (oxford academic press, 2006)," p. 322–328.

[37] H. A. Kramers and G. H. Wannier, "Statistics of the Two-Dimensional Ferromagnet. Part I," *Phys. Rev.*, vol. 60, p. 252, 1941.

[38] S. Blundell, *Magnetism in Condensed Matter.* Oxford University Press Inc., New York, 2001.

[39] D. Jiles, *Introduction to Magnetism and Magnetic Materials.* CRC Press, Taylor Francis Group, 2015.

[40] A. H. Morrish, *Canted Antiferromagnetism: Hematite.* WORLD SCIENTIFIC, 1995.

[41] R. M. F. Houtappel, "Order-disorder in hexagonal lattices," *Physica*, vol. 16, p. 425, 1950.

[42] G. H. Wannier, "Antiferromagnetism. The Triangular Ising Net," *Phys. Rev.*, vol. 79, p. 357, 1950.

[43] K. Kanô and S. Naya, "Antiferromagnetism. The Kagomé Ising Net," *Prog. Theor. Phys.*, vol. 10, p. 158, 1953.

[44] R. Moessner and J. T. Chalker, "Properties of a Classical Spin Liquid: The Heisenberg Pyrochlore Antiferromagnet," *Phys. Rev. Lett.*, vol. 80, p. 2929, 1998.

[45] R. Moessner, "Low-temperature properties of classical geometrically frustrated antiferromagnets," *Phys. Rev. B*, vol. 58, p. 12049, 1998.

[46] S. Haravifard, Z. Yamani, and B. D. Gaulin, *Chapter 2 - Quantum Phase Transitions.* Academic Press, 2015.

[47] O. A. Starykh, "Unusual ordered phases of highly frustrated magnets: a review," *Rep. Prog. Phys.*, vol. 78, p. 052502, 2015.

[48] J. E. Greedan, "Geometrically frustrated magnetic materials," *J. Mater. Chem.*, vol. 11, p. 37, 2001.

[49] C. E. Violet and R. J. Borg, "Magnetic Ordering in Dilute Solid Solutions of Iron in Gold. I," *Phys. Rev.*, vol. 149, p. 540, 1966.

[50] V. Cannella and J. A. Mydosh, "Magnetic Ordering in Gold-Iron Alloys," *Phys. Rev. B*, vol. 6, p. 4220, 1972.

[51] C. N. Guy, "Gold-iron spin glasses in low DC fields. I. Susceptibility and thermoremanence," *Journal of Physics F: Metal Physics*, vol. 7, p. 1505, 1977.

[52] P. Svedlindh, P. Granberg, P. Nordblad, L. Lundgren, and H. S. Chen, "Relaxation in spin glasses at weak magnetic fields," *Phys. Rev. B*, vol. 35, p. 268, 1987.

[53] C. A. M. Mulder, A. J. van Duyneveldt, and J. A. Mydosh, "Frequency and field dependence of the ac susceptibility of the AuMn spin-glass," *Phys. Rev. B*, vol. 25, p. 515, 1982.

[54] J. A. Mydosh, "Spin glasses: An experimental introduction," 1993.

[55] G. E. Brodale, R. A. Fisher, W. E. Fogle, N. E. Phillips, and J. van Curen, "The effect of spin-glass ordering on the specific heat of CuMn," *J. Magn. Magn. Mater.*, vol. 31-34, p. 1331, 1983.

[56] C. A. Cardoso, F. M. Araujo-Moreira, V. P. S. Awana, E. Takayama-Muromachi, O. F. de Lima, H. Yamauchi, and M. Karppinen, "Spin glass behavior in $RuSr_2Gd_{1.5}Ce_{0.5}Cu_2O_{10-\delta}$," *Phys. Rev. B*, vol. 67, p. 020407, 2003.

[57] S. F. Edwards and P. W. Anderson, "Theory of spin glasses," *J. Phys. F*, vol. 5, p. 965, 1975.

[58] C. De Dominicis and I. Giardina, *Random Fields and Spin Glasses: A Field Theory Approach.* Cambridge: Cambridge University Press, 2006.

[59] D. L. Stein and C. M. Newman, *Spin Glasses and Complexity.* Princeton University Press, 2013.

[60] K. H. Fischer, "Static Properties of Spin Glasses," *Phys. Rev. Lett.*, vol. 34, pp. 1438–1441, 1975.

[61] ——, "Theory of spin glasses: Susceptibility and specific heat in a magnetic field," *Solid State Commun.*, vol. 18, pp. 1515–1517, 1976.

[62] S. K. Das, S. K. Joshi, and R. S. Tripathi, "Effect of Magnetic Field on the Susceptibility and the Specific Heat of Spin Glasses," *Phys. Status Solidi B*, vol. 108, pp. 581–586, 1981.

[63] D. Sherrington and S. Kirkpatrick, "Solvable Model of a Spin-Glass," *Phys. Rev. Lett.*, vol. 35, pp. 1792–1796, 1975.

[64] D. Panchenko, *The Sherrington-Kirkpatrick Model.* Springer New York, NY, 2015.

[65] M. Mezard, M. A. Virasoro, and G. Parisi, *Spin Glass Theory and Beyond.* Singapore: World Scientific, 2004.

[66] J. R. L. d. Almeida and D. J. Thouless, "Stability of the Sherrington-Kirkpatrick solution of a spin glass model," *J. Phys. A. Math. Gen.*, vol. 11, p. 983, 1978.

[67] H. J. Sommers, "Solution of the long-range gaussian-random Ising model," *Z. Phys. B*, vol. 31, pp. 301–307, 1978.

[68] ——, "The Sherrington-Kirkpatrick spin glass model: Results of a new theory," *Z. Phys. B*, vol. 33, pp. 173–180, 1979.

[69] A. J. Bray and M. A. Moore, "Replica-Symmetry Breaking in Spin-Glass Theories," *Phys. Rev. Lett.*, vol. 41, pp. 1068–1072, 1978.

[70] A. Blandin, "Theories versus experiments in the spin glass systems," *J. Phys. C*, vol. 39, pp. C6–1499, 1978.

[71] A. Blandin, M. Gabay, and T. Garel, "On the mean-field theory of spin glasses," *J. Phys. C*, vol. 13, p. 403, 1980.

[72] C. Dominicis and T. Garel, "A solution of Sherrington Kirkpatrick model for Ising spin glass with physically acceptable entropy," *J. Physique Lett.*, vol. 40, pp. 575 – 578, 1979.

[73] A. J. Bray and M. A. Moore, "Metastable states in spin glasses," *J. Phys. C*, vol. 13, p. L469, 1980.

[74] G. Parisi, “Infinite Number of Order Parameters for Spin-Glasses,” *Phys. Rev. Lett.*, vol. 43, pp. 1754–1756, 1979.

[75] ——, “A sequence of approximated solutions to the S-K model for spin glasses,” *J. Phys. A: Math Gen.*, vol. 13, p. L115, 1980.

[76] ——, “The order parameter for spin glasses: a function on the interval 0-1,” *J. Phys. A: Math Gen.*, vol. 13, p. 1101, 1980.

[77] C. M. Soukoulis and K. Levin, “Cluster Mean-Field Theory of Spin-Glasses,” *Phys. Rev. Lett.*, vol. 39, pp. 581–584, 1977.

[78] ——, “Cluster mean-field model of the spin glasses: static properties,” *Phys. Rev. B*, vol. 18, pp. 1439–1445, 1978.

[79] C. M. Soukoulis, “Thermodynamic properties of concentrated spin glasses: A cluster mean-field theory,” *Phys. Rev. B*, vol. 18, pp. 3757–3759, 1978.

[80] A. Mody and A. A. Rangwala, “Dynamics of a cluster model of spin glasses,” *Physica B+C*, vol. 106, pp. 68–82, 1981.

[81] H. Fjellvåg, E. Gulbrandsen, S. Aasland, A. Olsen, and B. C. Hauback, “Crystal Structure and Possible Charge Ordering in One-Dimensional $Ca_3Co_2O_6$,” *J. Solid State Chem.*, vol. 124, pp. 190–194, 1996.

[82] T. Burnus, Z. Hu, M. W. Haverkort, J. C. Cezar, D. Flahaut, V. Hardy, A. Maignan, N. B. Brookes, A. Tanaka, H. H. Hsieh, H. J. Lin, C. T. Chen, and L. H. Tjeng, “Valence, spin, and orbital state of Co ions in one-dimensional $Ca_3Co_2O_6$: An x-ray absorption and magnetic circular dichroism study,” *Phys. Rev. B*, vol. 74, p. 245111, 2006.

[83] B. Leedahl, M. Sundermann, A. Amorese, A. Severing, H. Gretarsson, L. Zhang, A. C. Komarek, A. Maignan, M. W. Haverkort, and L. H. Tjeng, “Origin of Ising magnetism in $Ca_3Co_2O_6$ unveiled by orbital imaging,” *Nat. Commun.*, vol. 10, p. 5447, 2019.

[84] R. Vidya, P. Ravindran, H. Fjellvåg, A. Kjekshus, and O. Eriksson, “Tailor-Made Electronic and Magnetic Properties in One-Dimensional Pure and Y-Substituted $Ca_3Co_2O_6$,” *Phys. Rev. Lett.*, vol. 91, p. 186404, 2003.

[85] H. Kageyama, K. Yoshimura, K. Kosuge, H. Mitamura, and T. Goto, “Field-Induced Magnetic Transitions in the One-Dimensional Compound $Ca_3Co_2O_6$,” *J. Phys. Soc. Jpn.*, vol. 66, pp. 1607–1610, 1997.

[86] M. Mekata, “Antiferro-Ferrimagnatic Transition in Triangular Ising Lattice,” *J. Phys. Soc. Jpn.*, vol. 42, pp. 76–82, 1977.

[87] K. Wada and T. Ishikawa, “Monte Carlo Study of a Triangular Ising Lattice. I,” *J. Phys. Soc. Jpn.*, vol. 52, pp. 1774–1780, 1983.

[88] S. Niitaka, K. Yoshimura, K. Kosuge, M. Nishi, and K. Kakurai, “Partially Disordered Antiferromagnetic Phase in Ca_3CoRhO_6,” *Phys. Rev. Lett.*, vol. 87, p. 177202, 2001.

[89] D. P. Kozlenko, N. T. Dang, N. O. Golosova, S. E. Kichanov, E. V. Lukin, P. J. Lampen Kelley, E. M. Clements, K. V. Glazyrin, S. H. Jabarov, T. L. Phan, B. N. Savenko, H. Srikanth, and M. H. Phan, "Pressure-induced modifications of the magnetic order in the spin-chain compound $Ca_3Co_2O_6$," *Phys. Rev. B*, vol. 98, p. 134435, 2018.

[90] P. Lampen, N. S. Bingham, M. H. Phan, H. Srikanth, H. T. Yi, and S. W. Cheong, "Macroscopic phase diagram and magnetocaloric study of metamagnetic transitions in the spin chain system $Ca_3Co_2O_6$," *Phys. Rev. B.*, vol. 89, p. 144414, 2014.

[91] V. Hardy, M. R. Lees, A. Maignan, S. Hébert, D. Flahaut, C. Martin, and D. M. Paul, "Specific heat investigation of the magnetic ordering in two frustrated spin-chain oxides: $Ca_3Co_2O_6$ and Ca_3CoRhO_6," *J. Phys. Condens. Matter.*, vol. 15, p. 5737, 2003.

[92] C. L. Fleck, M. R. Lees, S. Agrestini, G. J. McIntyre, and O. A. Petrenko, "Field-driven magnetisation steps in $Ca_3Co_2O_6$: A single-crystal neutron-diffraction study," *EPL*, vol. 90, p. 67006, 2010.

[93] T. Moyoshi and K. Motoya, "Incommensurate Magnetic Structure and Its Long-Time Variation in a Geometrically Frustrated Magnet $Ca_3Co_2O_6$," *J. Phys. Soc. Jpn.*, vol. 80, p. 034701, 2011.

[94] Y. B. Kudasov, "Magnetic structure and phase diagram in a spin-chain system: $Ca_3Co_2O_6$," *EPL*, vol. 78, p. 57005, 2007.

[95] O. A. Petrenko, J. Wooldridge, M. R. Lees, P. Manuel, and V. Hardy, "Single crystal neutron diffraction study of the magnetisation process in $Ca_3Co_2O_6$," *Eur. Phys. J. B*, vol. 47, p. 79–83, 2005.

[96] S. De and A. Banerjee, "Field-temperature induced dimensionality crossover in $Ca_3Co_2O_6$ spin system," *J. Magn. Magn. Mater.*, vol. 539, p. 168349, 2021.

[97] V. Hardy, D. Flahaut, R. Frésard, and A. Maignan, "Anisotropic susceptibility of the geometrically frustrated spin-chain compound $Ca_3Co_2O_6$," *J. Phys. Condens. Matter.*, vol. 19, p. 145229, 2007.

[98] K. Motoya, T. Kihara, H. Nojiri, Y. Uwatoko, M. Matsuda, and T. Hong, "Time and Magnetic Field Variations of Magnetic Structure in the Triangular Lattice Magnet $Ca_3Co_2O_6$," *J. Phys. Soc. Jpn.*, vol. 87, p. 114703, 2018.

[99] J. W. Kim, E. D. Mun, X. Ding, A. Hansen, M. Jaime, N. Harrison, H. T. Yi, Y. Chai, Y. Sun, S. W. Cheong, and V. S. Zapf, "Metastable states in the frustrated triangular compounds $Ca_3Co_{2-x}Mn_xO_6$ and $Ca_3Co_2O_6$," *Phys. Rev. B*, vol. 98, p. 024407, 2018.

[100] I. Nekrashevich, X. Ding, F. Balakirev, H. T. Yi, S. W. Cheong, L. Civale, Y. Kamiya, and V. S. Zapf, "Reaching the equilibrium state of the frustrated triangular Ising magnet $Ca_3Co_2O_6$," *Phys. Rev. B*, vol. 105, p. 024426, 2022.

[101] N. G. Hegde, I. Levatić, A. Magrez, H. M. Rønnow, and I. Živković, "Magnetic dynamics across the in-field transition in $Ca_3Co_2O_6$," *Phys. Rev. B*, vol. 102, p. 104418, 2020.

[102] A. D. King, C. D. Batista, J. Raymond, T. Lanting, I. Ozfidan, G. Poulin-Lamarre, H. Zhang, and M. H. Amin, "Quantum Annealing Simulation of Out-of-Equilibrium Magnetization in a Spin-Chain Compound," *PRX Quantum*, vol. 2, p. 030317, 2021.

[103] G. Allodi, P. Santini, S. Carretta, S. Agrestini, C. Mazzoli, A. Bombardi, M. R. Lees, and R. De Renzi, "Exchange interactions in $\mathrm{Ca_3Co_2O_6}$ probed locally by NMR," *Phys. Rev. B*, vol. 89, p. 104401, 2014.

[104] E. V. Sampathkumaran, Z. Hiroi, S. Rayaprol, and Y. Uwatoko, "Heat-capacity anomalies in the presence of high magnetic fields in the spin-chain compound, $\mathrm{Ca_3Co_2O_6}$," *J. Magn. Magn. Mater.*, vol. 284, pp. L7–L11, 2004.

[105] S. W. Cheong and M. Mostovoy, "Multiferroics: a magnetic twist for ferroelectricity," *Nat. Mater.*, vol. 6, pp. 13–20, 2007.

[106] T. H. Arima, "Spin-Driven Ferroelectricity and Magneto-Electric Effects in Frustrated Magnetic Systems," *J. Phys. Soc. Jpn.*, vol. 80, p. 052001, 2011.

[107] N. Bellido, C. Simon, and A. Maignan, "Magnetodielectric coupling in a triangular Ising lattice: Experiment and modeling," *Phys. Rev. B.*, vol. 77, p. 054430, 2008.

[108] P. L. Li, X. Y. Yao, K. F. Wang, C. L. Lu, F. Gao, and J. M. Liu, "Steplike magnetocapacitance and dielectric relaxation in spin frustrated $\mathrm{Ca_3Co_2O_6}$," *J. Appl. Phys.*, vol. 104, p. 054111, 2008.

[109] T. Basu, K. Singh, and E. V. Sampathkumaran, "Modifications in the frustrated magnetism, oxidation state of Co and magnetoelectric coupling effects induced by a partial replacement of Ca by Gd in the spin-chain compound $\mathrm{Ca_3Co_2O_6}$," *J. Phys. Condens. Matter.*, vol. 25, p. 496013, 2013.

[110] T. Basu, K. K. Iyer, K. Singh, K. Mukherjee, P. L. Paulose, and E. V. Sampathkumaran, "Anisotropic magnetodielectric coupling behavior of $\mathrm{Ca_3Co_{1.4}Rh_{0.6}O_6}$ due to geometrically frustrated magnetism," *Appl. Phys. Lett.*, vol. 105, p. 102912, 2014.

[111] J. Shi, J. D. Song, J. C. Wu, X. Rao, H. L. Che, Z. Y. Zhao, H. D. Zhou, J. Ma, R. R. Zhang, L. Zhang, X. G. Liu, X. Zhao, and X. F. Sun, "Ferroelectricity of structural origin in the spin-chain compounds $\mathrm{Ca_3Co_{2-x}Mn_xO_6}$," *Phys. Rev. B.*, vol. 96, p. 064112, 2017.

[112] T. Basu, K. K. Iyer, P. L. Paulose, and E. V. Sampathkumaran, "Dielectric anomalies and magnetodielectric coupling behavior of single crystalline $\mathrm{Ca_3Co_2O_6}$, a geometrically frustrated magnetic spin-chain system," *J. Alloys Compd.*, vol. 675, pp. 364–369, 2016.

[113] K. Meera, R. Muralidharan, T. Y. Koo, and Y. H. Jeong, "Enhanced magneto dielectric effect on oxygen annealed geometrically frustrated spin-chain compound: $\mathrm{Ca_3Co_2O_6}$," *Solid State Commun.*, vol. 299, p. 113650, 2019.

[114] A. Banerjee, J. Sannigrahi, S. Giri, and S. Majumdar, "Polaronic charge transfer and large dielectric constant in $\mathrm{Ca_3CoRhO_6}$," *Phys. Status Solidi B.*, vol. 253, pp. 1849–1854, 2016.

[115] K. K. Iyer, T. Basu, K. Singh, and E. V. Sampathkumaran, "Dielectric and magnetodielectric behavior of polycrystalline $\mathrm{Ca_3CoRhO_6}$, a geometrically frustrated magnetic system," *AIP Conf. Proc.*, vol. 1665, p. 140045, 2015.

[116] N. Bellido, C. Simon, and A. Maignan, "Magnetodielectric coupling in $Ca_3Co_2O_6$ triangular Ising lattice," *J. Magn. Magn. Mater.*, vol. 321, pp. 1770–1772, 2009.

[117] S. D. Kaushik, S. Rayaprol, J. Saha, N. Mohapatra, V. Siruguri, P. D. Babu, S. Patnaik, and E. V. Sampathkumaran, "Magnetodielectric coupling in Ca_3CoMnO_6 triangular Ising lattice," *J. Appl. Phys.*, vol. 108, p. 084106, 2010.

[118] A. Jain, S. M. Yusuf, S. S. Meena, and C. Ritter, "Stabilization of the spin density wave structure with rare-earth substitution in $Ca_3Co_2O_6$," *Phys. Rev. B*, vol. 87, p. 094411, 2013.

[119] J. Y. Song, B. C. Zhao, Y. N. Huang, Y. F. Qin, X. B. Zhu, W. H. Song, and Y. P. Sun, "Structure, magnetic, electrical and thermal transport properties of Dy-doped $Ca_3Co_2O_6$ ceramics," *Ceram. Int.*, vol. 42, pp. 8955–8961, 2016.

[120] J. Y. Song, B. C. Zhao, Y. N. Huang, Y. F. Qin, J. F. Zhou, W. H. Song, and Y. P. Sun, "Tuning of magnetic interaction and transport properties of $Ca_3Co_2O_6$ through Sm-doping," *J. Alloys Compd.*, vol. 695, pp. 2506–2512, 2017.

[121] C. H. Hervoches, H. Fjellvåg, A. Kjekshus, V. M. Fredenborg, and B. C. Hauback, "Structure and magnetism of rare-earth-substituted $Ca_3Co_2O_6$," *J. Solid State Chem.*, vol. 180, pp. 628–635, 2007.

[122] G. Gong, Y. Wang, Y. Su, D. Liu, G. Zerihun, and Y. Qiu, "Effects of Ho-ion substitution on the magnetic properties of the $Ca_3Co_2O_6$ frustrated spin-chain compound," *Mater. Res. Bull.*, vol. 99, pp. 419–423, 2018.

[123] H. Kageyama, S. Kawasaki, K. Mibu, M. Takano, K. Yoshimura, and K. Kosuge, "Mössbauer Observation of the Quantum Levels of Fe^{3+} Ions Doped in 1D Ising Ferromagnet $Ca_3Co_2O_6$," *Phys. Rev. Lett.*, vol. 79, pp. 3258–3261, 1997.

[124] A. Jain, S. Singh, and S. M. Yusuf, "Structural and magnetic properties of spin chain compounds $Ca_3Co_{2-x}Fe_xO_6$," *Phys. Rev. B*, vol. 74, p. 174419, 2006.

[125] R. Das, N. T. Dang, V. Kalappattil, R. P. Madhogaria, D. P. Kozlenko, S. E. Kichanov, E. V. Lukin, A. V. Rutkaukas, T. P. T. Nguyen, L. T. P. Thao, N. S. Bingham, H. Srikanth, and M. H. Phan, "Unraveling the nature of Fe-doping mediated inter- and intra-chain interactions in $Ca_3Co_2O_6$," *J. Alloys Compd.*, vol. 851, p. 156897, 2021.

[126] J. Chen, Z. W. Ouyang, N. M. Xia, S. S. Sheng, Y. Y. Wu, Z. C. Xia, and L. Li, "Crystal structure, magnetic properties and ESR spectra of $Ca_3Co_{2-x}Fe_xO_6$," *J. Alloys Compd.*, vol. 511, pp. 139–143, 2012.

[127] A. Jain and S. M. Yusuf, "Short-range and long-range incommensurate magnetic ordering in the frustrated antiferromagnets $Ca_3Co_{2-x}Fe_xO_6$: A neutron diffraction study," *Phys. Rev. B*, vol. 83, p. 184425, 2011.

[128] A. Jain, S. M. Yusuf, J. Campo, and L. Keller, "Magnetic ordering in the spin-chain compounds $Ca_3Co_{2-x}Fe_xO_6$ ($x = 0.2$ and 0.4): A neutron diffraction study," *Phys. Rev. B*, vol. 79, p. 184428, 2009.

[129] I. Nowik, A. Jain, S. M. Yusuf, and J. V. Yakhmi, "Effect of Fe substitution on the magnetic ordering in $Ca_3(Co_{1-x}Fe_x)_2O_6$," *Phys. Rev. B*, vol. 77, p. 054403, 2008.

[130] S. M. Yusuf, A. Jain, and L. Keller, “Field induced incommensurate-to-commensurate magnetic phase transition in $\mathrm{Ca_3Co_{1.8}Fe_{0.2}O_6}$: a neutron diffraction study,” *J. Phys. Condens. Matter*, vol. 25, p. 146001, 2013.

[131] Z. W. Ouyang, S. S. Sheng, J. Chen, X. M. Shi, M. Y. Ruan, Z. C. Xia, and L. Li, “Spin-glass-like freezing in spin-chain compounds $\mathrm{Ca_3Co_{2-x}Mn_xO_6}$: Effect of disorder,” *J. Appl. Phys.*, vol. 112, p. 103923, 2012.

[132] M. Y. Ruan, Z. W. Ouyang, S. S. Sheng, X. M. Shi, Z. C. Xia, and G. H. Rao, “Effect of Mn doping on the 1/3 magnetization step in $\mathrm{Ca_3Co_{2-x}Mn_xO_6}$,” *J. Magn. Magn. Mater.*, vol. 341, pp. 118–121, 2013.

[133] V. Kiryukhin, S. Lee, W. Ratcliff, Q. Huang, H. T. Yi, Y. J. Choi, and S. W. Cheong, “Order by Static Disorder in the Ising Chain Magnet $\mathrm{Ca_3Co_{2-x}Mn_x}\mathbf{O_6}$,” *Phys. Rev. Lett.*, vol. 102, p. 187202, 2009.

[134] T. Lancaster, S. J. Blundell, P. J. Baker, H. J. Lewtas, W. Hayes, F. L. Pratt, H. T. Yi, and S. W. Cheong, “Spin freezing and dynamics in $\mathrm{Ca_3Co_{2-x}Mn_xO_6}$ ($\mathrm{x} \approx 0.95$) investigated with implanted muons: Disorder in the anisotropic next-nearest-neighbor Ising model,” *Phys. Rev. B*, vol. 80, p. 020409, 2009.

[135] D. Flahaut, A. Maignan, S. Hébert, C. Martin, R. Retoux, and V. Hardy, “Chromium site selective substitution in $\mathrm{Ca_3Co_2O_6}$: Influence on the magnetic properties of an Ising-like triangular lattice,” *Phys. Rev. B*, vol. 70, p. 094418, 2004.

[136] Y. J. Choi, H. T. Yi, S. Lee, Q. Huang, V. Kiryukhin, and S. W. Cheong, “Ferroelectricity in an Ising Chain Magnet,” *Phys. Rev. Lett.*, vol. 100, p. 047601, 2008.

[137] H. Wu, T. Burnus, Z. Hu, C. Martin, A. Maignan, J. C. Cezar, A. Tanaka, N. B. Brookes, D. I. Khomskii, and L. H. Tjeng, “Ising Magnetism and Ferroelectricity in $\mathrm{Ca_3CoMnO_6}$,” *Phys. Rev. Lett.*, vol. 102, p. 026404, 2009.

[138] Y. Zhang, H. J. Xiang, and M. H. Whangbo, “Interplay between Jahn-Teller instability, uniaxial magnetism, and ferroelectricity in $\mathrm{Ca_3CoMnO_6}$,” *Phys. Rev. B*, vol. 79, p. 054432, 2009.

[139] S. Rayaprol, K. Sengupta, and E. V. Sampathkumaran, “Magnetic frustration in the stoichiometric spin-chain compound $\mathrm{Ca_3CoIrO_6}$,” *Phys. Rev. B*, vol. 67, p. 180404, 2003.

[140] ——, “Structural and magnetic anomalies among the spin-chain compounds, $\mathrm{Ca_3Co_{1+x}Ir_{1-x}O_6}$,” *J. Chem. Sci.*, vol. 115, pp. 553–560, 2003.

[141] M. Y. Ruan, Z. W. Ouyang, J. Chen, S. S. Sheng, Z. C. Xia, and L. Li, “Effect of nonmagnetic Sc ion on the intrachain coupling in spin-chain compounds $\mathrm{Ca_3Co_{2-x}Sc_xO_6}$,” *J. Appl. Phys.*, vol. 111, p. 043910, 2012.

[142] A. R. West, *Solid State Chemistry and Its Applications.* Wiley India Pvt. Limited, 2007.

[143] P. Hagenmuller, *Preparative methods in solid state chemistry.* Academic Press New York, 1972.

[144] H. Mehrer, *Diffusion in Solids: Fundamentals, Methods, Materials, Diffusion-Controlled Processes.* Springer Berlin Heidelberg, 2007.

[145] B. D. Cullity and S. R. Stock, *Elements of X-ray Diffraction.* Prentice-Hall, 2001.

[146] H. M. Rietveld, "A profile refinement method for nuclear and magnetic structures," *J. Appl. Crystallogr.*, vol. 2, pp. 65–71, 1969.

[147] J. Rodríguez-Carvajal, "Recent advances in magnetic structure determination by neutron powder diffraction," *Physica B Condens. Matter*, vol. 192, pp. 55–69, 1993.

[148] E. Smith and G. Dent, *Modern Raman Spectroscopy – A Practical Approach.* John Wiley Sons, Ltd, 2004.

[149] B. Schrader, *Infrared and Raman spectroscopy: methods and applications.* VCH, 1995.

[150] C. N. Banwell and E. M. McCash, *Fundamentals of molecular spectroscopy.* McGraw-Hill, 1994.

[151] N. Brodusch, H. Demers, and R. Gauvin, *Field Emission Scanning Electron Microscopy.* Springer Singapore, 2017.

[152] J. I. Goldstein, D. E. Newbury, J. R. Michael, N. W. M. Ritchie, J. H. J. Scott, and D. C. Joy, *Scanning Electron Microscopy and X-Ray Microanalysis.* Springer New York, NY, 2017.

[153] J. Chastain, *Handbook of X-ray photoelectron spectroscopy.* Perkin-Elmer Corporation, 1993.

[154] C. Nordling, E. Sokolowski, and K. Siegbahn, "Precision Method for Obtaining Absolute Values of Atomic Binding Energies," *Phys. Rev.*, vol. 105, pp. 1676–1677, 1957.

[155] P. van der Heide, *X-ray Photoelectron Spectroscopy: An introduction to Principles and Practices.* John Wiley Sons, Ltd, 2011.

[156] S. Foner, "Versatile and Sensitive Vibrating-Sample Magnetometer," *Rev. Sci. Instrum.*, vol. 30, pp. 548–557, 2004.

[157] M. Born and R. Oppenheimer, "Zur Quantentheorie der Molekeln," *Annalen der Physik*, vol. 389, pp. 457–484, 1927.

[158] L. Thomas, "The calculation of atomic fields," *Math. Proc. Camb. Philos. Soc.*, vol. 23, pp. 542–548, 1927.

[159] E. Fermi, "Un metodo statistico per la determinazione di alcune priopriet̀a dell'atomo," *Rend. Accad. Naz. Lincei*, vol. 6, pp. 602–607, 1927.

[160] P. A. M. Dirac, "Note on Exchange Phenomena in the Thomas Atom," *Math. Proc. Camb. Philos. Soc.*, vol. 26, pp. 376–385, 1930.

[161] P. Hohenberg and W. Kohn, "Inhomogeneous Electron Gas," *Phys. Rev.*, vol. 136, pp. B864–B871, 1964.

[162] R. M. Martin, *Electronic Structure: Basic Theory and Practical Methods.* Cambridge University Press, 2004.

[163] W. Kohn and L. J. Sham, "Self-Consistent Equations Including Exchange and Correlation Effects," *Phys. Rev.*, vol. 140, pp. A1133–A1138, 1965.

[164] R. M. Dreizler and E. K. U. Gross, *Density Functional Theory.* Springer Berlin, Heidelberg, 2012.

[165] R. G. Parr and Y. Weitao, *Density-Functional Theory of Atoms and Molecules.* Oxford University Press, 1995.

[166] M. Gell-Mann and K. A. Brueckner, "Correlation Energy of an Electron Gas at High Density," *Phys. Rev.*, vol. 106, pp. 364–368, 1957.

[167] W. J. Carr, "Energy, Specific Heat, and Magnetic Properties of the Low-Density Electron Gas," *Phys. Rev.*, vol. 122, pp. 1437–1446, 1961.

[168] D. M. Ceperley and B. J. Alder, "Ground State of the Electron Gas by a Stochastic Method," *Phys. Rev. Lett.*, vol. 45, pp. 566–569, 1980.

[169] J. P. Perdew and A. Zunger, "Self-interaction correction to density-functional approximations for many-electron systems," *Phys. Rev. B*, vol. 23, pp. 5048–5079, 1981.

[170] S. H. Vosko, L. Wilk, and M. Nusair, "Accurate spin-dependent electron liquid correlation energies for local spin density calculations: a critical analysis," *Can. J. Phys.*, vol. 58, pp. 1200–1211, 1980.

[171] O. Gunnarsson and B. I. Lundqvist, "Exchange and correlation in atoms, molecules, and solids by the spin-density-functional formalism," *Phys. Rev. B*, vol. 13, pp. 4274–4298, 1976.

[172] J. P. Perdew and W. Yue, "Accurate and simple density functional for the electronic exchange energy: Generalized gradient approximation," *Phys. Rev. B*, vol. 33, pp. 8800–8802, 1986.

[173] A. D. Becke, "Density-functional exchange-energy approximation with correct asymptotic behavior," *Phys. Rev. A*, vol. 38, pp. 3098–3100, 1988.

[174] J. P. Perdew, K. Burke, and M. Ernzerhof, "Generalized Gradient Approximation Made Simple," *Phys. Rev. Lett.*, vol. 77, pp. 3865–3868, 1996.

[175] J. P. Perdew, J. A. Chevary, S. H. Vosko, K. A. Jackson, M. R. Pederson, D. J. Singh, and C. Fiolhais, "Atoms, molecules, solids, and surfaces: Applications of the generalized gradient approximation for exchange and correlation," *Phys. Rev. B*, vol. 46, pp. 6671–6687, 1992.

[176] K. Terakura, T. Oguchi, A. R. Williams, and J. Kübler, "Band theory of insulating transition-metal monoxides: Band-structure calculations," *Phys. Rev. B*, vol. 30, pp. 4734–4747, 1984.

[177] A. Svane and O. Gunnarsson, "Transition-metal oxides in the self-interaction-corrected density-functional formalism," *Phys. Rev. Lett.*, vol. 65, pp. 1148–1151, 1990.

[178] V. I. Anisimov, J. Zaanen, and O. K. Andersen, "Band theory and Mott insulators: Hubbard U instead of Stoner I," *Phys. Rev. B*, vol. 44, pp. 943–954, 1991.

[179] V. I. Anisimov, F. Aryasetiawan, and A. I. Lichtenstein, "First-principles calculations of the electronic structure and spectra of strongly correlated systems: the LDA + U method," *J. Phys. Condens. Matter*, vol. 9, p. 767, 1997.

[180] S. L. Dudarev, G. A. Botton, S. Y. Savrasov, C. J. Humphreys, and A. P. Sutton, "Electron-energy-loss spectra and the structural stability of nickel oxide: An LSDA+U study," *Phys. Rev. B*, vol. 57, pp. 1505–1509, 1998.

[181] S. Massidda, M. Posternak, and A. Baldereschi, "Hartree-Fock LAPW approach to the electronic properties of periodic systems," *Phys. Rev. B*, vol. 48, pp. 5058–5068, 1993.

[182] F. M. F. de Groot, J. C. Fuggle, B. T. Thole, and G. A. Sawatzky, "2p x-ray absorption of 3d transition-metal compounds: An atomic multiplet description including the crystal field," *Phys. Rev. B*, vol. 42, pp. 5459–5468, 1990.

[183] V. I. Anisimov, I. V. Solovyev, M. A. Korotin, M. T. Czyżyk, and G. A. Sawatzky, "Density-functional theory and NiO photoemission spectra," *Phys. Rev. B*, vol. 48, pp. 16 929–16 934, 1993.

[184] M. T. Czyżyk and G. A. Sawatzky, "Local-density functional and on-site correlations: The electronic structure of La_2CuO_4 and $LaCuO_3$," *Phys. Rev. B*, vol. 49, pp. 14 211–14 228, 1994.

[185] J. C. Slater and G. F. Koster, "Simplified LCAO Method for the Periodic Potential Problem," *Phys. Rev.*, vol. 94, pp. 1498–1524, 1954.

[186] K. Koepernik and H. Eschrig, "Full-potential nonorthogonal local-orbital minimum-basis band-structure scheme," *Phys. Rev. B*, vol. 59, pp. 1743–1757, 1999.

[187] O. K. Andersen, "Linear methods in band theory," *Phys. Rev. B*, vol. 12, pp. 3060–3083, 1975.

[188] P. E. Blöchl, "Projector augmented-wave method," *Phys. Rev. B*, vol. 50, pp. 17 953–17 979, 1994.

[189] D. R. Hamann, M. Schlüter, and C. Chiang, "Norm-Conserving Pseudopotentials," *Phys. Rev. Lett.*, vol. 43, pp. 1494–1497, 1979.

[190] D. Vanderbilt, "Soft self-consistent pseudopotentials in a generalized eigenvalue formalism," *Phys. Rev. B*, vol. 41, pp. 7892–7895, 1990.

[191] K. Laasonen, R. Car, C. Lee, and D. Vanderbilt, "Implementation of ultrasoft pseudopotentials in ab initio molecular dynamics," *Phys. Rev. B*, vol. 43, pp. 6796–6799, 1991.

[192] K. Laasonen, A. Pasquarello, R. Car, C. Lee, and D. Vanderbilt, "Car-Parrinello molecular dynamics with Vanderbilt ultrasoft pseudopotentials," *Phys. Rev. B*, vol. 47, pp. 10 142–10 153, 1993.

[193] J. C. Slater, "Wave Functions in a Periodic Potential," *Phys. Rev.*, vol. 51, pp. 846–851, 1937.

[194] D. J. Singh, *Planewaves, Pseudopotentials and the LAPW Method.* Springer New York, NY, 2013.

[195] K. Binder and A. P. Young, "Spin glasses: Experimental facts, theoretical concepts, and open questions," *Rev. Mod. Phys.*, vol. 58, pp. 801–976, 1986.

[196] V. Hardy, D. Flahaut, M. R. Lees, and O. A. Petrenko, "Magnetic quantum tunneling in $Ca_3Co_2O_6$ studied by ac susceptibility: Temperature and magnetic-field dependence of the spin-relaxation time," *Phys. Rev. B*, vol. 70, p. 214439, 2004.

[197] K. Jonason, E. Vincent, J. Hammann, J. P. Bouchaud, and P. Nordblad, "Memory and Chaos Effects in Spin Glasses," *Phys. Rev. Lett.*, vol. 81, pp. 3243–3246, 1998.

[198] A. Bhattacharyya, S. Giri, and S. Majumdar, "Spin-glass-like state in GdCu: Role of phase separation and magnetic frustration," *Phys. Rev. B*, vol. 83, p. 134427, 2011.

[199] Y. Kamiya and C. D. Batista, "Formation of Magnetic Microphases in $Ca_3Co_2\mathbf{O}_6$," *Phys. Rev. Lett.*, vol. 109, p. 067204, 2012.

[200] G. Allodi, R. De Renzi, S. Agrestini, C. Mazzoli, and M. R. Lees, "NMR study of magnetic order, metamagnetic transitions, and low-temperature spin freezing in $Ca_3Co_2O_6$," *Phys. Rev. B*, vol. 83, p. 104408, 2011.

[201] V. Hardy, S. Lambert, M. R. Lees, and D. McK. Paul, "Specific heat and magnetization study on single crystals of the frustrated quasi-one-dimensional oxide $Ca_3Co_2O_6$," *Phys. Rev. B*, vol. 68, p. 014424, 2003.

[202] H. Kageyama, K. Yoshimura, K. Kosuge, M. Azuma, M. Takano, H. Mitamura, and T. Goto, "Magnetic Anisotropy of $Ca_3Co_2O_6$ with Ferromagnetic Ising Chains," *J. Phys. Soc. Jpn.*, vol. 66, pp. 3996–4000, 1997.

[203] S. De and A. Banerjee, "Influence of cooling field on field induced magnetic states in $Ca_3Co_2\mathbf{O}_6$ compound," *Physica B Condens. Matter.*, vol. 572, pp. 125–128, 2019.

[204] D. L. Rousseau, R. P. Bauman, and S. P. S. Porto, "Normal mode determination in crystals," *J. Raman Spectrosc.*, vol. 10, pp. 253–290, 1981.

[205] S. Gohil, K. K. Iyer, P. Aswathi, S. Ghosh, and E. V. Sampathkumaran, "Raman study of $Ca_3Co_2\mathbf{O}_6$ single crystals," *J. Appl. Phys.*, vol. 108, p. 103517, 2010.

[206] J. Song, B. Zhao, Y. Huang, Y. Qin, J. Zhou, W. Song, and Y. Sun, "Carrier type change induced by fluorine doping in spin-chain compound $Ca_3Co_2\mathbf{O}_6$," *RSC Adv.*, vol. 7, pp. 2745–2752, 2017.

[207] V. A. Sirenko and V. V. Eremenko, "Irreversibility and anisotropy of the low-temperature magnetization in manganites. Spin-glass polyamorphism," *Low Temp. Phys.*, vol. 40, pp. 179–184, 2014.

[208] Z. Alborzi Avanaki and A. Hassanzadeh, "Modified Brillouin function to explain the ferromagnetic behavior of surfactant-aided synthesized α-Fe_2O_3 nanostructures," *J. Theor. Appl. Phys.*, vol. 7, p. 19, 2013.

[209] C. A. Angell, "Entropy and Fragility in Supercooling Liquids," *J. Res. Natl. Inst. Stand. Technol.*, vol. 102, pp. 171–185, 1997.

[210] A. Vasiliev, O. Volkova, E. Zvereva, and M. Markina, "Milestones of low-D quantum magnetism," *npj Quantum Mater.*, vol. 3, p. 18, 2018.

[211] R. Baral, H. S. Fierro, L. M. Martinez, S. R. Singamaneni, and H. S. Nair, "Low dimensional magnetism in the trirutile tantalates $Co_{1-x}Mg_xTa_2O_6$ with weak-ferromagnetic features," *J. Appl. Phys.*, vol. 125, p. 033904, 2019.

[212] Y. Karaki, K. Kuga, K. Kimura, S. Nakatsuji, K. Matsubayashi, and Y. Uwatoko, "Magnetic Order in the Frustrated Ising Quasi-One Dimensional Compound NaCo(acac)$_3$.Benzene," *J. Phys. Soc. Jpn.*, vol. 84, p. 084708, 2015.

[213] R. Shukla and R. S. Dhaka, "Anomalous magnetic and spin glass behavior in Nb-substituted $LaCo_{1-x}Nb_xO_3$," *Phys. Rev. B*, vol. 97, p. 024430, 2018.

[214] G. J. Kumar, A. Banerjee, A. S. K. Sinha, Y. Su, K. Nemkovski, and C. Rath, "Cation distribution and magnetic properties of Zn-substituted $CoCr_2O_4$ nanoparticles," *J. Appl. Phys.*, vol. 123, p. 223905, 2018.

[215] G. Kresse and J. Furthmüller, "Efficient iterative schemes for ab initio total-energy calculations using a plane-wave basis set," *Phys. Rev. B*, vol. 54, p. 11169, 1996.

[216] S. Li, Y. Li, M. Bäumer, and L. V. Moskaleva, "Assessment of PBE+U and HSE06 methods and determination of optimal parameter U for the structural and energetic properties of rare earth oxides," *J. Chem. Phys.*, vol. 153, p. 164710, 2020.

[217] M. Capdevila-Cortada, Z. Łodziana, and N. López, "Performance of DFT+U Approaches in the Study of Catalytic Materials," *ACS Catal.*, vol. 6, pp. 8370–8379, 2016.

[218] P. E. Blöchl, O. Jepsen, and O. K. Andersen, "Improved tetrahedron method for Brillouin-zone integrations," *Phys. Rev. B*, vol. 49, pp. 16 223–16 233, 1994.

[219] R. Dingle, M. E. Lines, and S. L. Holt, "Linear-Chain Antiferromagnetism in $[(CH_3)_4N]$ $[MnCl_3]$," *Phys. Rev.*, vol. 187, pp. 643–648, 1969.

[220] V. K. Pecharsky and K. A. J. Gschneidner, "Magnetocaloric effect from indirect measurements: Magnetization and heat capacity," *J. Appl. Phys.*, vol. 86, pp. 565–575, 1999.

[221] T. Burnus, Z. Hu, H. Wu, J. C. Cezar, S. Niitaka, H. Takagi, C. F. Chang, N. B. Brookes, H. J. Lin, L. Y. Jang, A. Tanaka, K. S. Liang, C. T. Chen, and L. H. Tjeng, "X-ray absorption and x-ray magnetic dichroism study on Ca_3CoRhO_6 and Ca_3FeRhO_6," *Phys. Rev. B*, vol. 77, p. 205111, 2008.

[222] J. Dolinšek, M. Feuerbacher, M. Jagodič, Z. Jagličić, M. Heggen, and K. Urban, "A thermal memory cell," *J. Appl. Phys.*, vol. 106, p. 043917, 2009.

[223] R. Xie, C. T. Bui, B. Varghese, Q. Zhang, C. H. Sow, B. Li, and J. T. L. Thong, "An Electrically Tuned Solid-State Thermal Memory Based on Metal–Insulator Transition of Single-Crystalline VO_2 Nanobeams," *Adv. Funct. Mater.*, vol. 21, pp. 1602–1607, 2011.

[224] R. W. Johnson, J. L. Evans, P. Jacobsen, J. R. Thompson, and M. Christopher, "The changing automotive environment: high-temperature electronics," *IEEE Trans. Electron. Packag. Manuf.*, vol. 27, pp. 164–176, 2004.

[225] D. C. Schmitt, J. C. Prestigiacomo, P. W. Adams, D. P. Young, S. Stadler, and J. Y. Chan, "Field-pulse memory in a spin-glass," *Appl. Phys. Lett.*, vol. 103, p. 082403, 2013.

[226] Z. Jagličić, D. Pajić, Z. Trontelj, J. Dolinšek, and M. Jagodič, "Magnetic memory effect in multiferroic $K_3Fe_5F_{15}$ and $K_3Cr_2Fe_3F_{15}$," *Appl. Phys. Lett.*, vol. 102, p. 242410, 2013.

[227] P. E. Jönsson, R. Mathieu, P. Nordblad, H. Yoshino, H. A. Katori, and A. Ito, "Nonequilibrium dynamics of spin glasses: Examination of the ghost domain scenario," *Phys. Rev. B*, vol. 70, p. 174402, 2004.

[228] A. Kumar, R. P. Tandon, and V. P. S. Awana, "Study of spin glass and cluster ferromagnetism in $\mathrm{RuSr_2Eu_{1.4}Ce_{0.6}Cu_2O_{10-\delta}}$ magneto superconductor," *J. Appl. Phys.*, vol. 110, p. 043926, 2011.

[229] F. Lefloch, J. Hammann, M. Ocio, and E. Vincent, "Can Aging Phenomena Discriminate Between the Droplet Model and a Hierarchical Description in Spin Glasses?" *Europhys. Lett.*, vol. 18, p. 647, 1992.

[230] S. Miyashita and E. Vincent, "A microscopic mechanism for rejuvenation and memory effects in spin glasses," *Eur. Phys. J. B*, vol. 22, pp. 203–211, 2001.

[231] M. Bernaschi, A. Billoire, A. Maiorano, G. Parisi, and F. Ricci-Tersenghi, "Strong ergodicity breaking in aging of mean-field spin glasses," *PNAS*, vol. 117, pp. 17 522–17 527, 2020.

LIST OF PUBLICATIONS

From Thesis work

1. Gajendra Singh Bisht and D Pal, "**Magnetic properties and Cluster-glass phenomena in 1-D spin chain compound** $Ca_{3-x}Dy_xCo_2O_6$," J. Magn. Magn. Mater. **537** 168141 (2021).
2. Gajendra Singh Bisht and D Pal, "**Memory and rejuvenation effect on the cluster-glass phase of 1-D spin-chain compound** $Ca_3Co_{2-x}Bi_xO_6$," J. Phys. Conf. Ser. **2164** 012047 (2022).
3. Gajendra Singh Bisht and D Pal, "**Spin-state transition of Co ion ($S = 2 \rightarrow S = 5/2$) in hole substituted 1-D chain of** $Ca_3Co_2O_6$," J. Phys.: Condens. Matter **34** 285803 (2022).
4. Gajendra Singh Bisht and D Pal, "**Effects on the glassy phase and electronic structure of** $Ca_3Co_2O_6$ **through Mg and Bi substitution**," Physica B Condens. Matter **654** 414707 (2023).
5. Gajendra Singh Bisht and D Pal, "**Multilevel thermal memory cell based on cyclic temperature experiment under glassy phase of frustrated magnet**," J. Phys. D: Appl. Phys. **56** 325001 (2023).
6. Gajendra Singh Bisht and D Pal, "**Correlation between magnetic and dielectric anomalies arising due to spin-chain arrangements in the paramagnetic phase of 1-D** $Ca_3Co_{1.9}Bi_{0.1}O_6$," J. Phys. Conf. Ser. **2518** 012001 (2023).

Outside the Thesis work

1. P Pathak, Gajendra Singh Bisht and A Srinivasan, "**Enhanced Magnetic Properties of Electrodeposited** Co_2FeSn **Film with High Structural Order**," J. Electrochem. Soc. **169** 092508 (2022).

2. Manisha Srivastava, Gajendra Singh Bisht and A Srinivasan, "**Single domain** Co_2FeGa **nanoparticles with high crystalline order synthesized by templateless chemical method**," J. Alloys Compd. **949** 169848 (2023).

National and International Conferences

1. Gajendra Singh Bisht and D Pal, "**Memory and rejuvenation effect on the cluster-glass phase of 1-D spin-chain compound** $Ca_3Co_{2-x}Bi_xO_6$," International Conference on Strongly Correlated Electron Systems (SCES 2020) **Oral** (invited).
2. Gajendra Singh Bisht and D Pal, "**Off-equillibrium dynamics manifested through memory and rejuvenation effets in 1-D spin-chain compound** $Ca_3Co_{2-x}Bi_xO_6$," International Conference on Advanced Materials And Mechanical Characterization (ICAMMC-2021) **Oral** (best oral presentation award).
3. Gajendra Singh Bisht and D Pal, "**Systematic study of large anisotropy in low-dimensional material and related peculiar magnetic phenomena**," North-East Research Conclave (NERC 2022) **Oral**.
4. Gajendra Singh Bisht and D Pal, "**Effects on the Glassy Phase of** $Ca_3Co_2O_6$ **Through Mg and Bi Substitution**," 29th International Conference on Low Temperature Physics (LT29) **Poster**.
5. Gajendra Singh Bisht and D Pal, "**Correlation between magnetic and dielectric anomalies arising due to spin-chain arrangements in the paramagnetic phase of 1-D** $Ca_3Co_{1.9}Bi_{0.1}O_6$," Emergent phenomena in Quantum Materials (E-QMAT) 2022 **Poster**.
6. Gajendra Singh Bisht and D Pal, "**Cluster-glass behavior in** $Ca_3Co_2O_6$ **and its substituents**," Around-the-Clock Around-the-Globe Magnetics Conference (ATC-ATG 2020) **Poster**.

Awards/Honor/Talks

- International Conference on Strongly Correlated Electron Systems (*SCES 2020*) *Oral* **(invited)**
- International Conference on Advanced Materials And Mechanical Characterization (*ICAMMC-2021*) (***best oral presentation award***)
- National Eligibility Test (*NET*) for Junior Research Fellowship (*JRF*) and for Lectureship (*LS*) in *PHYSICAL SCIENCE* conducted by Council of Scientific and Industrial Research (*CSIR*) **(2017)**
- National Eligibility Test (*NET*) for Junior Research Fellowship (*JRF*) and for Lectureship (*LS*) in *PHYSICAL SCIENCE* conducted by University Grants Commission (*UGC*) **(2018)**
- Graduation Aptitude Test in Engineering (*GATE*) **(2016)** in *PHYSICS*